Characterizing and Modeling the Effects of Mode Mixity and Bond Line Thickness on the Traction-Separation Response of Structural Adhesive Joints

by

Brock Watson

A thesis

presented to the University of Waterloo

in fulfillment of the

thesis requirement for the degree of

Doctor of Philosophy

in

Mechanical and Mechatronics Engineering

Waterloo, Ontario, Canada, 2021

Examining Committee Membership

The following served on the Examining Committee for this thesis. The decision of the Examining Committee is by majority vote.

External Examiner	David L. DuQuesnay Professor, Royal Military College of Canada
Supervisors	Duane Cronin Professor, University of Waterloo
	Michael Worswick Professor, University of Waterloo
Internal Examiner	John Montesano Assistant Professor, University of Waterloo
Internal Examiner	Adrian Gerlich Associate Professor, University of Waterloo
Internal-External Examiner	Thomas Willett Assistant Professor, University of Waterloo

Author's Declaration

I hereby declare that I am the sole author of this thesis. This is a true copy of the thesis, including any required final revisions, as accepted by my examiners.

I understand that my thesis may be made electronically available to the public.

Abstract

As adhesive bonding continues to become more prevalent in automotive structures, the need for high fidelity characterization and modelling of adhesive joints has gained in importance. In this thesis, new specimen geometry and analysis techniques are presented to characterize the properties necessary to model the traction-separation response in Mode I, Mode II, and mixed mode (MM) loading of adhesive joints using cohesive zone modelling (CZM) techniques. First, the Rigid Double Cantilever Beam (RDCB) geometry and analysis technique was developed to measure the full traction-separation response of a structural adhesive under Mode I loading. This test approach represents a substantial improvement over current test methodologies, where additional tests are required to extract the parameters necessary to construct the full traction-separation response. Next, the Bonded Shear Specimen (BSS) sample geometry was developed to measure the Mode II traction-separation response, using optical methods to measure separation. The BSS test was then adapted to allow for measurement of MM loading, providing the full traction-separation response for a range of mode mixity (ratio of shear to normal separation) and bond line thickness combinations. Statistically significant differences between the parameters necessary to construct the traction-separation response were found for different bond line thicknesses, identifying that bond line thickness should be accounted for in a generalizable CZM definition. With the full traction-separation response characterized for Mode I, Mode II and MM loading of nominal bond line thicknesses ranging from 0.18 mm to 0.64 mm, several deficiencies in current CZM implementations were identified. Critically, the MM traction-separation response is poorly predicted using conventional CZM implementations and the hardening response exhibited by the adhesive during Mode II and MM loading is not represented in current implementations. Validation testing was undertaken using more traditional Tapered Double Cantilever Beam

(TDCB) and Single Lap Shear (SLS) test specimens to provide independent test data with which to assess CZM models integrating the characterization data from the RDCB, BSS and MM specimens. These validation tests were selected due to the well controlled nature of the Mode I (TDCB) and MM (SLS) loading. One limitation of these tests, however, is the large levels of elastic and plastic deformation of the adherends, making the measured force and displacement highly dependant on the adherend properties.

To address the deficiencies identified in current CZMs, a new CZM modelling approach was developed, termed the Enhanced Mixed Mode Cohesive Zone Model (EMC). The benefit of the proposed ECM model was the integration of mode mixity and bond line thickness based on the measured experimental data. Using these data, the EMC model could predict the traction-separation response for any arbitrary mode mixity and bond line thickness combination rather than be inferred from relationships based on mixed mode energy release rates. Using this approach, in conjunction with the inclusion of the hardening behaviour observed experimentally, the MM traction-separation response was significantly improved relative to contemporary CZM implementations. Second, a single set of material parameters could be used to model bond line thickness and mode mixity effects, which is not possibly in current CZM approaches. Models of the RDCB, BSS and MM characterization tests using the EMC were shown to reduce the difference between the model predictions and measured traction and separation responses by more than half compared to a conventional CZM formulation. Unlike models of the characterization tests, the EMC models of the TDCB and SLS validation tests provided similar levels of fit to the test force, displacement and rotation data compared to a traditional CZM implementation, associated with large deflections and plastic deformation of the adherends, highlighting that important aspects of a CZM predictions can be masked depending on the load case for which the model is used. The

EMC model provided the greatest benefit in load cases where less adherend deformation was present, which is important in cases where high strength materials are to be bonded, such as modern ultra high-strength steel automotive bodies-in-white.

The traction-separation characterization methodology developed in this work led to the development of an improved CZM formulation, which demonstrated significant improvements in the ability to model the mechanical response of adhesive joints of various bond line thicknesses under Mode I, Mode II and mixed modes of loading.

Acknowledgments

First and foremost, I would like to acknowledge the extraordinary guidance and encouragement provided to me by my supervisors Duane Cronin and Mike Worswick. Duane, thank you for your continual support and mentorship over the dozen or so years since I first walked into your office and thank you for reminding me that it's what you learn after you know it all that really matters. Mike, thank you for your candor, your support, and sharing your insight, which informed not only the technical aspects of this work, but also hammered home the importance of communication.

I would like to gratefully acknowledge the financial support provided for this research by Honda Research and Development Americas, the 3M Canada Company, ArcelorMittal, the Natural Sciences and Engineering Research Council of Canada, the Government of Ontario, the Toyota Canada Automotive Safety Graduate Scholarship, the Alan Plumtree Graduate Scholarship, the Department of Mechanical and Mechatronics Engineering and the University of Waterloo. Additionally, the computational infrastructure provided by Compute Canada was invaluable in the completion of this research.

I would also like to thank Professor Cliff Butcher for his guidance and support during the development of the cohesive zone model in this work and Professor Hamid Jahed for the use of his test equipment during a critical time of this research. Additionally, without the support of our research associates, Jose Imbert-Boyd and Ryan George, lab technicians Tom Gawel, Eckhard Budziarek, Jeff Wemp, Andy Barber, Neil Griffett, Karl Janzen, and Doug Hirst, and our administrative staff Debbie Collins, Denise Porter, and Laurie Wilfong, this work would not have been possible. While I thank all members of the research groups of Professors Cronin and Worswick for their support during my studies, I would specifically like to thank my fellow adhesives researchers who stuck with me from start to finish; Luis Trimino, Yogi Nandwani, Khalid Boqaileh, Chi-Hsiang Liao, Brian Liu, Yu Zeng, Ahmed Ibrahim, Devin Hartlen, and Ramin Chitsaz Dehghani.

Finally, and most importantly, I cannot express what the unconditional love and support of my friends and family has meant to me, not only during my doctoral studies, but in all things that I do. As Joe Strummer said, "Without people, you're nothing".

Table of Contents

List of Figures

List of Tables

Nomenclature

b	Length of the bond line
B	Specimen thickness
D	Damage parameter
$E_{adherend}$	Young's modulus of adherend
E_I, E_{II}	Initial stiffness of traction-separation response in pure Mode I and Mode II loading
f_{G1}, f_{G2}	Ratio of area under plastic region of traction - separation response to critical energy release rate in Mode I and Mode II loading
F	Applied force measured by load cell
G_c	Mixed mode critical energy release rate
G_{IC}, G_{IIC}	Critical energy release rates for pure Mode I and pure Mode II loading
G_I, G_{II}	Mode I and Mode II contribution to mixed mode energy release rate
L	Distance from the edge of the specimen to the point of loading for RDCB specimen
S_{init}	Initial slope of bulk adhesive tensile stress-strain response for RDCB specimen
$t(x)$, $t(\delta)$	Arbitrary traction-displacement and traction-separation functions
t_c	Compression traction
T, S	Peak (plateau), undamaged traction in pure Mode I and Mode II loading
T_{max}, S_{max}	Peak (plateau) traction in pure Mode I and Mode II loading, when damage is considered
v	Length on axis perpendicular to bond line with origin at center of bond line for RDCB specimen
x	Length on axis parallel to bond line with origin at $\mu = 0$ for RDCB specimen
α	Rigidity ratio for RDCB specimen, mode mixity parameter for power law failure
δ	Crack opening (separation)
δ_3	Mode I direction separation in the element coordinate system
δ_I	Mode I separation
δ_{II}	Mode II separation
δ_c	Closing separation at the edge of the specimen due to the compression of the bond line for RDCB specimen
δ_m	Mixed mode separation
δ_I^0, δ_{II}^0	Separation-to-plateau response in pure Mode I and Mode II loading
δ^0	Mixed mode separation-to-plateau response
δ_I^d, δ_{II}^d	Separation-to-damage initiation in pure Mode I and Mode II loading
δ^d	Mixed mode separation-to-damage initiation
δ_I^f, δ_{II}^f	Separation-to-failure in pure Mode I and Mode II loading
δ_f	Mixed mode separation-to-failure
$\Delta\delta_I$, $\Delta\delta_{II}$	Separation increment in Mode I and Mode II
Δ	Load point opening displacement for RDCB specimen
β,Θ	Mode mixity parameter
θ_m	Mode mixity angle
θ_s	Nominal specimen angle
σ_{Res}	Resultant traction in direction of loading
σ_1, σ_2	Shear stress in the 1 and 2 element direction
σ_3	Mode I stress in the element coordinate system

σ_I	Mode I stress
σ_{II}	Mode II stress
η,γ	Mode mixity parameters for Benzeggagh – Kenane failure definition
$\upsilon_{adherend}$	Poisson's ratio of adherend material
μ	Distance from edge of specimen to transition between tensile and compressive loading of bond line for RDCB specimen

List of Acronyms and Initialisms

BIW	Body-in-white
BK	Benzeggagh-Kenane
CZM	Cohesive zone model
DCB	Double cantilever beam
DIC	Digital image correlation
DSLR	Digital single-lens reflex
EMC	Enhanced mixed mode cohesive zone model
ENF	End notch flexural
FE	Finite element
LEFM	Linear elastic fracture mechanics
LVDT	Linear variable differential transformer
MM	Mixed mode
RDCB	Rigid double cantilever beam
SD	Standard deviation
SLS	Single lap shear
TALS	Thick adherend lap shear
TDCB	Tapered double cantilever beam
UCZM	User-defined cohesive zone model

Chapter 1 Introduction

Adhesives have been used for millennia to create and repair useful objects, with some adhesively bonded objects dating from as far back as 3000 BC [Thrall & Shannon, 1985]. The use of structural adhesives, which are "a bonding agent used for transferring required loads between adherends exposed to service environments typical for the structure involved" [ASTM D907, 2012], is a much more recent phenomenon. In particular, the development of multi-material bodies-in-white (BIW) in automotive design, including high-strength steel, aluminum, carbon fiber reinforced polymers, all joined using adhesives, has been an increasing focus for vehicle manufacturers [Banea *et al*., 2018]. A modern automotive BIW generally consists of components formed from sheet metal (historically steel), which is spot welded together to create the primary load-bearing structure of the vehicle. The increase in multi-material BIW design has been driven by the need to reduce vehicle mass in order to improve fuel efficiency [US Federal Register, 2012; Natural Resources Canada, 2015], electric vehicle range, and ultimately to reduce greenhouse gas emissions [EU Parliament, 2014]. The BIW is also critical during crash loading to absorb kinetic energy and maintain the integrity of the occupant compartment. Vehicle crash testing is in a constant state of evolution, with new, more stringent test protocols being introduced [NHTSA, 2015] to reduce occupant injury risk in vehicle crash scenarios. The need to reduce vehicle mass to improve fuel economy and reduce CO_2 emissions while simultaneously improving vehicle crashworthiness are two competing design constraints, with larger, heavier vehicles tending to be safer in vehicle-to-vehicle impacts, all else being equal [IIHS, 2009]. Such competing design constraints drive the need to optimize multi-material structures, which requires advanced material

joining (including adhesive bonding), for structural and crash loading scenarios [Avalle *et al*., 2010].

To ensure the safety of vehicle occupants, it is critical to understand the mechanical behavior of multi-material structures under crash loading. The behavior of traditional materials (*e.g*. steel and aluminum) and joining techniques (e.g. resistance spot welding) that have been used in energy absorbing crash structures have been studied extensively [Palmonella *et al*., 2005], although there has more recently been an increase in use of adhesives to join multi-material structures [Pujol, 2010]. Adhesive bonding and hybrid joining, using adhesives in addition to more conventional joining techniques, have been shown to be a useful approach to join multi-material structures [Meschke *et al.,* 2017]. The need for high-fidelity characterization is important in modern vehicle design in which finite element modeling is used extensively during the design phase to virtually crash test the vehicle prior to the development of expensive prototypes [Becker *et al*., 2005]. Thus, the current study is focused on the development of new methods to characterize the traction-separation response of adhesives in complex loading conditions and using this characterization data to build accurate and efficient finite element models for use in full-scale vehicle crashworthiness simulation.

1.1 Motivation for Research

The primary motivation for the current research was driven by the need to join multi-material BIW. To utilize the hybrid joining techniques necessary in multi material BIW construction, adhesive-only joints need to be understood, characterized, and modeled with a high degree of fidelity. A study investigating hybrid joining of AZ61 magnesium using laser seam welding found that with 12 mm overlap, the adhesively-only joined shear specimens failed at 6.6 kN compared to 3 kN in

specimens joined only by laser welding [Ren *et al*., 2012]. When these two joining techniques were combined to create a hybrid joint, the shear force to failure increased to 7.4 kN. This study found that under Mode I loading there was little difference in peel strength between the hybrid joint (327 N) compared to the laser welded joint (320 N), while the adhesive only joint was significantly lower in strength (210 N). In another investigation of joining dissimilar metals, 45 mm wide specimens of 2 mm thick 6016-T6 aluminum were joined to 1.5 mm thick press-hardened high-strength boron steel using clinching, self-piercing rivets, a proprietary self-tapping screw design, resistance element welding and friction element welding. The average shear failure force for these technologies was 5.86 kN (maximum 7.99 kN). When hybrid joints were created with the aforementioned joining techniques in conjunction with an adhesive using a 16 mm overlap, the average shear failure force increased to 17.7 kN (maximum 18.2 kN). However, when only adhesive was used the failure force increased still further to 19.6 kN [Meschut *et al*., 2014] demonstrating the superior performance of adhesive joints in certain loading conditions (particularity under shear loading).

Conklin *et al*. [2015] discuss a project aimed at reducing vehicle mass beginning with a typical modern vehicle (2013 Ford Fusion) weighing 3431 lb (1556 kg) and having a BIW weighing 695 lb (315 kg), accounting for over 20% of the total vehicle mass. Through a number of techniques, including extensive use of structural adhesives, Conklin *et al*. were able to reduce the BIW weight to 509 lb (231 kg), a savings of 27% while maintaining acceptable vehicle crash performance in a 40% overlap frontal barrier test [IIHS, 2014]. In the BIW built in the Conklin *et al*. study, aluminum and steel were joined using structural adhesives and self-piercing rivets. The authors noted that the use of adhesives prevented direct contact between the two dissimilar metals, thus preventing galvanic corrosion, and kept moisture from contacting any non-coated metallic

surfaces. In similar work [Goded, 2009], the mass of the BIW of a Volkswagen Golf Mk V was reduced from 281 kg to 180 kg (a 35% reduction) through extensive use of high strength steel, magnesium, aluminum, and fiber reinforced polymers. Advanced joining, including adhesive bonding, was described as "the key for cost-efficient high-volume assembling of multi-material structures" [Goded, 2009] with 98 m of adhesively bonded joints being used to create a prototype BIW, along with various welding and mechanical fastening techniques.

The ability to implement adhesive joints in full-scale vehicle models is dependant on the ability to characterize these joints. A typical approach to characterizing an adhesive for implementation in CAE [May *et al.*, 2015] required compiling data from a number of tests to extract some of the parameters necessary to describe the adhesive in the model. Important parameters include peak traction, initial stiffness and critical energy release rate in the tensile opening, in-plane shear loading mode and mixed mode, along with a description of the shape of the traction-separation response. Additional inverse modelling was also required to fully characterize the model parameters of the adhesive, using tests that may or may not be sensitive to these same parameters, particularity those describing the shape of the traction-separation response, depending on the adhesive used [Rocha & Campilho, 2018]. This approach has several limitations. First, many tests are required to fully characterize an adhesive, with each test often providing only a single parameter for the model. Aside from the inefficiency of such testing, variability that may occur with respect to surface preparation, curing characteristics and experimental methodologies is more likely to occur with a higher number of independent tests. The number of tests can easily become unwieldly, especially if effects such as loading rate, bond line thickness or temperature are investigated. For example, in the study by May *et al*. [2015], four tests were required to extract the peak traction and critical energy release rate in each mode of loading for each loading rate tested.

Additionally, while inverse modeling can provide good correlation to a known set of experiments, there is always uncertainty as to the ability of models relying on this approach to predict other loading scenarios. Therefore, there is a need to develop a testing approach to fully characterize the traction-separation response of adhesive joints under a range of loading modes and implement the test data into advanced adhesive joint models for finite element modeling purposes. By extracting the full traction-separation response, ideally with low variability tests, the number of tests required to fully characterize an adhesive joint can be greatly reduced and inverse modeling is not needed.

1.2 Objectives and Scope of Research

The overall goal of this study is to develop a methodology to characterize structural adhesives commonly used in an automobile BIW and to develop models with this characterization data for use in full-scale finite element crash models.

The first objective was to develop of a set of novel experimental specimen geometries and analysis techniques to measure the traction-separation response of a typical structural adhesive (3M Impact Resistant Structural Adhesive 7333, 3M Canada Company). These specimens were designed to measure the adhesive response for Mode I, Mode II and mixed mode loading conditions while also assessing the effect of bond line thickness on the traction-separation response.

The second objective was to fit the measured experimental test data to contemporary cohesive zone model (CZM) implementations used in commercial finite element software. The main intention with this objective was to critically evaluate the ability of CZM implementations to capture the full traction-separation response of the adhesive under all modes of loading tested.

Once the fit was completed, the results were used to identify potential areas for improvement in the representation of the test data within a CZM model.

To address the shortcomings identified in contemporary CZMs, particularity with regards to the mixed mode traction-separation response and bond line thickness effects, an improved CZM was developed as a third objective. The new CZM utilized the full traction-separation responses available from the newly proposed test methods to describe the adhesive joint. The new CZM was verified by modelling the characterization tests and a new validation test methodology was developed using the single lap shear (SLS) test specimen to measure both global (force, displacement) and local (joint rotation) response. The response of the new CZM was compared to a current baseline model to quantitatively assess the ability of the new approach to capture the mechanical behaviour of adhesive joints.

1.3 Organization of Thesis

This thesis is organized into six chapters, including this introductory chapter. Chapter 2 provides background information on the characterization of adhesives and their implementation in finite element models for structural applications. The discussion in Chapter 2 includes the testing of bulk material properties, test techniques for bonded specimens and the implementation of measured adhesive material properties into FE models using the cohesive zone modelling (CZM) approach.

Chapter 3 discusses the experimental techniques developed in the present work that were used to characterize a typical crash-toughened epoxy structural adhesive used in automobile BIW applications. The test specimen geometry, specimen preparation, test protocol and analysis techniques use to extract data for use in finite element modeling are discussed in detail.

Additionally, the test methodology of SLS testing, which was used to validate the material characterization development, is presented.

In Chapter 4, the experimental results of the characterization are presented. The measured data was fit to current CZM implementations and the shortcomings of these implementations to accurately describe the measured traction-separation response are discussed. Additionally, the experimental results of validation testing are presented.

Chapter 5 discusses the development of a new CZM, the Enhanced Mixed Mode Cohesive Zone Model (EMC), which incorporates improvements to the mixed mode traction-separation response and the incorporation of bond line thickness. The characterization work presented in Chapters 3 and 4 was implemented in the EMC approach to develop a numerical representation of the tested epoxy adhesive. A validation study was carried out using the new EMC to model a series of SLS experiments with steel and aluminum adherends.

The results of the EMC model are presented in Chapter 6, along with a comparison of the pertinent test data from Chapter 4. A baseline model, using a traditional CZM approach, is also presented in order to demonstrate the improvement provided by the EMC in both the output of the traction-separation response of the characterization tests and the force, displacement and rotation response of the validation tests.

Conclusions of this thesis and recommended future work are presented in Chapter 7.

Some of the work presented in this thesis has been published in peer reviewed journals. Watson *et al.* [2020a] outlines the development and verification of the Rigid Double Cantilever Beam (RDCB) test specimen and modeling used to measure the Mode I traction-separation response of a toughened structural adhesive. The development of the specimens to measure Mode II and mixed

mode traction-separation, along with a discussion of the fit of the test data to modelling approaches common in the literature was presented in Watson *et al.* [2020b]. Finally, Watson *et al.* [2019b] presents the SLS test and modeling methodologies used for model assessment in the present work, with a variety of adherend materials. In addition to these peer reviewed articles, some aspects of the bulk material testing (primarily the shear stress-strain response) were presented at the 2018 Society of Experimental Mechanics Annual Conference [Watson *et al.*, 2019a].

Chapter 2 Background

An adhesive is any substance used to bond adherends (parts being bonded) together by surface attachment [DeLollis, 1970]. Present commercial structural adhesives are generally one of three broad chemistry types: Epoxy, Acrylic or Urethane [3M, 2014]. Epoxy-based adhesives account for 95% of current automotive metal bonding applications owing to their high strength, durability, and relative insensitivity to temperature effects [Dupont, 2019]. Because the adhesives used throughout the work presented here was epoxy-based, epoxy-based adhesives will be the primary focus of this literature review.

Epoxies are polymers containing epoxide groups, which, when cured, are highly cross-linked [Kinloch, 2003]. A curing agent is added to an epoxy resin, which is activated by elevated temperatures by an exothermic reaction over a longer time span. Two-part epoxies can often be cured at room temperature or at elevated temperatures for increased cross-linking.

2.1 Mechanical Response of Bulk Epoxy Adhesives

Epoxy based adhesives tend to have relatively high elastic modulus, high failure strength, and reasonable performance at higher temperatures when compared to other structural adhesives [Dupont, 2019]. Their major drawback is that epoxy adhesives generally have a low resistance to crack growth, causing them to be quite brittle [Kinloch, 2003]. To improve the toughness of epoxy adhesives, the addition of rubbery particles to the epoxy polymer has been found to increase fracture toughness without affecting other material properties. An early study on the effect of the addition of rubber particles (carboxyl-terminated butadiane-acrylonitrile rubber) to an epoxy on the fracture toughness of the material [Yee & Pearson, 1986] found that there was an order of

magnitude increase in the fracture toughness of rubber toughened epoxies when compared to untoughened epoxies. This dramatic increase in fracture toughness was attributed to changes in the stress state of the matrix near the rubber particles, which caused a stress concentration in the matrix under loading. These stress concentrations promoted the initiation and growth of shear yield deformation, which tended to terminate at an adjacent particle, leading to localization of this deformation in bands of material, known as shear bands. Shear bands are highly localized zones of shear yielding, which create a cross-hatched appearance in the bulk material due to localized shear softening [Young & Lovell, 1991]. Additionally, the localized deformation around the rubber particle causes dilation of the matrix, leading to void formation and cavitation of the rubber particle, dissipating energy, and promoting further shear yielding [Kinloch *et al*., 1983].

Despite the constants imposed by stiff metal adherends having a strong effect on the mechanical response of bonded joints, testing of bulk adhesive has been carried out by a number of researchers [*e.g.* Trimino & Cronin, 2016]. While some authors claim that the response of bonded joints can be well predicted using bulk material data [Dolev & Ishai, 1981], others suggest bulk material data is most useful in providing context to the bonded joint testing [Adams & Coppendale, 1979]. Material properties measured using bulk material represent the lower bound for strength relative to a bonded joint, due to the lack of adherend constraint, which alters the stress state from plane stress, at the surface of an adhesive joint, to plane strain towards the center of the of the joint [Kinloch & Shaw, 1981]. Bulk material tests may also provide lower variability and are generally easier to perform compared to bonded joint tests [da Silva *et al*., 2012].

Tensile testing of bulk polymers is usually performed with a dog bone shaped specimen, such as that outlined in ASTM D638 type V [2014]. The tensile stress-strain response (Figure 1) of toughened epoxy systems is highly dependent on the presence and amount of toughening agent.

For example, Bucknall and Yoshii [1978], demonstrated that when no toughening agent was present (0.0 vol. %) the stress-strain curve showed the material was brittle and essentially elastic up to the ultimate failure strain (0.038 mm/mm) with a relatively high Young's modulus (1.6 GPa). As rubber particles were added to the epoxy, the material stiffness decreased and the strain to failure increased due to a small amount of plastic deformation. At 20.5 vol. %, the Young's modulus decreased to 1.3 GPa, while the strain to failure increased to 0.150 mm/mm, with a yield point at 0.07 mm/mm. Interestingly, the peak stress was similar between the 0.0 vol % (55.8 MPa) and the 20.5 vol % (61.2 MPa) specimens, which was attributed to brittle failure of the untoughened epoxy. Most importantly for impact resistant applications, the toughness (area under the stress-strain curve) of the toughened epoxy system was 500% larger than that of the untoughened system, indicating a significant increase in the ability of the material to absorb energy prior to failure.

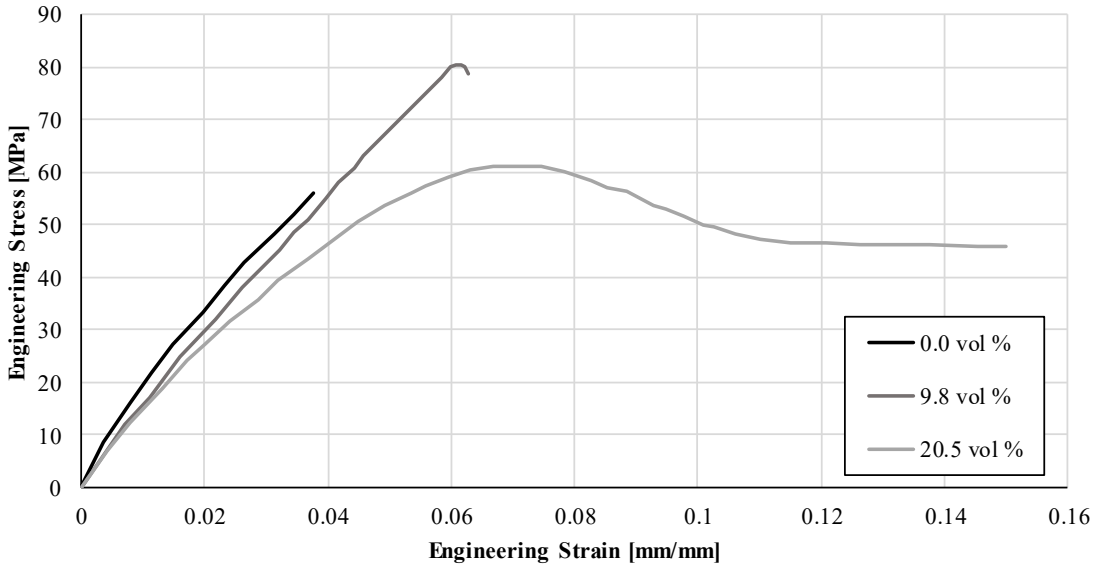

Figure 1: Quasi-static stress-strain response of epoxy with 0.0%, 9.8% and 20.5% rubber toughening particles by volume [adapted from Bucknall & Yoshii, 1978]

When testing in compression, the geometry is typically a right-prism with a rectangular or round cross-section. For quasi-static testing, the ASTM standard governing compressive testing of rigid plastics [ASTM D695, 2010] suggests a geometry of 12.7 mm x 12.7 mm x 25.4 mm or 12.7 mm diameter by 24.4 mm long or other convenient dimensions with the test gauge twice the principal width or diameter. Some researchers have identified compression-tension asymmetry [Goglio *et al.*, 2008], while others have reported symmetric compression-tension moduli [Morin *et al.*, 2010], indicating this property may be adhesive-specific and should be investigated with both compression and tension testing.

For testing in shear, several different geometries have been investigated using toughened epoxy (Figure 2). For example, the torsion test of toughened epoxy conducted by Garcia *et al*. [2011], shows a spiral fracture indicative of tensile fracture and the Iosipescu specimen of toughened epoxy tested by Morin *et al*. [2010], fractured at the root of the specimen notch along the direction of maximum 1st principal stress. This behaviour confirms the findings of the study by Liu and Piggot [1998], which found that most thermoset plastics loaded in shear fail due to scission of polymer chains resulting from tensile stresses at particular locations within the test sample. When measuring the shear stress-strain response of a bulk polymer, care must be taken to only use data that represents a state of actual shear loading. The data after damage begins to localize or cracks begin to form due to local tensile stress should be disregarded [Morin *et al.*, 2010].

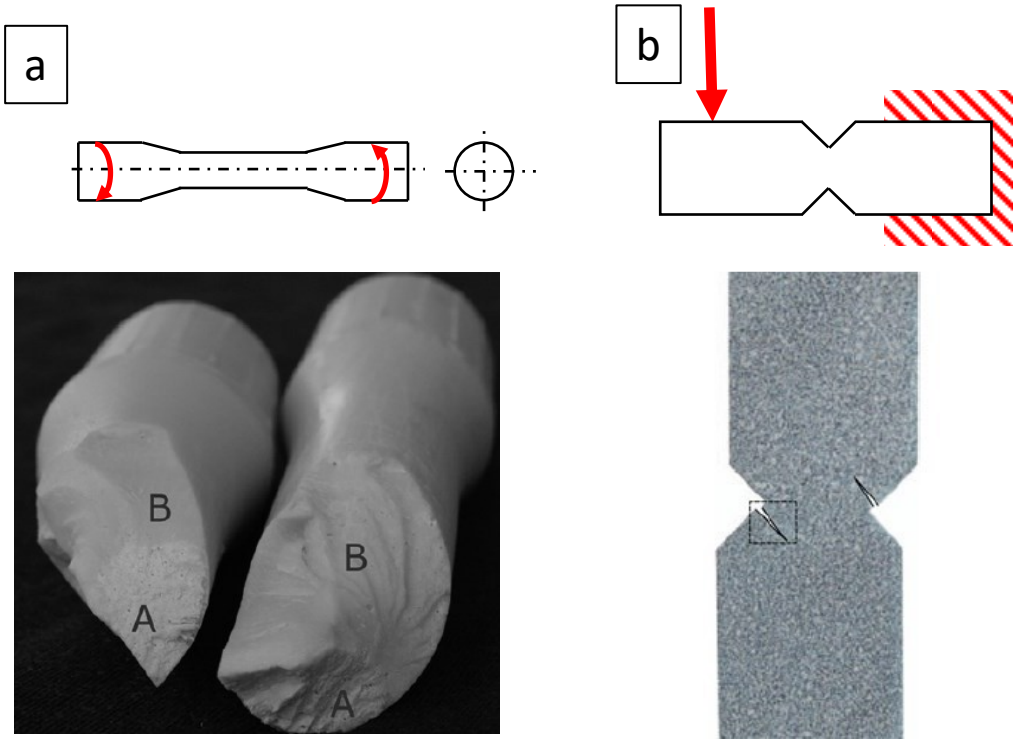

Figure 2: Comparison of failure of torsion [Garcia et al., 2011 used with permission from Elsevier] (a), and Iosipescu [Morin et al., 2010 used with permission from Elsevier] (b) shear specimen geometries using toughened epoxies

2.2 Mechanical Response of Bonded Joints

The loading of bonded joints can be described by one of three modes (Figure 3). Mode I loading occurs when the adherend is loaded normal to the joint surface. Mode II loading occurs when the load is applied such that the joint is sheared along the length of the bond line (perpendicular to the crack front). Finally, Mode III deformation is associated with shear across the bond line (parallel to the crack front). In real-world loading scenarios, loading is generally some combination of the three modes; termed mixed mode (MM) loading.

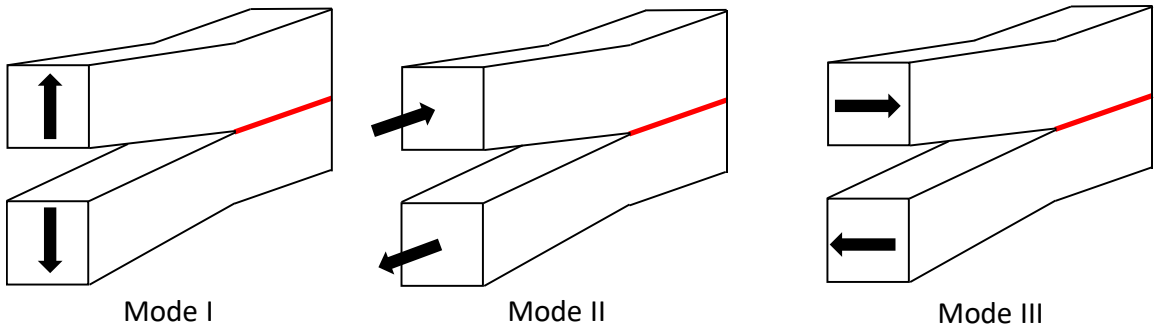

Figure 3: Modes of loading of an adhesive joint

Adhesive joints can fail in one of three ways: interfacial (or adhesion) failure, cohesive (or cohesion) failure, or adhered failure (Figure 4). Interfacial failure is said to have occurred due to a failure at the interface of the adhesive and adhered, cohesive failure occurs when failure is observed within the adhesive [ASTM D907, 2005], and adherend failure has occurred when the adherend fails while the adhesive joint itself is still intact. Generally, well designed and well bonded joints should fail cohesively or in the adherend (if the adherend material is lower strength than the adhesive) [Choupani, 2008]. Interfacial failure is generally caused by poor surface preparation and is undesirable because the full strength of the joint is not realized [Spaggiari & Dragoni; 2013]

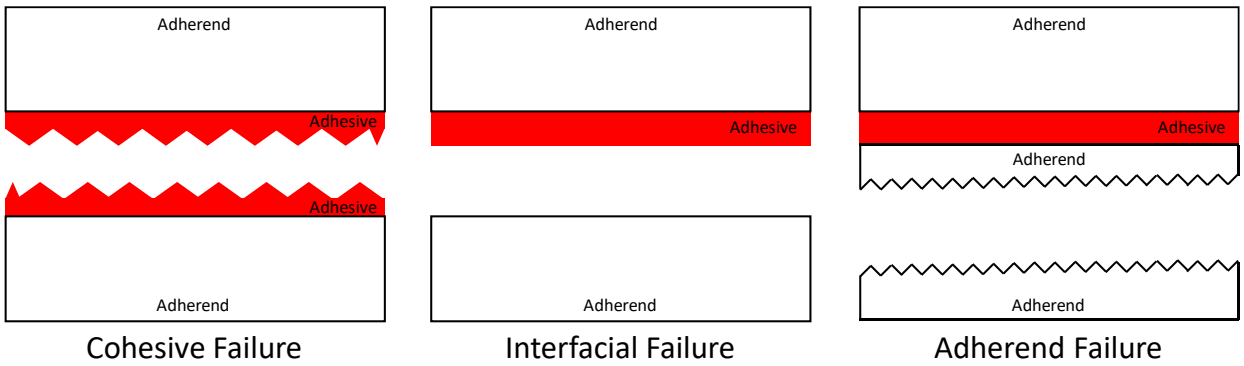

Figure 4: Adhesive joint failure modes

The interface between adherends and the adhesive is critical to mitigate interfacial failure and achieve maximum joint strength. The adhesive-adherend interface is generally understood to be due to van der Waal's forces between the metal and polymeric adhesive. Stronger covalent bonds may occur and can be promoted with an intermediary treatment, such as organosilane solutions, which react with hydroxyl groups on the surface of a metallic component to form a covalent bond [Plueddemann, 1991]. Even when the interaction between the adhesive and adherend is primarily due to van der Waal's forces, the energy associated with this interaction can be an order of magnitude larger than than the energy associated with joint failure. The total energy can be further increased by roughening the surface of the adherend, thus increasing the surface area available for interaction between the adhesive and adherend [Packham, 2018].

2.2.1 Mode I Loading of Adhesive Joints

When adhesive joints are tested under Mode I loading, the geometry tends to be some variation on the butt joint test configuration, such as that outlined in ASTM D2095 [2015] (Figure 5). For example, Ikegami *et al*. [1996] used the butt joint configuration to carry out a round-robin assessment of epoxy adhesives at several labs, in order to assess the strength and scatter inherent in this type of testing. Additionally, May *et al*. [2015] used butt joint testing to measure the peak Mode I traction of a toughened epoxy adhesive for implementation into a finite element model. In the butt joint test proposed by Yokoyama [2003], aluminum and steel adherends were bonded with cyanoacrylate adhesive in butt joint configurations. Yokoyama found that the maximum failure stress occurred with a bond line thickness of roughly 0.035 mm and that the aluminum adherend joints failed at lower failure stresses than the steel adherend joints. Yokoyama attributed the lower

strength of the aluminum adherend samples to interfacial failure of the joint as a result of the oxide layer typically present on aluminum surfaces.

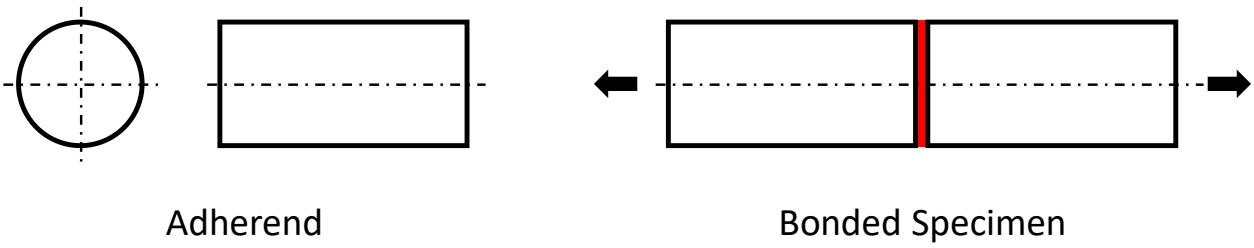

Figure 5: Typical butt joint specimen for axial testing [ASTM D2095, 2015]

There are several important aspects of the butt joint geometry that should by accounted for when using this test specimen. First, the stress-strain response of the bonded joint is often different than that of the bulk adhesive [Neumayer *et al.*, 2016], due to the adherend being considerably stiffer than the adhesive (for metallic adherends). For example, the apparent Young's modulus of a thin film adhesive butt joint should be higher than that measured from bulk adhesive material testing due to the circumferential and radial stresses induced in the joint from the transverse restraint imposed on the adhesive by the adherend [Adams & Coppendale, 1976]. Additionally, the failure stress can be affected by high stress concentrations at the edge of the specimen in the bonded joint, particularly with brittle adhesives [Yokoyama, 2003].

In general, adhesive joints are essentially linear elastic in compression compared to the more complicated tension response, as shown in the stress-strain curve showing results of testing a thin-film butt joint specimen (Figure 6) [Adams & Coppendale, 1979]. This nearly linear compressive response leads to infrequent testing in compression.

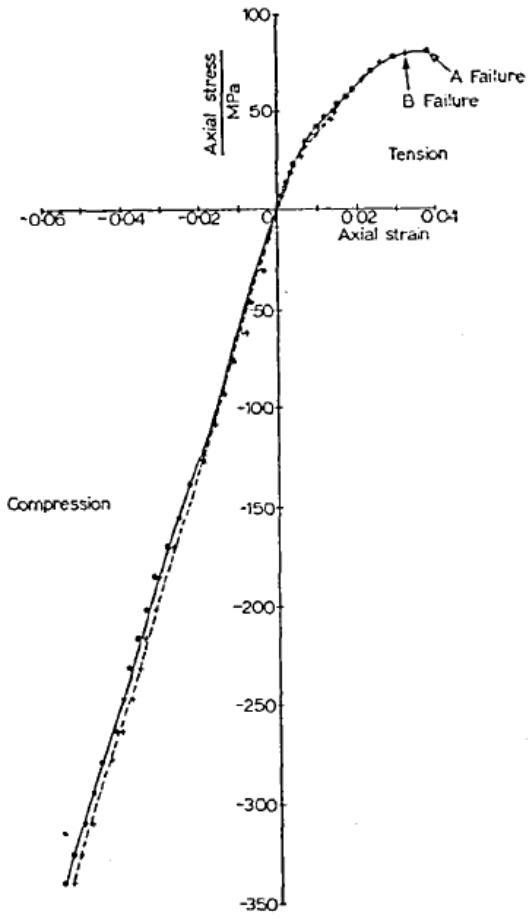

Figure 6: Stress-strain response of a thin-film adhesive butt joint tested in tension and compression [Adams & Coppendale, 1979]

2.2.2 Mode II Loading of Adhesive Joints

A number of different geometries have been proposed to assess the shear strength of adhesive bonds (Figure 7, with the location of the adhesive being tested highlighted in red for each geometry) due to challenges associated with obtaining pure shear loading.

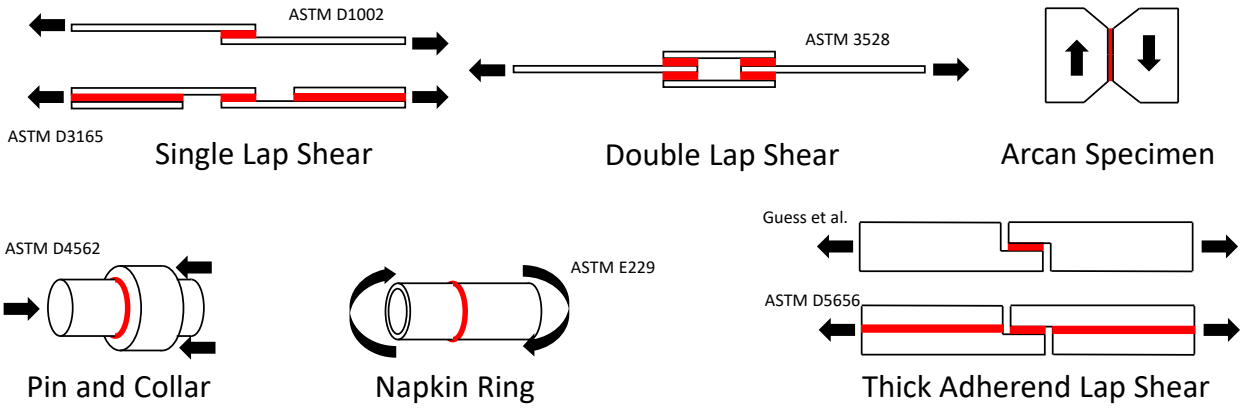

Figure 7: Various test specimen geometries to assess shear loading of adhesively bonded joints (adhesive shown in red)

Perhaps the most common specimen used to test adhesive joints is the single lap shear test, which is used to evaluate the combined properties of the adhesive, adherend and surface preparation [Guess *et al*., 1977]. The application of force to the single lap shear specimen geometry typified by ASTM D1002 [2005] is not along the centerline of the adhesive bond. The ASTM D3165 [2007] type specimen geometry addresses this eccentricity of loading by the inclusion of backing adherends (Figure 7) to move the center of force to the middle of the bond line. Despite the addition of this backing plate, both specimens often show a propensity to induce joint rotation during testing, leading to bending of the specimen prior to failure (Figure 8). This bending complicates the analysis by introducing both tensile and shear stresses in the adhesive, leading to MM loading, but also potentially introducing plasticity into the adherend response. The double lap shear test also moves the center of force to the middle of the bonded joint; however, the need for a high level of control of the bond thickness and length at four locations makes it very difficult to create properly balanced specimens. This unbalanced geometry and variability in the specimen

manufacture then leads to failure initiating in a single bond, leading to difficulty in quantifying the failure strength of the adhesive-adherend-surface preparation combination.

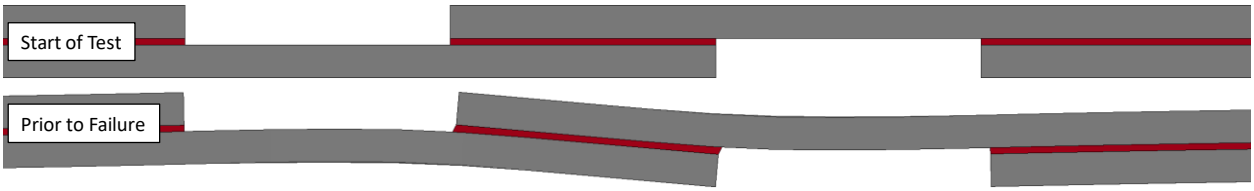

Figure 8: Bending induced during single lap shear test with thin adherends (ASTM D3165 specimen)

To counteract the issues arising from the adherend bending in single lap shear tests, thicker adherends have been used in the Thick Adherend Lap Shear Test (TALS). The adherends in this test are significantly thicker, with 9.53 mm thick adherends suggested in ASTM D5656 [2010], compared to typical thicknesses of 1.62 mm in ASTM D1002. By increasing the thickness of the adherend (and thus the 2nd moment of area), the bending deformation is significantly reduced or eliminated. In an early study by Guess *et al*. [1977], the ASTM D1002 and a geometry similar to that which would later be incorporated into ASTM D5656 were compared (using a single adherend per side with the ends milled thinner to accommodate the lap joint). They found that the MM loading led to significantly lower calculated failure stresses for the thin geometry than the TALS specimen (21.6 MPa vs. 59.0 MPa for one adhesive and 32.0 MPa vs. 41 MPa for another). These values also led to questions regarding the assumption that the single lap shear test with thin adherends is truly representative of the comparative strengths between adhesives, suggesting that different adhesives may respond to mixed-mode loading differently. The obvious limitation to the use of this thicker geometry is the need for more complicated adherends, with high precision

machining being necessary to ensure a consistent bond-line thickness between specimens and added mass of the adherends leading to potentially strong inertial effects at elevated testing rates.

In a manner similar to the use of stiff adherends in TALS geometries, Weissberg and Arcan [1988], made use of a modified version of the test geometry originally developed by Arcan *et al*. [1978] to study fiber reinforced polymers in plane shear stress. With the adaptation of the geometry to study adhesive joints, Weissberg and Arcan used FE analysis to predict that the new specimen produced a more uniform stress state than a 6 mm long TALS specimen. Experimentally, the more uniform stress state was borne out by measuring a higher shear failure stress with the Arcan-style specimen, due to the lack of normal stresses. The authors were also able to use pre-cracked specimens to measure the energy release rate in Mode II, which they found to be insensitive to the initial crack length. Weissberg and Arcan noted an added benefit with this geometry was that the specimen could be mounted to assess pure shear, pure tension or any intermediate loading combination by rotating the specimen in a high-stiffness fixture and loading in different orientations. More recently, Cognard *et al*. [2008] have used this type of geometry to compare the shear stress response to TALS specimens. In their work, they modified the adherends to include a 'beak' near the surface of the adhesive and were able to show higher displacement to failure and more repeatability when this feature was added to the geometry due to a reduction in the effect of stress concentrations near the edge of the adhesive-adherend interface. Cognard *et al*. were also able to show that the Arcan geometry provided more homogeneous stress state within the adhesive. The limitation of the Arcan test geometry was the complexity of the apparatus needed to perform this testing, which is highly sensitive to alignment issues generating off-axis loading of the specimen [Cognard *et al*., 2005].

One early test used to measure the shear stress response of adhesive joints involved testing tubular specimens under torsion. This type of geometry has been called the 'napkin ring' specimen. Thin-walled tubing was used in an attempt to produce a near constant shear stress field through the adhesive, with the underlying assumption being made that a constant stress field is present when the thickness of the tube is much less than the mean radius of the tube [Bryant & Dukes, 1964]. While this specimen is attractive due to a lack of sharp corners, which can cause stress concentrations, the need for specialized torsional test equipment and high sensitivity to specimen manufacture make this type of testing less widely used.

Another proposed shear test uses a pin and collar geometry, with a solid cylindrical pin bonded within a tubular collar and loaded axially in compression to measure the shear stress response of the adhesive. One of the main attractions with this type of specimen geometry is that, unlike the other shear specimens requiring the specimen to be loaded in tension or torsion, this specimen is tested in compression, which lends itself to high deformation rate testing using an apparatus such as the compressive SPHB. In a study by Yokoyama and Shimizu [1998] steel and aluminum adherends were bonded with a cyanoacrylate adhesive and tested at both low strain rates in a typical universal testing machine and high rates in a compression SHPB. They found that at higher rates, the shear strength of the joint increased with the applied stress rate, with failure stress increasing from 12 MPa (at 15 MPa/s) to 25 MPa (at 10×10^6 MPa/s) for aluminum adherends; and from 25 MPa (at 50 MPa/s) to roughly 45 MPa (at 20×10^6 MPa/s) for steel adherends.

One common challenge with exiting shear test methods is the difficulty to accurately measure the very small displacements associated with shear testing of thin bond line adhesives (0.1 mm to 1.0 mm). One approach to capture this small displacement is to use a linear variable differential transformer (LVDT) mounted close to the specimen joint. For example, ASTM D5656 suggests

using an LVDT with a sensitivity sufficient to capture 1/1000 of the expected full-scale measurement. The use of such a fine-scale LVDT requires mounting holes to be drilled relatively close to the bond-line. Additionally, the extra inertia associated with the LVDT could be problematic at higher rates. To address some of these issues, da Silva *et al*. [2008] tested TALS specimens using a simple clip gauge mounted at some distance from the adhesive joint while simultaneously capturing video with a 200x zoom lens (Figure 9a) focused on the center of the bond line (Figure 9b). When comparing the stress-strain responses (Figure 9c), the shear strain measured using clip gauge signal, which accounts for displacement due to deformation of the adhesive and adherend, was larger than that calculated locally using optical displacement field measurements for cases where the adhesive was stiff (G = 1559 MPa, $\tau_{Failure}$ = 30.2 MPa). Thus, the measurement of displacement in shear tests is an identified limitation of many existing test methods, with the use of optical methods gaining widespread adoption in more recent testing.

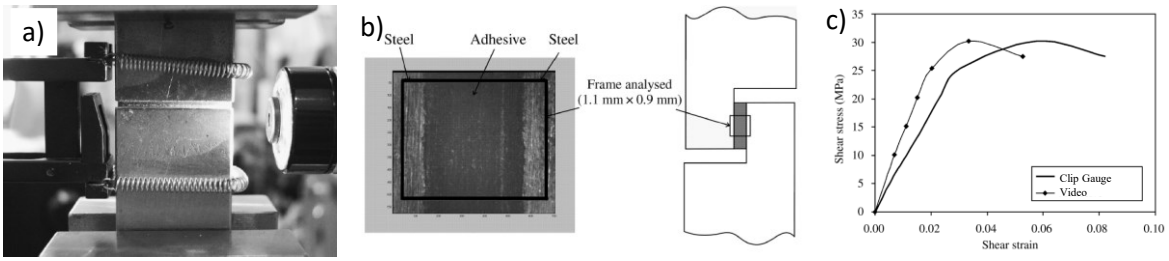

Figure 9: Comparison of mechanical and optical displacement measurement setup and results [da Silva *et al*., 2008]

In contrast, tests with lower stiffness and lower strength adhesives (G = 159 MPa, $\tau_{Failure}$ = 8.4 MPa) demonstrated nearly identical stress-strain response for the local (optical) and remote (LVDT) measurement methods. Da Silva *et al.* noted that for stiffer and higher strength adhesives, in the elastic region, a single scale factor could be used to relate the two deformation

measurements, but after the yield point this relationship began to break down. For thick adherends, it was reasonable to assume that the adherend (if metal) would remain in the linear region of its stress-strain relationship, simplifying the analysis somewhat. The authors summarized their findings by suggesting that optical measurement should be used when the shear strain was less than 100% (at strains above this level the material needed for the reference frame in the image left the field of view). For compliant and lower strength adhesives, conventional methods such as a clip gauge worked well due to the low strain in the adherends compared to the adhesive. Optical techniques have also been used to measure the traction-separation response of high-rate Mode I, Mode II and 45º MM specimens by Lißner *et al.* [2019]. They used ultra-high-speed photography to measure the unloading response, although difficulty in synchronization between cameras at different frame rates could lead to missing the unloading portion of the response completely.

2.2.3 Fracture Mechanics Approach to Adhesive Bond Failure Analysis

The bonded specimens discussed above provide useful data to characterize the strength of adhesive bonds; however, it is often useful to consider a fracture mechanics framework to describe the failure of adhesively bonded joints. When polymers are tested below their glass transition temperature they tend to fail in a brittle manner, fracturing at low strain values with little to no plastic deformation. Early work in fracture mechanics was carried out on glass by Griffith [1921] who showed that materials had a much lower strength than would be theoretically calculated in a perfect crystalline material. The difference between the theoretical and observed results was due to the presence of defects and flaws in the material acting as stress concentrators and thus lowering the overall stress needed to fracture the material.

One approach to understanding the resistance of a material to fracture is to consider the energy required to extend a crack, which can be thought of as the creation of a new surface [Griffith, 1921]. In the most basic sense this can be expressed as

$$\frac{\partial}{\partial a}(F - U) \geq \gamma \frac{\partial A}{\partial a}, \tag{1}$$

where F is the external work added to extend the crack, U is the internal energy in the material surrounding the crack, ∂a is the incremental increase in crack length, ∂A is the incremental increase in area and γ is the free surface energy [Irwin, 1956].

For a body with thickness b this can be written as

$$\frac{1}{b}\frac{\partial}{\partial a}(F - U) \geq G_{IC}, \tag{2}$$

where G_{IC} is energy needed to fracture a unit area of the material under Mode I loading, known as the critical energy release rate. G_{IC} encompasses the energy lost in the surrounding material due to plasticity, rate effects and temperature increase.

In general, Linear Elastic Fracture Mechanics (LEFM) is only applicable to linear elastic solids with no plasticity; however, LEFM has been applied to situations where there are nonlinearities in the immediate vicinity of the crack tip, but where the bulk material still remains linear. If one assumes a linear material response, Equation (2) can be expressed as

$$\partial F - \partial U = \frac{1}{2}(P\,\partial\Delta - \Delta\,\partial P), \tag{3}$$

where P is the applied force to extend the crack and Δ is the extension of the crack. If the specimen compliance C is defined as $C = \Delta/P$ the critical energy release rate needed to extend a crack can be expressed as

$$G_{IC} = \frac{{P_c}^2}{2b}\frac{\partial C}{\partial a}\,. \qquad \textbf{(4)}$$

A more detailed derivation can be found in Kinloch and Young [1983]. For materials in which the plastic region is large, advanced analysis techniques, such as the use of the J-Integral as described in ASTM E1820 [2015], are more appropriate. For situations where the plastic material behaviour is somewhat localized (such as within an adhesive between high strength adherends), another approach to describing the plastic response surrounding a crack tip is the strip yield model, originally developed by Dugdale [1960] and Barenblatt [1962]. The strip yield model assumes a long slender plastic zone exists in front of the crack tip (Figure 10**Error! Reference source not found.**a). A closing stress, which is equal to the yield strength of the material and is a function of the crack opening (Figure 10**Error! Reference source not found.**b) acts to represent the reduced resistance of the plastically deformed material to resist the crack growth [Anderson, 2017]. This approach has been shown to adequately represent the crack propagation in an aluminum-epoxy adhesive joint [Chow *et al.*, 1979].

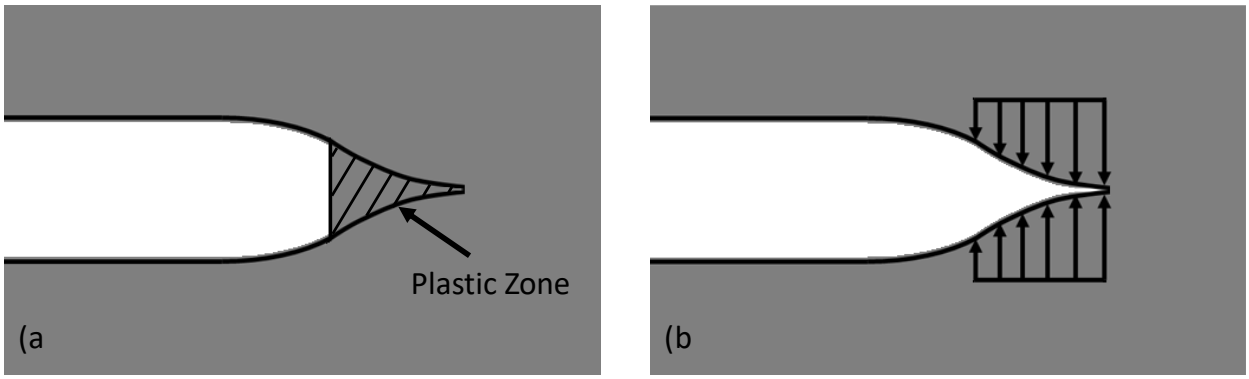

Figure 10: Schematic of the strip yield model showing plastic zone (a), and numerical representation with compressive stresses at the crack tip (b)

To measure the energy release rates of adhesively bonded joints, the double cantilever beam test (Mode I) and end notch flexural test (Mode II) are the most common tests used (Figure 11).

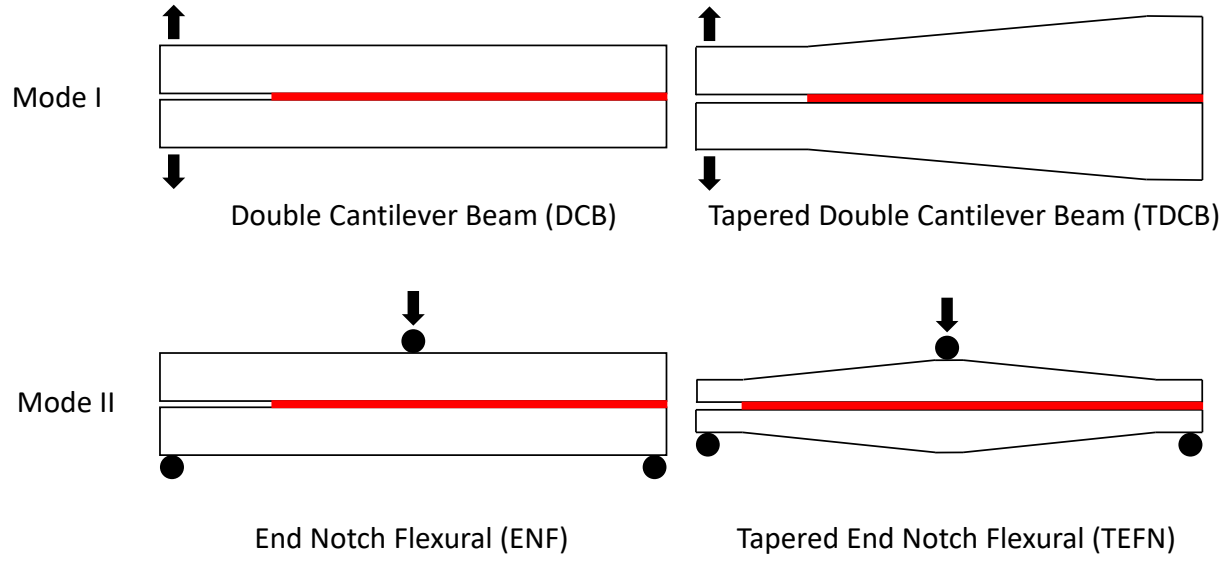

Figure 11: Common test geometries to measure adhesive joint critical energy release rate in Mode I and Mode II (adhesive in red)

To assess the Mode I fracture toughness of adhesive joints, the double cantilever beam (DCB) test is often used. During this test, originally developed by Rippling *et al*. [1964], two bonded beams are loaded near their ends, to create a cleavage load at the bond line. As with the bulk specimen, the energy release rate has the form

$$G_{IC} = \frac{{P_c}^2}{2b}\frac{\partial C}{\partial a}\,. \tag{5}$$

It is generally assumed that the deformation energy in the system is primarily elastic and stored in the adherends, and this energy is released during fracture to create free surfaces in the adhesive. This assumption relies on the fact that the energy in the adhesive is low relative to the energy in the adherend, which is often reasonable due to the relatively small volume of adhesive in a typical

thin bond-line. Additionally, any plastic zone that is present in the adhesive, which is assumed to have a considerably smaller yield strength than the metal adherend, is contained in a small volume of material due to constraint effects of the adherend. Following these assumptions, the energy release rate as measured by a DCB test can be expressed as

$$G_{IC} = \frac{4{P_c}^2}{Eb^2}\left(\frac{3a^2}{h^3} + \frac{1}{h}\right), \quad \textbf{(6)}$$

where P_c is the critical load at fracture, E is the Young's modulus of the adherend, h is the height of the adherend perpendicular to the bonded surface, b is the width of the adherend along the crack front, and a is the distance from the crack tip to the point at which the load is applied. The limitation of using the DCB stems from the energy release rates being a function of both the applied load and the crack length (P_c and a). By using the tapered double cantilever beam (TDCB) geometry, the bracketed term in the previous equation (6) can be set to a constant value (suggested to be 90 in^{-1} in ASTM D3433 [2012]) by tapering the beam such that the height of the beam increases along its length in the appropriate ratio. While this method simplifies the analysis of DCB testing, one study showed that the energy release rate measured from TDCB testing was significantly lower (30.1 %) for a toughened epoxy compared to several analyses using standard DCB geometry [Lopes *et al*., 2016]. Other issues associated with the TDCB geometry include non-constant compliance in the portion of the beam between the pin loading location and the start of the tapered section and a rotation of the adherends during testing, leading to 'beam root rotation', which can increase the complexity of the analysis required to obtain a correct G_{IC} value [Blackman *et al.*, 2003a].

A different geometry has been suggested by Dastjerdi *et al*. [2013], which is much stiffer in the bending direction (Figure 12), leading the authors to term the specimen the rigid double cantilever beam (RDCB). With this geometry the underlying assumption is that the adherends are so stiff that they may be considered rigid when compared to the adhesive. Using this assumption, not only can

the energy release rate be measured, but the traction-separation law can be extracted from a relatively simple test setup. One particularly attractive aspect of this geometry is its small size, making this geometry conducive to high deformation rate testing.

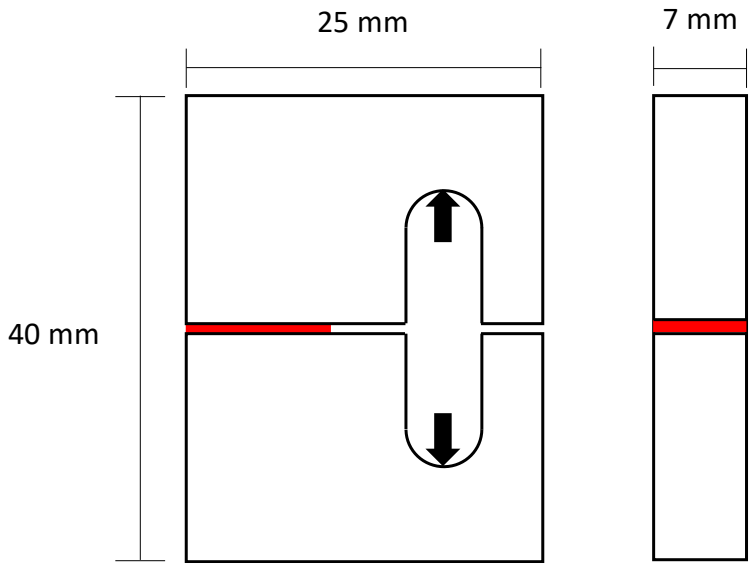

Figure 12: Ridged double cantilever beam test geometry [Dastjerdi *et al*., 2013]

To assess the fracture response of adhesive joints in Mode II loading, the end notch flexural test was originally developed by Barrett and Foschi [1977]. This Mode II test was extended to adhesive joints by Chai [1988]. Unlike the DCB and TDCB tests, in which simple beam theory is assumed to provide adequate analysis of the test specimens, using beam theory in the data reduction of ENF testing leads to an underestimate of G_{IIC} due to the absence of a correction to account for shear deformation [da Silva *et al*., 2012]. A number of methods have been proposed to address this shortcoming, but no consensus seems to have been reached as to the optimal method. The most basic analysis of this test, known as the direct beam method, can yield an estimation of the Mode II energy release rate expressed as

$$G_{IIC} = \frac{9a^2P^2}{16b^2Eh^3}, \quad \textbf{(7)}$$

where a is the distance between the crack tip and the lower support of the 3-point bending apparatus, P is the applied force, b is the specimen width, E is the adherend Young's modulus, and h is the height of the adherend [Chaves *et al*., 2014]. In a manner similar to that used for the double cantilever beam tests, a tapered version of the ENF test has been proposed by Marzi [2012] in which the compliance of the specimen remains constant as a function of crack length, removing the need to track the position of the crack during testing. This testing involved relatively long (725 mm), thin (6 mm) maraged steel adherends to minimize the effect of the compressive stress transferred to the adhesive at the neutral axis of the beam and avoid the plastic deformation that has been shown to occur with shorter specimen lengths.

While various test geometries have been proposed to measure Mode I and Mode II fracture response, MM loading is also of importance for practical applications such as vehicle structures. One approach to assess the MM loading of adhesive bonds used by several researchers [Benzeggagh & Kenane, 1996; Liu *et al*., 2002; Högberg & Stigh, 2006] is essentially to use a mechanism to combine the DCB and ENF tests simultaneously (Figure 13). The mixed mode beam (MMB) test was originally developed to assess the delamination of composite materials, making the applicability of this test with stiff adherends somewhat questionable due to the large differences in stiffness between the metal adherends and adhesive. [Chaves *et al*., 2014].

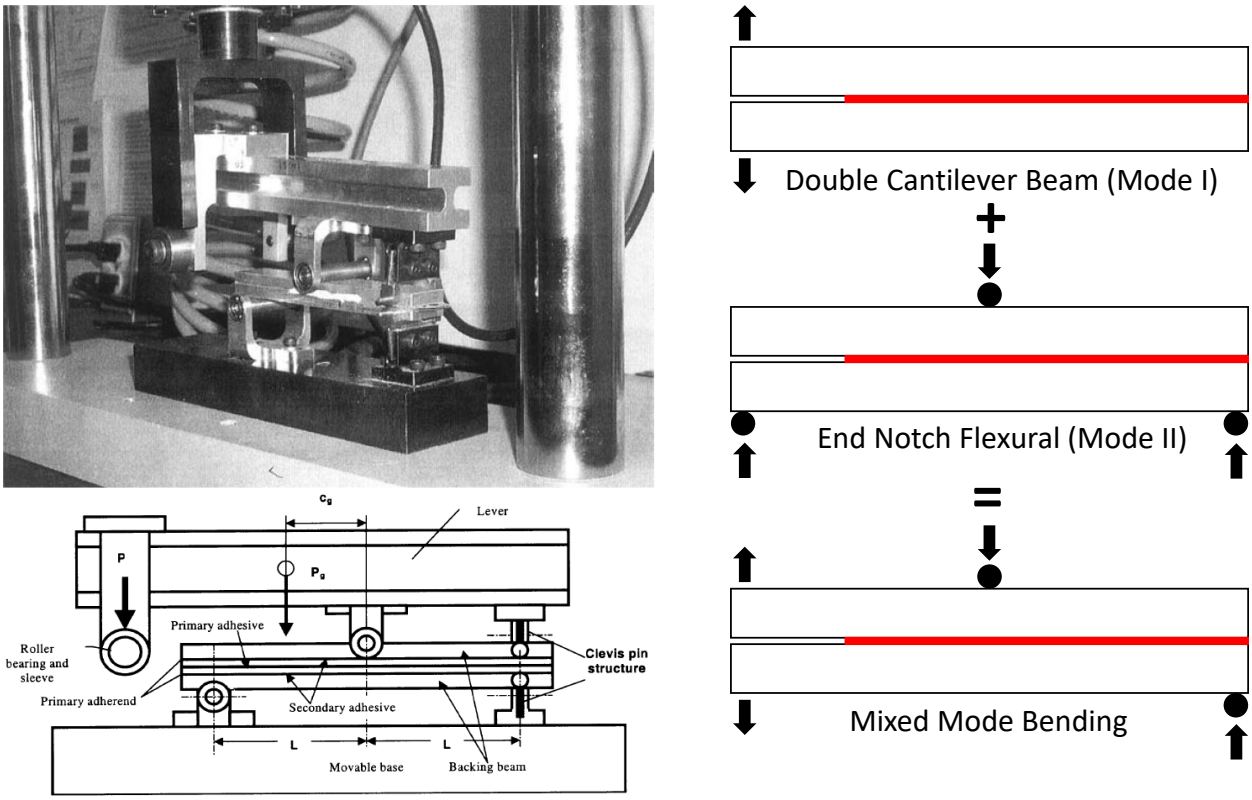

Figure 13: Example of mixed mode testing mechanism [Liu *et al.*, 2002]

Using the MMB test, the components of the energy release rates in Mode I and Mode II can be summarized as

$$G_I = \frac{3a^2P^2}{4b^2Eh^3L^2}(3c - L)^2 \tag{8}$$

and

$$G_{II} = \frac{9a^2P^2}{16b^2Eh^3L^2}(c + L)^2 \ , \tag{9}$$

where a is the crack length from the point of tensile loading, P is the applied force, b is the specimen width, E is the adherend Young's modulus, h is the height of the adherend, L is the distance between the bending support and the center of the beam, and c is the distance between the

point of loading and the center loading point for the 3-point bending loading mode [Chaves *et al*., 2014]. These G_I and G_{II} vales are not equal to the critical energy release rate values, G_{IC} and G_{IIC}, described previously, which are defined for pure Mode I and Mode II loading. The derivation of Equation (8) and Equation (9) relied on simple beam theory, although as with the DCB and ENF tests, application of different beam theories can lead to other, generally more complicated, energy release rate calculations, such as those presented by Liu *et al*. [2002].

2.2.4 Effect of Bond Line Thickness on Joint Response

One common question that arises when characterizing adhesives is whether the behaviour of the bonded joint can be readily related to the behaviour of the bulk material. To address this question, Kinloch and Shaw [1981] investigated the fracture toughness of a rubber toughened epoxy in the bulk form using the compact tension specimen and in the bonded form using TDCB specimens. They studied the effect of the bond-line thickness and compared the results to the bulk specimen, with the energy release rate of the bonded specimen being larger than that of the bulk specimen for a variety of test conditions, unless the bond-line was very thin (0.15 mm). Kinloch and Shaw also found that the curve describing the energy release rate as a function of bond thickness was low for very thin bond-lines, increased to some maximum value (t_m) and finally decreased until the value was roughly the same as the energy release rate measured in the bulk material (Figure 14a). The authors cite Bascom and Cottington [1976] who employed an elastic-plastic model to calculate the radius of the plastic-deformation zone of a sharp crack (r_{Iy});

$$r_{Iy} = \frac{1}{2\pi}\frac{E_a G_{Ic}}{\left(\sigma_{Yield,Tension}\right)^2}\,. \qquad \textbf{(10)}$$

Using this logic, Kinloch and Shaw [1981] were able to show that the maximum energy release rate occurred when the bond line was approximately equal to $2r_{Iy}$. When the bond-line thickness is below this value the full plastic zone may not develop and since fracture toughness in toughened epoxy systems is caused by energy dissipation in the plastic zone of the material, the fracture toughness would decrease as the bond-line becomes thinner.

At the same time, it has been shown that the constraints of stiff substrates on an adhesive can increase the length to which the stress concentration extends in front of the crack tip. Thinner bonds have higher stresses further in front of the crack tip (represented graphically by the 'Plastic Zone Shape' column in Figure 14b). Despite extending further along the bond-line, the volume of the plastic zone (represented by the hatched area in the image) is, in total, smaller than the case when $t > 2\ r_{Iy}$. For cases when the bond line is thicker still, the plastic zone contracts until it is circular (in 2D) as in the bulk material and the energy release rate of the adhesive joint equals that of the bulk material.

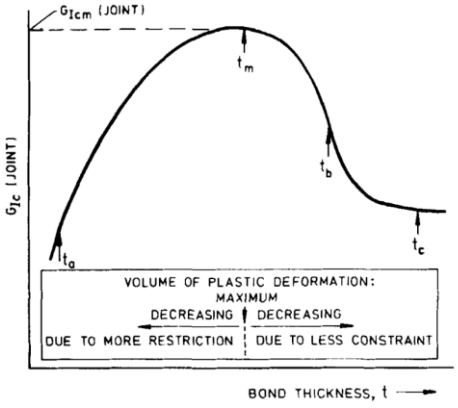

Bond Thickness (t)	Constraint due to bond thickness	Plastic Zone Shape	G_{Ic} (Joint)
t_a (< $2r_{Iy}$)	High		Low
t_m (= $2r_{Iy}$)	Moderate		Maximum
t_b (> $2r_{Iy}$)	Low	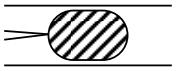	Below $G_{Ic,max}$
t_c (>> $2r_{Iy}$)	Almost Nil	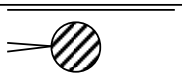	Approx. $G_{Ic,bulk}$

Figure 14: Summary of constraint effect in bonded joints [Kinloch & Shaw, 1981]

2.3 Finite Element Modeling of Adhesive Joints

A number of techniques for computational modeling of adhesive joints have been investigated including the use of the finite difference method, the boundary element method and the finite element method. For automotive structural applications, finite element modeling is the most common of these approaches and includes the use of the fully defined continuum mechanics, the CZM approach, tiebreak constraints, or more recently the extended finite element method [da Silva & Campilho, 2012].

An example of using solid continuum elements with bulk material properties used for the adhesive was used in a study by Goncalves *et al*. [2002] to investigate the three-dimensional stress response of a single lap shear test. Goncalves *et al*. showed that the shear stress near the edges of the bond line were twice the average stress (calculated by dividing the loading force by the bond area). Furthermore, tensile stresses developed at the same location due to bending of the adherends. Unfortunately, to resolve the stress gradient at these locations, a very fine mesh (<0.1 mm elements) was needed, making this approach somewhat limited in large scale applications. Tiebreak constraints, while computationally efficient, provide less detail in capturing the response of adhesive joints, due to the simplified approach in their implementation in commercial FE codes [Trimino, 2012]. Using XFEM to model adhesives has been shown to provide unphysical results (cracks propagating from the adhesive through the adherend or not propagating along the material interface) in a common FE code (Abaqus) [Campilho *et al*., 2011]. The CZM approach can be seen to provide a middle ground between computational efficiency, a high level of detail in capturing the joint response and ease of implementation in current commercial codes. Consequently, the CZM approach was selected for the modeling work in the current thesis.

2.3.1 Cohesive Zone Modeling for Adhesive

To avoid the very fine mesh density required to use the continuum-based approach to modeling, the cohesive zone modelling approach, which is able to use a coarser mesh (> 1 mm mesh in-plane and a single element through thickness), is often used to implement adhesive joints in large-scale finite element models. The CZM approach was originally presented by Hillerborg *et al*. [1976] and was used to model the development and growth of cracks in concrete. Cohesive zone modeling relies on the strip yield model of plasticity at a crack tip. Using the CZM approach to model failure in adhesive joints rests on the assumption that a zone ahead of the crack tip is deformed at the same time as the joint. This deformation then leads to damage and, ultimately, the creation of a new surface once a critical amount of energy has been introduced to the joint [LS-DYNA Aerospace Working Group, 2012]. The approach is particularly attractive for modeling adhesives since the path of the crack propagation (i.e. along the bond line) is obvious beforehand and a single row of cohesive elements can be used to model the adhesive joint. While the constitutive models applied to typical finite element models define the relationship between stress and strain, the behavior of cohesive elements is governed primarily by traction (stress between the bonded surfaces) and separation (relative displacement) between a top and bottom surface of the element [Hallquist, 2017b]. Cohesive elements are typically defined by a strict node numbering scheme where, for example, nodes 1-4 define the bottom surface and nodes 5-8 define the top surface (Figure 15). At each corner (node pair), the relationship between the top and bottom node can be treated in an analogous manner as an integration point in a typical finite element. The separation of each node pair is calculated by tracking the change in displacement between the nodes.

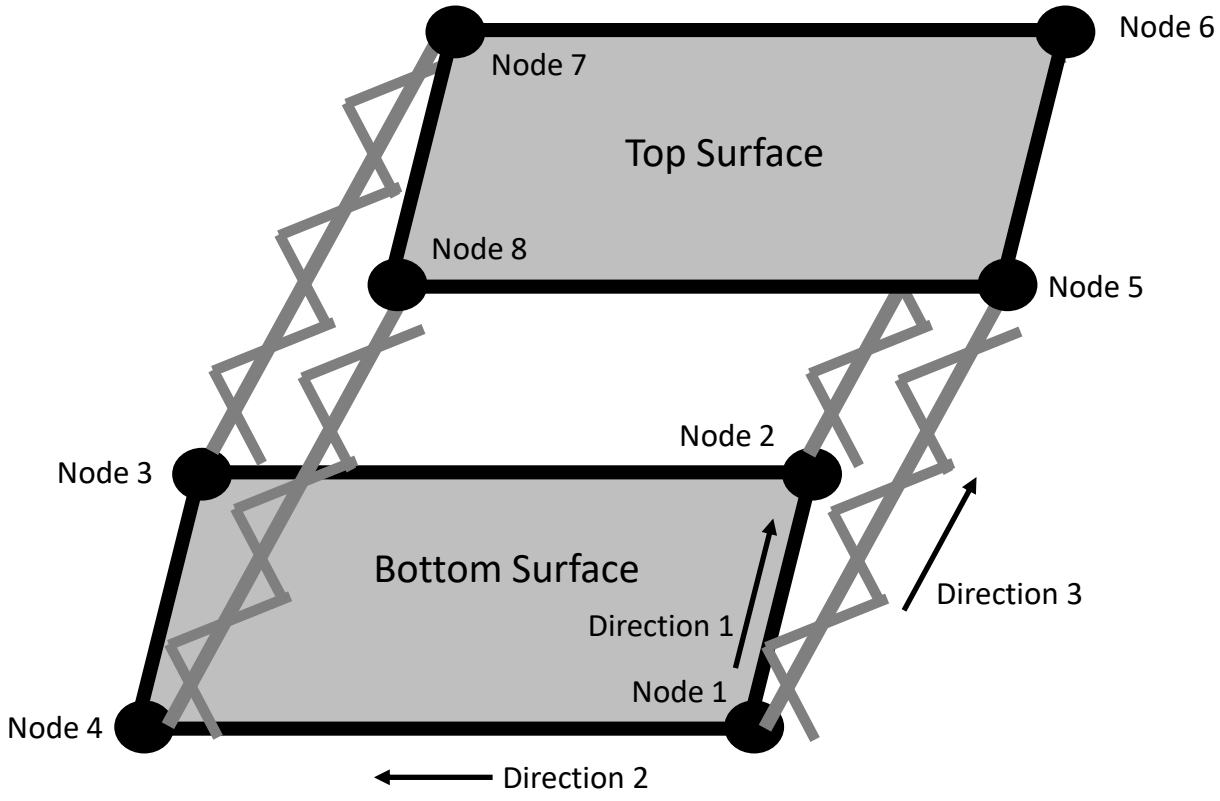

Figure 15: Typical node numbering of cohesive element defining top and bottom surface

The element can then be considered as a set of four trios of springs connecting upper and lower node pairs at each corner of the element. One of these 'springs' controls the traction response in the normal direction (Mode I, direction 3 in LS-DYNA and many other codes [e.g. Dassault Systèmes, 2008; ESI Group, 2016; Siemens AG, 2016]). The other two 'springs' independently control the response in the two tangential directions (Mode II, directions 1 and 2 in LS-DYNA), although often (and, importantly, in the work that follows here) these tangential responses are resolved and treated as a single shear response. In the LS-DYNA solver, the '1' and '2' directions are assigned based on the nodal numbering given in the input deck to the bottom surface in the

manner typical to orthotropic element definitions. The '3' direction is defined by the cross product of the vectors used to define directions '1' and '2'.

Typically, a traction-separation relationship is defined independently for Mode I (tension, compression) and Mode II (shear) behavior. While brittle behaviour can be represented by a purely elastic CZM, other shapes are often implemented in which the traction grows from zero to some peak traction and back to zero as damage is accumulated, at which point the element no longer supports any load and is removed from the calculation. The most basic form of this traction-separation response is a simple triangular (bilinear) response where both the initial loading and softening response are linear [Alfano & Crisfield, 2001]. For example, in the simplest form, cohesive elements can be described by

$$\begin{bmatrix}\sigma_1\\ \sigma_2\\ \sigma_3\end{bmatrix} = (1-D)\begin{bmatrix}E_{II} & 0 & 0\\ 0 & E_{II} & 0\\ 0 & 0 & E_I\end{bmatrix}\begin{bmatrix}\delta_1\\ \delta_2\\ \delta_3\end{bmatrix}, \tag{11}$$

where σ_1 and σ_2 are the tractions in the Mode II directions, σ_3 is the traction in the Mode I direction, E_{II} is the Mode II initial stiffness, E_I is the initial Mode I stiffness, δ_1 and δ_2 are the separations in the Mode II directions, δ_3 is the separation in the normal direction, and D is a damage parameter between zero and one [Hallquist, 2017b]. It is clear from Equation (11) that Poisson's effects are not considered directly in the CZM formulation. However, it can be argued that, because Poisson's ratio plays a role in the confinement effects present in thin bond lines, Poission's effects are embedded in the model when using parameters extracted from tests with the same bond line thickness as that being modeled.

Other shapes of the traction-separation response have been proposed, such as an exponential softening response [Chandra *et al*., 2002], or fully generalized CZM shapes, which start and end at zero traction with the remainder of the CZM law being governed by an arbitrarily defined curve.

Materials that exhibit some ductility are often represented by a trapezoidal CZM (Figure 16) originally proposed by Tvergaard and Hutchinson [1992].

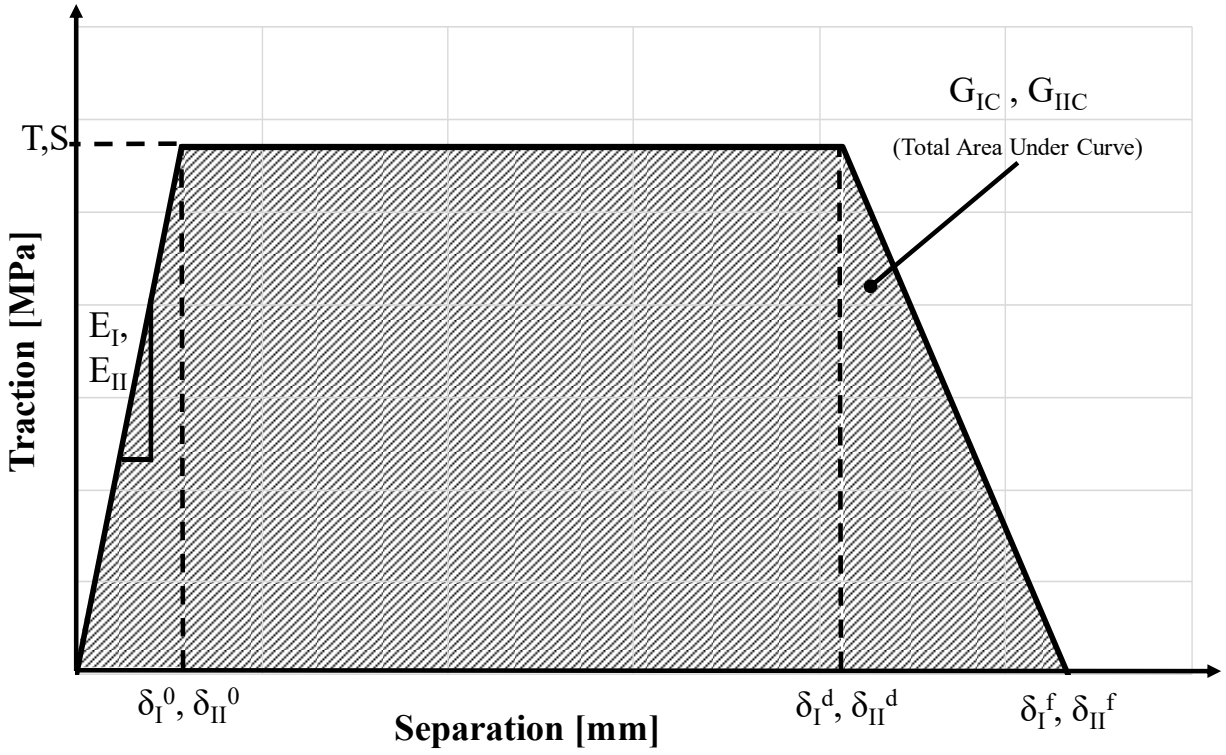

Figure 16: Typical trapezoidal traction-separation cohesive zone model used for ductile failure [adapted from Tvergaard & Hutchinson, 1992]

In one example of this type of CZM [Marzi *et al*., 2009], Mode I and Mode II are defined independently, using the following parameters: the initial stiffness in the Mode I (E_I) and Mode II (E_{II}), the peak traction in Mode I (T) and Mode II (S), and the critical energy release rate (area under the traction-separation response) in Mode I (G_{IC}) and Mode II (G_{IIC}). Finally, the ratio of the area under the plastic portion of the traction-separation response to the total critical energy release rate (termed 'area ratio', for brevity) in Mode I (f_{GI}) and Mode II (f_{GII}) define the length of the plateau. These parameters implicitly define three important separation values for both Mode I and

Mode II; the separation-to-plateau in Mode I (δ_I^0) and Mode II (δ_{II}^0) loading, the separation-to-softening in Mode I (δ_I^s) and Mode II (δ_{II}^s) loading, and the separation-to-failure in Mode I (δ_I^f) and Mode II (δ_{II}^f) loading. These separations can be defined by the Mode I and Mode II parameters using the following expressions:

$$\delta_I{}^0 = \frac{T}{E_I}, \tag{12}$$

$$\delta_I{}^d = \delta_I{}^0 + \frac{f_{GI} \cdot G_{IC}}{T}, \tag{13}$$

$$\delta_I{}^f = \frac{2 \cdot G_{IC}}{T} + \delta_I{}^0 - \delta_I{}^d, \tag{14}$$

$$\delta_{II}{}^0 = \frac{S}{E_{II}}, \tag{15}$$

$$\delta_{II}{}^d = \delta_{II}{}^0 + \frac{f_{GII} \cdot G_{IIC}}{S}, \tag{16}$$

and

$$\delta_{II}{}^f = \frac{2 \cdot G_{IIC}}{S} + \delta_{II}{}^0 - \delta_{II}{}^d. \tag{17}$$

To this point, the definition of the CZM traction-separation response is only applicable for pure Mode I or Pure Mode II loading. In most situations, the loading of a cohesive element will not be purely Mode I or Mode II, but will exhibit some degree of mode mixity (Figure 17).

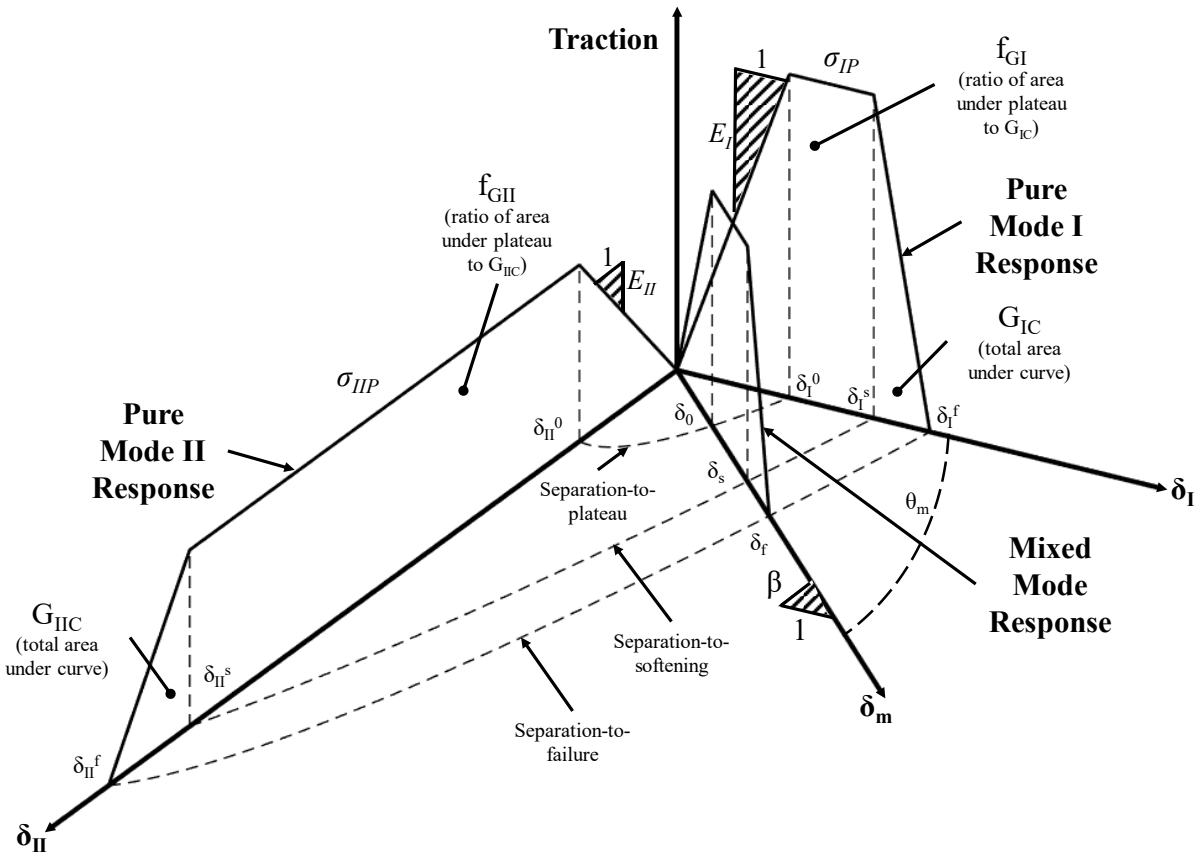

Figure 17: Mode I, Mode II and Mixed mode response of a trapezoidal traction-separation response [adapted from May *et al*., 2015]

It is generally most convenient to consider the MM separation-to-yield (δ^0), separation-to-damage initiation (δ^s) and separation-to-failure (δ^f) when working with MM loading. A convenient measure of mode mixity is defined by

$$\beta = \frac{\delta_{II}}{\langle \delta_I \rangle}, \tag{18}$$

where

$$\delta_I = \delta_3 \tag{19}$$

and

$$\delta_{II} = \sqrt{{\delta_1}^2 + {\delta_2}^2}\,. \tag{20}$$

Note the use of a Macaulay function in the definition of β, which stems from the assumption that compressive stresses can be ignored when considering mixed mode loading. The MM separation can then be described as

$$\delta_m = \sqrt{{\delta_I}^2 + {\delta_{II}}^2}. \tag{21}$$

The MM relationship leads to the following definitions;

$$\delta_I = \frac{\delta_m}{\sqrt{1+\beta^2}}\,, \tag{22}$$

$$\delta_{II} = \frac{\beta\cdot\delta_m}{\sqrt{1+\beta^2}}\,, \tag{23}$$

$$T = {\delta_I}^0 \cdot E_I = \frac{\delta_0\cdot E_I}{\sqrt{1+\beta^2}}\,, \tag{24}$$

and

$$S = {\delta_{II}}^0 \cdot E_{II} = \frac{\beta\cdot\delta_0\cdot E_{II}}{\sqrt{1+\beta^2}}\,. \tag{25}$$

The separation-to-plateau (δ^0) criterion as a function of mode mixity is often defined as [Hallquist, 2017a]

$$\left(\frac{\delta_I}{{\delta_I}^0}\right)^2 + \left(\frac{\delta_{II}}{{\delta_{II}}^0}\right)^2 = 1\,. \tag{26}$$

Equation (26) can be rewritten to solve for the mixed-mode yield separation;

$$\delta^0 = {\delta_I}^0 \cdot {\delta_{II}}^0 \sqrt{\frac{1+\beta^2}{\left({\delta_{II}}^0\right)^2 + \left(\beta{\delta_I}^0\right)^2}}\,. \tag{27}$$

The separation-to-softening initiation can be treated similarly so that

$$\left(\frac{\delta_I}{{\delta_I}^d}\right)^2 + \left(\frac{\delta_{II}}{{\delta_{II}}^d}\right)^2 = 1\,, \tag{28}$$

which leads to

$$\delta^d = {\delta_I}^d \cdot {\delta_{II}}^d \sqrt{\frac{1+\beta^2}{\left({\delta_{II}}^d\right)^2 + \left(\beta \cdot {\delta_I}^d\right)^2}}\,. \tag{29}$$

Several relationships have been proposed to define the failure separation when using CZMs, which are based on relationships involving energy release rates. One common example being a power law relationship [Camanho *et al.*, 2003];

$$\left(\frac{G_I}{G_{IC}}\right)^\alpha + \left(\frac{G_{II}}{G_{IIC}}\right)^\alpha = 1\,, \tag{30}$$

where α is a constant that must be measured experimentally. The Mode I and Mode II energy release rates at failure for a given β mixity ratio can be defined by

$$G_I = \frac{\delta_0 \cdot E_I}{2(1+\beta^2)}\left(\delta_f + \delta_d - \delta_0\right) \tag{31}$$

and

$$G_{II} = \frac{\beta^2 \cdot \delta_0 \cdot E_{II}}{2(1+\beta^2)}\left(\delta_f + \delta_d - \delta_0\right)\,. \tag{32}$$

Note that G_I and G_{II} are not, in general, the same as the critical values (G_{IC}, G_{IIC}), which are descriptions of the energy release rate in pure Mode I or Mode II loading. Using the expressions for the energy release rates in Mode I and Mode II for general MM loading, the final failure separation can be expressed as

$$\delta_f = \frac{2(1+\beta^2)}{\delta_0}\left[\left(\frac{E_I}{G_{IC}}\right)^\alpha + \left(\frac{\beta^2 \cdot E_{II}}{G_{IIC}}\right)^\alpha\right]^{\frac{-1}{\alpha}} + \delta_0 - \delta_d\,. \tag{33}$$

This failure description has been used with a trapezoidal traction law, implemented in LS-DYNA (*MAT_240) [May *et al.*, 2015] with α fixed at a value of unity.

Other ultimate failure descriptions have been proposed, including that originally proposed by Gong and Benzeggagh [1995], who were attempting to experimentally fit the summation of the Mode I and Mode II energy release rates to a single critical energy release rate parameter (G_c) for fiber reinforced composites and proposed that

$$G_c = G_I + G_{II} = G_{IC} + (G_{IIC} - G_{IC}) \left(\frac{G_{II}}{G_{IIC}}\right)^{\eta}, \tag{34}$$

where η is an experimentally measured value. Sometime later, Benzeggagh and Kenane [1996] updated this to the more commonly used form

$$G_c = G_I + G_{II} = G_{IC} + (G_{IIC} - G_{IC}) \left(\frac{G_{II}}{G_I + G_{II}}\right)^{\eta}, \tag{35}$$

which, using the expressions for Mode I and Mode II energy release rates at failure as a function of mode mixity, can be expressed as

$$G_c = G_I + G_{II} = G_{IC} + (G_{IIC} - G_{IC}) \left(\frac{\beta^2 \cdot E_{II}}{E_I + \beta^2 \cdot E_{II}}\right)^{\eta}. \tag{36}$$

If one considers the Mode I and Mode II energy release rates as scalar values, the summation leads to

$$G_I + G_{II} = \frac{\delta_0 \left(\delta_f + \delta_d - \delta_0\right)}{2} \left(\frac{E_I + \beta^2 \cdot E_{II}}{(1 + \beta^2)}\right) \tag{37}$$

and the final separation to failure of

$$\delta_f = \frac{2\left[G_{IC} + (G_{IIC} - G_{IC})\left(\frac{\beta^2 \cdot E_{II}}{E_I + \beta^2 \cdot E_{II}}\right)^{\eta}\right]}{\delta_0 \left(\frac{E_I + \beta^2 \cdot E_{II}}{1 + \beta^2}\right)} + \delta_0 - \delta_d \,. \tag{38}$$

The damage of a CZM is a critical aspect to the overall response of the model. The implementation of damage is required to define the traction response between the end of the plateau and zero traction, when load is no longer supported by the element and can be removed from the calculation.

The softening response is most commonly assumed to be linear, although exponential responses are also somewhat common [da Silva & Campilho, 2012]. The tractions in the softening portion of the Mode I and Mode II traction-separation responses can be described as

$$T_{max} = \frac{\delta_0 \cdot E_I}{\sqrt{1+\beta^2}}(1-D) \tag{39}$$

and

$$S_{max} = \frac{\beta \cdot \delta_0 \cdot E_{II}}{\sqrt{1+\beta^2}}(1-D). \tag{40}$$

where D is the damage parameter, which ranges from zero prior to softening (δ^s) and one when the element no longer supports a load (δ^f).

The damage model also has some effect on the unloading/reloading response of the CZM. In the undamaged state (*i.e.* when the element has only been loaded within the initial linear elastic loading portion of the traction-separation response or in compression), unloading and subsequent reloading will only occur along the path of the initial stiffness. After the accumulation of damage, this unloading/reloading stiffness will be modified to reduce the stiffness. Two approaches to this unloading have been suggested, termed the 'elastic-plastic' response (Figure 18a) and the 'elastic-damage' response (Figure 18b) by Biel & Stigh [2010]. Note that for loading in compression, CZMs are usually defined such that no damage is initiated and the response is purely linear following the E_I stiffness.

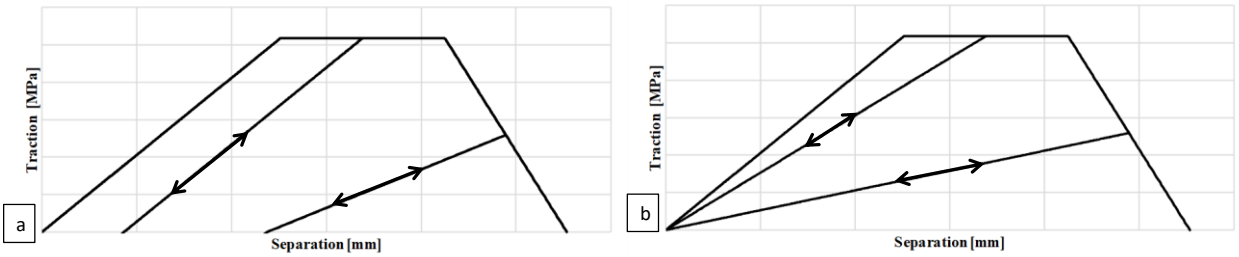

Figure 18: Typical elastic-plastic (a), and elastic-damage (b) softening damage applied to trapezoidal traction-separation responses, showing unloading/reloading responses from the plateau and softening portions of the response

In the context of a trapezoidal traction-separation response, the elastic-plastic damage for a given time step *i* can be defined as [Marzi et al., 2009b]

$$D_i = max\left(\frac{\delta_{m,i}-\delta^s}{\delta^f-\delta^s}, D_{i-1}, 0\right), \tag{41}$$

where D_{i-1} is the damage from the previous time step and $\delta_{m,i}$ is the MM displacement for the current time step. The elastic-damage response is usually defined by [de Moura et al., 2008]

$$D_i = max\left(1-\frac{\delta^0}{\delta_{m,i}}, 1-\frac{\delta^0}{\delta_{m,i}}\cdot\frac{\delta^f-\delta_{m,i}}{\delta^f-\delta^s}, D_{i-1}, 0\right). \tag{42}$$

The important distinction between these two approaches is the presence of residual displacement when the model is fully unloaded with the elastic-plastic approach, while the elastic-damage approach causes the element displacement to return to zero when unloaded. The initiation of damage in the elastic-plastic approach defined by Equation (41) occurs when the MM separation reaches the separation-to-softening, while for the elastic-damage response given by Equation (42), damage is initiated when the MM separation reaches the separation-to-plateau. This behaviour can be seen by the unloading/reloading slope being parallel to the initial stiffness for scenarios when

an elastic-plastic model is unloaded from the plateau portion of the traction-separation (Figure 18a).

While both approaches have been applied to CZMs in the literature, experimental data to guide the choice of damage model has been relatively scarce. Biel & Stigh [2010] investigated the load/unload response of adhesive joints by loading and unloading DCB specimens to a number of predefined load states, which did not allow the crack tip to advance. Subsequent, reloading cycles were then carried out with the damaged specimens and models of these damaged specimens were developed using both approaches. The elastic-damage approach tended to slightly underpredict the energy release rate – pin opening response while the elastic-plastic approach tended to significantly overpredict the response, suggesting that the true response was somewhat between the two approaches, but tending to be similar to the elastic-damage response. A similar study was carried out by Blackman *et al.* [2003b], who loaded and unloaded DCB specimens beyond crack opening displacements, making the outcome somewhat harder to isolate. Nevertheless, Blackman *et al.* found <5% offset displacement (roughly 0.05 mm) and suggested this was primarily due to the rough facture surface of the adhesive propping the crack open slightly when unloaded. This finding provides further evidence suggesting the elastic-damage approach provides a response in agreement with the limited data.

2.4 Summary

Adhesive bonding is becoming widely adopted in the automotive industry as a structural joining method; however, advanced characterization and modeling techniques are critical to provide detailed information to improve BIW design. The use of cohesive zone modeling is an attractive modeling methodology due to its computational efficiency, although specialized testing is required

to extract the parameters required to fully characterize the joint. These specialized tests typically do not provide the full traction-separation response required to implement a CZM, necessitating multiple tests for each mode of loading. For example, a double cantilever beam test is needed to extract energy release rate in conjunction with butt-joint testing to measure initial stiffness and peak stress in Mode I. Thick adherend lap shear or pin on collar and ENF are typically carried out to measure the Mode II properties. The results of these characterization tests are then combined, often with inverse modelling, to provide the response necessary to define the CZM. For both the TDCB and ENF tests, the choice of beam theory used in the analysis of the tests can have a strong effect on the measured response and additional correction factors are commonly used to ensure consistency between test results and model responses of the tests. Furthermore, current test approaches to measure the fracture properties of bonded joints use linear elastic fracture mechanics assumptions, which may not be appropriate for more modern ductile toughened structural adhesives. Experimental techniques that can more directly measure adhesive joint Mode I and Mode II traction-separation response thus enabling a model response with better correlation with measured behavior remain a significant deficit within the current scientific literature.

Significant aspects of the CZM approach are often defined for expedience and computational efficiency rather than using experimentally measured traction-separation responses to drive the model definition. This limitation is particularly true for mixed modes of loading. The mixed mode energy release rate is commonly measured using the MMB test, but the full traction-separation response is generally unknown. Thus, the development of experiments that directly measure the mixed mode traction-separation response represent a further deficit in the scientific literature and is a key focus of the current research. Furthermore, a model built using full traction-separation responses for several mixed mode loading cases would represent an improvement to the cohesive

zone modeling approach for adhesive joints, which is addressed by the model developed in this thesis.

Chapter 3 Experimental Methods and Data Analysis

The experimental work carried out in this thesis can be broadly divided into two categories: characterization testing and validation testing. The first step in characterizing the adhesive was to undertake bulk specimen testing to establish the unconfined strength of the material and to provide context in terms of the peak stresses that could be expected when testing bonded specimens. Following this, the Mode I characterization work was undertaken using the RDCB test specimen with an updated analysis, as detailed below. A new specimen geometry and analysis was then developed to characterize the adhesive under both Mode II and MM loading. Validation testing was subsequently carried out using TDCB testing to validate the RDCB test analysis and single lap shear testing was carried out to validate the shear and MM validation and material model development.

The adhesive used throughout this thesis was a commercially available two-part toughened epoxy (3M Impact Resistant Structural Adhesive 7333, 3M Canada Company). This adhesive was designed specifically for automotive structural bonding applications [3M, 2016] and is primarily composed of epoxy with a small amount of acrylic copolymer along with aluminum and synthetic rubber for toughening and several other filler materials [3M, 2018]. For all specimens described in this section, curing was carried out in a convection oven (ED-53, Binder, Tuttlingen, Germany) for 30 min after the specimen (and associated fixturing) reached 80^{o} C.

3.1 Bulk Material Testing

Bulk material testing was carried out in order to provide understanding of the adhesive material in the unconstrained condition. In particular, the peak stress in tension and shear, the degree of

symmetry in tension versus compression and and fracture behavior of the bulk adhesive were of interest. Due to the complex behavior of polymeric materials, bulk material testing was carried out under tension, compression and shear loading.

3.1.1 Bulk Specimen Preparation

The specimen geometries used for the bulk tension and bulk shear testing required adhesive to be cast into plaques, which were then machined to the appropriate geometry. To create these plaques, adhesive was carefully pooled onto a 304.8 mm x 304.8 mm (12" x 12") plate of tempered glass (Figure 19a), taking care to avoid introducing air voids into the pool. A second glass plate was then placed on top of the pool and metal spacers of the desired final specimen thickness (3.175 mm) were placed around the pooled adhesive. Binder clamps were then placed around the edges of the glass plates to provide a small amount of pressure to the assembly during curing (Figure 19b). After the entire assembly was cured according to the manufacture's recommendations the final plaque was ready for machining (Figure 19c). While every attempt was made to reduce the introduction of air into the plaques, when pores were found in the failed cross section of tested specimens, the results of that test were discarded. No special climate control system was used during the preparation or testing of any of the specimens used in this research in order to mimic typical production environments which would be expected for automotive applications of the adhesive. The experimental work was carried out in a room in which the temperature ranged from 19 ºC to 22 ºC and humidity ranged from 33% RH to 52 % RH, based on measurements taken over several years whenever specimens were prepared.

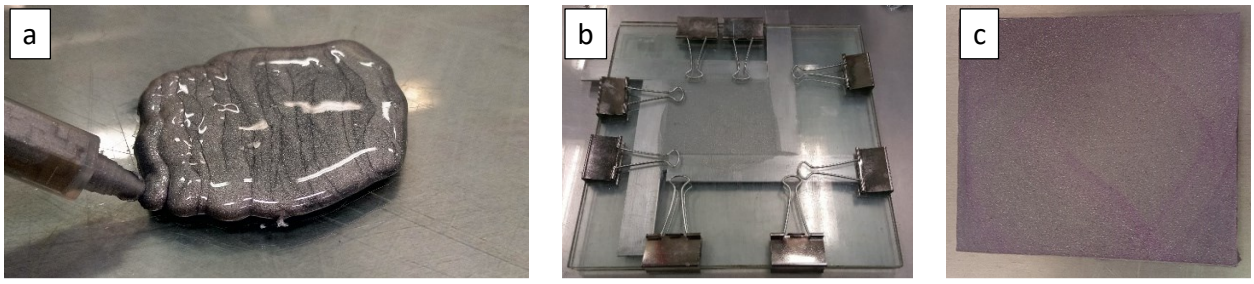

Figure 19: Application of adhesive(a), and full assembly (b), to create bulk adhesive plaque (c)

Tensile specimens were machined from the cured plaques to the geometry suggested in ASTM D638 type V [2014] (Figure 20a). The cross-sectional area of each specimen was measured using a micrometer prior to testing. After measurement, the gauge section of each specimen was painted using matte white spray paint followed by the application of a black speckle pattern to allow digital image correlation (DIC) to be used to measure the full strain field during testing.

Unlike the tensile specimen, no agreed-upon standard test geometry exists to test the shear stress-strain response of plastics. A small study was carried out using a variety of specimen geometries from the literature (Figure 20b) in an attempt to select a geometry that provided a good measure of the shear response of bulk structural adhesives. Five test geometries were selected based on a survey of appropriate candidates and were machined from bulk plaques: the 'mini shear' [Peirs *et al.*, 2012]; a modification of the mini shear geometry termed the 'micro shear' [Rahmaan *et al.*, 2015]; the 'block shear' [Gardner, 2013]; the ASTM B831; and the alternate ASTM B831 [2014] test specimens. Note that the 'block shear' and alternate ASTM B831 specimens incorporate a thickness reduction in their gauge section while the other specimens had a consistent thickness across the entire specimen. As with the tensile specimens, a speckle pattern was applied to each specimen to allow strain measurement using DIC.

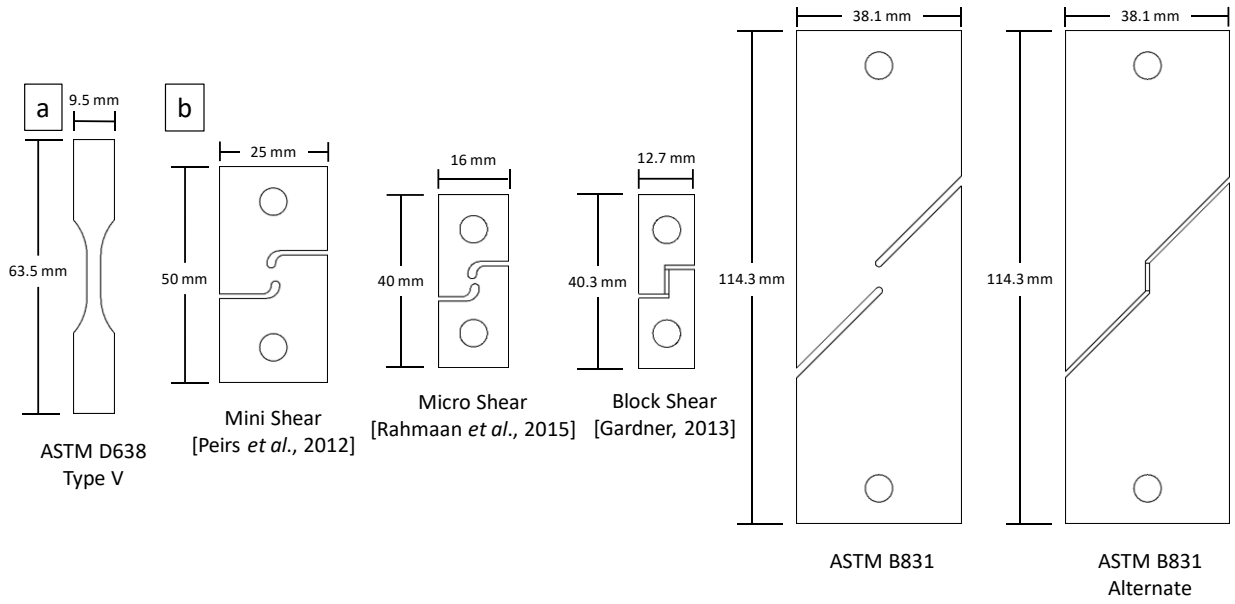

Figure 20: Tensile (a), and shear (b) bulk specimen geometries

To assess the compression stress-strain response of the adhesive, a series of compression tests were carried out on 9.525 mm ø x 19.05 mm ($^3/_8$" ø x $^3/_4$") right cylindrical specimens. While these specimens conformed to the aspect ratio suggested in ASTM D695, they were slightly undersized to minimize the volume of adhesive used in the specimen, avoiding any potential fire safety hazards associated with the exothermic reaction occurring during curing in large volume specimens. The specimens were allowed to cool slowly from the curing temperature to room temperature before being removed from the fixture, in order to minimize any residual stresses [da Silva *et al*., 2012].

3.1.2 Bulk Material Test Procedure and Analysis

Testing of the tensile and shear specimens was carried out using a hydraulic load frame (Figure 21), termed the '2 kN capacity frame' in the subsequent discussion of experimental tests carried

out in this thesis. This load frame was equipped with a 29.7 mm (1.1675") bore x 127 mm (5") stroke hydraulic cylinder (MTS Servoram 204.11; Eden Prairie, Minnesota, USA) controlled using an MTS Flex Test SE hydraulic controller (MTS; Eden Prairie, Minnesota, USA). A 2.2 kN (500 lb) load cell (Omega LC412-500; St. Eustache, QC, Canada) was used to measure force and a cylinder mounted linear variable differential transformer (LVDT) was used to measure displacement of the cylinder. Data was acquired using two National Instruments USB-6211 data acquisition systems and Labview 7.1 software (National Instruments; Austin, TX, USA). For both shear and tension, the tests were carried out using a constant cross-head velocity of 0.0254 mm/s (0.001 in/s). Each test was also recorded at a resolution of 1920 x 1080 pixels and 30 fps using a single, digital single-lens reflex (DSLR) camera (Nikon D3200; Tokyo, Japan) fitted with a 105 mm f2.8 macro lens (Sigma Corporation; Setagaya, Japan). A 2X teleconverter (Kenko TelePlus PRO 300 AF DGX 2x; Tokyo, Japan) was added for shear testing to improve the pixel density of the video. The load cell and video data were synchronized using an LED, which was illuminated at the start of data acquisition and placed in the frame of the video.

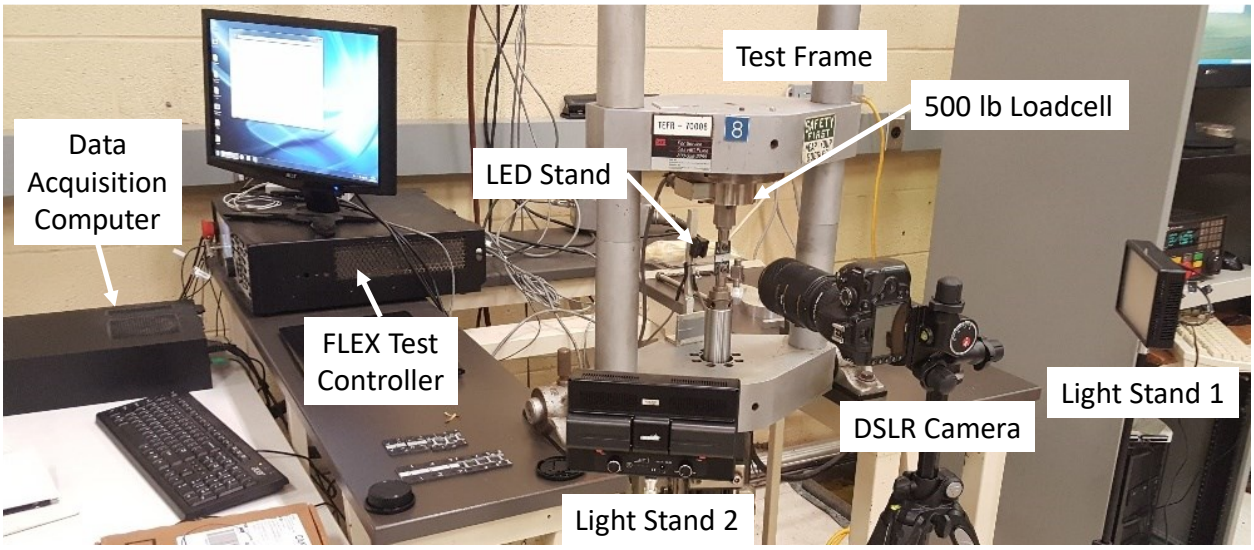

Figure 21: 2kN capacity load frame

Two dimensional DIC analysis was carried out using Vic-2D 2009 (Correlated Solutions; Irmo, SC, USA) to measure the full-field strain of the specimen. For the tension tests, the DIC analysis was carried out using images acquired at 5 Hz with a pixel density in the area of interest of 83 pixel/mm, DIC subset size of 41 pixels, a step size (the distance between subset centers) of 1 and a strain filter of 5 pixels. The average measurement of three parallel virtual extensometers along the gauge length of each specimen was used to determine the measured strain for each test. For the shear specimens, the DIC analysis was carried out at a frame rate of 5 fps with the resolution in the area of interest being 167 pixel/mm. A DIC subset size of 41 pixels, a step size of 1, and a strain filter of 15 pixels were used for each analysis. The shear strain for each specimen was reported from the central location of the gauge area as described in Rahmaan *et al*. [2015].

The compression specimens were tested using a custom-made hydraulic load frame (Figure 22), termed the '90 kN capacity frame' in the following discussion of the experimental investigations. This load frame was equipped with a 101.6 mm (4") bore x 152.4 mm (6") stroke hydraulic cylinder (Parker Cylinder Division; Owen Sound, Ontario, Canada) controlled using an MTS 407 hydraulic controller (MTS 407; Eden Prairie, Minnesota, USA). The test force was measured using a 90 kN (20 000 lb) load cell (Transducer Techniques SWP 20k; Temecula, California, USA) and the cylinder displacement was measured with a cylinder mounted linear variable differential transformer (LVDT). The data was acquired using a National Instruments Daqpad-6015 data acquisition system and Labview 7.1 software (National Instruments, Austin, TX, USA). Optical tracking (Tracker; [Brown & Christian, 2011]) was used to measure the change in height (and thus the strain) of the specimen during loading in a hydraulic frame at a loading rate of 0.0254 mm/s (0.001 in/s). Several tests had petroleum jelly added to assess the effect of lubricant between the

specimen and platens, with no appreciable difference measured in cases with and without lubrication.

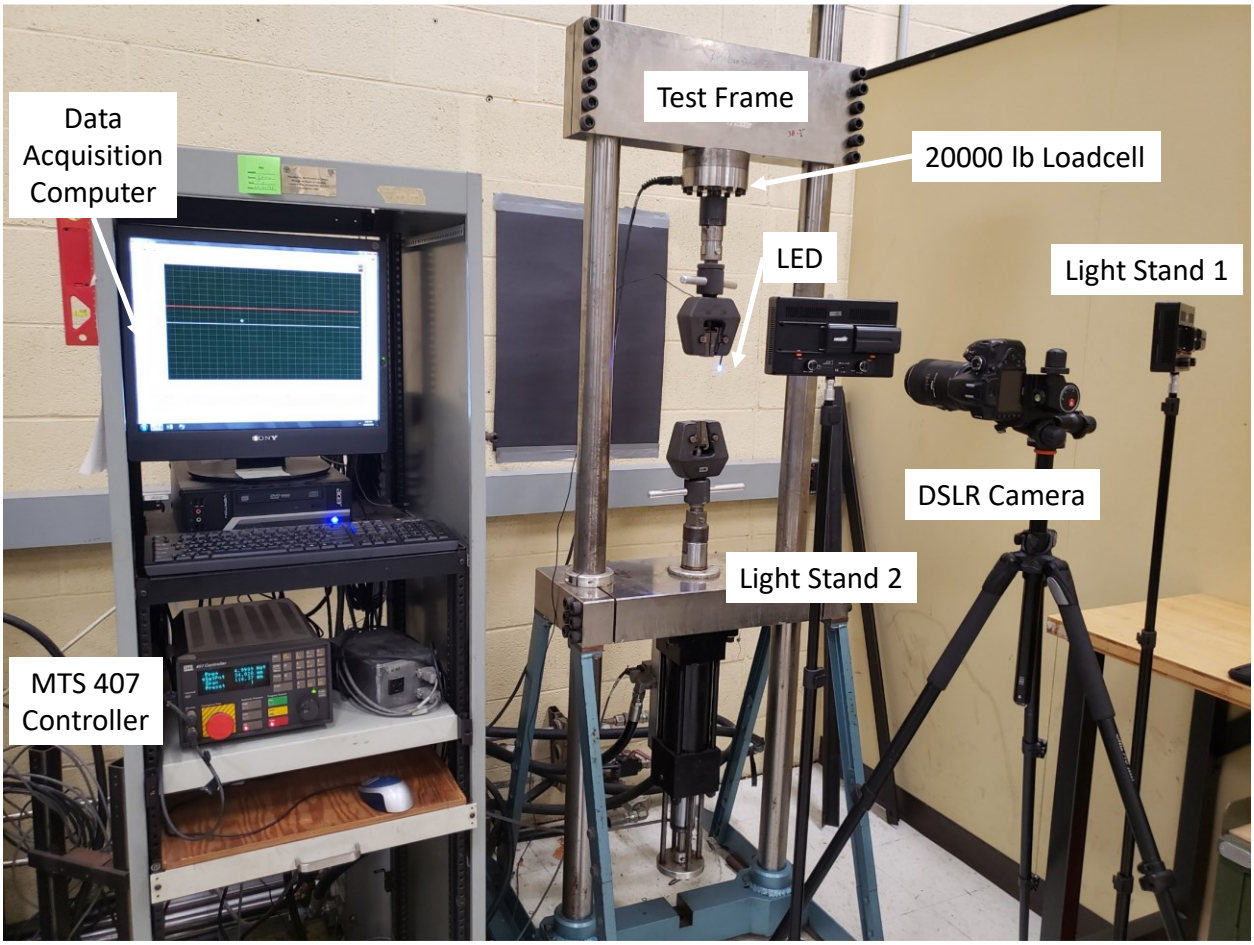

Figure 22: 90 kN capacity load frame

3.2 Mode I Characterization Testing

As discussed in the literature review, a number of techniques have been used to extract the parameters necessary to construct the traction-separation response of adhesively bonded joints. The classical tests (cantilever beam tests, butt joint tests, etc.) do not generally provide sufficient information with which to independently characterize the joint, requiring multiple test types to be carried out and several independent measurements combined. Dastjerdi *et al*. [2013] originally

developed the RDCB specimen to provide a single test to extract the traction-separation response of a bonded joint under Mode I loading. The small size of the specimen also makes this test attractive to measure the high loading rate response of adhesives by avoiding potential inertial effects that may be present in standard double cantilever beam tests using high mass adherends. A slightly updated specimen geometry (Figure 23) as suggested by Liao *et al.* [2017] for structural adhesive application was used in this work.

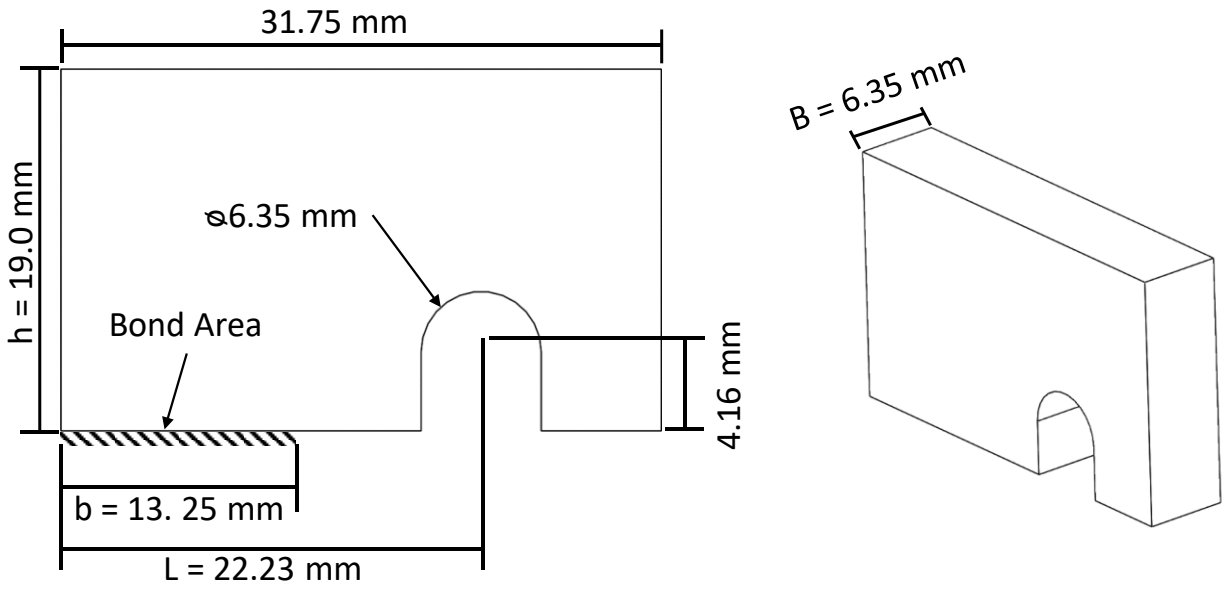

Figure 23: RDCB adherend dimensions

3.2.1 RDCB Specimen Preparation

To create the specimens to be tested, mild steel adherends were first machined to the proper dimensions (Figure 23). The adherends were grit blasted with 60 grit silicon carbide abrasive media for roughly 10 seconds per surface using a pressure of 350 kPa and cleaned with acetone immediately prior to bonding to remove any potential contamination from the adherend surfaces.

A bead of adhesive was applied to each adherend and spread to cover the entire surface. The adherends where then placed in a curing fixture (Figure 24a) with a steel shim of the desired bond line thickness inserted at the proper location in order to create a blunt crack tip. Three nominal bond line thicknesses were investigated; 0.18 mm (0.007”), 0.30 mm (0.012”) and 0.64 mm (0.025”). The edge of this shim was also used to provide a blunt notch at the leading edge of the bond line. The fixture was designed to ensure proper alignment of the specimens during curing and to allow excess adhesive to flow away from the bond area *via* channels machined into the bottom surface of pocket used to hold the specimen (Figure 24b). Once the specimens were aligned in the fixture, set screws on the perimeter of the fixture (Figure 24c) were tightened to hold the specimens firmly in place during the cure cycle.

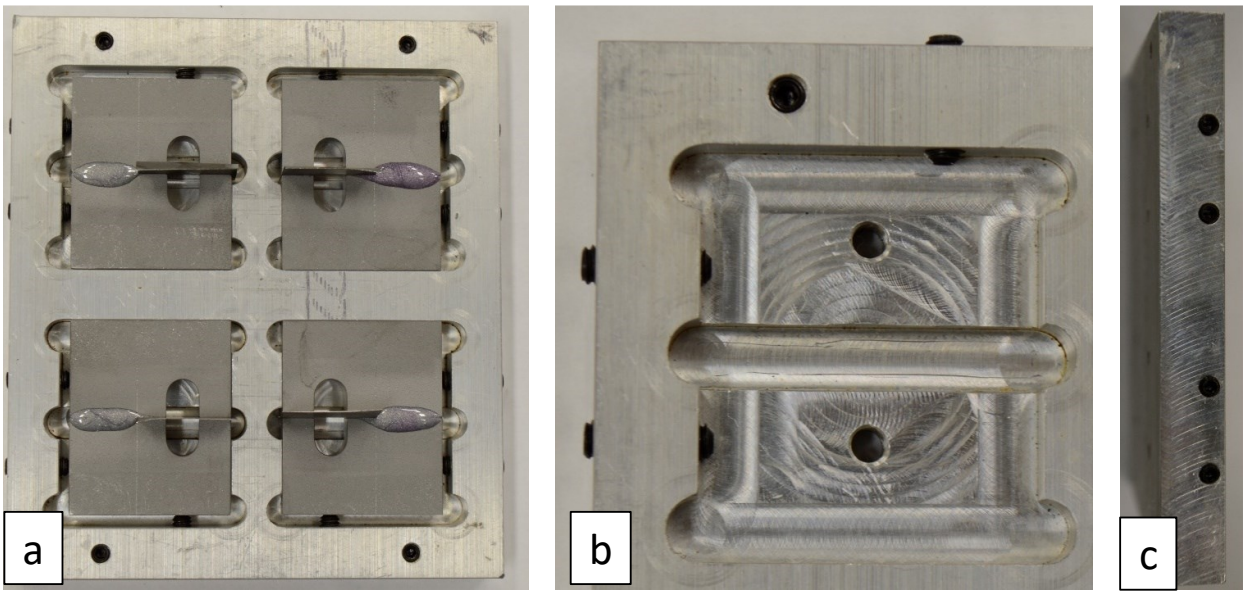

Figure 24: RDCB fixture (a), with excess adhesive channels (b), and set screws for specimen fixation during curing (c)

The specimens and fixture were then placed in a forced convection oven (Binder ED-53) to be cured for 30 minutes after reaching 80 ^{o}C, as recommended by the manufacturer. After curing, the

specimens were cooled to room temperature, the shims removed, and excess adhesive was removed with a sharp blade to ensure the bond area was flush to the adherend surfaces. The specimens were imaged using an opto-digital microscope (Keyence VHX 5000; Osaka, Japan) to inspect each specimen for potential defects. Additionally, the dimensions necessary for analysis (b, *L*) (Figure 25a) and the bond line thickness (Figure 25b) were measured. The thickness of each specimen (*B*) was then measured using a micrometer centered over the crack tip.

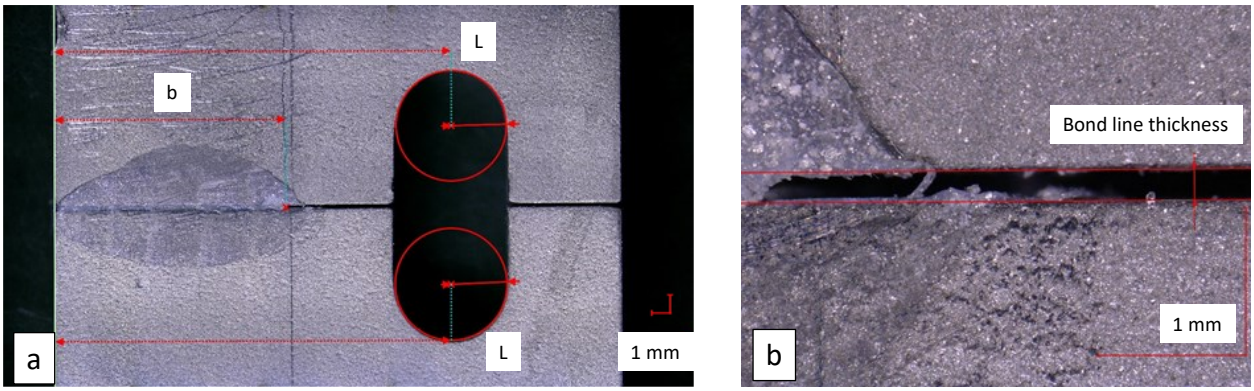

Figure 25: Measurement of RDCB specimen (a), and bond line thickness (b)

3.2.2 RDCB Test Procedure

The specimens were tested on the 2 kN capacity load frame at a crosshead velocity of 0.025 mm/s (0.001 in/s) as measured by the cylinder-mounted LVDT. To avoid machine compliance affecting the displacement measurement, which can be on the same order of magnitude as the displacement necessary to cause failure of a bonded joint, video of the loading pins was captured. The video was recorded at 30 fps using a DSLR camera mounted with 105 mm macro lens and a 2X teleconverter, which provided a pixel density of approximately 95 pixels/mm.

To prevent damage to the load cell by ramming the clevises together while setting up the machine, a custom designed slack adaptor (Figure 26a) was designed to attach to the cylinder end of the 2

kN capacity load frame. The slack adaptor allowed roughly 18 mm of travel between the point of clevis contact and the point at which significant compressive force could be applied to the load cell by the hydraulic cylinder. A small study was carried out to assess the effect of this addition using bulk tension specimens, and no measurable effect was noticed. To provide a length scale for optical tracking, two dots were added to the clevis mounted to the load cell (Figure 26b), which were measured using an opto-digital microscope prior to mounting the clevis into the load frame. During initial testing, two points on the pins were tracked to measure the opening of the specimen. After further investigation, rotation of the pin was found to affect this displacement measurement. To ameliorate this issue, in the testing described in this work two dots applied directly to the clevises were tracked to provide the pin opening used in the data analysis. After testing, the images of the adherends were captured to investigate the facture surface of the adhesive.

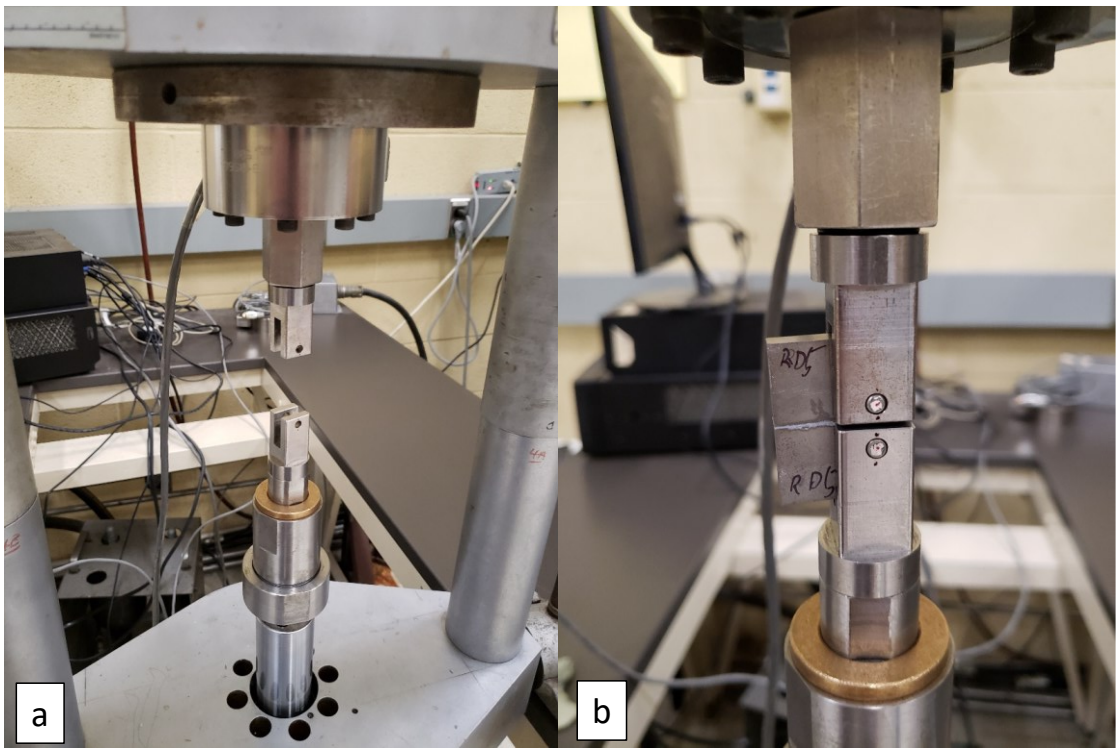

Figure 26: RDCB test setup including slack adaptor (a), with detailed view of loading clevis (b)

3.2.3 RDCB Analysis Technique

The RDCB specimen was originally developed by Dastjerdi *et al.* [2012] to measure the Mode I traction-separation response of proteinaceous bio adhesives and was later adapted to structural adhesives [Dastjerdi *et al.* 2012; Liao *et al.*, 2017]. Unfortunately, early work in the current research demonstrated the inability of the method described by Dastjerdi *et al.* to produce a traction-separation response in which a model of the test was able to reproduce the force-displacement response of that same test. For example, the traction-separation measured from a test performed by Liao *et al.* [2017] (Figure 27a) was used to create a finite element model of that same test in LS-DYNA. If the analysis was able to measure the traction-separation response, one should expect the mode and test force response to match. However, when the model force-displacement response was compared to the measured response (Figure 27b), the model underpredicted the peak force by 32%.

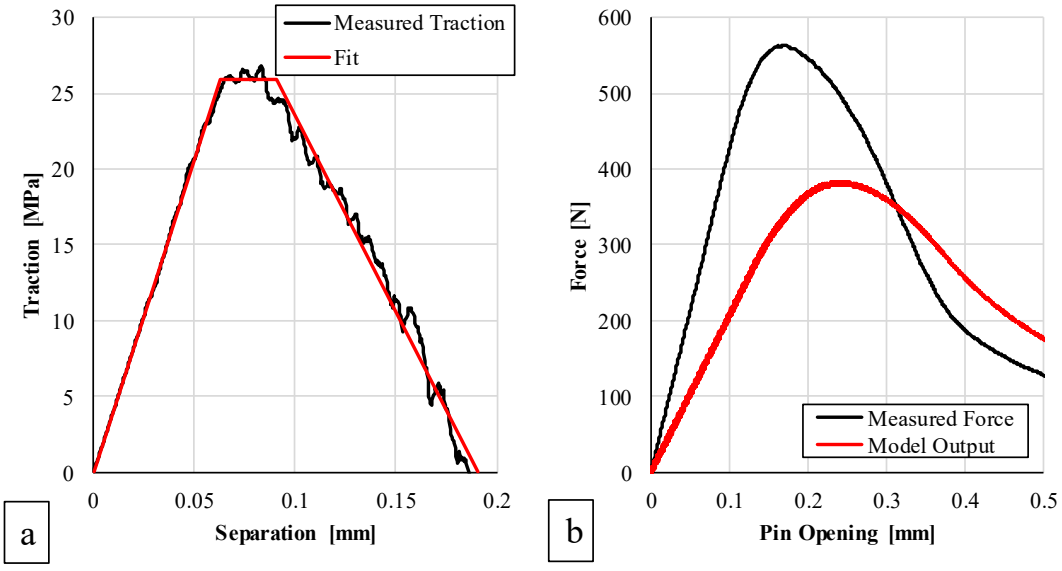

Figure 27: Traction-separation response measured from measured force-displacement response using Dastjerdi *et al.* [2013] analysis (a), and force-displacement model response using extracted traction-separation response (b)

Further investigation showed a zone of compressive stress in the bond line opposite the location of the pin loading (Figure 28). The compression zone had not been accounted for in the original analysis, which assumed that the entire bond line was loaded under tension. This finding necessitated the development of a new analysis technique for this specimen geometry.

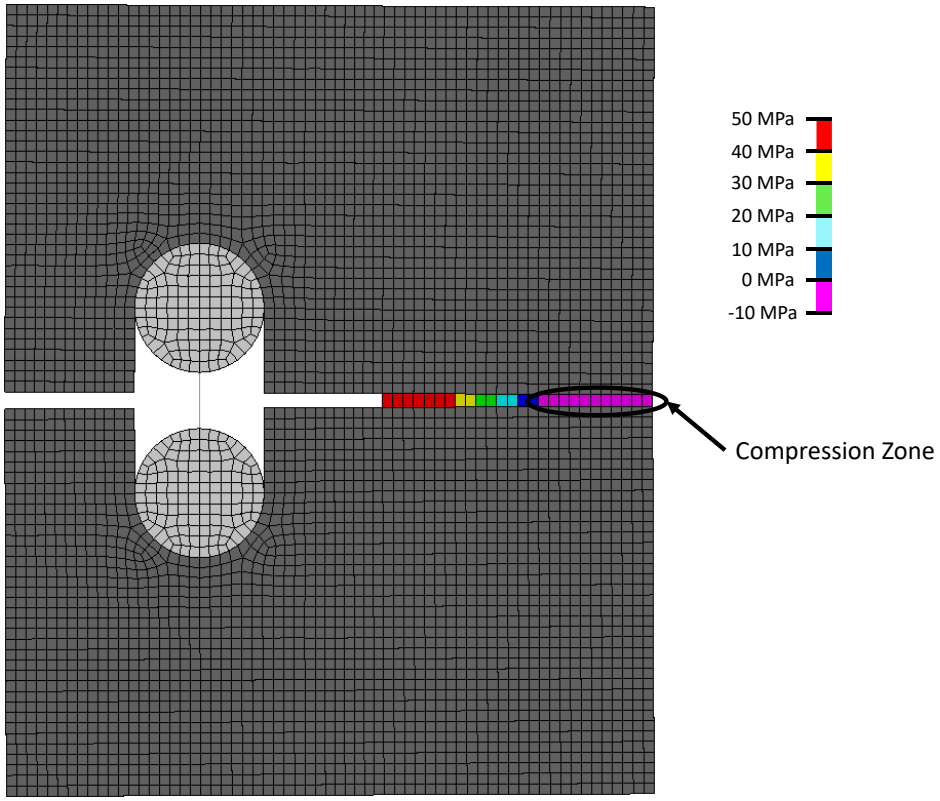

Figure 28: Stress distribution along RDCB model bond line

The first step in the updated analysis was to enhance the original free-body-diagram (Figure 29a) to include the region of compressive loading in the bond line (Figure 29b).

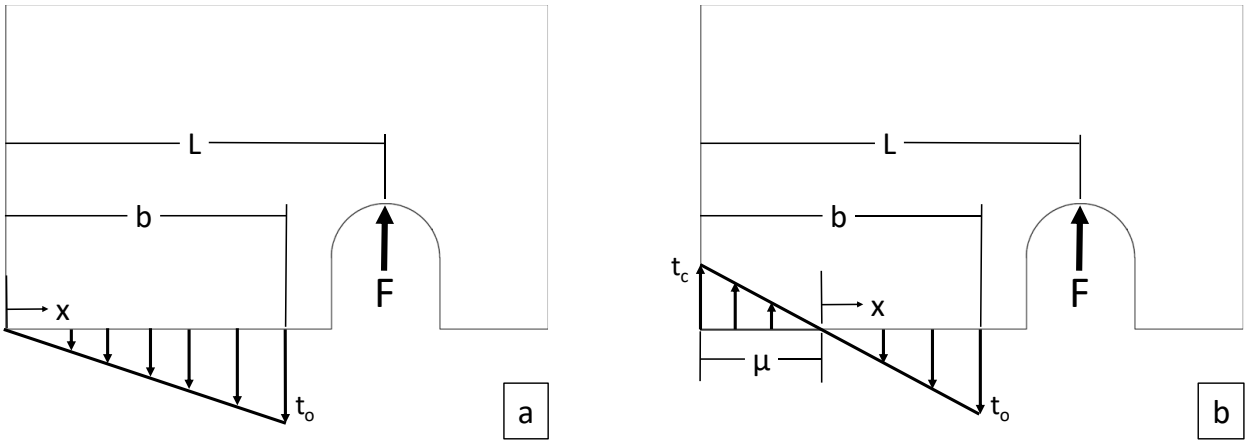

Figure 29: Free body diagram for analysis developed by Dastjerdi *et al.* [2013] (a), and updated analysis (b) [Watson *et al*., 2020a]

L (the distance from the edge of the specimen to the point of loading of the specimen) and *b* (the distance from the edge of the specimen to the end of the bond line) were carried over from the initial analysis. The variable μ was introduced to denote the distance between the edge of the specimen and the transition from tension to compression in the bond line. Additionally, t_o represented an arbitrary traction. By assuming perfectly rigid adherends (due to the very high resistance of bending of the adherends in the loading direction), the kinematics of the adherend (Figure 29b) led to the compatibility equations at the pin loading location, the blunt crack and the end of the bond line furthest from the pin;

$$\frac{\Delta}{L-\mu} = \frac{\delta}{b-\mu} = \frac{\delta_c}{\mu}, \tag{43}$$

where Δ is the pin displacement, δ is the opening displacement at the end of the bond line (separation), and δ_c is the closing displacement at the edge of the specimen. An arbitrary opening displacement (u) can be expressed as a function of distance from the point of rotation (x) by

$$u(x) = \frac{\delta}{b-\mu} x = \frac{\Delta}{L-\mu} x \,. \tag{44}$$

The distance, μ, and traction, $t(x)$, represent two unknown quantities necessitating simultaneously solving the force and moment balances for each increment of force-displacement to calculate the full traction-separation response. By assuming a perfectly linear, non-damaging traction response in compression, the force balance in the u direction can be described by

$$F + \frac{1}{2}\mu B t_c = B \int_0^{b-\mu} t(x) dx, \tag{45}$$

where B is the thickness of the specimen. Similarly, the moment balance about the point of transition from tension to compression (i.e. $x = 0$) can be written as

$$F(L-\mu) - \frac{2}{3}\mu \frac{1}{2}\mu B t_c = B \int_0^{b-\mu} x t(x) dx \,. \tag{46}$$

If one assumes a perfectly linear initial response of the traction-separation curve, the integrals of Equation (45) and Equation (46) become

$$\int_0^{b-\mu} t(x) dx = \frac{1}{2} t_o (b-\mu) \tag{47}$$

and

$$\int_0^{b-\mu} x t(x) dx = \frac{1}{3} t_o (b-\mu)^2 \,. \tag{48}$$

These simplified integrals lead to

$$F + \frac{\mu B t_c}{2} = \frac{B t_o (b-\mu)}{2}. \tag{49}$$

The following relationship from the moment balance can then be defined during the initial linear loading;

$$F(L-\mu) - \frac{\mu^2 B t_c}{3} = \frac{B t_o (b-\mu)^2}{3} \,. \tag{50}$$

Because the traction-separation response is purely linear initially, the relationship between δ and δ_c in Equation (43) can also be applied to t_o and t_c so that

$$t_c = \frac{\mu t_o}{b-\mu}. \tag{51}$$

Additionally,

$$t_c = E_I \delta_c = \frac{E_I \mu \Delta}{L-\mu} \tag{52}$$

the also holds true, where E_I is the initial slope of the Mode I traction-separation response.

By substituting Equation (52) into Equation (49) the loading force can be expressed as

$$F = B t_o \left(\frac{(b-\mu)}{2} - \frac{\mu^2}{2(b-\mu)}\right). \tag{53}$$

Additionally, substituting Equation (52) into Equation (50) yields

$$F = B t_o \left(\frac{(b-\mu)^2}{3(L-\mu)} + \frac{\mu^3}{3(b-\mu)(L-\mu)}\right). \tag{54}$$

By equating Equation (53) and Equation (54), one arrives at

$$\frac{(b-\mu)}{2} - \frac{\mu^2}{2(b-\mu)} = \frac{(b-\mu)^2}{3(L-\mu)} + \frac{\mu^3}{3(b-\mu)(L-\mu)}. \tag{55}$$

Equation (55) can be simplified to

$$\mu_{elastic} = \frac{3Lb-2b^2}{6L-3b}. \tag{56}$$

Note that the subscript *elastic* has been added to μ to clearly note that this relationship only holds in the initial linear portion of the traction-separation response.

By substituting Equation (52) into Equation (49) and rearranging, t_0 can be show to be

$$\frac{2F}{B(b-\mu_{elastic})} + \frac{E_I {\mu_{elastic}}^2 \Delta}{(b-\mu_{elastic})(L-\mu_{elastic})} = t_o. \tag{57}$$

Similarity, rearranging Equation (53) lead to

$$\frac{2F}{B}\left((b-\mu_{elastic})-\frac{{\mu_{elastic}}^2}{(b-\mu_{elastic})}\right)^{-1}=t_o\ . \tag{58}$$

By equating Equation (57) and Equation (58) and rearranging, the initial slope of the traction-separation response can be calculated;

$$E_I\ =\frac{F}{\Delta}\left(\frac{2\left(b-\mu_{elastic}\right)\left(L-\mu_{elastic}\right)}{B{\mu_{elastic}}^2}\right)\left(\left(\left(b-\mu_{elastic}\right)-\frac{{\mu_{elastic}}^2}{\left(b-\mu_{elastic}\right)}\right)^{-1}-\left(b-\mu_{elastic}\right)^{-1}\right). \tag{59}$$

By performing a change of variable from x to u in Equation (45) and Equation (46) using the derivatives of Equation (44) and replacing t_c with the expression from Equation (52), the generalized force and moment balances can be expressed as

$$\frac{F\Delta}{B(L-\mu)}+\frac{\mu^2E_I\Delta^2}{2(L-\mu)^2}=\int_0^\delta t(u)du \tag{60}$$

and

$$\frac{F\Delta^2}{B(L-\mu)}-\frac{\mu^3E_I\Delta^3}{3(L-\mu)^3}=\int_0^\delta ut(u)du\ . \tag{61}$$

Note that in these expressions, μ is generally unknown and only equal to $\mu_{elastic}$ during the initial linear elastic loading phase of the traction-separation response. Differentiating Equation (60) and Equation (61) with respect to δ and rearranging leads to

$$\frac{d\Delta}{d\delta}\frac{d}{d\Delta}\left(\frac{F\Delta}{B(L-\mu)}+\frac{\mu^2E_I\Delta^2}{2(L-\mu)^2}\right)=t(\delta) \tag{62}$$

and

$$\frac{(L-\mu)}{\Delta(b-\mu)}\frac{d\Delta}{d\delta}\frac{d}{d\Delta}\left(\frac{F\Delta^2}{B(L-\mu)}-\frac{\mu^3E_I\Delta^3}{3(L-\mu)^3}\right)=t(\delta)\ . \tag{63}$$

In these equations, both the traction and μ distance are unknown and therefore a script was written to solve these equations using numerical methods. μ cannot be less than zero and must always be

less than or equal to $\mu_{elastic}$, providing lower and upper bounds for μ. Knowing these bounds, Equation (62) and Equation (63) were calculated for 1000 values of μ between 0 and $\mu_{elastic}$ for each displacement increment after applying a 21-point running average filter to the force-displacement response. The value of μ that produced the minimum residual for these two equations was then determined as the μ value for a given pin opening, and the process was repeated for the next pin opening increment. In this manner, the entire traction response could be calculated with the separation (δ) calculated using Equation (43). After calculation of the traction-separation response a set of parameters necessary to define a trapezoidal traction-separation CZM response (initial stiffness (E_I), plateau traction (T), critical energy release rate (G_{IC}) and area ratio (f_{GI})) was fit to each test using a least squared error approach for each tracked displacement increment and a generalized reduced gradient nonlinear optimization scheme [Lasdon *et al.*, 1978].

3.3 Mode II and Mixed-Mode Characterization Testing

Characterization of the Mode II traction-separation of adhesive joints is typically carried out using a combination of end notch flexural testing and thick adherend lap shear, napkin ring or pin and collar testing. However, early investigation into the end notch flexural testing highlighted some challenges with this approach. A simple finite element model using the tapered geometry developed by Marzi [2012] was undertaken to assess the potential of this type of testing using elastic solid elements to model the adherends and a simple trapezoidal cohesive zone model to model the adhesive joint (Figure 30a). Despite the long span of the specimens (0.8 m) used to minimize the effect of the compressive loading on the joint crack front, a substantial amount of compressive loading (12 MPa, Figure 30b) was still apparent in the model.

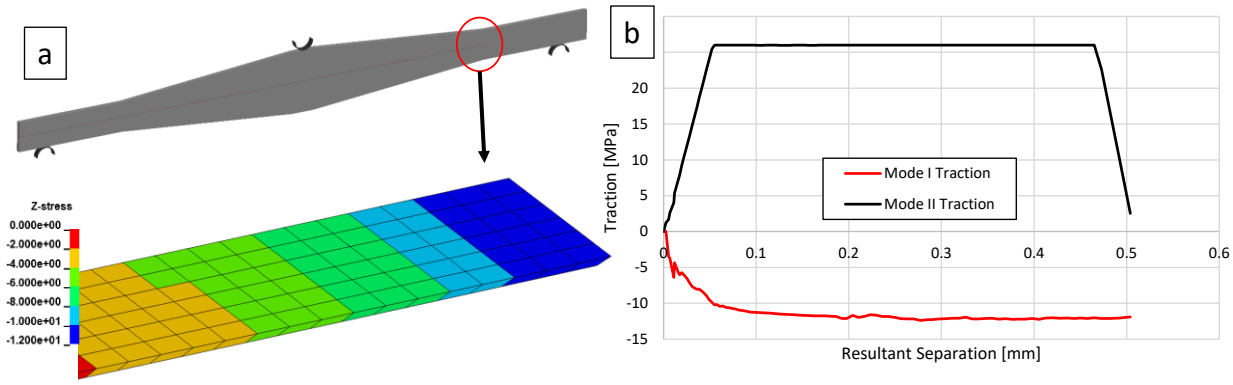

Figure 30: Model of the crack tip of TENF test specimen highlighting the presence of compressive stress (a), and traction-separation response of elements at crack tip (b)

Rather than trying to address this inherent issue in the ENF test, in the current research, a more direct approach was used, in which a new specimen geometry was developed to measure the Mode II traction-separation response. The specimen, termed the bonded shear specimen (BSS), was developed using a similar concept to the thick adherend lap shear specimen. The second moment of area was very large in the bending direction of the specimen, allowing for the assumption that all deformation was localized in the adhesive joint. Furthermore, the specimen adherend (Figure 31a) was designed so that the MM traction-separation response of the adhesive could be investigated by changing the angle of the bonded surface. Additionally, the bond line thickness could be well controlled using high precision machining of the adherend. For the investigation that follows, specimen angles of 90º (pure Mode II loading), 75º and 45º were investigated (Figure 31b).

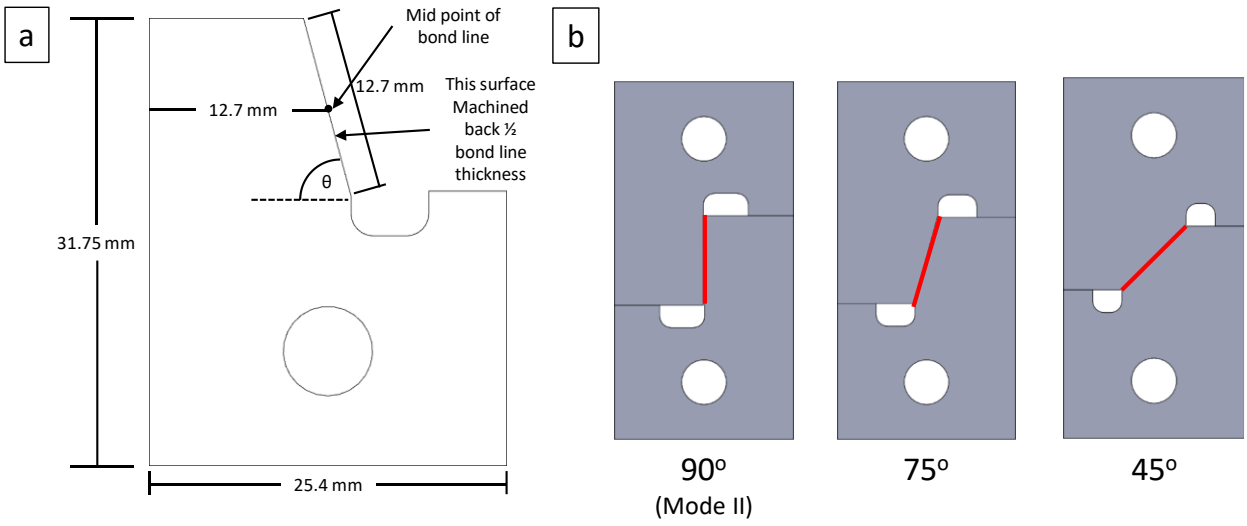

Figure 31: Dimension of bonded shear and mixed mode adherend (a), and schematic of tested specimen geometries with bond line highlighted in red (b)

To assess different nominal bond line thicknesses (0.18 mm, 0.30 mm and 0.064 mm), the adherends were machined to a nominal geometry (Figure 31a), after which half the bond line thickness was removed from the bonded surface to create the desired geometry.

3.3.1 Mode II and Mixed Mode Specimen Preparation

The adherends were machined from mild steel to the proper dimensions, after which the specimens were grit blasted and degreased using the same procedure as for the RDCB specimens. Adhesive was applied to the bonded surface and the specimens were placed in a precision ground machinists vice (Figure 32a) with spacers (Figure 32b) placed between pairs of adherends to allow for easy removal after curing. After assembly, the machinist vice was placed in the forced convection oven to cure according to the manufacture's specifications.

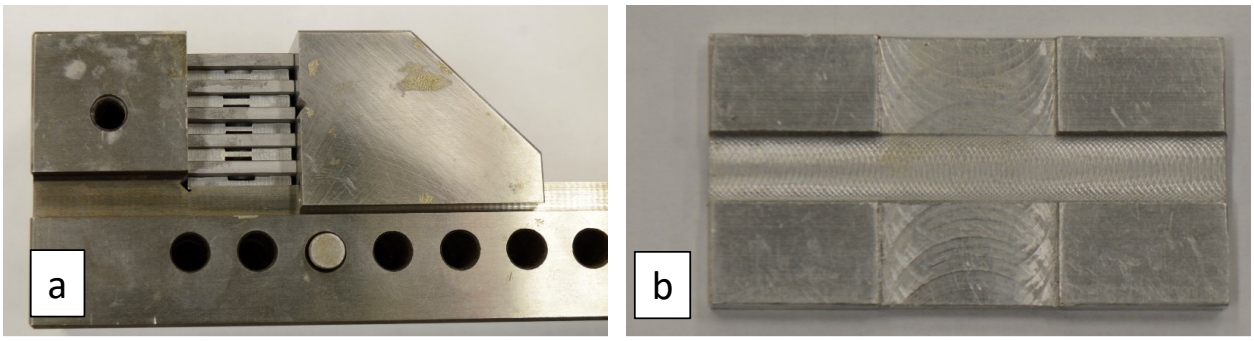

Figure 32: Bonded shear specimens in vice (a), separated by spacers (b)

After curing, the assembly was allowed to cool to room temperature under ambient conditions. Excess adhesive was removed from the surface of the specimen using a sharp blade while the cured adhesive in the pocket used to allow excess adhesive to pool (Figure 33) was removed using a diamond coated burr with a 1 mm diameter.

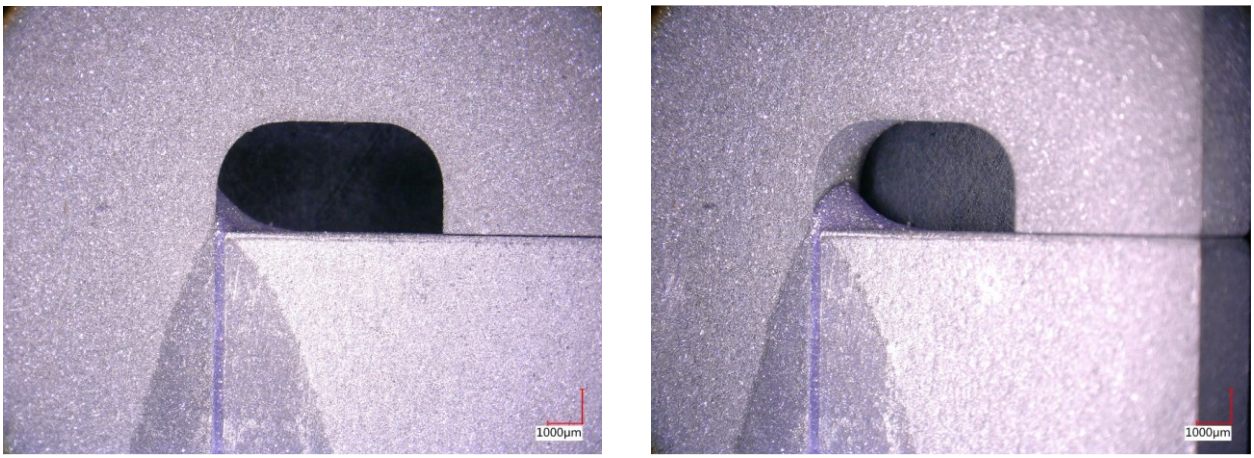

Figure 33: Excess adhesive in adherend pocket

After the excess adhesive was removed from the specimen, two lines were added to the surface of the specimen using a fine felt tip permanent marker to provide a length gauge to use for optical tracking of the relative displacement between the two adherends when testing. Two dots were also

added to each side of the bond line to provide tracking targets for post-test analysis. The bond line length and thickness and the distance between the two measurement lines were then measured using the opto-digital microscope (Figure 34) for each specimen.

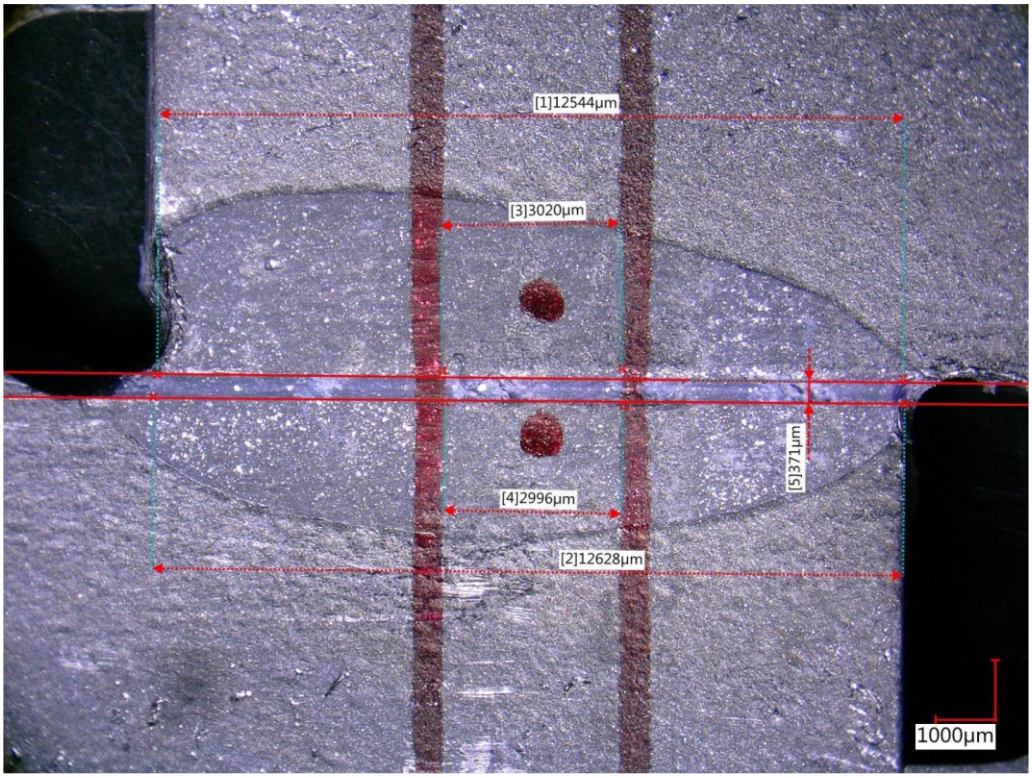

Figure 34: Measurement of bonded shear specimen using the opto-digital microscope

3.3.2 Mode II and Mixed Mode Test Procedure

The specimens were tested in the 2kN capacity load frame, fitted with the slack adaptor. Loading was carried out at 0.025 mm/s (0.001 in/s), the same rate as the RDCB specimens. Video of the tests were captured using a DSLR camera fitted with a 105 mm macro lens, with an approximate pixel density of 87 pixels/mm. An LED, which was illuminated when data was being acquired was placed within the camera frame in order to synchronize the force data acquired from the 2.2 kN (500 lb) load cell attached to the load frame and the test video.

After testing, optical tracking was carried out using the two points added to the adherend surface, with the distance between the two lines as a length gauge, to provide a separation measurement for the CZM response. As with the RDCB specimens, images of the fracture surfaces were taken after testing.

3.3.3 Mode II and Mixed Mode Analysis Technique

The analysis of the BSS was relatively straightforward, based on the assumption of a uniform stress distribution across the bond line due to a lack of bending of the adherends. For example, the shear samples used in this work were designed to have a very high second moment of area (4336 mm^4 *vs.* 69 mm^4 for a typical single lap shear specimen) to keep the bonded surfaces straight and parallel as the specimen was loaded. The resultant traction response was calculated using

$$\sigma_{Res} = \frac{F}{B \cdot b}, \tag{64}$$

where F was the measured load cell force, B was the specimen thickness, and b was the bond line length measured prior to testing. The separation response was measured by calculating the difference in displacement in the loading direction from the tracked displacement of each adherend. These data were then fit to a trapezoidal response, using a least squares fit to find the initial stiffness (E_{II}), plateau traction (S), critical energy release rate (G_{IIC}) and area ratio (f_{GII}) for each test. These values were then averaged for each bond line thickness to provide an average traction-separation response for a given bond line thickness.

Due to the unequal initial stiffness response in Mode I and Mode II loading, the mixity angle (θ_m) was not, in general, equal to the specimen angle (θ_s) and thus, for the MM specimens, it was necessary to first calculate the mode mixity angle applied to the bonded joint. In order to ensure

force equilibrium during loading, the resultant stress must align with the loading direction (Figure 35), due to the use of pins to load the specimen, which do not support a moment. If fixed grips were used, the loading and mixity angle would be equal, although the angle between the Mode I and Mode II stress directions would not align with the specimen and would need to be accounted for in the analysis. For the pin joint loading case used in this study, the mixity angle was related to the specimen angle using

$$\theta_m = \tan^{-1}\left(\frac{E_I}{E_{II}} \cdot \tan(\theta_S)\right). \quad \textbf{(65)}$$

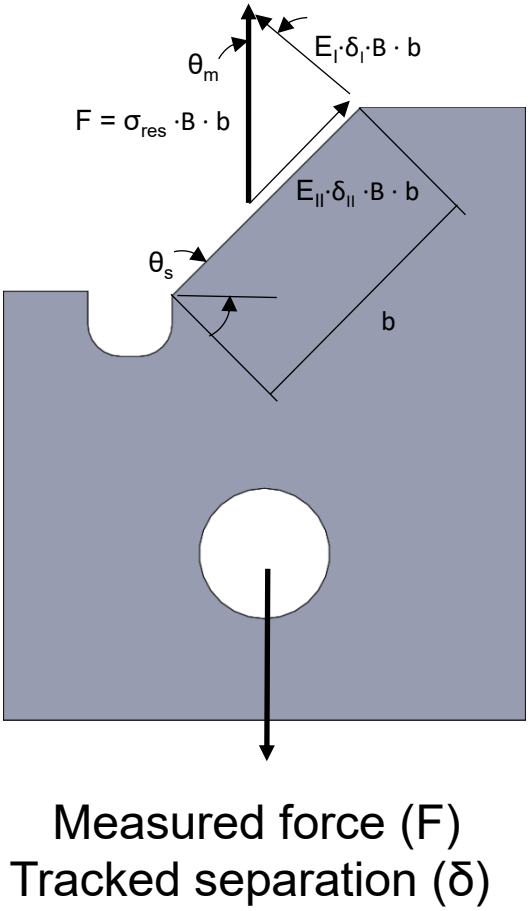

Figure 35: Free body diagram of the mixed mode specimen analysis

Note that in this expression, E_I and E_{II} were the values measured for a given nominal bond line thickness from the RCDB and BSS testing. Using Equation (64) to calculate the traction along with the relative displacement between the two adherends tracked in the loading direction, a resultant traction (σ_{Res})-resultant separation (δ_m) response was generated for each test. As with the Mode I and Mode II testing, resultant initial stiffness, plateau traction, critical energy release rate and area ratios were calculated for each test, using a least squared fit. Finally, the Mode I and Mode II energy release rates at failure were calculated based on the trapezoidal fit for each test using the following expressions;

$$G_I = \frac{\sigma_{Res,P} \cdot cos(\theta_m)}{2} \left({\delta_I}^f + {\delta_I}^s - {\delta_I}^0 \right) \tag{66}$$

and

$$G_{II} = \frac{\sigma_{Res,P} \cdot sin(\theta_m)}{2} \left({\delta_{II}}^f + {\delta_{II}}^s - {\delta_{II}}^0 \right), \tag{67}$$

where ($\sigma_{Res,P}$) is the resultant plateau traction fit for each test. Following the procedure described above, it could be shown that for each MM test, the simple summation of G_I and G_{II} was equal to the measured critical energy release (G_c) rate by calculating the area under the MM traction (σ_{Res})-separation (δ_m) fit.

3.4 TDCB Testing

Tapered double cantilever beam (TDCB) testing was carried out to provide data with which to compare the RDCB analysis. Specimens were constructed using the geometry described in the ASTM D3433 [2012] standard in order to provide a comparison between the data extracted from the RDCB analysis and a widely accepted, existing characterization methodology. After the adherends were machined from A36 steel, the same surface preparation used to prepare the RDCB

specimens (grit blasting and degreasing with acetone) was performed. As with the RDCB specimens, shim stock of the appropriate thickness was used maintain the specimen bond line thickness (0.18 mm, 0.30 mm and 0.64 mm). Additional shims were added at the rear of the specimen and the specimens were clamped using cap screws through holes in both adherends (Figure 36a). After curing, the excess adhesive was removed from the specimens and the bond line was inspected under an opto-digital microscope in order to measure the bond line thickness at the blunt crack tip and to inspect the specimens for any defects. The specimens were then tested using the 90 kN capacity load (Figure 36b) frame. Due to the comparatively large displacement associated with this testing, LVDT data was used to provide a measure of pin opening displacement. In early testing, this method was compared to optical tracking methods described earlier with no difference between the two measurement methods. A total of three specimens for each bond line thickness were loaded at a constant rate (0.015 mm/s) to failure.

Figure 36: Assembly of TDCB specimen (a), and TDCB test (b)

3.5 Single Lap Shear Testing

In order to validate the characterization work and cohesive zone model described in Chapter 5, a series of single lap shear tests were carried out. The specimen geometry (Figure 37) was based on that outlined in ASTM D1002.

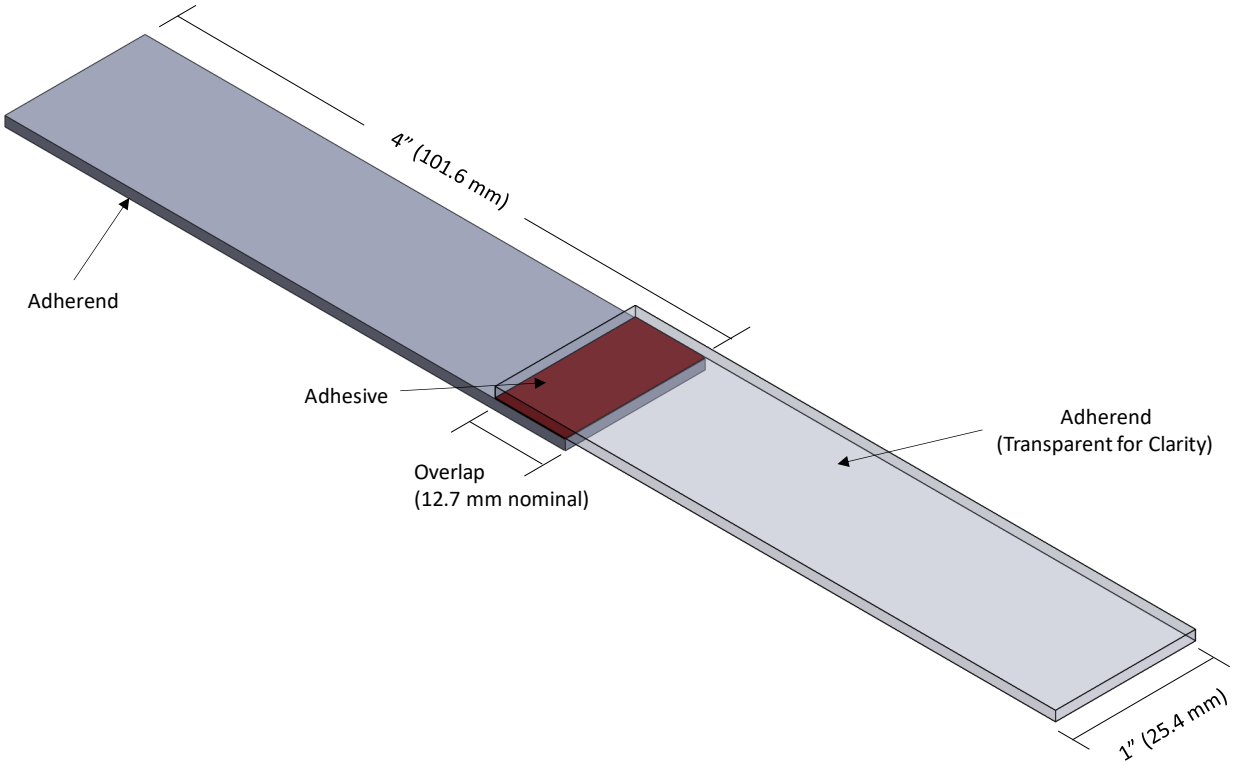

Figure 37: Single lap shear tests specimen geometry

While single lap shear testing is generally used as a quick, relatively simple way to compare the load carrying capacity of various adhesive / adherend / surface treatment combinations, additional data was collected during this testing series to allow direct comparison between the model and test force, displacement, and rotation responses. In this way, this series of tests provide straight-forward, well-controlled conditions to provide model validation data.

3.5.1 Single Lap Shear Specimen Preparation

The adherends were sheared into 101.6 mm x 25.4 mm (4" x 1") rectangular parts from a single sheet of 1.29 mm (16 ga) A366 steel and a single 1.63 mm (14 ga) 6061-T6 aluminum sheet. Prior

to bonding, the adherends were grit blasted and cleaned with acetone using the same procedure as the characterization testing specimens. Specimens were created in batches of 6 using a custom-made curing fixture. Six adherends were placed into the curing fixture (Figure 38a) and butted against the end stop, which was set to ensure the correct specimen length and overlap of 12.7 mm (½”). The bottom strap was then tightened across the bottom adherends, to prevent motion during the bonding process. These adherends were separated by thin strips with a thickness slightly less than twice the adherend bond line thickness, which, in addition to easing removal of the specimens from the fixture after curing, ensured the specimens were properly aligned in the longitudinal direction. Additionally, two non-gritblasted adherends were placed on the opposite side of the fixture, transverse to the bottom adherends in order to support the top adherends after bonding. Finally, three stacks of two 76.2 mm x 25.4 mm (3” x 1”) adherends and one piece of shim stock equal to the desired bond line thickness were placed at the edges and at the center point of the fixture to provide the correct specimen thickness once the bonding procedure was finished. For these tests, only 0.3 mm (0.012”) and 0.64 (0.025”) nominal bond line thicknesses were investigated due to the difficulty in producing well controlled bond line thicknesses under 0.3 mm with this specimen geometry due to the relatively light clamping pressure that could be applied compared to the RDCB, BSS and MM specimens.

A bead of adhesive was then laid along the width of each of the bottom adherends, in place in the fixture (Figure 38b). The top adherends were then laid in the fixture and the top strap was tightened, with care being taken to ensure the non-gritblasted adherends were centered below this strap to prevent bending of the top adherends (Figure 38c). Finally, the top plate of the fixture was screwed to the base plate to provide a consistent pressure across all specimens (Figure 38d). The entire assembly was then paced in a forced convection oven (Binder ED-53) and cured for 30

minutes after reaching 80 ºC, as measured by a thermocouple placed near the bond area of the center adherends.

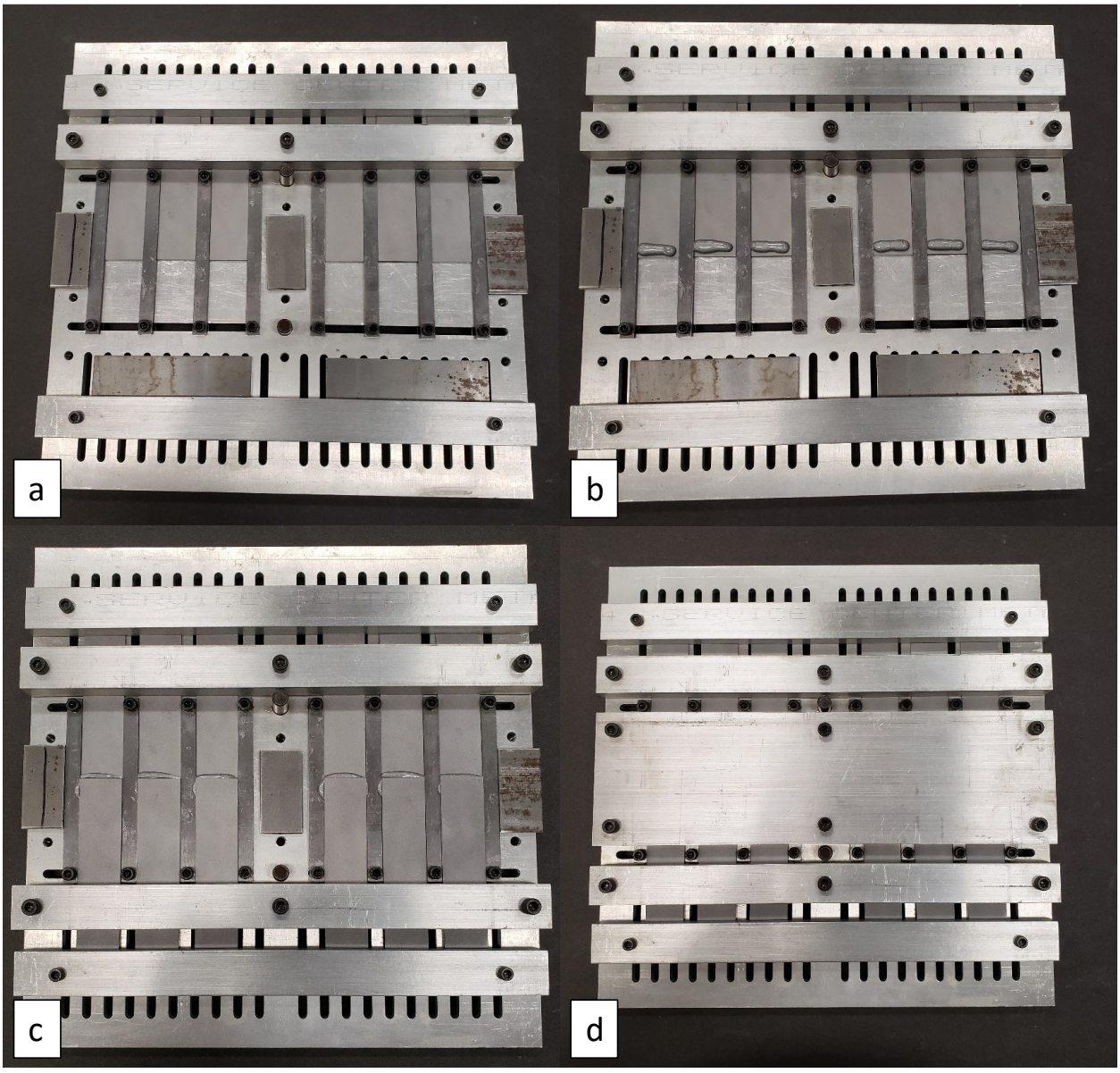

Figure 38: Summary of single lap shear specimen preparation

After curing the specimens were allowed to cool to room temperature and removed from the fixture. Excess adhesive was then removed from the specimens using a sharp blade to make the

bond area flush with the sides of the adherends. The specimens were then imaged using an opto-digital microscope to measure the bond line length and thickness and to identify any potential defects in the adhesive joint, although none were found in this study.

3.5.2 Single Lap Shear Test Procedure and Analysis

The single lap shear specimens were tested using the 90 kN capacity load frame. Prior to testing, four dots were added to the side of the specimen along the centerline of the adherend (Figure 39) to provide points to optically track. These tracking points provided a local measured of displacement (the change in longitudinal length from Point A to Point B) and the rotation of the bond line (change in angle of the line segment created by Point C and Point D). Points A and B were located 76.2 mm (3") from each end of the specimen (marked using a digital height gauge on a marble slab) with points C and D being located at the edge of the adherend over the bond area.

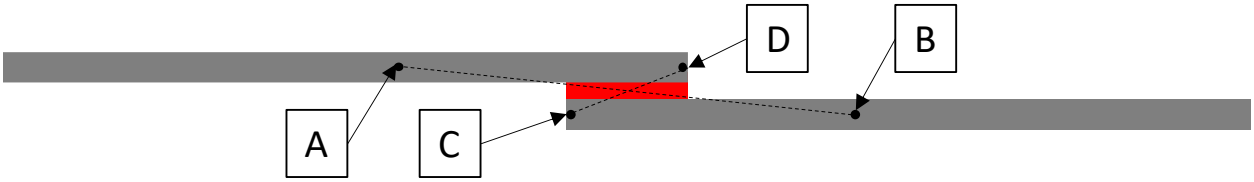

Figure 39: Points tracked on single lap shear specimens to measure displacement (segment A-B) and rotation (segment C-D)

In order to keep the specimen centered along the centerline of the testing machine, 25.4 mm x 25.4 mm (1" x 1") tabs sheared from sheet used to create the adherends were attached to the specimen using double sided tape. The specimens were loaded into mechanical wedge grips with the tabs and the last 25.4 mm (1") of each end of the specimen in the grip leaving the central 139.7 mm (5 $^1/_2$") of the specimen between the grips. The specimens were loaded at a constant loading rate of

0.1 mm/s with load cell data output at 120 Hz. Video of the tests were captured using a DSLR camera mounted with a 105 mm f2.8 macro lens at a resolution of 1920 x 1080 at 30 fps, with a pixel density roughly 40 pixel/mm. After testing, tracking was carried out to produce load cell force-tracked displacement and rotation-tracked displacement plots for each adherend-bond line thickness combination.

Chapter 4 Experimental Results and Discussion

In the sections that follow, the results of the experimental testing described in the previous chapter will be presented, along with discussion of these results, particularly with regard to their use in cohesive zone modeling. First, discussion of the bulk material testing is presented, followed by the results and discussion pertaining to the newly-developed characterization methodologies for Mode I (RDCB), Mode II (BSS) and MM loading. Finally, results of the single lap shear testing, undertaken to provide tests with which to validate the characterization and modeling methodologies developed in this research are presented.

4.1 Bulk Material Test Results and Discussion

The stress-strain response of the bulk 7333 adhesive subjected to tensile loading (Figure 40) provided a baseline response for much of the characterization work that followed. The average maximum true stress of all tests (n = 5) was 43.57 MPa (SD = 1.71 MPa), the Young's modulus was 2.24 GPa (SD = 0.094 GPa) and the average true failure strain was 0.085 mm/mm (SD = 0.031 mm/mm). The non-linear portion of the response was found to be flat with no hardening behavior. The Young's modulus fell within values typically reported in the literature for quasi-static loading of bulk toughened epoxy adhesives (1.3 GPa to 2.7 GPa [Garcia et al., 2011; Morin et al., 2010; Trimino & Cronin, 2016]) while the peak tensile stress was roughly the same as reported in the same studies (31 MPa to 43 MPa). Of course, these properties are dependant on the particular formulation of a given adhesive. The intention in comparing the results of the current work to those presented in the literature was to highlight that the experimental methods and 3M 7333 used in the current study did not exhibit abnormal responses. Furthermore, the Young's modulus and

maximum stress measured in the current study (44 MPa and 2.2 GPa, respectively) were somewhat higher than that reported by the manufacturer (34 MPa and 2.1 GPa, respectively [3M, 2016]). The manufactures data was obtained using adhesive that had cured at room temperature, which would exhibit less crosslinking that that measured in the current study, and thus exhibit lower strength and stiffness, highlighting the importance of the curing cycle on the performance of the adhesive.

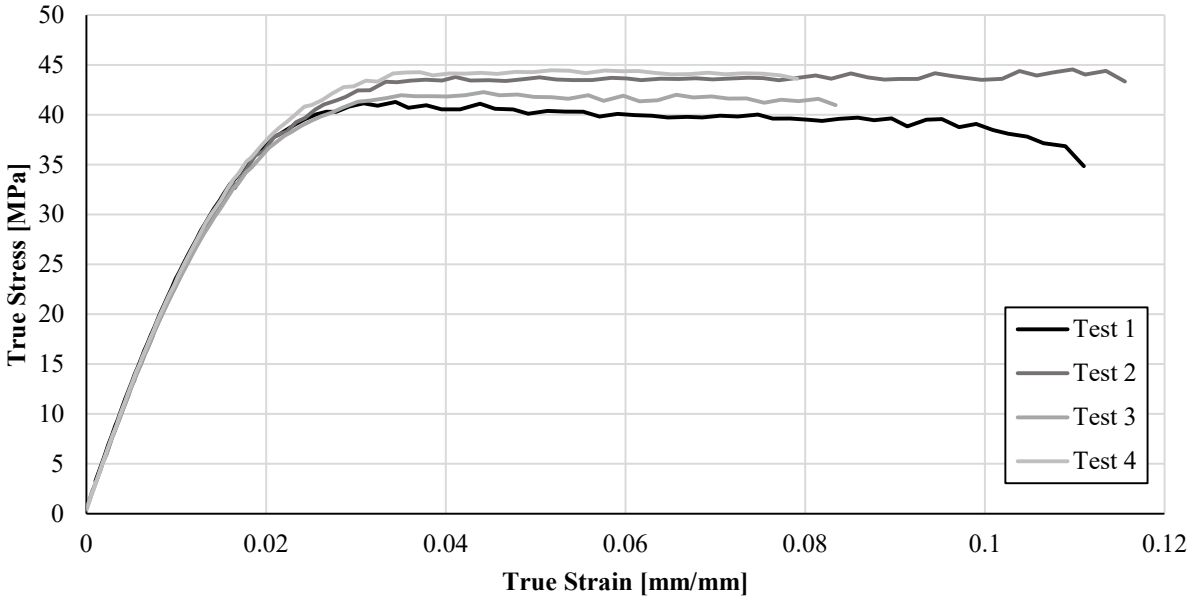

Figure 40: Stress-strain response of bulk 3M 7333 adhesive under tensile loading

The compressive stress-strain response of the adhesive (Figure 41) was characterized using a standard cylindrical geometry. During testing, the specimens were found to deform out-of-plane (Figure 42), which began to dominate the response after the initial linear elastic portion of loading. This deformation pattern was also apparent in a study of neat epoxy resin by Littell et al. [2008], who described this response as a buckling mode of deformation. For this reason, the tests were arrested rather than proceeding until failure. The initial portion of the stress-strain response (prior to the out-of-plane deformation) was used to measure the Young's modulus of the adhesive under

compressive loading (2.01 GPa, SD = 0.16 GPa, n = 4). A t-test comparison of the compressive and tensile Young's moduli indicated no statistically significant difference for these two measurements (p value = 0.12). A comparison of failure strength was not undertaken because the maximum compression response was dominated by geometric considerations (buckling) rather than material failure.

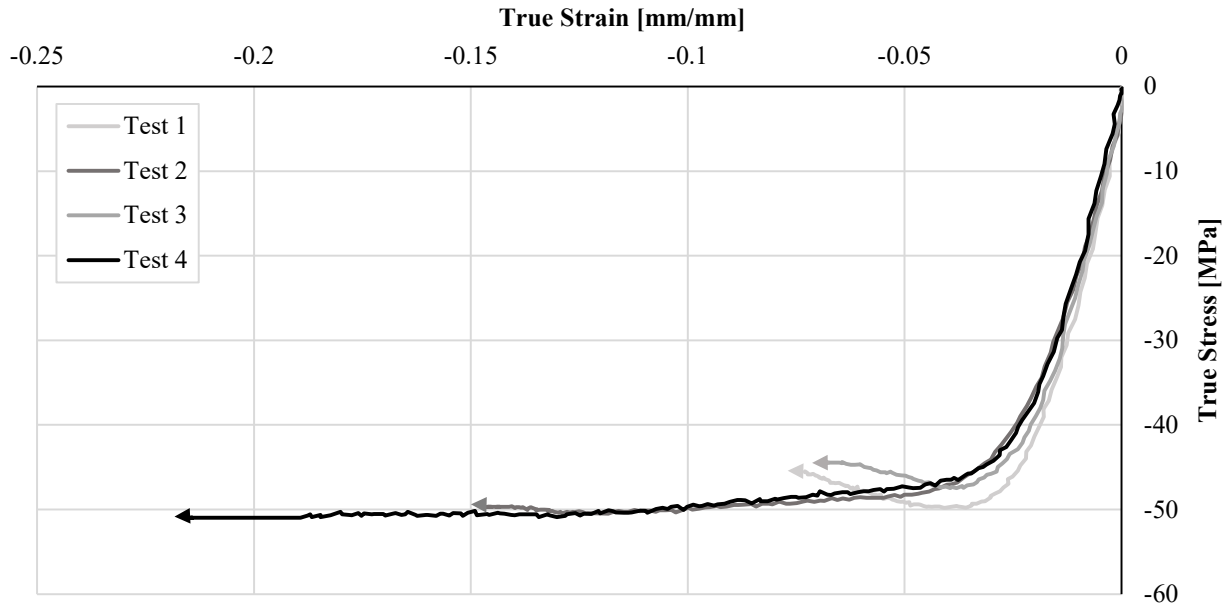

Figure 41: Stress-strain response of bulk 3M 7333 adhesive under arrested compressive loading

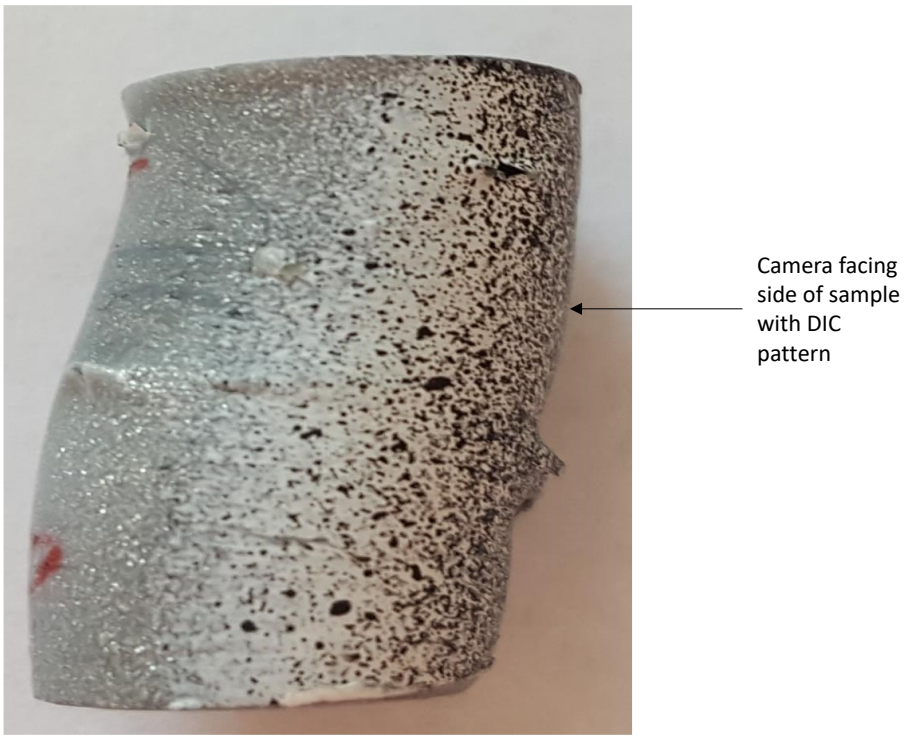

Figure 42: Out-of-plane deformation of compression specimen

The stress-strain response of the tested shear specimens (Figure 43) generally exhibited reasonable consistency in the shape of the response and average peak stress values ranging between 23 MPa and 28 MPa. Large scatter was present in the measurement of average strain-to-failure (0.15 mm/mm to 0.30 mm/mm).

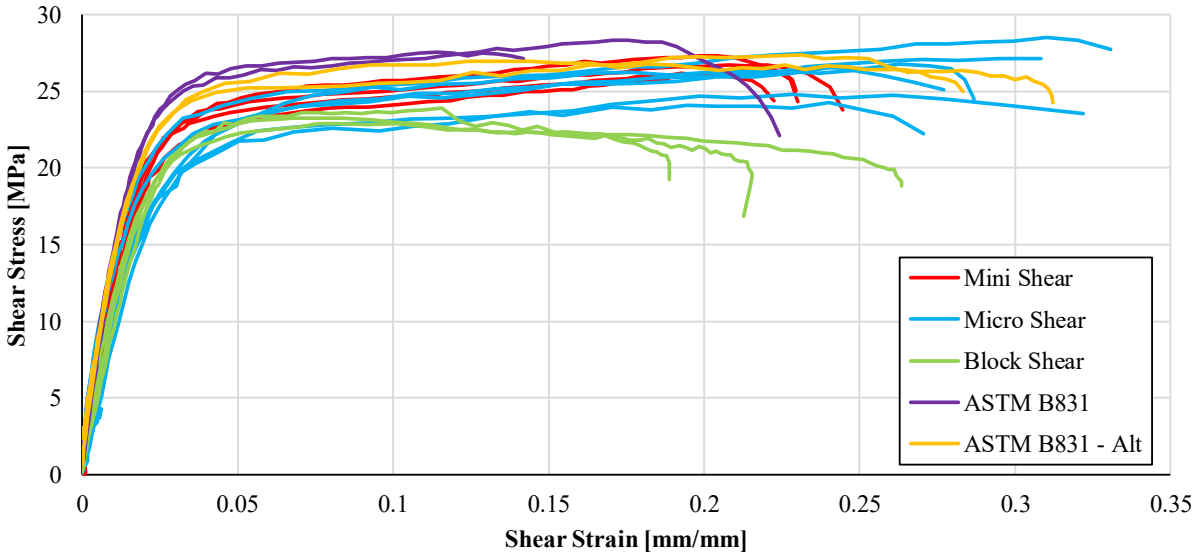

Figure 43: Stress-strain response of bulk 3M 7333 adhesive under shear loading

This scatter was associated with the tensile nature of the ultimate failure that was present across all geometries (Figure 44). In specimens for which there was no reduction in specimen thickness (the mini-shear, micro-shear and ASTM B831 specimens), failure initiated outside of the gauge areas in locations of high tensile strain (*i.e.* the location of the maximum 1st principal strain). For specimens with a stepped-down gauge area (the block-shear and Alternate ASTM B831 specimens), failure tended to initiate at the root of stepped region, due to large stress concentrations at these locations. The more gradual pull-out type failure led to a flat or softening stress-strain response with these specimens as opposed to the hardening behavior present with the other specimens.

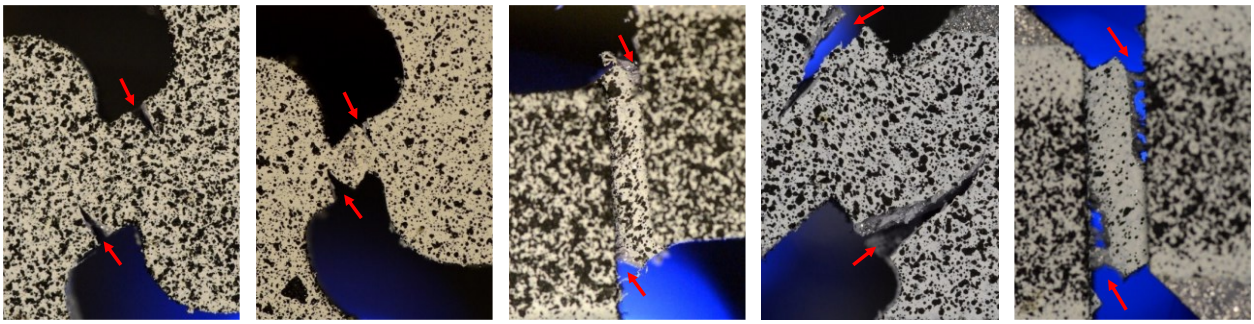

Figure 44: Fracture location of each bulk shear specimen tested, with fracture initiation noted with red arrows

Due to the micro-shear specimen exhibiting the largest measured shear strain of the specimens tested prior to fracture initiating due to tension, this specimen was selected to serve as the 'baseline' bulk test geometry with which to compare to the Mode II traction of the BSS (discussed below). The average shear modulus was measured for each specimen (n = 6) by fitting a linear response to the stress-strain response between 1 MPa and 15 MPa, leading to an average of 0.91 GPa (SD = 0.14 GPa). Each test was then fit to an elastic-perfectly plastic response in order to calculate an 'average plastic stress-strain curve' of 24.28 MPa (SD = 1.14 MPa). This approach was, in principle, similar to the approach used to fit the bonded shear specimen test results to a trapezoidal CZM, allowing for a direct comparison of the bulk and bonded specimen response. Finally, the average measured maximum shear stress was 26.31 MPa (SD = 1.43 MPa). Compared to other values reported in the literature for quasi-static loading of bulk toughened epoxy adhesives [Garcia et al., 2011; Morin et al., 2010; Trimino & Cronin, 2016] the shear modulus and maximum shear stress were on the higher end of expected values (0.91 GPa *vs*. 0.48 GPa to 0.91 GPa and 26 MPa *vs*. 24 MPa to 26 MPa, respectively). As noted in Watson *et al.* [2019a], the micro-shear geometry was based on a specimen used to assess the shear properties of sheet metal. The original

specimen [Peirs *et al.*, 2012] was developed by an iterative approach with a finite element model of the specimen using a Johnson-Cook material model, which is not generally appropriate for polymeric materials. In the original study, the authors noted that as the eccentricity of the cut-out was increased, further compressive stress was induced in the gauge area to counteract the tensile stress apparent at the location of fracture apparent in the specimens tested in the current work. Consequently, further development of this specimen geometry may provide improved results to those presented here in terms of strain-to-failure. However, since the current study primarily required only the stress responses, this was not investigated further.

A summary of the bulk properties measured in tension, compression and shear is presented in Table 1.

Table 1: Summary of average and standard deviation of measured bulk material properties

	Average	Standard Deviation
Young's Modulus in Tension [GPa]	2.24	0.094
Maximum Tensile Stress [MPa]	43.57	1.71
True Tensile Strain to Failure [mm/mm]	0.085	0.031
Young's Modulus in Compression [GPa]	2.01	0.16
Shear Modulus [GPa]	0.91	0.14
Maximum Shear Stress [MPa]	26.31	1.43

4.2 RDCB Test Results and Discussion

It is apparent from the force-displacement response (Figure 45) of the RDCB tests, that as bond line thickness increased, the initial slope of the response tended to decrease. There was also a slight reduction in average peak force as bond line thickness increases (780 N (SD = 23 N), 766 N (SD = 48 N), and 680 N (SD = 27 N) for 0.18 mm, 0.6 mm and 0.64 mm, respectively). These responses can be attributed to the reduction in the confinement effects exerted from the adherends on the adhesive as the bond line thickness increases. It is also important to note that the point at which

the calculated traction of the crack tip reached zero (noted by black 'x's in Figure 45) was after the peak force. During the initial loading, the portion of the bond line in tension was in the first phase of the traction-separation response. As loading continued, the area of the bond line near the crack tip reached the traction plateau and eventually began to soften. The softening near the crack tip, then led to an overall reduction in force and eventually the opening of the crack. In general, specimens with thicker bond lines tended to exhibit more consistent shape of the force-displacement responses, particularly in the initial loading portion of the response. The reduced variability associated with thicker bond lines can be attributed to a reduction in variability of bond line thickness, relative to the average, for a given nominal bond line thickness.

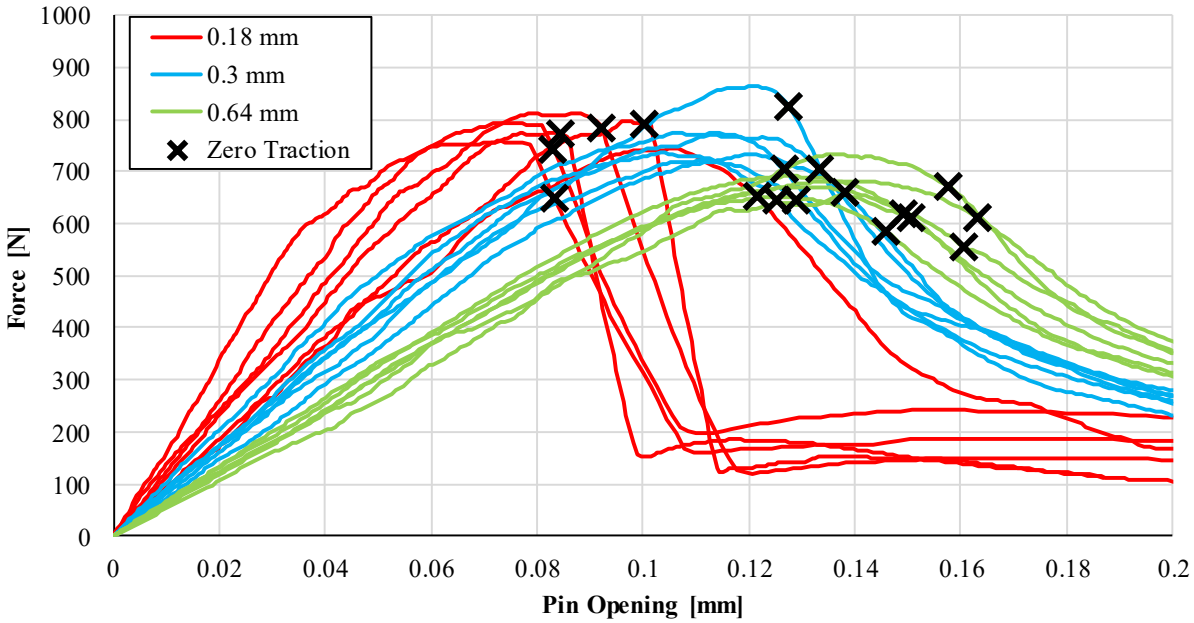

Figure 45: Force-displacement response of RDCB specimens with bond line thickness 0.18 mm, 0.3 mm and 0.64 mm (n = 5)

The force-displacement response for each test was used to extract the traction-separation behaviour (Figure 46) following the methodology outlined in Chapter 3. Each test then had the cohesive zone

model parameters required to construct a trapezoidal response (E_I, T, G_{IC}, f_{G1}) extracted by using a least squared approach (results for each test presented in Appendix A). These parameters were then averaged to create a representative traction-separation response for each bond line thickness tested (Table 2). The use of a trapezoidal cohesive law generally provided a good fit to the test data.

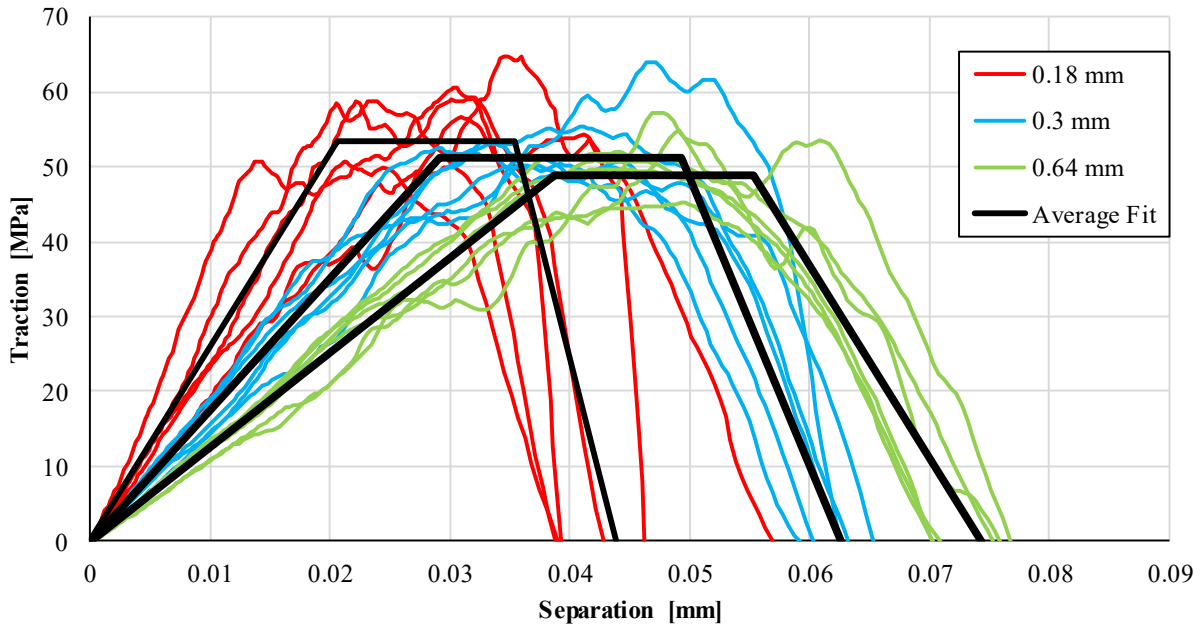

Figure 46: Mode I traction-separation response measured using the RDCB specimen and average fit

As expected, the average traction-separation response reflected the trends in the force-displacement response as bond line thickness was increased (Figure 47). Namely, the initial slope and peak traction were reduced as bond line thickness increased, while critical energy release rate increased. The area ratio also tended to decrease with increasing bond line thickness. In general, a more brittle response was measured with thinner bond lines. The peak traction values tended to decrease towards the maximum tensile stress measured from the bulk material specimens (43.57

MPa). The slightly larger peak traction of the 0.64 mm thick specimen (48.72 MPa) would indicate the continued presence of some confinement effects at this bond line thickness, although these effects were smaller than that operative with the bond line thicknesses. While the RDCB test is a new test, which is not common in the literature, the measured CZM parameters were consistent with those presented in the literature. For example, the critical energy release rate of 3M 7333 measured using the RDCB (1.6 kN/m to 2.2 kN/m) was similar to those measured using DCB specimens in a study by Kinloch and Shaw [1981] who measured the critical energy release rate of an early toughened epoxy. They measured critical energy release rates between 0.9kN/m and 3.3 kN/m for bond line thicknesses between 0.1 mm and 0.5 mm.

Table 2: Average Mode I CZM parameters for nominal bond line thicknesses of 0.18 mm, 0.3 mm and 0.64 mm

Nominal Bond Line Thickness [mm]	Measured Bond Line Thickness [mm]	Initial Stiffness [MPa/mm]	Peak Traction [MPa]	Critical Energy Release Rate [N/mm]	Area Ratio
0.18	0.190	25889	53	1.57	0.51
0.30	0.312	1762	51	2.13	0.49
0.64	0.626	1259	49	2.22	0.36

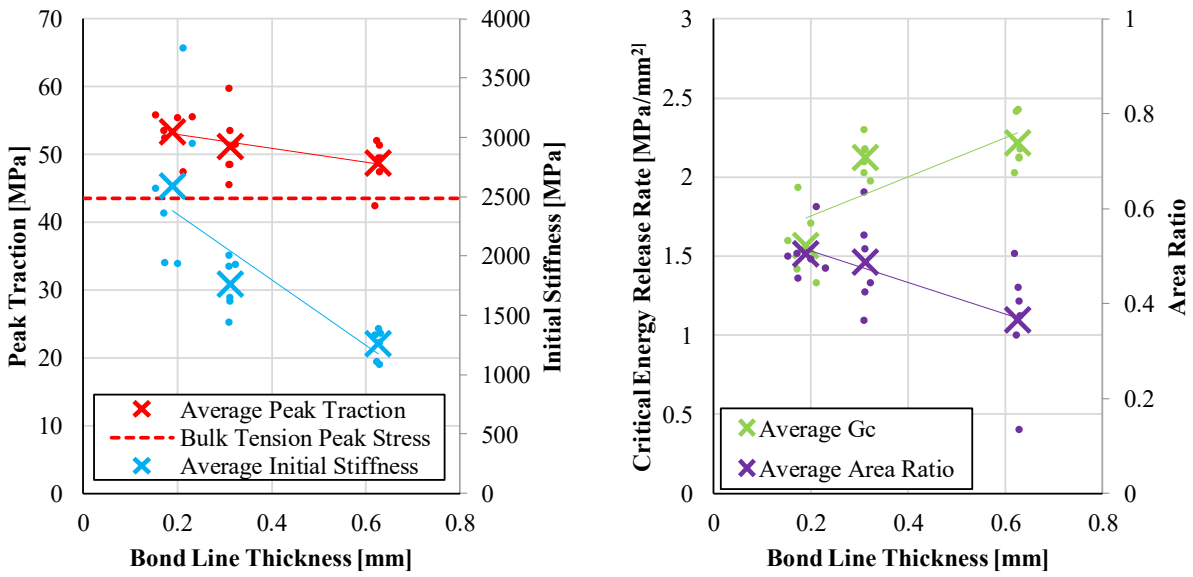

Figure 47: Mode I CZM parameters vs. bond line thickness measured from RDCB testing

A series of t-tests were carried out to assess the statistical significance of differences in the parameters measured for different bond line thicknesses. To this end, the measured parameters of the 0.17 mm specimens (n = 6) and the 0.64 mm specimens (n = 6) were compared for initial stiffness, peak traction, critical energy release rate and area ratio. The evaluation was primarily carried out to determine whether it was necessary to include bond line thickness effects in the finite element model developed in the next chapter. In order to obtain clear trends, the specimens providing the highest likelihood to produce a measurable difference (*i.e.* the larges difference in bond line thickness) were assessed. For this reason, the intermediate bond line thickness was not included in this analysis.

The p-value for each parameter (9.14×10^{-4}, 3.47×10^{-2}, 2.10×10^{-4}, 3.05×10^{-2} for initial stiffness, peak traction, critical energy release rate and area ratio, respectively) indicated that there was

strong evidence to reject the hypothesis that these values were the same for nominal bond line thicknesses of 0.18 mm and 0.64 mm. In other words, the responses were significantly different.

Using the individual test fits, the average separation-to-plateau, separation-to-softening and separation-to-failure were computed for each bond line thickness (Table 3). As one would expect these values increase with bond line thickness, although not in a direct relationship. For example, while the 0.64 mm specimens are 3.55 times the thickness of the 0.18 mm specimens; the separation-to-failure of the 0.64 mm specimens was only 1.69 times that of the 0.18 mm specimens. This finding further demonstrates that bond line thickness specific testing is required to measure the effect of bond line confinement, not only on the stress response, but also the separation-based response. The scaling of bulk material strain response is thus unlikely to provide a good fit with which to model the bonded specimen geometry.

Table 3: Mode I CZM displacement values for nominal bond line thicknesses of 0.18 mm, 0.3 mm and 0.64 mm

Nominal Bond Line Thickness [mm]	Displacement to plateau [mm]	Displacement to softening [mm]	Displacement to failure [mm]
0.18	0.022	0.037	0.044
0.30	0.030	0.050	0.063
0.64	0.039	0.056	0.074

The post-test failure surfaces of the specimens (Figure 48) exhibited fully cohesive failure along the entire length of the specimens. Throughout the characterization testing, no tests were discarded due to issues relating to differing fracture surfaces. The type of fracture surface (cohesive, mixed cohesive-interfacial) was found to be consistent for each specimen, regardless of bond line thickness. An apparent increase in surface roughness was discernable as the bond line thickness

was increased. This increase in roughness was due to the ability of the crack front to more readily deflect in the direction of loading (i.e. perpendicular to the bonded surface) to a preferred region of the adhesive in order to progress along the length of the specimen. The increase in measured energy release rate may then be correlated, in part, to the increase in roughness.

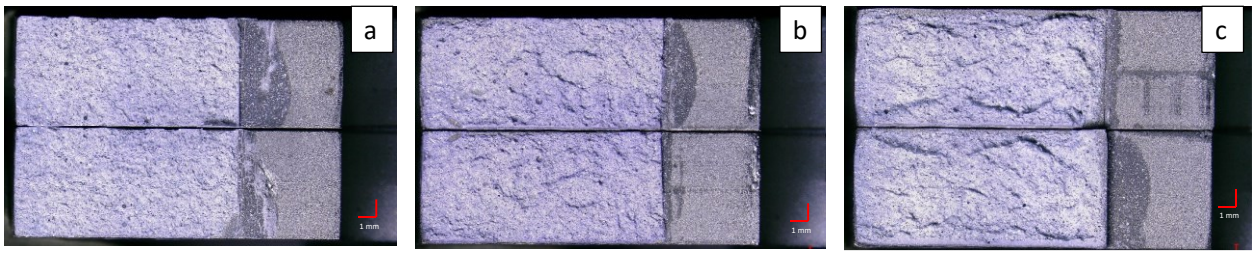

Figure 48: Typical fracture surface of RDCB specimens for 0.18 mm (a), 0.3 mm (b) and 0.64 mm (c) bond line thickness

4.3 Bonded Shear Specimen Test Results and Discussion

The traction-separation response of the BSS tests (Figure 49) exhibited broadly similar behavior to the Mode I traction-separation response measured using the RDCB specimens. As with the RDCB testing, the traction-separation response of each individual test was fit to a trapezoidal traction-separation response. The average of each parameter (E_{II}, S, G_{IIC}, f_{G2}) for each nominal bond line thickness was then used to create an average traction-separation response, which was generally well-fit to the test data.

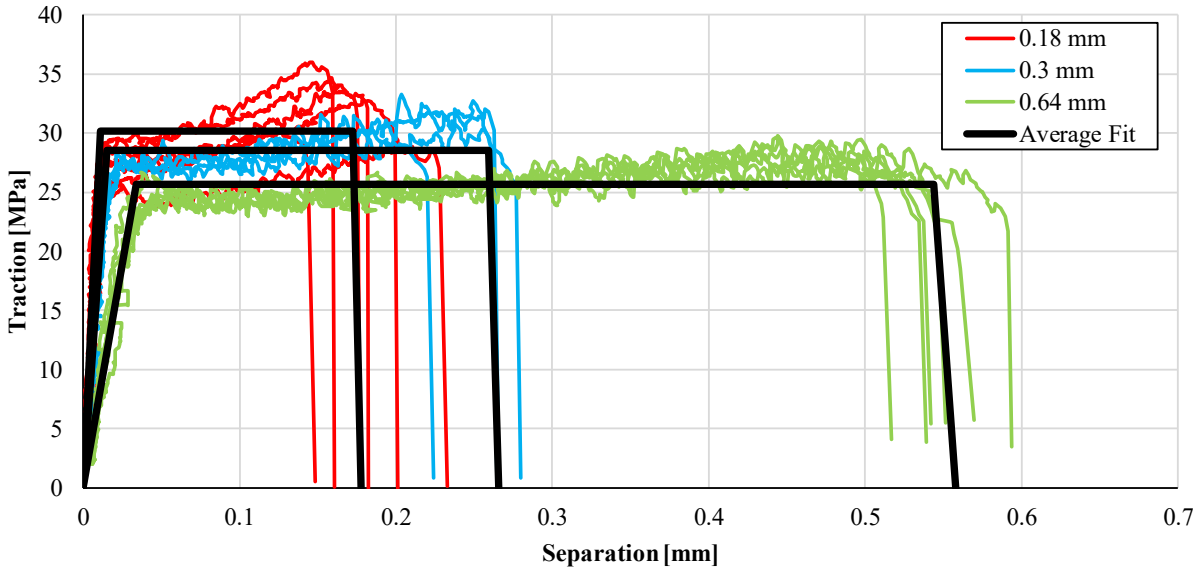

Figure 49: Traction-separation response of bonded shear specimen results for nominal bond line thicknesses of 0.18 mm, 0.3 mm and 0.64 mm along with average CZM fit

One unique feature of the Mode II traction-separation response was a tendency to exhibit hardening behavior, rather than a flat traction-separation response. The flat plateau meant that when the CZM parameters were fit to the test data (average values presented in Table 4) the fit response tended to overpredict the test data for lower separation values and underpredict the test data at higher separation values.

Table 4: Average Mode II CZM parameters for nominal bond line thicknesses of 0.18 mm, 0.3 mm and 0.64 mm

Nominal Bond Line Thickness [mm]	Measured Bond Line Thickness [mm]	Initial Stiffness [MPa/mm]	Peak Traction [MPa]	Critical Energy Release Rate [N/mm]	Area Ratio
0.18	0.205	2688	30	5.11	0.95
0.30	0.382	1880	29	7.28	0.96
0.64	0.585	760	26	13.69	0.96

The peak traction (25 MPa to 31 MPa) was in agreement with that reported by May *et al.* [2015] who measured a maximum shear stress of roughly 30 MPa using a one-part toughened adhesive with a 0.3 mm bond line thickness in a napkin ring configuration. Lißner *et al.* [2019] used a lap shear sample with optically tracked separation to measure the quasi-static traction-separation response of a rubber toughened epoxy film adhesive. The authors reported maximum stress values of 30 MPa to 35 MPa and critical energy release rates of 5.0 kN/m to 12.5 kN/m (compared to 5.1 kN/m to 12.5 kN/m in the current study) for bond line thicknesses between 0.1 mm and 0.5 mm. Lißner *et al.* also reported a negatively sloped plateau region, counter to the hardening response of the current study, suggesting the hardening or softening behavior of the plateau may depend on the specific adhesive.

The general trends measured in Mode I with varying bond line thickness, held with Mode II (Figure 50). Namely, as the bond line thickness increased, the initial slope and peak traction tended to decrease, while the critical energy release rate increased. However, unlike the Mode I case, a slight increase was seen in the area ratio with increasing bond line thickness. As with Mode I, the plateau traction remains higher than the average plastic stress measured using the bulk material specimen (24.28 MPa) indicating that some form of confinement effects are still present at 0.64 mm bond line thickness. Using a series of t-tests to compare the 0.18 mm (n = 5) to the 0.64 mm (n = 6) parameters, statistically significant differences were measured for the initial stiffness, plateau stress and critical energy release rates (p-values of 1.62×10^{-5}, 1.62×10^{-4}, 8.14×10^{-9}, respectively) while no statistical difference was apparent for the area ratio (p-value of 0.774).

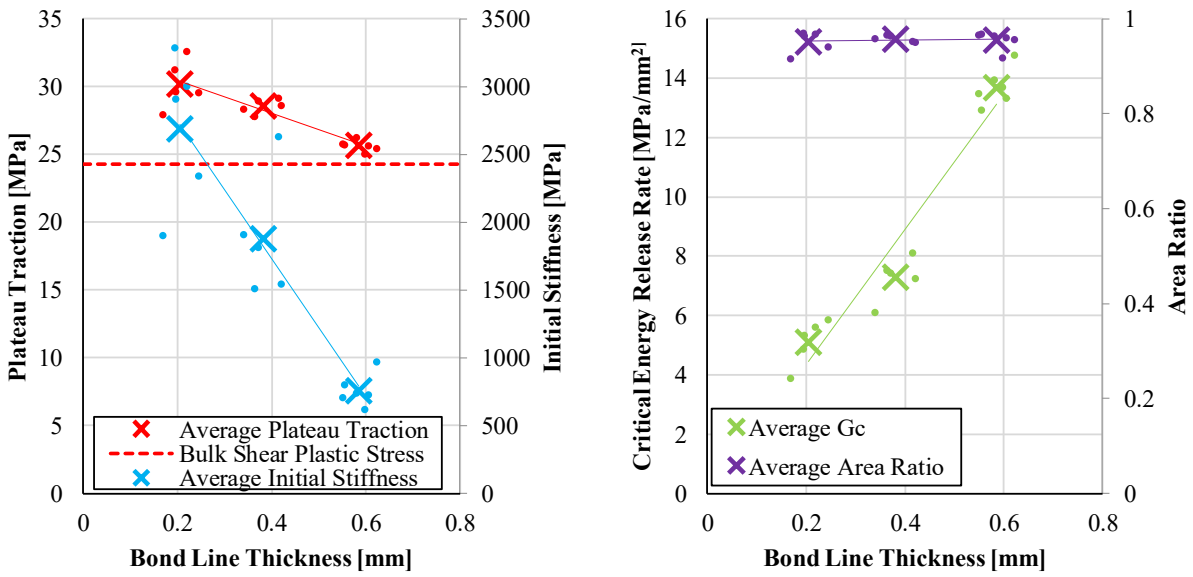

Figure 50: Mode II CZM parameters vs. bond line thickness measured from RDCB testing

Using the traction-separation response fit to each test, the average separation-to-plateau, separation-to-softening and separation-to-failure were calculated for each nominal bond line thickness measured (Table 5). The Mode II separation measurements exhibited similar behavior to that measured for Mode I loading, although the ratio of bond line thickness to displacement tended to be closer to unity compared to the Mode I measurements.

Table 5: Mode II CZM displacement for nominal bond line thicknesses of 0.18 mm, 0.3 mm and 0.64 mm

Nominal Bond Line Thickness [mm]	Displacement to plateau [mm]	Displacement to softening [mm]	Displacement to failure [mm]
0.18	0.012	0.172	0.177
0.30	0.016	0.260	0.266
0.64	0.034	0.544	0.558

Unlike the RDCB failure surfaces, the BSS tended to exhibit mixed-failure (Figure 51). This behavior is linked to the shear cusp (hackle) formation apparent in the adhesive during testing.

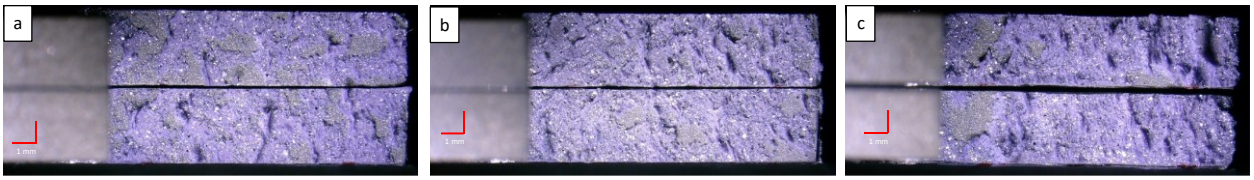

Figure 51: Typical fracture surface of bonded shear specimens for 0.18 mm (a), 0.3 mm (b), and 0.64 mm (c) bond line thickness

The formation of shear cusps has been extensively studied in epoxy-carbon fiber composites, where they tend to occur in matrix-rich regions that fail due to shear loading [Greenhalgh *et al.*, 2009]. An early description of the mechanism of this behavior was provided by Purslow [1986] for carbon fiber-epoxy composites. When epoxy is confined between stiff layers, such as between carbon fiber or metal adherends, and subjected to shear loading, small cracks begin to form normal to the resolved tensile loading direction (*i.e.* 45^{o} to the direction of loading) (Figure 52a). This preferential failure in the tensile direction was also seen during the bulk material testing in which the bulk shear specimen failure initiated outside the gauge area in locations of maximum principal stress and strain. With further loading, these small cracks then enlarge and reach either the edge of a shear band (as described by Purslow), or the surface of the adherend in the current case (Figure 52b). After this point, the cracks then coalesce (Figure 52b) and ultimate failure occurred.

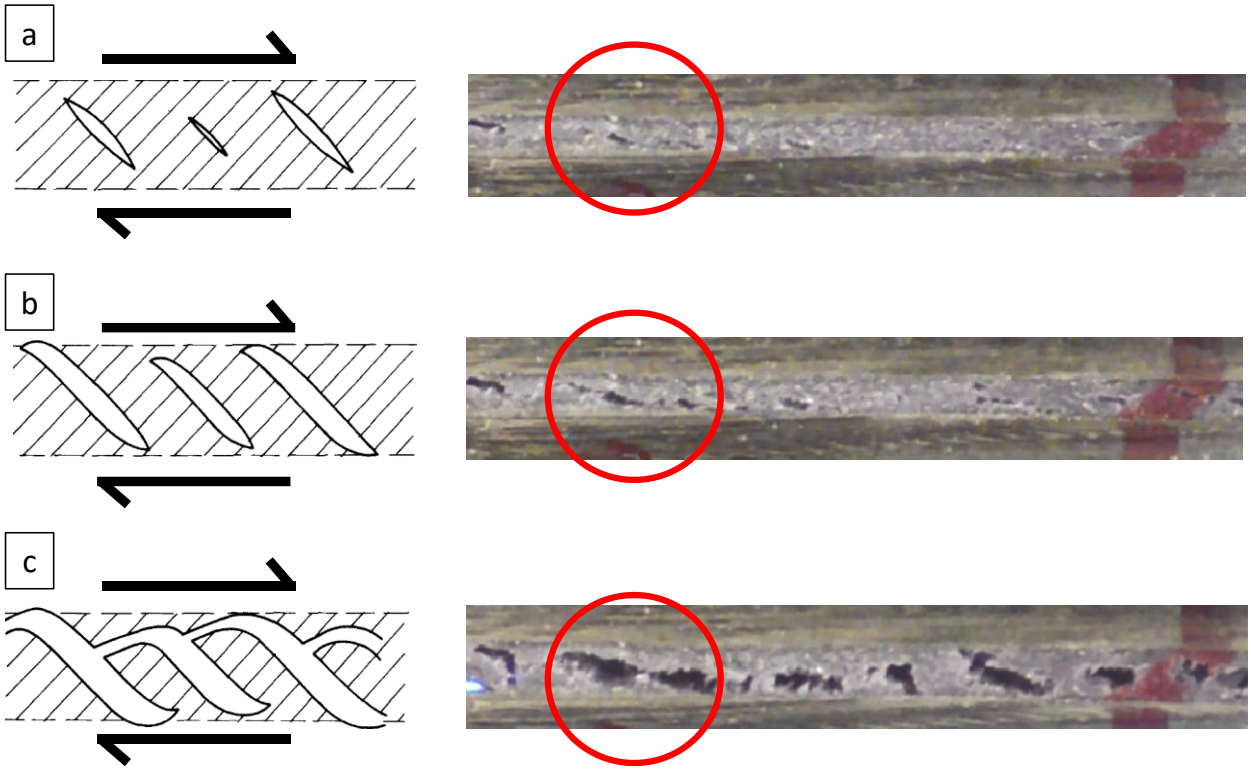

Figure 52: Formation of shear cusps through crack initiation (a), growth (b), and coalescence (c) [adapted from Purslow, 1986 used with permission from Elsevier]

While the physical failure mechanism changes between Mode I and Mode II, the failure criterion used in CZM modeling are typically phenomenological-based. That is, the failure criterion explains the empirical description of failure, generally based on some combination of the energy release rate in Mode I and Mode II and the critical energy release rate values. While further investigation of the relationship of the mechanism of failure the bulk and bonded specimens is possible, it was outside the scope of the current research, which focused on describing failure using an empirical relationship of measurable quantitates.

4.4 Mixed Mode Specimen Test Results Discussion

The first step in analyzing the MM traction-separation response was to calculated the mixity angle of both specimen angles (45º and 75º) for each nominal bond line thickness (Table 6), based on the initial stiffness measured using the RDCB and BSS using Equation (65).

Table 6: Specimen angle (θ_s) and mixity angle (θ_m) for nominal bond line thicknesses of 0.18 mm, 0.3 mm and 0.64 mm

	Initial Stiffness [MPa/mm]		Loading Angle [deg]			
Nominal Bond Line Thickness [mm]	**Mode I**	**Mode II**	**Specimen**	**Mixity**	**Specimen**	**Mixity**
0.18	2589	2688	45	43.9	75	74.5
0.30	1762	1880		43.1		74.0
0.64	1259	760		58.9		80.8

Using the calculated mixity angles, the resolved traction-separation response for the 45º (Figure 53) and 75º (Figure 54) specimens exhibited less clear trends than were apparent with the pure Mode I or Mode II loading. As with the RDCB and BSS, each individual MM test was fit to a trapezoidal traction-separation response. For a given nominal bond line thickness, the results were then averaged to create an average traction-separation response (Table 7 for 45º loading and Table 8 for 75º loading).

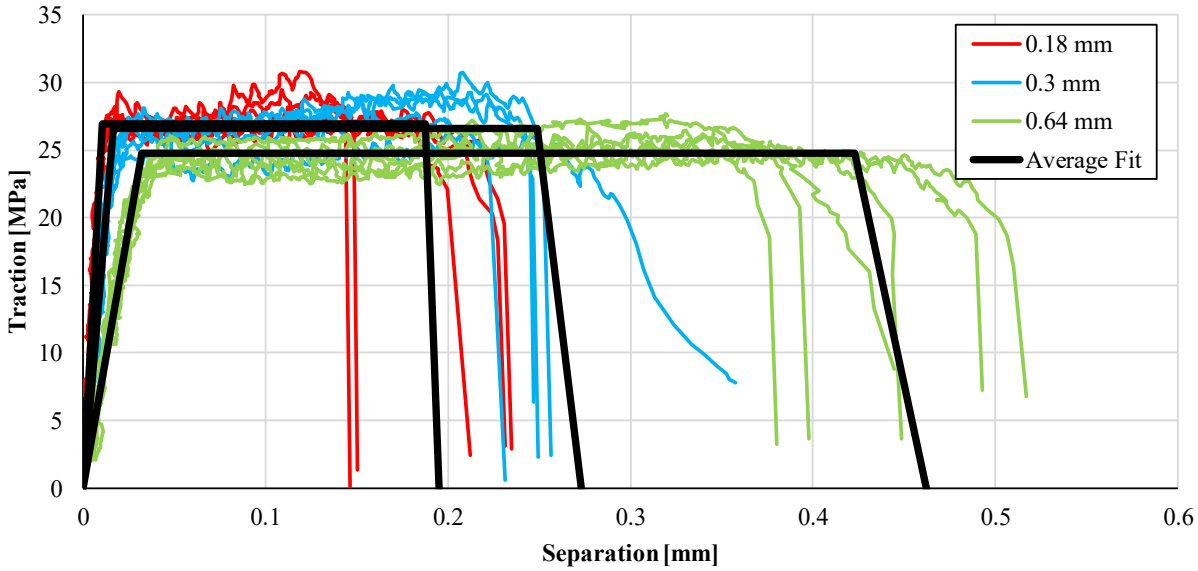

Figure 53: Resultant traction-separation response of 75º mixed mode specimen results for nominal bond line thicknesses of 0.18 mm, 0.3 mm and 0.64 mm along with average CZM fit

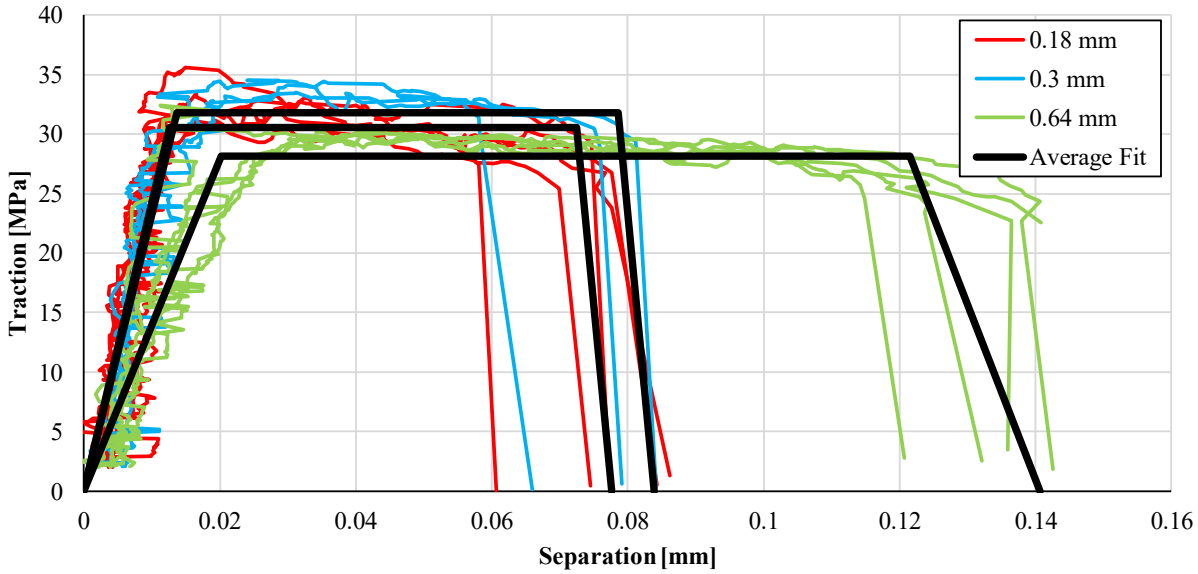

Figure 54: Resultant traction-separation response of 45º mixed mode specimen results for nominal bond line thicknesses of 0.18 mm, 0.3 mm and 0.64 mm along with average CZM fit

While a clear trend of increasing critical energy release rate with increasing bond line thickness was present, the reduction of initial stiffness and peak traction with increasing bond line thickness was less discernable with these specimens. The lack of systemic trends can primarily be attributed to the increased variability of bond line thickness. These specimens required pressure in both the lateral and longitudinal directions during the curing process, which led to some variability that was especially apparent with the 0.18 mm nominal thickness specimens. When considering only the 0.3 mm and 0.64 mm specimens, the trends seen in Mode I and Mode II were readily apparent. The bond line thickness dependence on mixity angle also confounds these results to some degree.

Table 7: Average CZM parameters measured from 45° mixed mode specimen for nominal bond line thicknesses of 0.18 mm, 0.3 mm and 0.64 mm

Nominal Bond Line Thickness [mm]	Measured Bond Line Thickness [mm]	Initial Stiffness [MPa/mm]	Peak Traction [MPa]	Critical Energy Release Rate [N/mm]	Area Ratio
0.18	0.225	2402	31	2.06	0.87
0.30	0.329	2175	32	2.43	0.87
0.64	0.603	1395	28	3.41	0.84

Table 8: Average CZM parameters measured from 75° mixed mode specimen for nominal bond line thicknesses of 0.18 mm, 0.3 mm and 0.64 mm

Nominal Bond Line Thickness [mm]	Measured Bond Line Thickness [mm]	Initial Stiffness [MPa/mm]	Peak Traction [MPa]	Critical Energy Release Rate [N/mm]	Area Ratio
0.18	0.244	2538	27	5.01	0.95
0.30	0.319	1616	27	6.72	0.92
0.64	0.612	773	25	10.56	0.92

The 45° MM specimen provided a slightly lower measure of peak traction compared to a similar study by Lißner *et al.* [2019] (34 MPa to 38 MPa *vs*. 28 MPa to 32 MPa in the current study) who

bonded specimens made from round bar stock machined to 45° angles with bond line thicknesses between 0.1 and 0.5 mm. Lißner *et al.* also measured slightly larger critical energy release rates (2.50 kN/m to 4.60 kN/m). A study measuring the critical energy release rates of a one-part toughened epoxy under mixed modes loading of loading using the mixed mode bending apparatus [Liu *et al*. 2002], reported a critical energy release rate value of 2.1 kN/m for a bond line a thickness of 0.26, which is somewhat lower than the 2.4 kN/m measured for the 45° load case with a 0.3 mm bond line thickness in the current study. As discussed previously, the intention in comparing the results of the current study to values presented in the literature was primarily to demonstrate that the current methodology does not provide parameters values that are substantially different from those accepted in the literature. The peak traction and critical energy release rate are adhesive dependent, so one should expect some differences between the values measured in the current study and those presented in the literature for different adhesives.

As with the Mode I and Mode II cases, the average separation-to-plateau, separation-to-softening and separation-to-failure were computed for each nominal bond line thickness based on the fit to each test (Table 9 for 45° case and Table 10 for 75° case). As expected, a clear increase in displacement was present with increasing bond line thickness.

Table 9: CZM displacement values from 45° mixed mode specimen for nominal bond line thicknesses of 0.18 mm, 0.3 mm and 0.64 mm

Nominal Bond Line Thickness [mm]	Displacement to plateau [mm]	Displacement to softening [mm]	Displacement to failure [mm]
0.18	0.0130	0.0713	0.0765
0.30	0.0159	0.0844	0.0873
0.64	0.0233	0.1217	0.1419

Table 10: CZM displacement values from 75° mixed mode specimen for nominal bond line thicknesses of 0.18 mm, 0.3 mm and 0.64 mm

Nominal Bond Line Thickness [mm]	Displacement to plateau [mm]	Displacement to softening [mm]	Displacement to failure [mm]
0.18	0.0107	0.1879	0.1962
0.30	0.0168	0.2476	0.2770
0.64	0.0325	0.4237	0.4633

The fracture surfaces of the 45° (Figure 55) and 75° (Figure 56) specimens showed a step in the progression from cohesive failure under Mode I loading to the shear cusp formation under Mode II loading. The θ_s = 45° specimens exhibited fully cohesive failure for the 0.18 mm and 0.3 mm bond line thickness specimens, while some mixed failure was noted with the thickest bond line (0.64 mm). Some amount of shear cusp formation was apparent in for all θ_s =75° specimens, although with less interfacial failure apparent than in the BSS case. The resulting failure surface demonstrated that the progression from cohesive failure in Mode I to failure due to shear cusp formation in Mode II is somewhat progressive and dependent on the mixity of loading. This finding lends credence to the choice to consider failure based on a phenomenological approach in which the mechanism of failure changes somewhat gradually as the mode mixity changes.

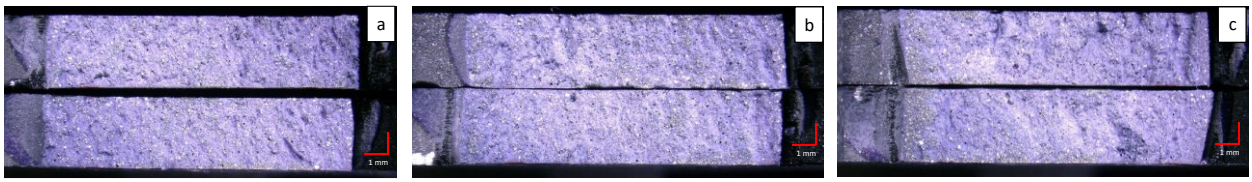

Figure 55: Typical fracture surface of 45° mixed mode specimens for 0.18 mm (a), 0.3 mm (b), and 0.64 mm (c) bond line thickness

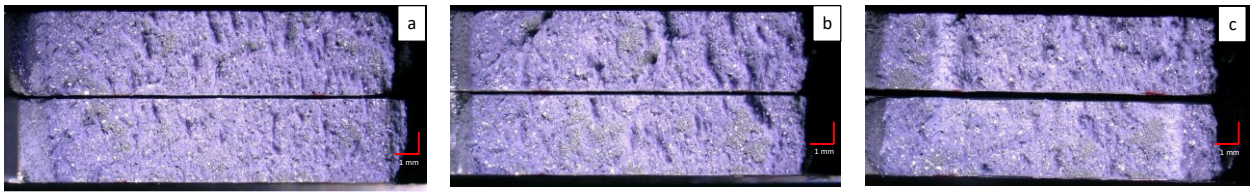

Figure 56: Typical fracture surface of 75º mixed mode specimens for 0.18 mm (a), 0.3 mm (b), and 0.64 mm (c) bond line thickness

With the Mode I, Mode II and MM traction-separation responses measured, it was possible to evaluate the MM response of the adhesive for all modes of loading, using common CZM criteria. The Mode I vs. Mode II separation-to-plateau (Figure 57a) and separation-to-softening (Figure 57b) test response were plotted along with the typical CZM behavior used to fit this response;

$$\left(\frac{\delta_I}{\delta_I{}^0}\right)^2 + \left(\frac{\delta_{II}}{\delta_{II}{}^0}\right)^2 = 1 \tag{68}$$

and

$$\left(\frac{\delta_I}{\delta_I{}^s}\right)^2 + \left(\frac{\delta_{II}}{\delta_{II}{}^s}\right)^2 = 1\,. \tag{69}$$

Note that for any given MM displacement (δ_m), the Mode I and Mode II components ($\delta_I{}^m$, $\delta_{II}{}^m$) can be calculated by

$$\delta_I{}^m = \delta_m \cdot cos(\theta_m) \tag{70}$$

and

$$\delta_{II}{}^m = \delta_m \cdot sin(\theta_m)\,. \tag{71}$$

In the plots that follow, the average measured value is denoted by an ‘X’ with the range of measured values denoted by the colored lines.

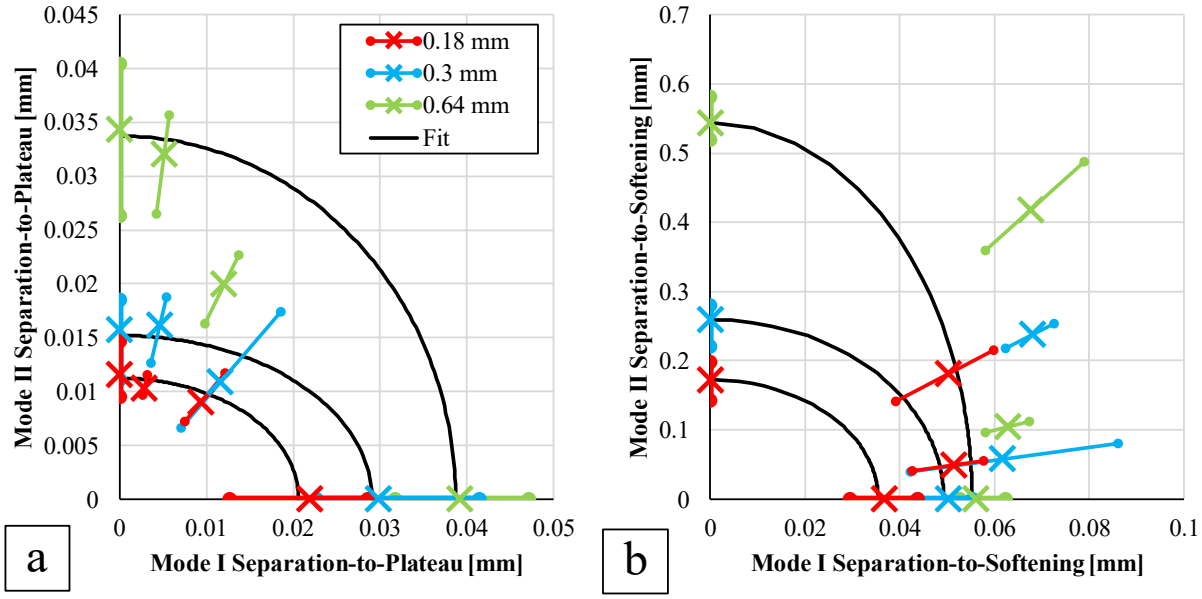

Figure 57: Mode I vs. Mode II separation-to-plateau (a), and separation-to-softening (b) test and fit

The separation-to-plateau measurements fell within the typical CZM description, aside from the thickest bond line with $\theta_s = 45^o$. Due to the very small displacement required to reach the plateau stress, this was not unexpected. Note that there was a slight discrepancy in the average test displacement and that predicted by the mode mixty criterion due to the use of averaged CZM parameters to construct the traction-separation response. These differences were less than 0.0015 mm, well within the variability that can be expected from this type of testing. Unlike the separation-to-plateau response, the separation-to-softening response tended to significantly underpredict the response measured at 45° and 75° across all bond line thicknesses measured.

A comparison of the Mode I *vs*. Mode II energy release rate was undertaken for each test using Equation (66) and Equation (67) to calculate the Mode I and Mode II critical energy release rate.

The results of this analysis were then grouped by nominal bond line thickness (Figure 58a, Figure 59a, and Figure 60a).

After decomposing the critical energy release rate test response into the Mode I and Mode II response, the power law (Equation (30)) and Benzeggagh-Kenane (Equation (35)) failure criteria were fit using a least squares fit approach to minimize the error between the six measured MM responses (0.18 mm, 0.3 mm and 0.64 mm bond line thicknesses at two mixty angles). The failure criterion was calculated using the Mode I and Mode II CZM parameters measured using the RDCB and BSS, respectively. Using this approach, optimal fits were found for $\alpha = 0.83$ for the power law criterion and $\eta = 4.68$ for the Benzeggagh-Kenane failure criterion. This fitting approach assumed that the mixity parameter was not a function of bond line thickness. A comparison of the Mode I and Mode II displacement response (Figure 58b, Figure 59b, and Figure 60b) was also carried out using the parameters fit to the energy release rate data with Equation (33) and Equation (38). Note that the power law criterion was plotted using the more common $\alpha = 1$ rather than the optimal fit to simplify the discussion of modelling that follows where the baseline model was defined with α fixed to a value of 1.

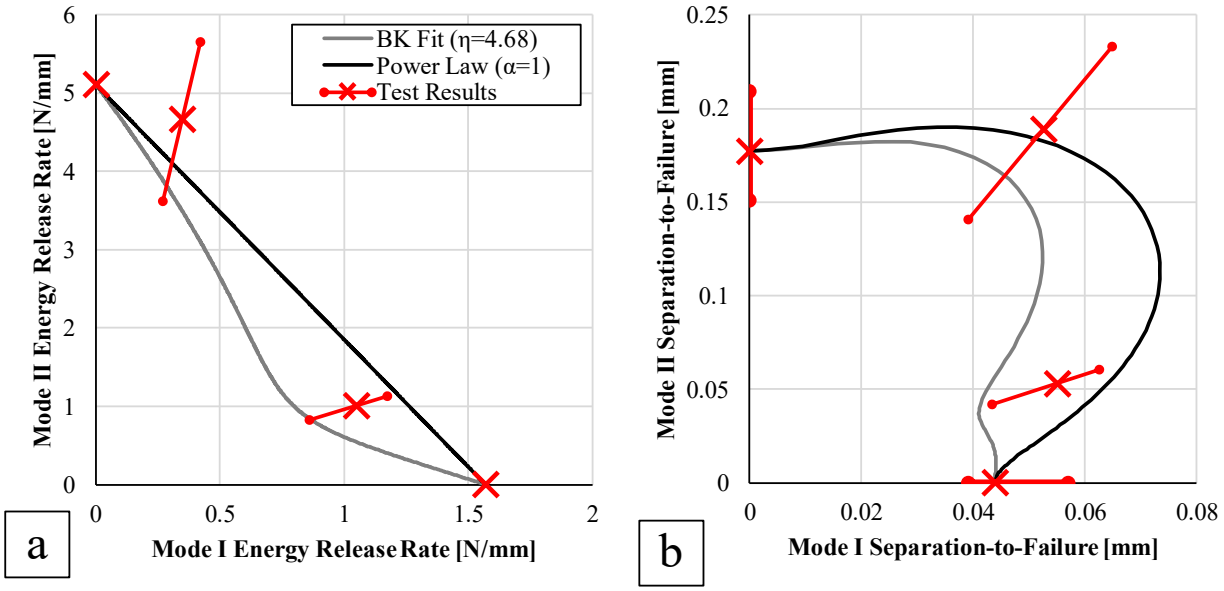

Figure 58: Mode I vs. Mode II energy release rate at failure (a), and separation-to-failure (b) for 0.18 mm nominal bond line thickness

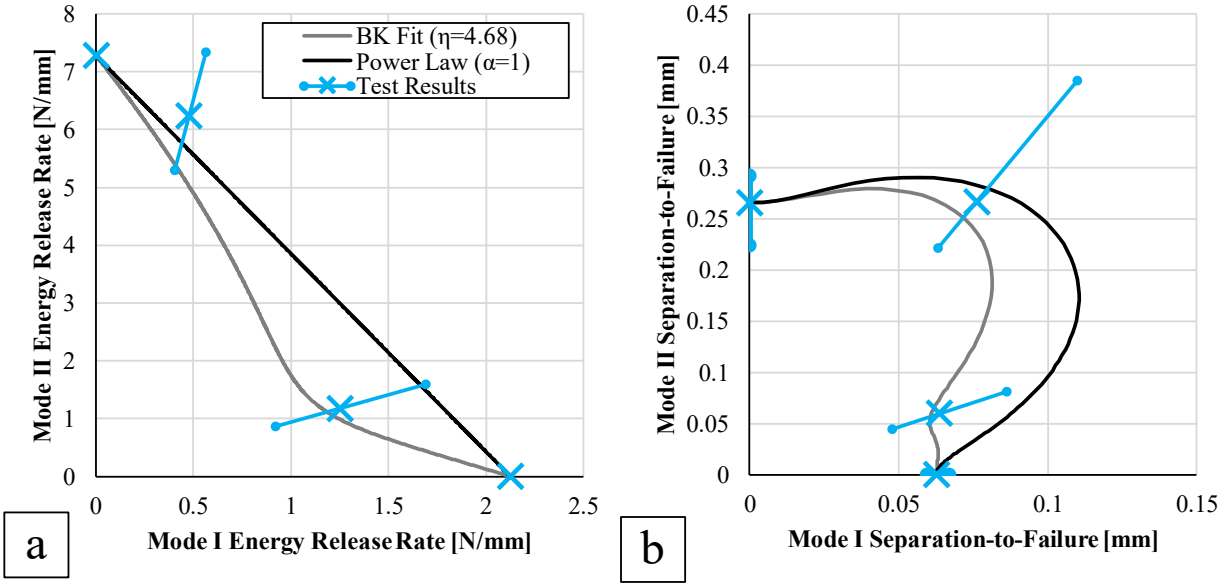

Figure 59: Mode I vs. Mode II energy release rate at failure (a), and separation-to-failure (b) for 0.3 mm nominal bond line thickness

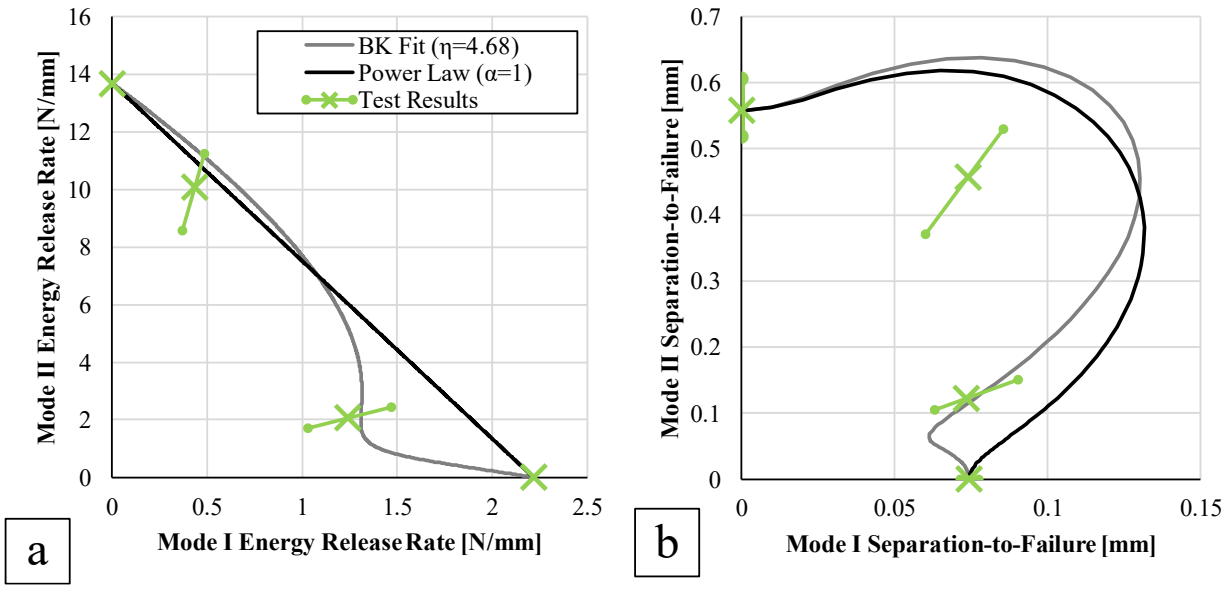

Figure 60: : Mode I vs. Mode II energy release rate at failure (a), and separation-to-failure (b) for 0.64 mm nominal bond line thickness

Both criteria provided a fit within the experimental energy release rate responses for all measurements, with the exception of the power law-based fit lying outside the experimental bounds at $\theta_s = 75^\circ$ for the 0.64 mm and 0.3 mm bond line thicknesses. When assessing the criteria based on the separation-to-failure, the Benzeggah-Keane fit tended to predict the experimental response better, although the response at $\theta_s = 45^\circ$ and 0.18 mm was underpredicted while the results at $\theta_s = 75^\circ$ and 0.64 mm were overpredicted. These failure criteria described the test reasonably well despite using the relatively ill-fitting separation-to-softening response described previously, which underpredicted the test response across both MM loading angles for all bond line thicknesses. The poor separation-to-softening fit implied that using the current criteria, the traction-separation response for all MM loading would have a significantly shorter plateau region and begin to soften much sooner than in the measured response. Further development is required

for a set of criteria that can provide a good fit to the full traction-separation response for a range of loading.

4.5 TDCB Test Results and Discussion

The TDCB force-displacement response (Figure 61), exhibited an increase in peak force with increasing bond line thickness. This behaviour is the expected result due to this force being proportional to the critical energy release rate. When measured with the RDCB specimen, for the bond line thicknesses measured in this work, the critical energy release rate increased with bond line thickness.

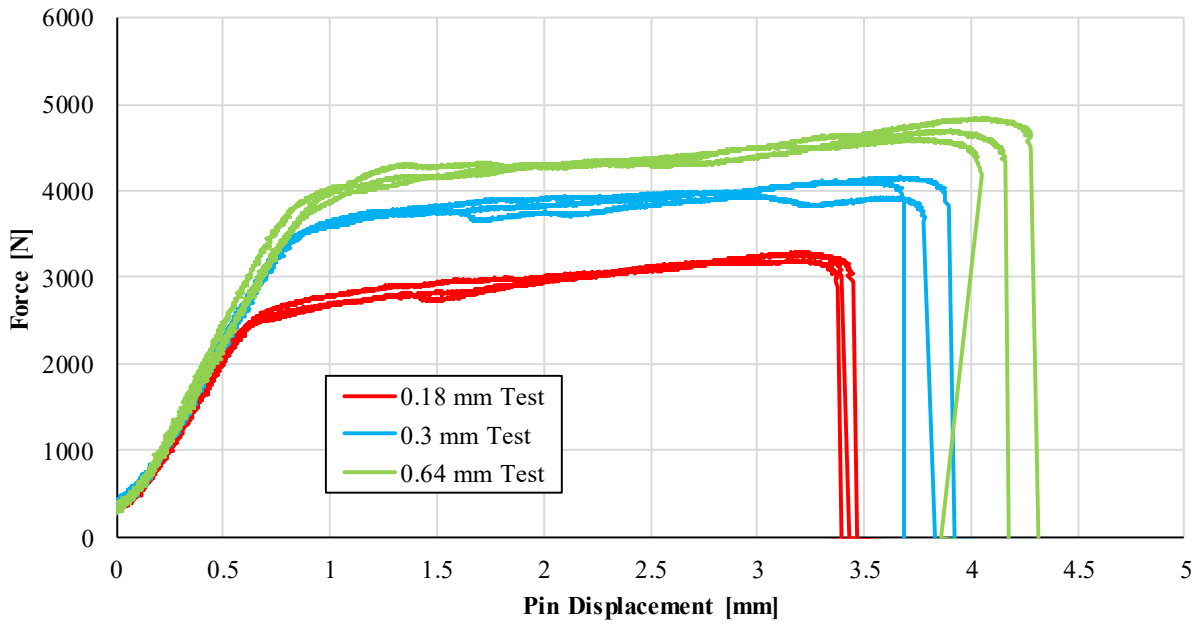

Figure 61: Force-displacement response of TDCB specimens for nominal bond line thicknesses of 0.18 mm, 0.3 mm and 0.64 mm

To calculate the force for each test, an average of the plateau force between 1 mm and 3 mm, 3.5 mm and 4 mm (for 0.18 mm, 0.3 mm and 0.64 mm, respectively) was computed for each specimen (Table 11). While the theoretical force-displacement response provides a perfectly flat plateau, the measured data exhibited a slight increase in force as the crack extended. This increase in force has been attributed to a change in compliance of the specimen as the crack length increases and has been noted by several authors in the literature [Blackman *et al.*, 2003a; Karac *et al.*, 2011; Alvarez *et al.*, 2014].

Table 11: TDCB force response for nominal bond line thicknesses of 0.18 mm, 0.3 mm and 0.64 mm

Nominal Bond Line Thickness [mm]	Measured Bond Line Thickness [mm]	Plateau Force [N]	Standard Deviation [N]	Plateau Start for Average [mm]	Plateau End for Average [mm]
0.18	0.158	2980	30	1	3
0.30	0.329	3520	3520	1	3.5
0.64	0.723	3884	68	1	4

Based on the force responses (Table 11) and the geometry tested, the critical energy release rates were calculated to be 0.97 N/mm (0.18 mm bond line), 1.64 N/mm (0.3 mm bond line) and 2.10 N/mm (0.64 mm bond line) based on the analysis described in ASTM D3433 [2012]. These values are 5% - 38% lower than those measured using the RDCB specimen, similar to the findings of Lopes et al. [2016], who reported a 30% lower G_{IC} response when testing using TDCB geometry analyzed using simple beam theory compared to DCB testing carried out using more advanced analysis techniques. The largest deviation between the TDCB and RDCB result (38%) was measured using the 0.18 mm nominal bond line thickness specimen. Due to the brittle nature of the failure of the RDCB specimens with this bond line thickness, the analysis technique developed using the RDCB specimen tended to assume a larger area under the plateau than would be expected, leading to an apparent larger G_{IC} response. The apparently larger G_{IC} value was

exaggerated by the running average filter used to smooth the force-displacement response in order to provide a sufficiently smooth curve to perform numerical differentiation necessary to solve the ODEs in the RDCB analysis technique. Interestingly, the TDCB specimen demonstrated stable crack growth rather than the unstable fracture exhibited by the RDCB specimen.

4.6 Single Lap Shear Test Results Discussion

The force-displacement response (Figure 62a to Figure 65a) and rotation-displacement response (Figure 62b to Figure 65b) for each adherend-bond line thickness combination, demonstrated reasonably good repeatability (less than 10% variation in peak force and maximum angle for all conditions) for this type of testing and was deemed sufficient to provide validation data to the modeling work that followed.

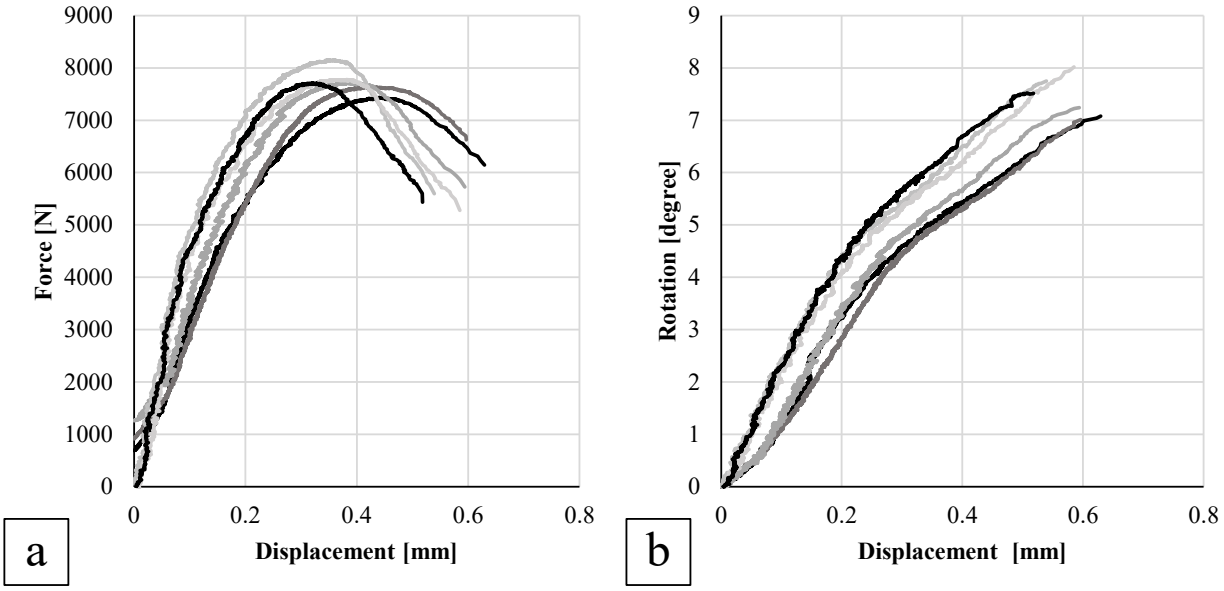

Figure 62: Single lap shear force – displacement (a), and rotation – displacement (b) response for A366 steel adherends with a 0.3 mm nominal bond line thickness

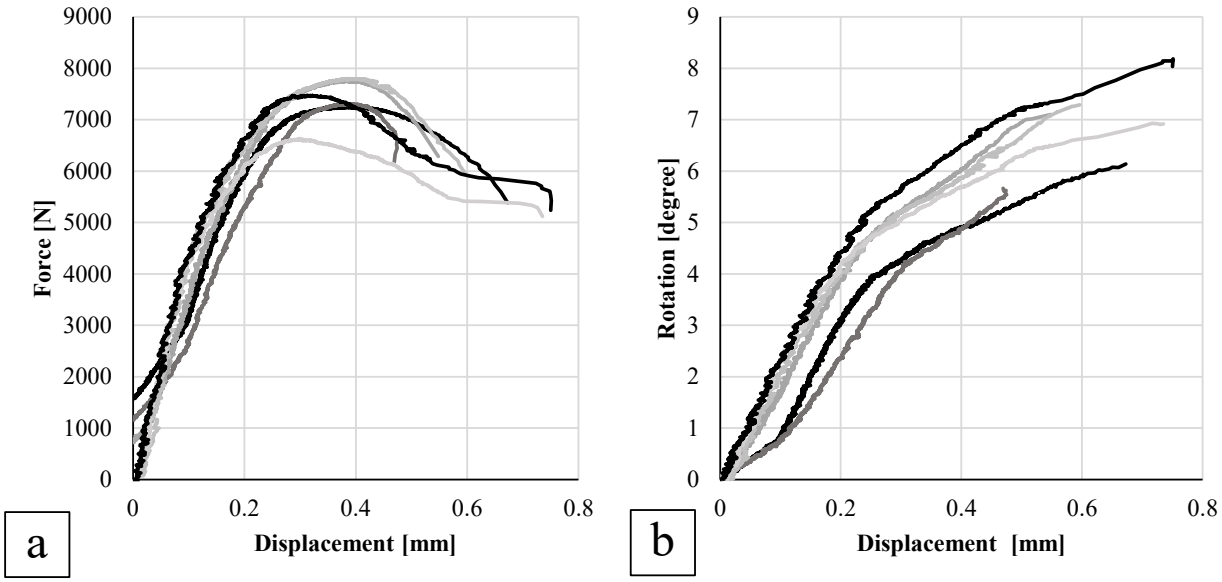

Figure 63: Single lap shear force – displacement (a), and rotation – displacement (b) response for A366 steel adherends with a 0.64 mm nominal bond line thickness

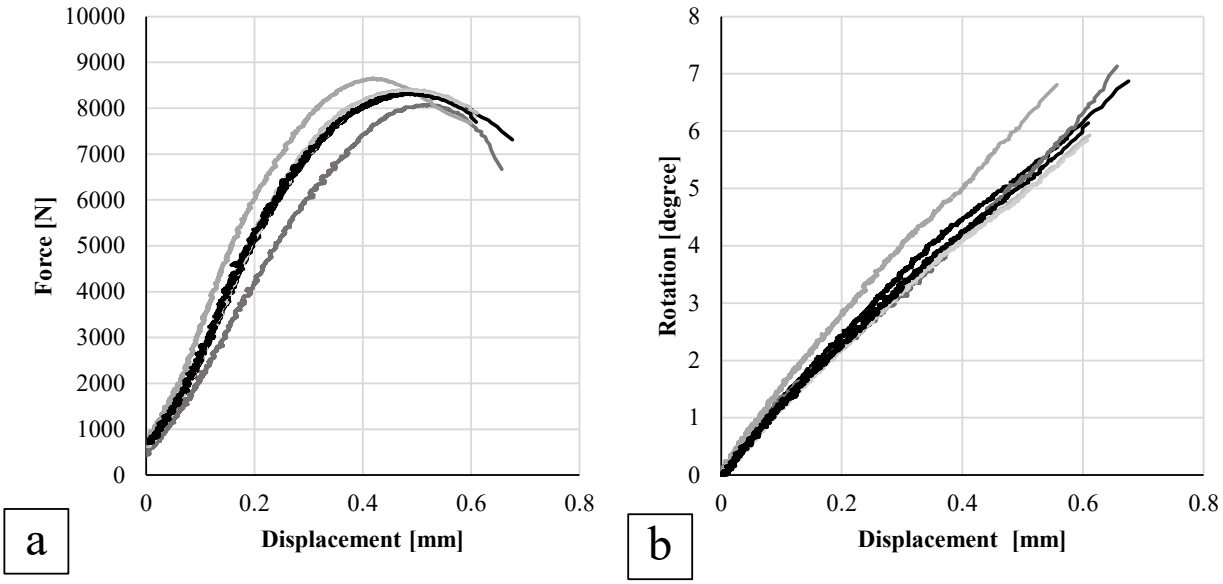

Figure 64: Single lap shear force – displacement (a), and rotation – displacement (b) response for 6061-T6 adherends with a 0.3 mm nominal bond line thickness

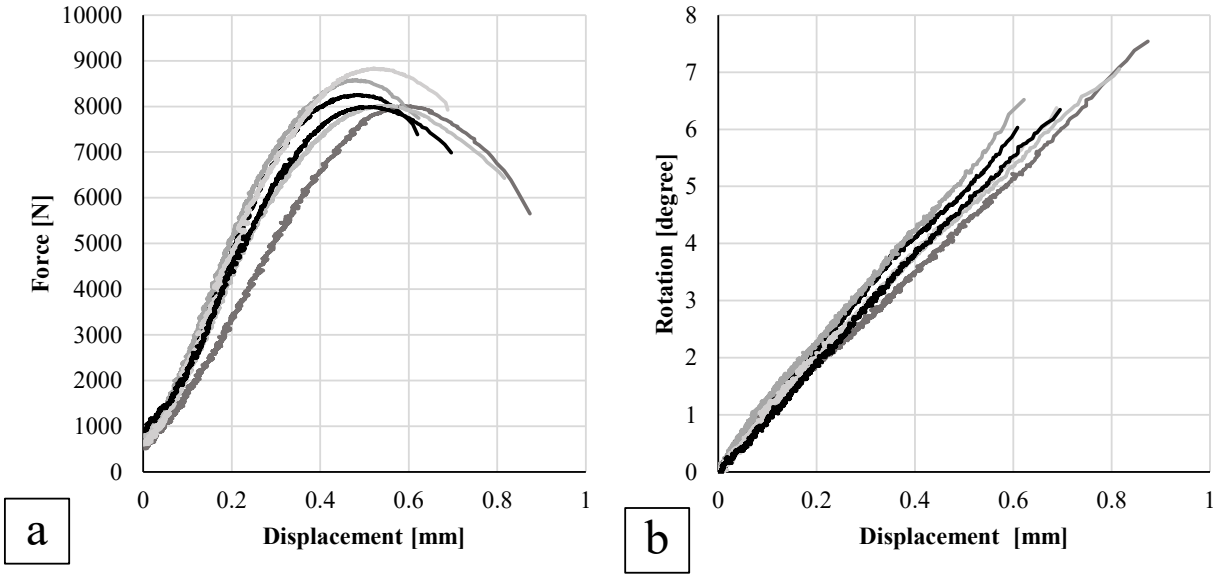

Figure 65: Single lap shear force – displacement (a), and rotation – displacement (b) response for 6061-T6 adherends with a 0.64 mm nominal bond line thickness

The results of the single lap shear tests (Table 12, Figure 66) did not provide any statistically significant differences between bond line thicknesses for either adherend material. Statistically significant differences were apparent in maximum force when comparing the two adherend materials ($p = 4.4 \times 10^{-4}$ for 0.3 mm nominal bond line thicknesses and $p = 1.0 \times 10^{-3}$ for 0.64 mm nominal bond line thicknesses) as well as the maximum joint rotation ($p = 5.3 \times 10^{-3}$ for 0.3 mm nominal bond line thicknesses and $p = 1.9 \times 10^{-2}$ for 0.64 mm nominal bond line thicknesses). The peak force measured in the current study (7373 N to 8360 N) was somewhat larger than that specified by the manufacturer (6450 N) [3M, 2015], although the manufacturer curing the adhesive at room temperature and using thinner adherends (0.85 mm vs. 1.3 mm to 1.6 mm) likely accounts for the discrepancy.

Table 12: Single lap shear test result average and standard deviation for nominal bond line thicknesses of 0.3 mm and 0.64 mm

		Average		Standard Deviation	
Nominal Bond Line Thickness [mm]		0.3	0.64	0.3	0.64
Specimen Width [mm]	A336 Steel	25.67	25.63	0.37	0.09
	Al 6061-T6	25.30	25.31	0.04	0.51
Overlap Length [mm]	A336 Steel	12.40	12.44	0.33	0.22
	Al 6061-T6	12.37	12.91	0.28	0.55
Bond Line Thickness [mm]	A336 Steel	0.368	0.451	0.038	0.115
	Al 6061-T6	0.369	0.507	0.132	0.122
Failure Displacement [mm]	A336 Steel	0.577	0.630	0.037	0.099
	Al 6061-T6	0.627	0.719	0.029	0.095
Maximum Force [N]	A336 Steel	7736	7373	214	389
	Al 6061-T6	8360	8281	167	321
Maximum Joint Rotation [degree]	A336 Steel	7.43	6.89	0.36	0.81
	Al 6061-T6	6.45	6.64	0.50	0.50

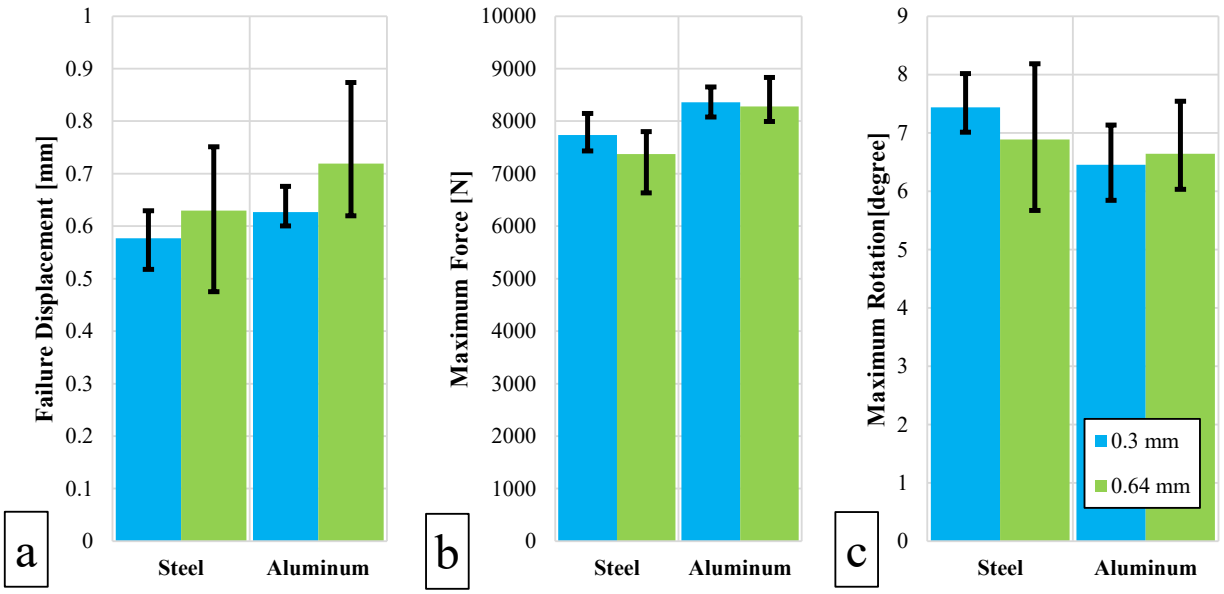

Figure 66: Comparison of average and range of failure displacement (a), maximum force (b), and maximum joint rotation (c) for steel and aluminum adherends with bond line thicknesses of 0.3 mm and 0.64 mm

The average failure force was reduced when bond line thickness increased, which has been noted in the literature [*e.g.* Arenas *et al.*, 2010]. The failure displacement, while not statistically significant, increased with increasing bond line thickness. Similar trends were noted for the RDCB, BSS and MM specimens, which would seem to indicate that this behavior can be expected for both (nearly) rigid and deformable adherends, although the effect may be masked somewhat in the case of deformable adherends under less well controlled loading. The aluminum adherend specimens tended to exhibit both higher strength and higher displacement to failure. The higher maximum force may be related to the slightly higher yield strength of the aluminum adherends, which has been shown to cause an increase in failure force when comparing ultra-high strength steels to common aluminum and magnesium adherends [Watson *et al.*, 2019b].

The somewhat unclear trend in maximum bond line rotation prior to failure compared to bond line thickness may be attributed to the difference in shape of the rotation-displacement response exhibited by the two adherend materials. The A336 steel specimens exhibited a bi-linear response, while the 6061-T6 aluminum specimens exhibited a linear response from the start of loading to failure. This difference was caused by the somewhat larger displacement after the maximum force for the steel specimens. During this phase of loading, the adhesive peeled from the surface of the steel adherends (Figure 67) while the aluminum adherends promoted failure at lower displacement and thus the failure surfaces did not tend to show this peeling (Figure 68).

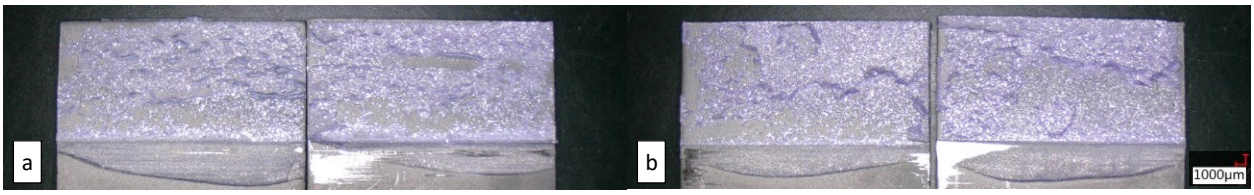

Figure 67: Fracture surface of single lap shear specimens of A336 steel adherends bonded with nominal bond line thickness of 0.3 mm (a), and 0.64 mm (b)

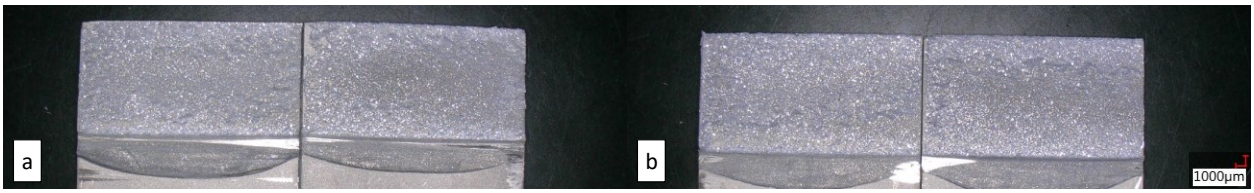

Figure 68: Fracture surface of single lap shear specimens of 6061-T6 aluminum adherends bonded with nominal bond line thickness of 0.3 mm (a), and 0.64 mm (b)

The fracture surface of the steel SLS specimens more closely resembled the surfaces present from the BSS characterization testing. Namely, both had the presence of shear cusps and regions of interfacial failure. Further characterization testing using aluminum adherends may be of interest to attempt to resolve the differences in fracture surface seen with SLS specimens. The differentiation between adherend interface adhesion properties is important to understand the differences in joint response when larger structures are designed with these materials.

Chapter 5 Finite Element Modeling Methodology

Following the experimental investigations carried out to measure the mechanical properties of the structural adhesive (3M Impact Resistant Structural Adhesive 7333, 3M Canada Company), the implementation of these test data into a finite element code was carried out. First, a user defined cohesive zone model was developed to address several limitations identified during the characterization work that are generally not featured in current or available CZMs. The new CZM mode was run through a series of single element verification models in order ensure the model functioned as expected. This CZM was then used to model the RDCB, BSS and MM specimen geometries that were developed to characterize the adhesive. Finally, models of the TDCB and single lap shear tests were developed to validate the CZM model.

5.1 Development of a User Defined Cohesive Zone Model

Based on the traction-separation responses measured in the previous chapters, several shortcomings of typical CZM implementations (as described in Section 2.3.1) were identified:

I. The separation-to-stress plateau and separation-to-softening displacement is fixed for a given Mode I and Mode II traction-separation response. Typical power law fits exhibited poor correspondence to the measured separation-to-softening response and mixed mode plateau traction.

II. Under shear and MM loading, a hardening response is often identified rather than the assumed non-hardening plateau region in the traction-separation response.

III. Typical CZM implementations assume a single bond line thickness and therefore require a unique set of parameters for each bond line thickness to be modeled.

In order to address these deficiencies, a new cohesive zone model was developed using a new treatment of mode mixity. Commonly, in past characterization efforts, only the Mode I and Mode II traction-separation responses are known or are inferred via some testing combined with inverse modelling. The mixed mode response is typically only governed using critical energy release values measured with the mixed mode beam test apparatus [Liu *et al.*, 2002], if at all [May *et al*., 2015]. In a typical CZM, the Mode I and Mode II separation values are input to the subroutine and the Mode I and Mode II tractions are calculated independently as a function of mixty (see Figure 17 and Equation (12) through Equation (42) in Chapter 2). In the current characterization effort, the full traction-separation response for the mixed mode loading cases measured in Chapter 4 allow the effect of loading mode on each parameter to be considered separately in the CZM model.

A new CZM, termed the Enhanced Mixed Mode Cohesive Zone Model (EMC), was developed to take advantage of the measurement of each parameter as a function of loading angle, available by virtue of the current experimental approach. In the EMC, functions of mixity and bond line thickness were fit for each parameter used to define the MM traction-separation response for each loading step. The output Mode I and Mode II tractions were only partitioned from the resultant traction at the end of the calculation. Bond line thickness effects were included to demonstrate the ability of the EMC to capture factors affecting the traction-separation responses beyond the effect of mode mixity. The model could be further adapted to model other effects such as temperature or loading rate in future studies.

For the EMC, a slightly different definition of mixity (Θ) was used;

$$\Theta = \frac{2}{\pi} \cdot atan(\beta) \; . \tag{72}$$

This proposed definition, which ranges from zero for Mode I to one for Mode II, avoided potential round-off errors that could occur when using β, which varies from 0 to ∞. Avoiding an infinite mixity value was particularity important to avoid divergence when fitting the test data to the rational expressions required for the model implementation, as discussed below. To define the traction-separation response of the EMC, the initial stiffness (E), plateau traction (σ_0), critical energy release rate (G_C) and the ratio of area under the plateau to total area (area ratio, f) were used in the normal manner (Figure 69). To characterize the hardening of the response measured in the BSS and MM specimen tests, the slope of the second segment of the trapezoid (E_{Tan}) was introduced.

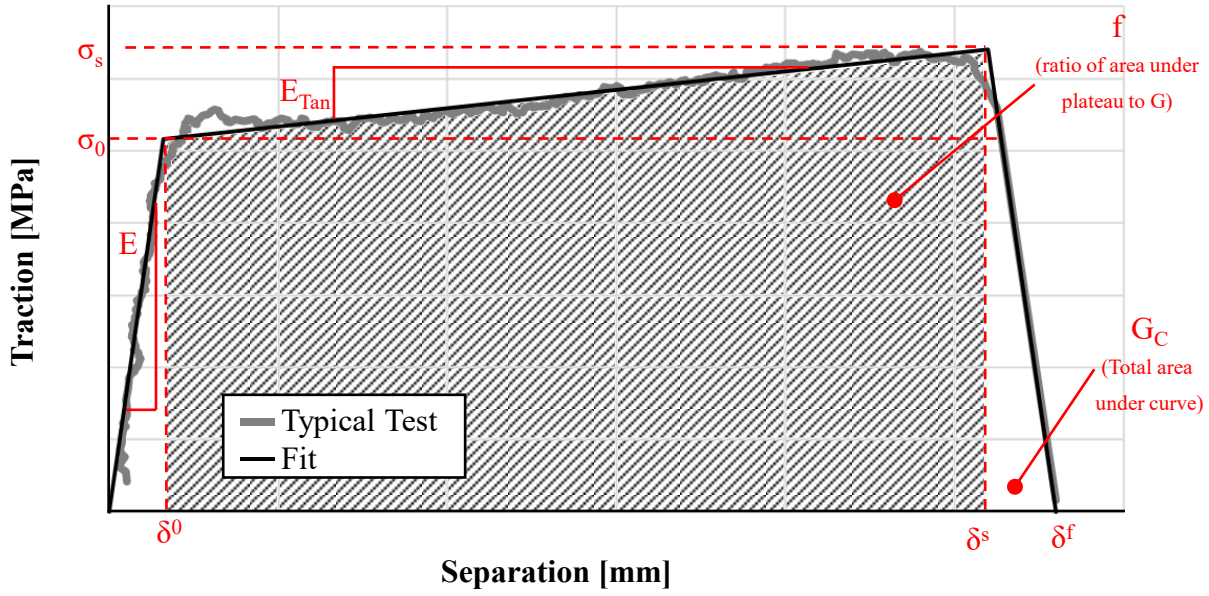

Figure 69: Parameter definitions for the Enhanced Mixed Mode Cohesive Zone Model

The separation-to-softening was calculated in the standard way,

$$\delta^0 = \frac{\sigma_0}{E} . \tag{73}$$

It was convenient to define the softening traction (σ_s) as

$$\sigma_s = \sigma_0 + E_{Tan} \cdot \left(\delta^s - \delta^0\right) . \tag{74}$$

The area under the plateau was calculated using

$$f \cdot G_C = \frac{1}{2} \cdot (\sigma_0 + \sigma_s) \cdot \left(\delta^s + \delta^0\right) . \tag{75}$$

The definition of G_C (the total area under the traction-separation response) was found by adding the area under the initial, plateau and softening portions of the response;

$$G_C = \frac{1}{2} \cdot \sigma_0 \cdot \ \delta^0 + f \cdot G_C + \frac{1}{2} \cdot \sigma_s \cdot \left(\delta^f - \delta^s\right) . \tag{76}$$

With δ^0 being calculated using Equation (73), Equation (74) through Equation (76) provide three equations to solve three unknowns (σ_s, δ^s, and δ^f). Solving and rearranging these equations, the separation-to-softening was expressed as

$$\delta^s = \frac{-b+\sqrt{b^2-4 \cdot E_{Tan} \cdot c}}{2 \cdot E_{Tan}} , \tag{77}$$

where

$$b = 2 \cdot \sigma_0 \left(1 - \frac{E_{Tan}}{E}\right) \tag{78}$$

and

$$c = \frac{E_{Tan} \cdot {\sigma_0}^2}{E^2} - \frac{2 \cdot {\sigma_0}^2}{E} - 2 \cdot f \cdot G_C . \tag{79}$$

The Mode II separation-to-failure can be shown to be

$$\delta^f = \frac{2 \cdot G_C(1-f) - \frac{{\sigma_0}^2}{E}}{E_{Tan} \cdot \delta^s - \frac{E_{Tan} \cdot S}{E} + \sigma_0} + \delta^s \ . \tag{80}$$

Due to the addition of hardening, the damage definition required for the CZM needed to be updated. Based on the experimental work of Biel & Stigh [2010], a damage model was developed in which the separation returned to zero when the element was unloaded (see Figure 18 in Chapter 2). The damage parameter for each increment, *i*, was defined as

$$D_i = max\left(1 - \frac{\delta^0}{\delta_i}, 1 - \frac{\delta^0}{\delta_i} \cdot \frac{\delta^f - \delta_i}{\delta^f - \delta^s}, D_{i-1}, 0\right) . \tag{81}$$

This damage parameter, which modifies the joint stiffness in unload/reload cycles, can be thought of as being related to the irreversible toughening mechanisms of the adhesive, such as particle cavitation during shear band formation. A second damage parameter was defined to describe the softening portion of the traction-separation response caused by the coalescence of damage leading to final failure;

$$D_{soft,i} = max\left(1 - \frac{\delta^f - \delta_i}{\delta^f - \delta^s}, D_{Soft,i-1}, 0\right) . \tag{82}$$

5.1.1 Refitting of Characterization Data to Include Hardening Response

The addition of hardening in the EMC model required the measured traction-separation response from the previous chapter to be fit to the new traction-separation definition that included E_{Tan}, using a least-squared fit approach to derive parameters. As in the previous chapter, the mean values for a given nominal bond line thickness were then calculated to provide a set of average parameters (Table 13). For the Mode I response, E_{Tan} was assigned a value of $1e^{-9}$ for each of these tests due to convergence issues caused by the noise in the traction-separation response associated with the

RDCB test and analysis. For cases when convergence was reached, E_{Tan} tended to be nearly zero, so the choice of $1e^{-9}$ was adopted for numerical convenience since this value would still allow Equation (77) and Equation (80) to be defined and reflected the low value of hardening in the Mode I experiments. The new EMC model allowed for both the hardening behavior of the traction-separation response measured in Chapter 4 as well as potential softening, seen in the current measurements and by those of Lißner *et al.* [2019].

Table 13: Measured Parameters for Enhance Mixed Mode Cohesive Zone Model

Loading Angle [degree]	Mixity (Θ)	Thickness (t) [mm]	Initial Stiffness (E) [GPa/m]	Plateau Traction (σ_0) [MPa]	Critical Energy Release Rate (G_C) [kN/m]	Area Ratio (f)	Tangent Stiffness (E_{Tan}) [GPa/mm]
0	0	0.190	2589	53.38	1.57	0.51	$1e^{-9}$
		0.312	1762	51.24	2.13	0.49	$1e^{-9}$
		0.626	1259	48.72	2.22	0.36	$1e^{-9}$
45	0.5	0.2252	2417	30.60	2.05	0.87	0.04
		0.329	2099	31.47	2.43	0.87	7.78
		0.603	1242	28.42	3.60	0.79	0.03
75	0.833	0.244	2542	26.36	5.01	0.95	10.46
		0.319	1647	25.22	6.71	0.92	12.38
		0.612	777	23.95	10.56	0.91	3.90
90	1	0.205	2693	26.65	5.05	0.96	42.61
		0.382	1903	26.71	7.29	0.97	16.28
		0.585	772	23.65	13.76	0.95	8.33

In order to have a continuous value for each parameter for any arbitrary mixity and bond line thickness combination, each parameter was fit to a rational function of the bond line thickness (t) and mixity (Θ) of the form

$$f(\Theta, t) = \frac{P(\Theta,t)}{Q(\Theta,t)}. \quad \textbf{(83)}$$

For these functions, t did not evolve during the simulation (*i.e.* the thickness at the start of the simulation was used), while Θ was calculated for each time step and could evolve throughout the simulation. In order to decide on the form of rational expression used to express each parameter,

surface fitting software (TableCurve 3D, Systat Software; San Jose, CA, USA) that fit the input test data to a series of rational expressions and returned the r^2 value for each fit. By eliminating all functions that caused singularities over the t-Θ domain for which test data existed, a function that was found to fit the initial stiffness, plateau traction, area ratio and tangent stiffness well was found to be

$$p(\Theta,t) = p_a + p_b\Theta + p_c t + p_d\Theta t + p_e\Theta^2 + p_f t^2 + p_g\Theta^2 t + p_h\Theta t^2\,, \qquad \textbf{(84)}$$

where p represents the arbitrary parameter being fit and p_a through p_h are a series of curve-fit parameters (Table 14) calculated using the non-linear fitting toolbox in MATLAB (Mathworks, Natick, MA, USA). For G, the function providing the best fit was

$$G(t,\Theta) = \frac{p_a+p_b\Theta+p_c t+p_d t^2}{1+p_e\Theta+p_f\Theta^2+p_g\Theta^3+p_h t}\,. \qquad \textbf{(85)}$$

The rational expressions provided an excellent set of surface fits to the average test data (Figure 70), with an average r^2 value of 0.97.

Table 14: Fitting Parameters for Enhanced Mixed Mode Cohesive Zone Model

	p_a	p_b	p_c	p_d	p_e	p_f	p_g	p_h
Initial Stiffness (E) [GPa/m]	4464	-1293	-11980	8937	660	10987	-2741	-10138
Plateau Traction (σ_0) [MPa]	56.84	-70.51	-21.33	52.39	38.00	13.14	-14.04	-43.46
Critical Energy Release Rate (G) [kN/m]	0.76	0.13	4.85	-5.74	1.11	-4.13	2.46	-0.53
Area Ratio (f)	0.49	1.02	0.21	-0.23	-0.57	-0.65	0.12	0.51
Tangent Stiffness (E_{Tan}) [GPa/mm]	-13.98	-9.62	86.65	-158.81	99.92	-104.31	-151.44	283.96

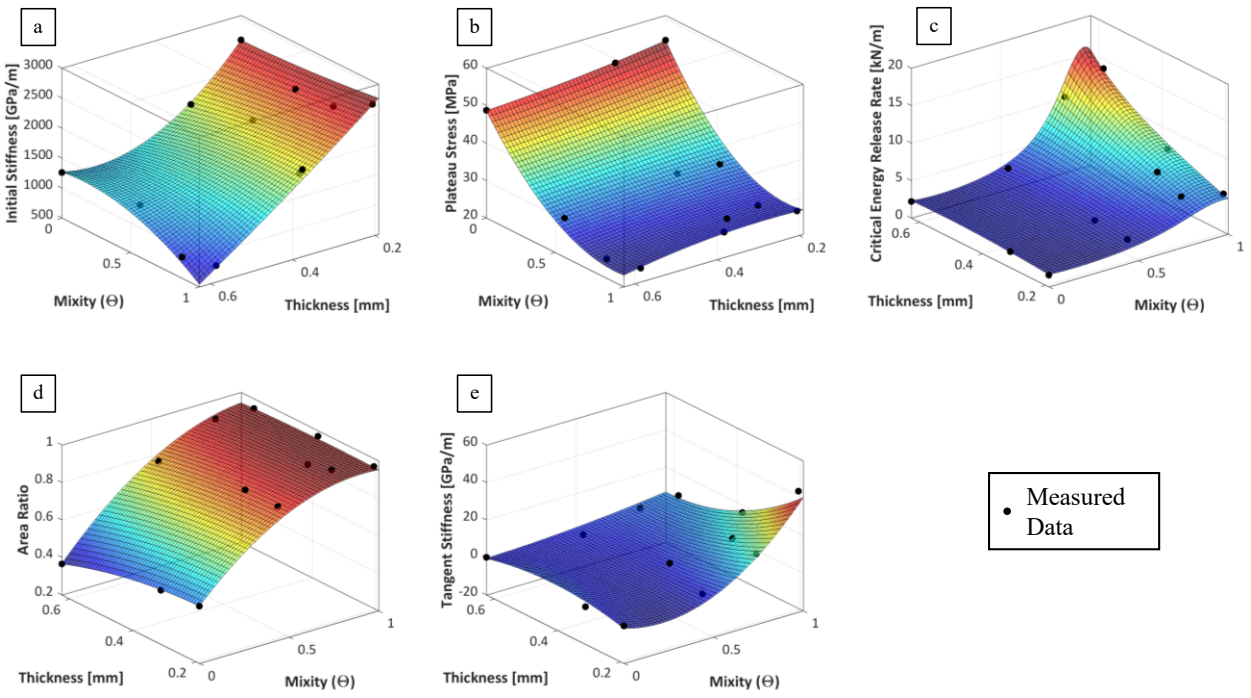

Figure 70: Response surface of initial stiffness (a), plateau traction (b), critical energy release rate (c), area ratio (d) and tangent stiffness (e) as functions of mixty (Θ) and bond line thickness (t)

Using average test data to fit Equation (84) and Equation (85) provided little difference to the traction-separation responses compared to the case when each individual test was used (a maximum of 3% for δ^0, δ^S, and δ^f and 0.2% for σ_0 and σ_s). The mean parameter values were used to simplify the fitting process.

One attractive aspect of this implementation is that the stiffness of the EMC model was represented by a single value, which governs both the Mode I and Mode II response. Using a single stiffness value avoided the cumbersome and somewhat counterintuitive decomposition of the MM test response outlined in Chapter 3 (see Equation (64) to Equation (67)), caused by the unequal initial stiffness in Mode I and Mode II using the conventional assumptions. Consequently, when considering mode mixity using the new approach, the stress angle and sample angle were equal

(which is reflected in the 'Mixity' column of Table 13). Furthermore, Equation (84) and Equation (85) could, in future work, be updated to include the effects of temperature, strain rate, or environmental factors in the model, provided the experimental data is available.

5.2 Implementation of Enhanced Mixed Mode Cohesive Zone Model in LS-DYNA

To implement the EMC in LS-DYNA, a user defined cohesive zone model was written in FORTRAN and implemented in the (64-bit double precision MPP version 9.2.0 Linux Redhat OS; Open MPI solver, build 119543).

For user defined cohesive subroutines in LS-DYNA, the total separation values are passed to the subroutine from the main solver (as opposed to incremental displacement), meaning the equations used to define the traction-separation response must be cast in terms of total separation. Additionally, a parameter, *ek*, must be defined within the subroutine (analogous to a Young's modulus) to provide a stiffness for the time step calculation for each element. For the model described hereafter, this parameter was set to the Mode I initial stiffness for the element thickness (*i.e.* $ek = E_I = E(0°,t)$) and not updated by subsequent damage [Hallquist, 2017a].

During initialization of the simulation (*i.e.* the first time step of the model), the thickness (t) of each element was calculated based on the average distance between the top and bottom node pairs of the CZM element. The thickness value was then stored as a history variable that was referenced for all subsequent time steps.

In the discussion that follows, the steps required for the user defined CZM subroutine to calculate the traction in the Mode I and two Mode II directions based on the respective separation inputs from the main solver are described (summary shown in Figure 71).

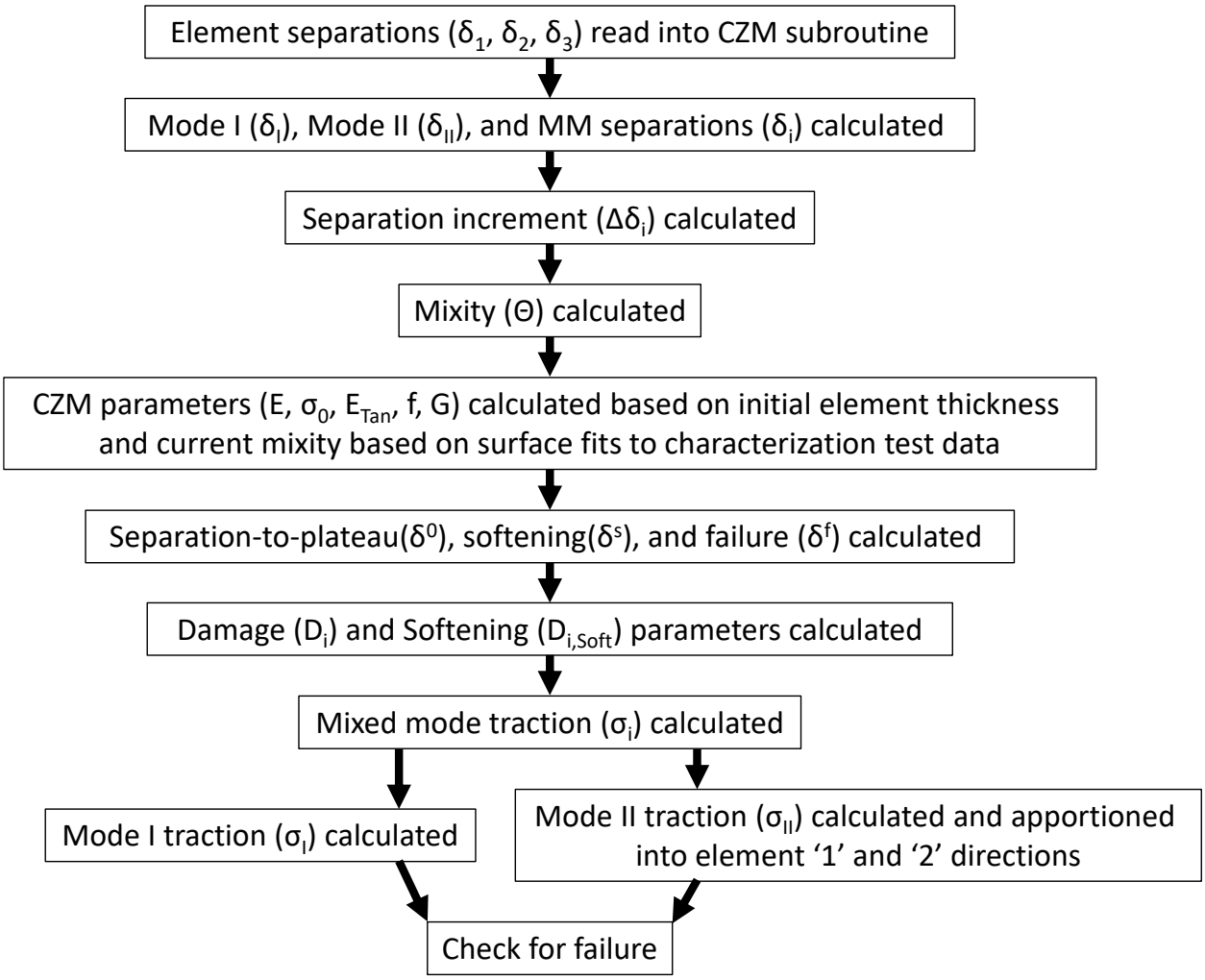

Figure 71: Flow chart summarizing traction calculation using EMC

Step I: Initialization of separation variables

Double precision variables were defined and assigned for each of the three separation values (δ_1, δ_2, δ_3) provided to the subroutine by the LS-DYNA solver.

Step II: Calculate resultant separation and mixity

During this step, the Mode II separation (δ_{II}) was calculated using the vector summation of the two Mode II values (δ_1 and δ_2) in the element coordinate system (Figure 72). The vector summation of

the Mode II and Mode I ($\delta_3 = \delta_1$) separation was then calculated to find the resultant mixed mode separation (δ). Additionally, the mixity parameter (Θ) was calculated using Equation (72).

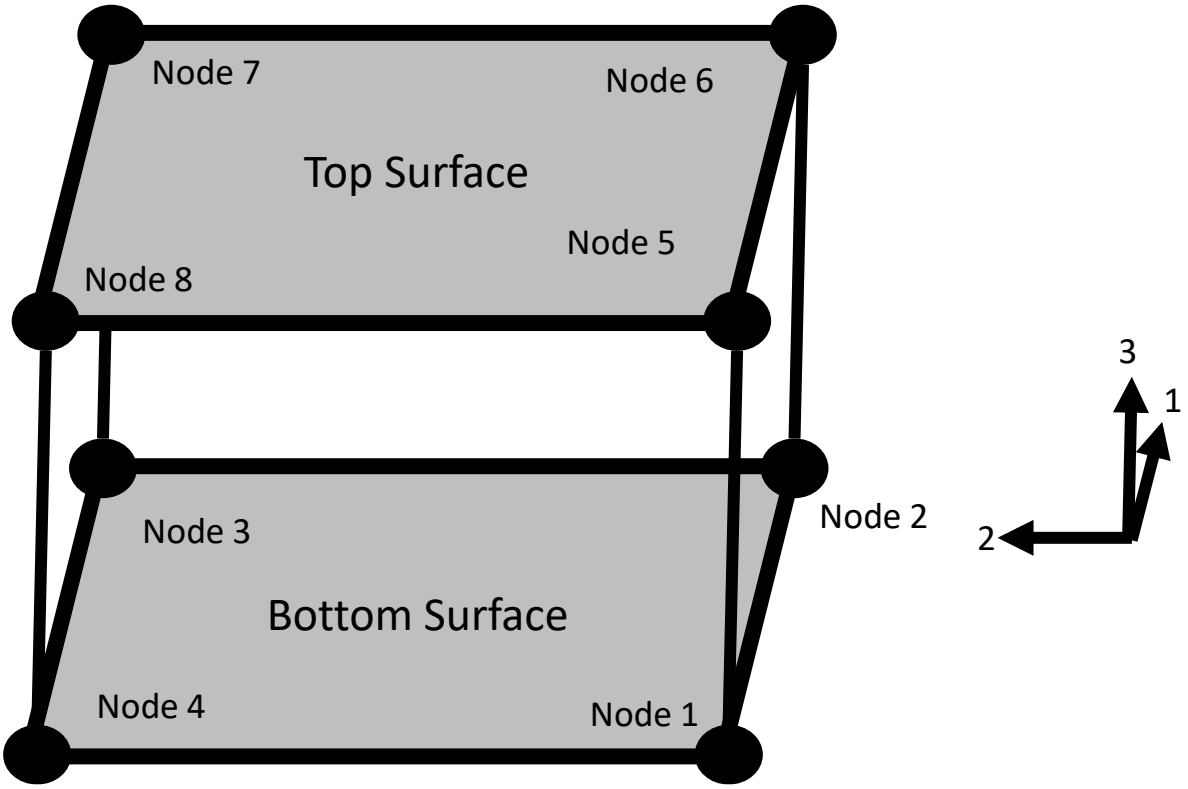

Figure 72: Node numbering and element coordinate system to define separation in the EMC

Additionally, the displacement increment ($\Delta\delta$) was calculated at this point using the current separation (δ) and previous time step separation (δ_{t-1});

$$\Delta\delta = \delta - \delta_{t-1} \,. \tag{86}$$

Step III: Calculate parameters for traction-separation calculation

At this step, the parameters necessary to construct the traction-separation responses (E, σ_0, G_I, E_{Tan}, f) were calculated using Equation (84) and Equation (85) and the model parameters defined in

Table 14. The element thickness was defined at the first timestep of the simulation and was not updated, while the mixity for the current time step was used in each calculation and evolved throughout the simulation.

Step IV: Calculate δ^0, δ^s, and δ^f

The separation-to-plateau (δ^0), separation-to-softening (δ^s) and separation-to-failure (δ^f) were calculated for the current time step using Equation (73), Equation (77), and Equation (80), respectively based on the mixity-dependent parameters calculated in Step III.

Step V: Calculate damage parameters

In this step, the unload-reload damage parameter (D) was calculated using Equation (81) and the softening damage parameter (D_{soft}) was calculated using Equation (82).

Step VI: Calculate mixed mode traction

For the initial loading portion of the MM traction-separation response prior to the stress plateau and unloading/reloading cycles, traction was defined using an incremental approach;

$$\sigma = \Big((1-D)\cdot\Big(E - E_{Tan}\cdot\big(1-\ D_{soft}\big)\Big) + E_{Tan}\cdot\big(1-\ D_{soft}\big)\Big)\cdot\Delta\delta + \sigma_{t-1}\ . \tag{87}$$

Equation (87) can be viewed as a stiffness value (which considerers unloading/reloading damage and softening damage) multiplied by the separation increment being added to the stress from the previous time step.

For all other cases (the plateau and softening portions of the traction separation response), the MM traction was defined as

$$\sigma = \big(\sigma_0 + E_{Tan}\cdot(\delta-\delta^0)\big)\big(1-\ D_{soft}\big)\ . \tag{88}$$

Step VII: Calculate Mode I traction

With the mixed mode traction calculated using Equation (87) or Equation (88), the Mode I contribution of the traction response was computed. Due to the asymmetric tension/compression treatment typical for CZMs, for cases when the element was in compression, the Mode I traction was computed using

$$\sigma_I = E_I \cdot \delta_I \ . \tag{89}$$

Equation (89) uses the typical assumption that compression follows the undamaged Mode I stiffness response, as discussed in Section 2.3.1. The use of symmetric compression and tension stiffnesses for this adhesive is somewhat bourn out by the bulk testing, which did not demonstrate a statistically significant difference for these values.

For the case where the Mode I loading was in tension, the Mode I traction was calculated from the MM traction, calculated in Step VII. Recall, from the general discussion of CZM treatments in Chapter 2, the Mode I separation (δ_I) is related to the mixed mode separation (δ_m) by

$$\delta_I = \frac{\delta_m}{\sqrt{1+\beta^2}} \ . \tag{90}$$

The current approach defined a constant stiffness in Mode I tension and Mode II loading (including all degradation due to load/unload damage and softening damage), which implies that displacement and traction are directly related, *i.e.*

$$\frac{\sigma_i}{\delta_m} = \frac{\sigma_I}{\delta_I} = \frac{\sigma_{II}}{\delta_{II}} = Stiffness\ value\ which\ includes\ damage \ . \tag{91}$$

Consequently, for the Mode I tension case, the Mode I traction could be calculated using

$$\sigma_I = \frac{\sigma}{\sqrt{1+\beta^2}}. \quad \textbf{(92)}$$

Step VIII: Calculate and apportion Mode II traction to shear direction 1 and 2

Using a similar approach to the Mode I case, the Mode II displacement (δ_I) can be shown to be

$$\delta_{II} = \frac{\delta_m \cdot \beta}{\sqrt{1+\beta^2}}. \quad \textbf{(93)}$$

With a similar logic outlined in Equation (91), the Mode II traction was defined by

$$\sigma_{II} = \frac{\sigma \cdot \beta}{\sqrt{1+\beta^2}}. \quad \textbf{(94)}$$

Using the same logic again, the contribution to the Mode II stress for each shear direction was apportioned according to

$$\sigma_1 = \frac{\delta_1 \cdot \sigma_{II}}{\delta_{II}} \quad \textbf{(95)}$$

and

$$\sigma_2 = \frac{\delta_2 \cdot \sigma_{II}}{\delta_{II}}. \quad \textbf{(96)}$$

Step IX: Check for failure

In this step, if D >1, the element failure flag was set that is used by LS-DYNA to erode the element in the main simulation.

Step X: Update stress for output and history variables

In the final step of the subroutine, the tractions calculated in Step VIII and Step IX were assigned to the input/output stress variables sent from the solver to the subroutine. Additionally, the damage (D), current Mode I displacement (δ_I), current Mode II displacement (δ_{II}), current Mode I stress

(σ_I), current Mode II stress (σ_{II}), mode mixity ratio (Θ), element thickness, and softening damage (D_{Soft}) values were assigned to their respective history variables.

5.3 Verification and Validation Modeling of Enhanced Mixed Mode Cohesive Zone Model

To verify that the new cohesive model functioned as expected, a series of single element models were simulated using the LS-DYNA solver. Following this, models of the RDCB, BSS and MM characterization tests were carried out, using deformable adherends, to ensure that the rigidity assumption used in the characterization testing was reasonable and the models were able to provide the expected traction-separation response. Finally, models of the TDCB and SLS tests were developed to simulate validation tests, which were not used in the development of the EMC material parameters.

5.3.1 Baseline CZM Model for Comparison Purposes

To provide a comparison for the EMC models, a conventional CZM model (*MAT_240 in LS-DYNA, as described by Marzi *et al*. [2009]) was used as a baseline for all simulations. *MAT_240 uses a trapezoidal traction-separation response and assumes a displacement-based power law criterion (η = 2) to describe the MM response for yield and softening. Failure is defined based on a critical energy release rate power law criterion with α =1. The material properties for *MAT_240 (Table 15) were extracted from the Mode I (RDCB) and Mode II (BSS) testing carried out in the previous chapters, which ignored hardening in the plateau region. Three sets of CMZ parameters were used; one for each bond line thickness modeled.

Table 15: *MAT_240 cohesive zone model parameters for three bond line thicknesses

	Mode I				Mode II			
Bond Line Thickness [mm]	E_I *[MPa/mm]*	T *[MPa]*	G_{IC} *[N/mm]*	f_{GI}	E_{II} *[MPa/mm]*	S *[MPa]*	G_{IIC} *[N/mm]*	f_{GII}
0.18	2589	53.38	1.57	0.51	2688	30.19	5.11	0.95
0.03	1762	51.24	2.13	0.49	1880	28.57	7.28	0.96
0.64	1259	48.72	2.22	0.36	760	25.64	13.69	0.96

5.3.2 Single Element Verification Modeling Methodology

To verify the EMC implementation within the LS-DYNA solver, a series of single element simulations were carried out. A single 1 mm x 1 mm element was assigned the average measured thickness for each nominal bond line thickness – loading mode combination tested (12 models total). The nodes of the bottom surface of the cohesive element were fixed in all directions, while 3 prescribed motions were applied to the top nodes of the element in each of the normal and two shear directions in order to investigate pure Mode I and Mode II loading along with any mixed mode loading condition, depending on the load curve definition. The EMC had material properties based on the given element thickness while the *MAT_240 models used average properties for a given bond line thickness. For the mixed mode models, the loading was based on the specimen angle (θ_s).

5.3.3 RDCB Verification Modeling Methodology

Two types of models were developed to verify the RDCB analysis; a rigid model (Figure 73a) and a deformable model (Figure 73b). For each bond line thickness investigated, a representative test was selected using the CZM parameters and bond line length measured from that specific specimen

to model. A representative test was used to ensure that the force-displacement response of a given test could be replicated for a given traction-separation response and bond line geometry.

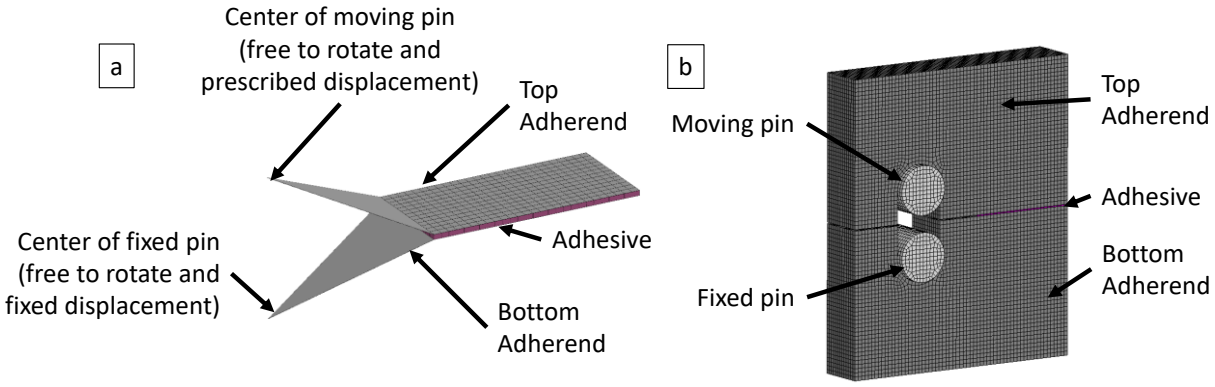

Figure 73: Rigid (a), and deformable (b) model of the RDCB test

For the deformable model, steel elastic material properties were assigned to the adherends (ρ = 7800 kg/m^3, E = 207 GPa and ν = 0.3), while a rigid material property was assigned to the rigid material model. A row of 0.5 mm hexahedral cohesive elements (of the correct thickness for a given test being modeled) was added between the two adherends and the user defined cohesive zone model was applied. A small mesh sensitivity study showed no effect when these elements were split into 0.25 mm elements.

The rigid model was defined using rigid shell element adherends that were generated on the top and bottom faces of the cohesive elements to represent the adherends. The center of gravity of the rigid adherends were then defined such that they were coincident with the center radius cut-out used to load the specimen (*i.e.* the same location as the center of the pins in the test). The moments of inertia were defined for each shell adherend based on that of the adherends to ensure proper rotational motion of the shell adherends. The displacement of the bottom adherend was fixed in all three translation directions, while rotation was allowed about the axis parallel to the front surface

of the specimen to allow the peeling motion of the test. A 1.0 mm/s prescribed displacement was applied to the center of gravity of the top adherend to mimic the pin loading. This modeling approach avoided noise that would be introduced due to contact between rigid parts if solid elements had been used to define the adherends.

For the deformable model, the loading pins and adherend geometry were meshed using rigid 0.5 mm elements. The bottom loading pin was fixed in all directions and a 1.0 mm/s velocity was applied in the vertical direction to the top pin in order to load the specimen, with contact being defined between the pins and adherends.

The models were run for 1 s with a zero-force discrete element used to output the pin opening displacement and a boundary force output of the pin/top adherend used to output force.

5.3.4 Mode II and Mixed Mode Verification Modeling Methodology

As with the RDCB test, models of the BSS and MM tests were developed to provide verification of the test analysis and rigidity assumption (Figure 74). To this end, models were developed for each of the three bond line thicknesses tested using the average bond line lengths and thicknesses. The adherends were meshed using 0.5 mm selectively reduced, fully integrated hexahedral elements. A steel elastic material model was applied to the adherend mesh (ρ = 7800 kg/m^3, E = 207 GPa and ν = 0.3). A row of cohesive elements with a CZM described in the previous sections was used to model the adhesive. The *MAT_240 model was not examined using these models to avoid redundancy in the discussion of the single element models. Likewise, it was found that the deformable material provided a near-exact match to the expected outcome, so the results using rigid adherends were not reported. Rigid pins were created to model the loading pins from the

experiment. The lower pin was fixed in all directions, while the top pin was fixed in all but the vertical (loading) direction. A 1 mm/s prescribed motion was applied to the top pin to load the specimen. A symmetric surface-to-surface contact was defined between the pins and the adherend mesh.

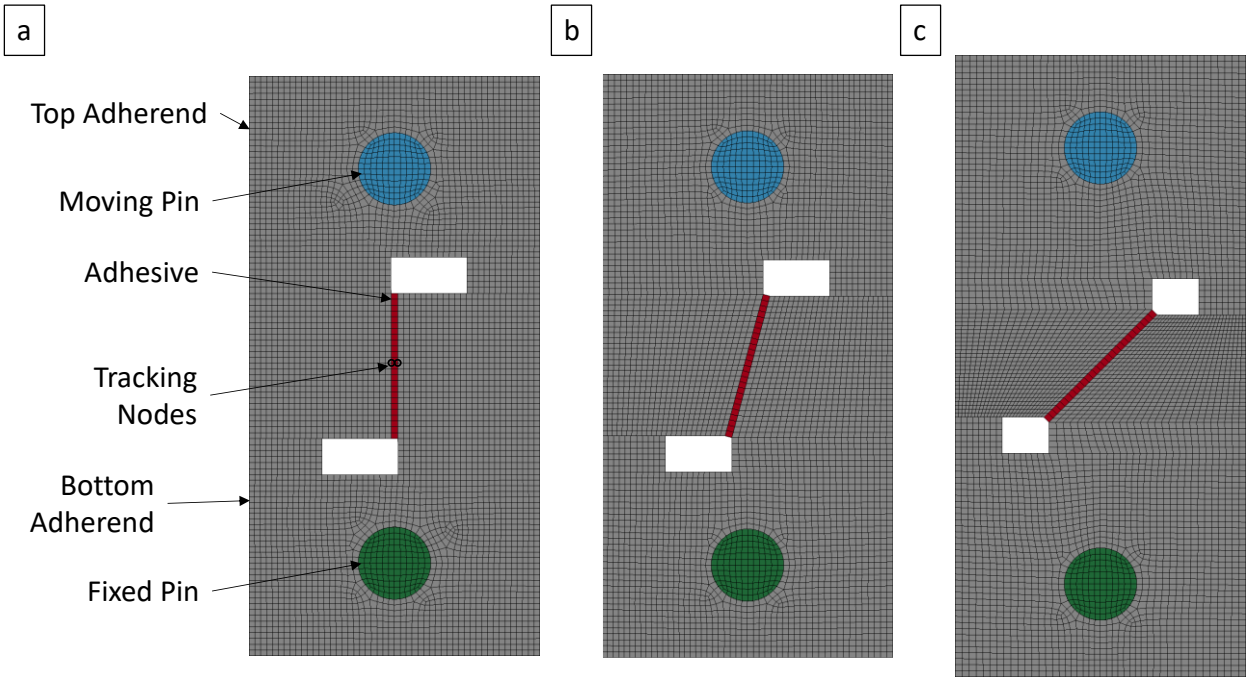

Figure 74: Model of the bonded shear (a), 75º (b), and 45º (c) mixed mode test specimens

The displacement of each model was measured using the difference in vertical nodal displacement of the nodes on either side of the adhesive bond at the center of the bond line ('Tracking Nodes' in Figure 74a), mimicking the measurement location of the test. The force was output by monitoring the boundary force required to maintain the pin motion in the direction of loading.

5.3.5 TDCB Validation Modeling Methodology

To validate the newly developed RDCB analysis technique, modeling of the TDCB validation testing was carried out using the CZM parameters extracted from RDCB testing. For each of the bond line thicknesses tested, a model was constructed to compare to the test data (Figure 75). The adherends were meshed using 1 mm selectively reduced, fully integrated hexahedral elements. Steel elastic material properties were applied to the adherends (ρ = 7800 kg/m^3, E = 207 GPa and ν = 0.3). A row of cohesive elements of the appropriate thickness were attached to the top and bottom adherends, with CZM properties described previously. Rigid pins were meshed using 1 mm hexahedral elements. The bottom pin was fixed in all directions, and a constant velocity (5 mm/s) was applied to the top pin in the vertical direction to load the specimen to failure. For computational efficiency, the loading rate applied in the model was roughly 300 times that of the test. To ensure inertial effects did not dominate the simulation, the kinetic energy of the model was carefully tracked and found to be well below the deformation energy of the model. As with the RDCB specimens, both the pin displacement and boundary force responses were monitored for comparison to the test data.

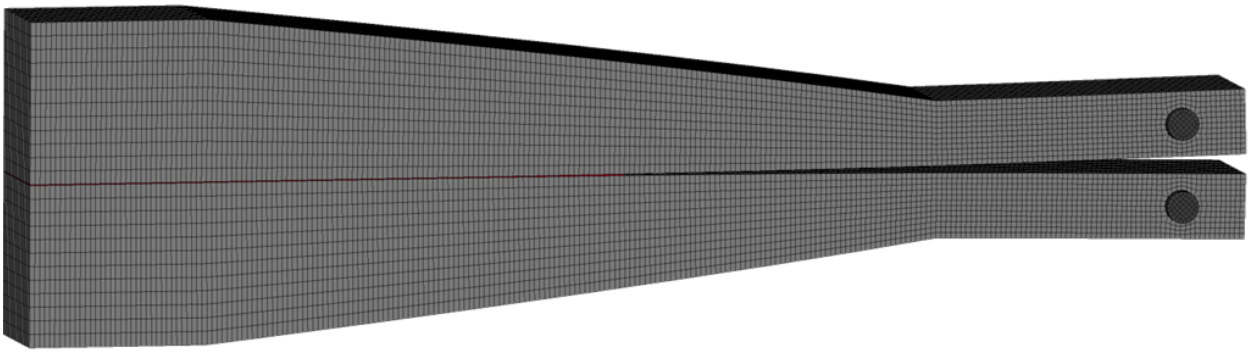

Figure 75: Model of the TDCB validation test

5.3.6 Single Lap Shear Validation Modeling Methodology

To validate the characterization testing and CZM development, single lap shear testing was carried out and modeled. The single lap shear model (Figure 76) was designed to be easily adapted to large-scale body in white simulations. In practice, this meant using shell elements to model the adherends and a method to integrate the adhesive joint that did not require matching mesh morphologies on the two adherends.

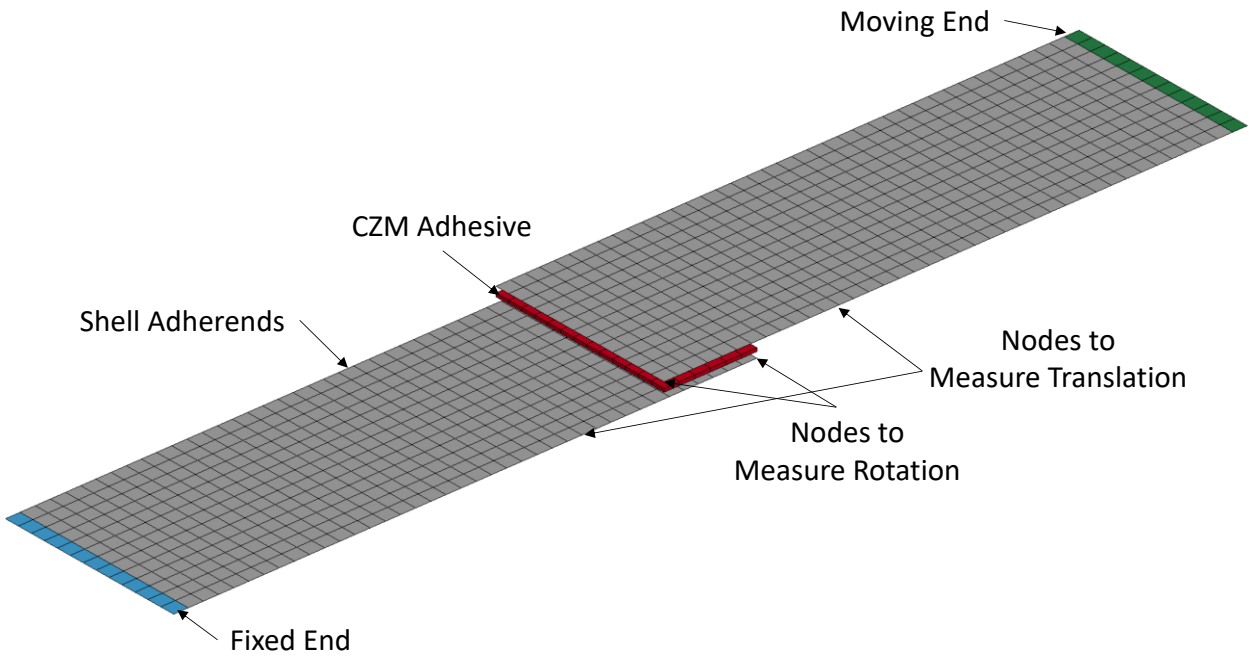

Figure 76: Model of single lap shear test

With these requirements in mind, the portion of the adherends outside the grips were meshed with fully-integrated Reissner-Mindlin-based shell elements [Hallquist, 2017a] with assumed strain interpolants to treat in-plane bending behavior (Type 16 shells in LS-DYNA) and 7 integration points through-thickness. A shell thickness of 1.551 mm was applied to these elements for models of the steel adherends, while a shell thickness of 1.633 mm was applied to the shell mesh used to

model the 6016-T6 aluminum tests, both based on measurements made on grit blasted adherends using a micrometer. A row of rigid elements was meshed at each end of the specimen to represent the loading grips. One of these rows of rigid elements was fixed in the axial directions while a 2 mm/s prescribed displacement was applied in the axial direction to the opposite end. Both ends were fixed in rotation about the axial direction of the specimen and motion in all other degrees of freedom were allowed. Note that for each bond line thickness and adherend combination, the model overlap and bond line thickness were set to the average values measured on the specimens for that specific condition to allow direct comparison to the test data.

The shell mid-planes were positioned to lie at the position of the center of the adherend. The cohesive elements were then meshed between the top shell surface of the bottom adherends and the bottom shell surface of the top adherends. (Figure 77). The top and bottom surfaces of the cohesive elements were then constrained to their adjacent shell mid planes using a constraint that allowed moment transfer (*CONTACT_TIED_SHELL_EDGE_TO_SURFACE_ CONSTRAINED_OFFSET in LS-DYNA). The user defined CZM described previously was assigned to these cohesive elements.

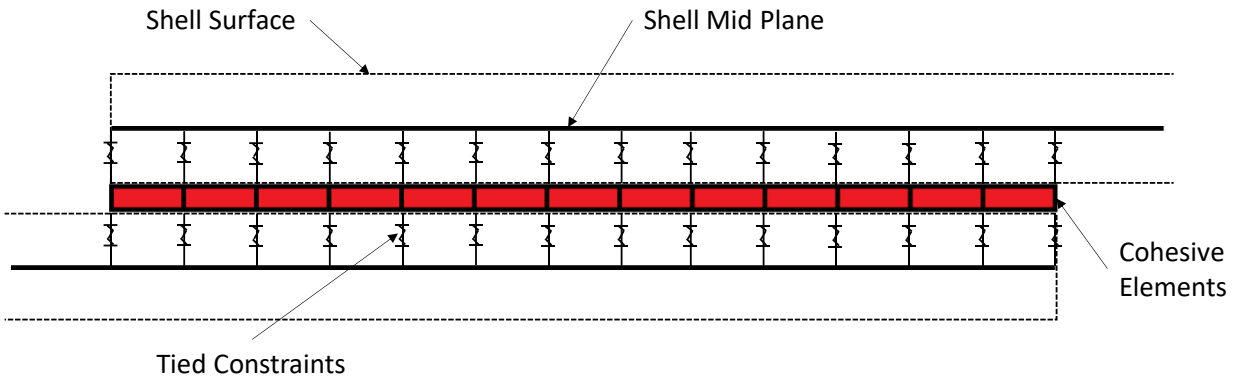

Figure 77: Detailed schematic of the bond area of the single lap shear validation model

A piecewise plastic model was applied to the adherends with typical elastic material properties (ρ = 7800 kg/m^3, E = 200 GPa and ν = 0.3 for steel and ρ = 2700 kg/m^3, E = 69 GPa and ν = 0.33 for aluminum). The plastic response was based on tensile testing carried out using standard ASTM E8 specimens. The flow stress response for each test repeat (n=3 for each material) was fit to a simplified Johnson-Cook expression [1983];

$$\sigma_y = A + B \cdot \bar{\varepsilon}_p{}^n \,, \tag{97}$$

where σ_y is the flow stress of the metal, $\bar{\varepsilon}_p{}^n$ is the effective plastic strain and A, B and n are model fitting parameters, which were identified for each test using a least square fit (average $r^2 = 0.9989$). An initial investigation found that less than 2% plastic strain was present at the top and bottom surfaces of the shell elements prior to failure of the CZM elements. To optimize the fit in this region, the parameter fit was only performed up to this point. A pointwise average of the fit parameters at each 0.0002 strain increment was then performed to produce the average stress-strain curve necessary for the piecewise plasticity model for each material (Figure 78).

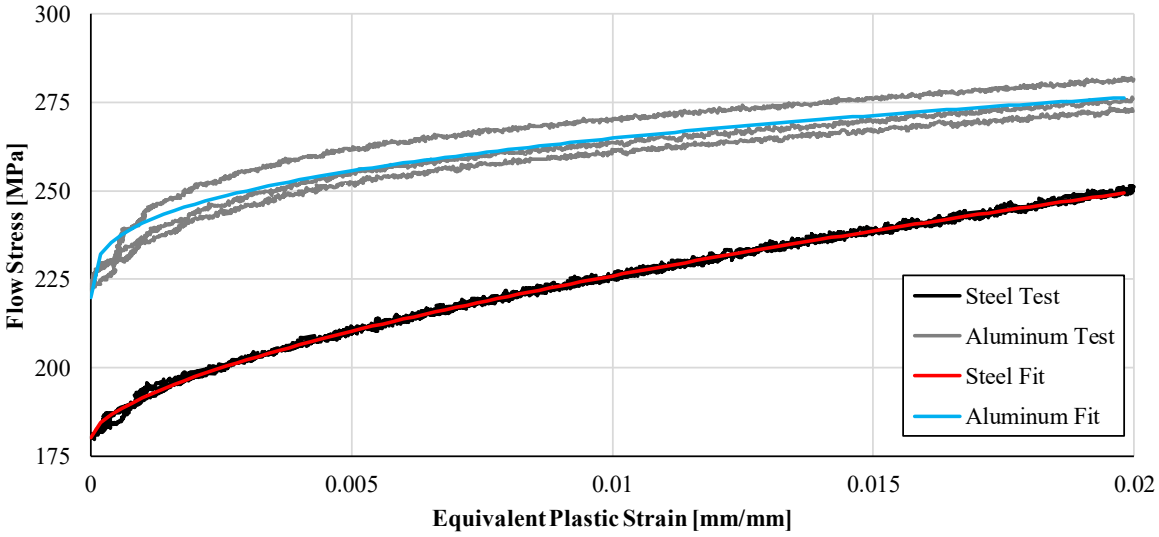

Figure 78: Flow stress of A366 steel and 6061-T6 aluminum used for single lap shear adherend models

The position of nodes 25.4 mm (1”) from the end of the adherend (i.e. 12.7 mm (1/2”) from the overlap, see Figure 76) and at the end of each adherend were monitored to provide a displacement and rotation measurement representing the same measures from testing (Figure 76). Force was output by monitoring the boundary force required to maintain the prescribed motion of the moving end of the adherend.

A small mesh refinement study was carried out using 8 mm, 4 mm and 2 mm shell and cohesive elements, following the procedure outlined by Roache [1994; 1997; 1998] (as suggested by ASME [2006]) to decide on an in-plane mesh size. Using the 0.3 mm *MAT_240 CZM and steel material properties with a 2 mm in-plane mesh yielded mesh-size error estimates of less than 1% for the peak force and maximum displacement measurements. Thus, the 2 mm mesh size was deemed to have converged and was used to model the SLS tests.

Chapter 6 EMC Cohesive Zone Method Finite Element Model Verification and Validation Results and Discussion

In this chapter, the finite element predictions are presented and discussed. Here, the measured properties are implemented within the CZM model and then the model is assessed in terms of its ability to predict the response of the experiments discussed in Chapter 5. First, a single element verification study of the new EMC model is presented to demonstrate the ability of the CZM model to predict the expected results for a given input without complications that arise from more complex models. Second, a series of "model verification" studies are presented in which the model is applied to simulate the experiments used to calibrate the material data. These include models of the Mode I characterization (RDCB) tests and the Mode II (BSS) and MM tests and models. Finally, "model validation" was assessing using two experiments, the TDCB and single lap shear tests, that were not used in the calibration of the CZM properties. The TDCB and SLS were selected due to these tests loading the adhesive in reasonably well controlled Mode I (TDCB) and Mode II / MM (SLS) conditions. Modeling the TDCB and SLS tests allows for comparison between the model and test data which exhibit elastic and elastic-plastic-deformation of the adherends, in order to assess the ability of the CZM model to interact with adherends exhibiting these phenomena.

6.1 EMC Model Single Element Verification in Mode I, Mode II and Mixed Model Loading

A total of 36 single element cases (input separation and output traction responses are presented in Appendix B) were simulated to verify the EMC model response and assess robustness of the EMC. The results were compared to a contemporary CZM model (*MAT_240) for reference. The EMC

model, which included bond line thickness dependence, was fit to all three bond line thicknesses considered in the experiments, while *MAT_240 models were fit to each individual bond line thickness characterized.

The Mode I single element EMC model (Figure 79) provided an excellent fit to the average experimental data for all three bond line thicknesses considered. There was some deviation of the EMC models in the unloading zone due to the parameter fitting process based on bond line thickness. The % difference,

$$\%\, difference = \frac{\text{Model Response} - \text{Experimental Average}}{\text{Experimental Average}} \times 100\,, \tag{98}$$

was within 5% for each of the separation values (δ_0, δ_s, and δ_f), and 0.3% for the plateau traction value.

The Mode I single element traction-separation response of the *MAT_240 model provided a precise fit to the Mode I experimental test average, since there were three sets of model parameters fit individually to each bond line thickness. In contrast, the surface fitting process used to extract the EMC parameters, which did not reproduce the exact measured parameters for a given bond line thickness, led to the deviation noted above for the EMC model.

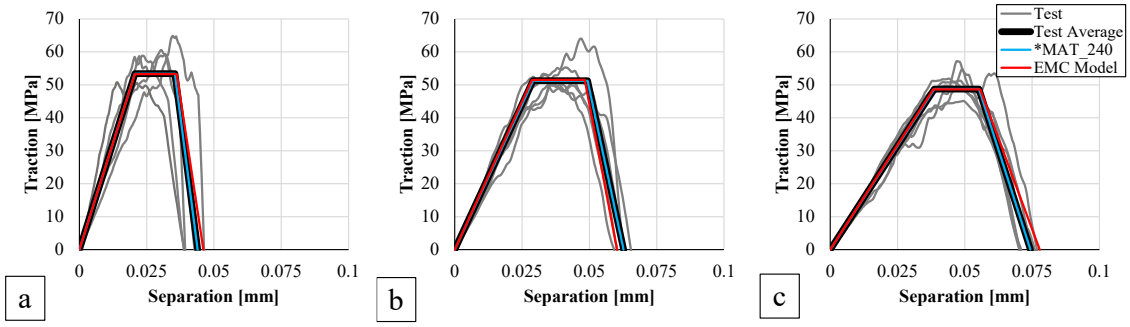

Figure 79: Comparison of traction-separation response between average Mode I experimental test data and single element EMC model compared to the *MAT_240 model for 0.18 mm (a), 0.3 mm (b), and 0.64 mm (c) nominal bond line thickness

The Mode II single element EMC traction-separation response (Figure 80) was also in good agreement with the experimental average (4% average difference for δ^0, δ^s, and δ^f and a 0.7% difference for the average of the plateau traction (σ_0) and softening traction (σ_s)). Variations were attributed to the fitting process, which required some compromise to fit a range of bond line thicknesses, rather than using different sets of parameters to fit a specific bond line thickness, as with the *MAT_240 model which does not account for bond line thickness. Importantly, the EMC model demonstrated the ability to capture the displacement hardening response of the experimental response. The *MAT_240 model also assumes a zero slope plateau for the Mode II traction-separation response and therefore did not accurately represent the rising slope present in the experimental data. The average difference was 4% for δ^0, δ^s, and δ^f and 0.4% for the mean value of σ_0 and σ_s. The plateau traction of the *MAT_240 model was closer to the mean of the measured σ_0 and σ_s values than the EMC model, masking the poorer fit of the *MAT_240 to the positive slope of the test response. Choosing another metric to evaluate the response would more readily highlight this point. For example, the average root-mean-square deviation for the EMC model to the onset of failure was 0.38 MPa compared to 1.40 MPa for the *MAT_240 models. The use of % difference throughout the model analysis was meant to provide a consistent measurement between the models and the test data for all metrics.

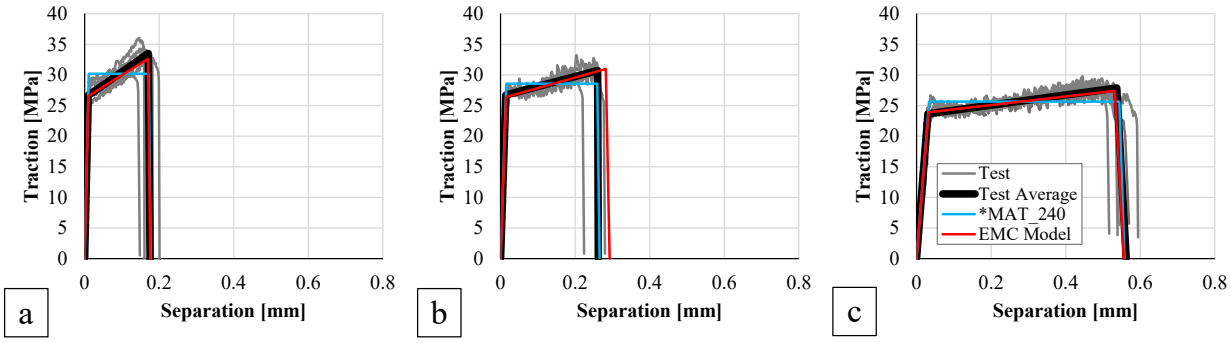

Figure 80: Comparison of traction-separation response between average Mode II experimental test data and single element EMC model compared to the *MAT_240 model for 0.18 mm (a), 0.3 mm (b), and 0.64 mm (c) nominal bond line thickness

The EMC model was applied to the two mixed-mode loading scenarios. The 75° MM (Figure 81) and 45° MM single element traction-separation responses (Figure 82) highlighted an important benefit of the EMC model, which was able to represent the positive slope, and the separation at failure with an average difference of 9% from the experimental data. In contrast, the percent difference for the *MAT_240 model was 25% on average. Furthermore, the *MAT_240 models predicted a 16% average difference between the plateau traction and the mean of the σ_0 and σ_s measurements. The goodness of fit for the EMC model was attributed to considering the MM traction-separation response in the parameter fitting, unlike the *MAT_240 model, which inferred the MM response from the Mode I and Mode II response.

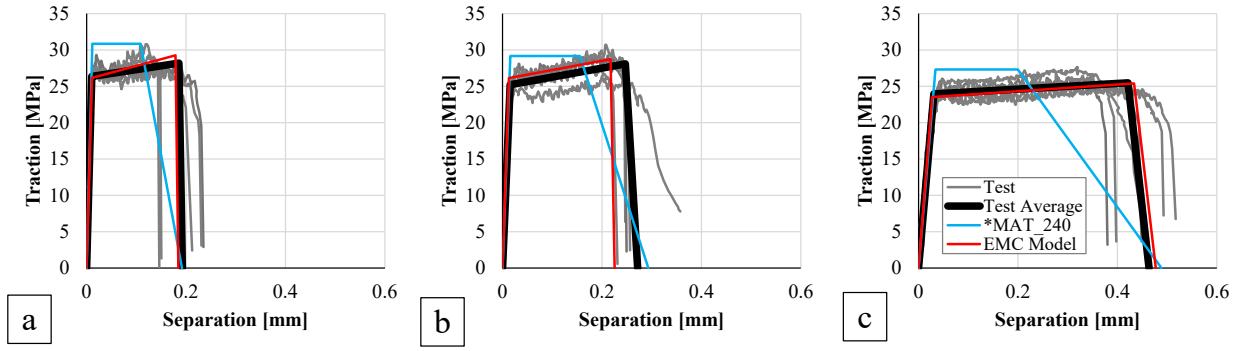

Figure 81: Comparison of traction-separation response between average 75° mixed mode experimental test data and single element CZM models for 0.18 mm (a), 0.3 mm (b), and 0.64 mm (c) nominal bond line thickness

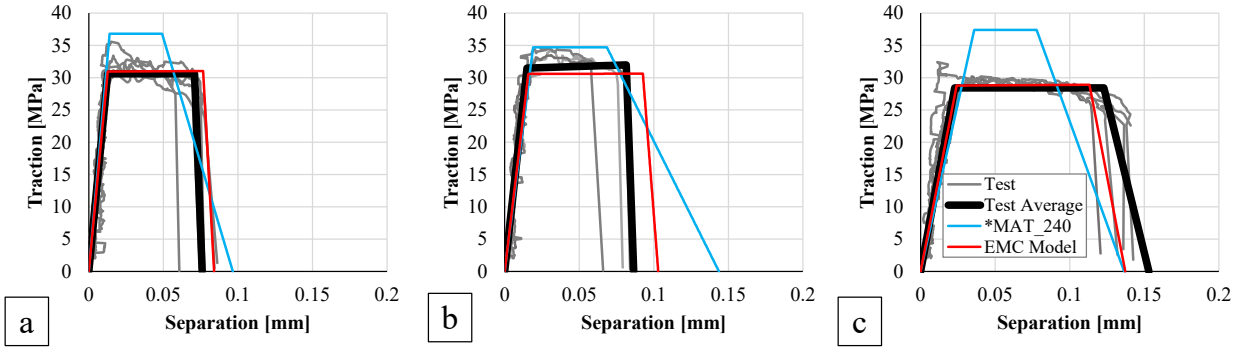

Figure 82: Comparison of traction-separation response between average 45° mixed mode experimental test data and single element CZM models for 0.18 mm (a), 0.3 mm (b), and 0.64 mm (c) nominal bond line thickness

In all MM cases, the separation-to-plateau of the *MAT_240 model was less than the experimental average (between 16% and 53%). Additionally, in all cases, the plateau traction of the *MAT_240 model exceeded the experimental plateau traction. Part of the poor fit for the *MAT_240 model stemmed from loading the single element based on the specimen angle (θ_s) rather than the mixity angle (θ_m), defined in Chapter 3, which is dependant on the Mode I and Mode II initial stiffnesses. When the *MAT_240 model was loaded at θ_m for each of the six MM cases, the average difference

between the model and test data was 26% for the separation response and 12% for the traction response, compared to 25% and 16% for loading based on θ_s. Due to the equal initial stiffness in Mode I and Mode II under MM loading assumed with the EMC, θ_s and θ_m were aligned causing the difference between the EMC model and the test data to be lower than for either case with the *MAT_240 models. The effect of the difference between MM loading at θ_m or θ_s is particularity important when considering situations in which little deformation is expected in the adherends, which, in effect, forces a prescribed displacement on the CZM. Care must be taken when interpreting results in such cases to ensure that the predicted traction values align with the expected MM loading angle.

6.2 Model Verification Simulations

In the section that follows, the results of the verification models are presented and compared to test results on which the models were based. These models were intended to demonstrate the ability of the EMC model to capture the traction-separation response of the characterization tests, when considering deformation of the adherends. The verification models also provide a quantitative assessment of the assumption that the adherends acted as rigid bodies during the analysis of the characterization tests. First, the results of the RDCB verification models are presented, followed by the BSS and MM configurations. Finally, a summary of the verification models is presented.

6.2.1 EMC Model Verification in the RDCB Configuration

The first step in modeling the RDCB tests was to assess the effect of adherend deformation on the force-displacement response of the RDCB test. To perform this comparison, a single test from

each of the nominal bond line thicknesses was modeled using the Mode I parameters extracted from that individual test. The response of these RDCB verification models (Figure 83) demonstrated the ability of the data reduction scheme described in Chapter 3 to extract the traction-separation response by assuming adherend rigidity in order to simplify the analysis.

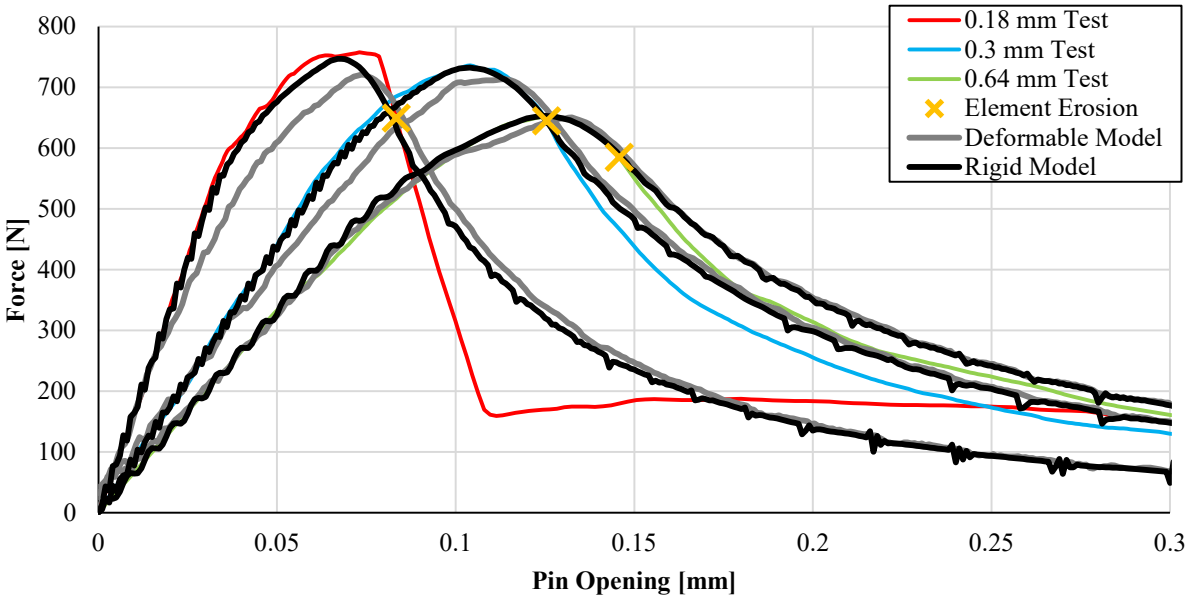

Figure 83: Comparison of RDCB EMC model incorporating rigid and deformable adherends to experimental test force-displacement response for nominal bond line thicknesses of 0.18 mm, 0.3 mm, and 0.64 mm with the point at which the crack tip erodes marked with an 'X'

The models that used rigid adherends provided initial stiffness (defined as the average slope of the force-displacement response up to 500 N) within 2.9% of the measured response (Table 16) and peak forces within 1.5% confirming that the rigid adherend assumption was reasonable. The differences were attributed, in part, to the noise in the force displacement test response (necessitating filtering of the response); however, the small differences between the model and test data highlight the ability of the RDCB analysis to reproduce the test response.

The difference between the initial slope and peak force of the models using deformable adherends and the test ranged from -18.7% to -4.9%, respectively, for the model of the 0.18 mm test to only -0.2% and -0.02%, respectively, for the 0.64 mm test. The improved prediction with thicker bond lines can be attributed to the lower initial stiffness causing less deformation of the adherends and thus less difference to the experiment in the force-displacement response. Although the traction-separation properties could be calibrated to account for the deformation of the test samples, the aim of this work was to propose a consistent data processing method for the experimental data, and verify the outcome using the improved EMC model, which was demonstrated for thicker bond lines.

Table 16: Comparison of experimental and predicted EMC model force-displacement response for representative RDCB tests

Bond Line Thickness [mm]	0.18	0.3	0.64	0.18	0.3	0.64
Parameter	**Initial Slope [N/mm]**			**Peak Force [N]**		
Test	16716	8847	6437	758	736	651
Rigid Model	16535	8754	6622	747	732	653
Difference	-1.1%	-1.1%	2.9%	-1.5%	-0.5%	0.4%
Deformable Model	13601	8082	6452	721	713	650
Difference	-18.6%	-8.7%	0.2%	-4.9%	-3.0%	-0.02%

For the 0.3 mm and 0.64 mm bond line thickness cases, the rigid models were able to reproduce the force-displacement response up to the point at which the element at the crack tip eroded (indicated by the yellow *X* in Figure 83), after which the test was effectively completed (*i.e.* the crack had started to open in the experiment and the element at the crack tip was eroded in the model). The brittle fracture of the thinnest bond line (0.18 mm) experiment provided some challenges for the data reduction scheme. The sudden drop in force caused by the unstable fracture propagation could not be properly modeled using a CZM, which models ductile fracture by

assuming that the propagation of the crack is due only to the relative motion of the top and bottom surface of the cohesive element. During brittle fracture, the crack tip propagates much faster than in ductile fracture [Meyers, 1994]. The precipitous drop in the experimental force-displacement response was somewhat reduced due to the 21-point running average smoothing of the force-displacement carried out during the RDCB test analysis. Irrespective of the difficulties in extracting the traction-separation response, the analysis method was able to provide a reasonable fit to the experimental data, particularly during the loading and peak traction phase of the response, considering the deviation from the underlying assumptions associated with the cohesive zone element method. Care must be taken in interpreting the results of tests where rapid fracture occurs and whether the CZM approach, which typically is used to model progressive fracture, is appropriate. Further refinement of the CZM approach to account for brittle fracture and the transition between brittle and ductile fracture would provide further improvement to the model response for thin bond lines.

When considering models of the characterization tests based on the average fit parameters using deformable adherends, only minor differences were apparent between the models of the average EMC and *MAT_240 models of the RDCB test (Figure 84), attributed to the inclusion of bond line thickness in the EMC fitting process. The peak force of the EMC models was within 1% of the *MAT_240 model and 2.5% of the measured values.

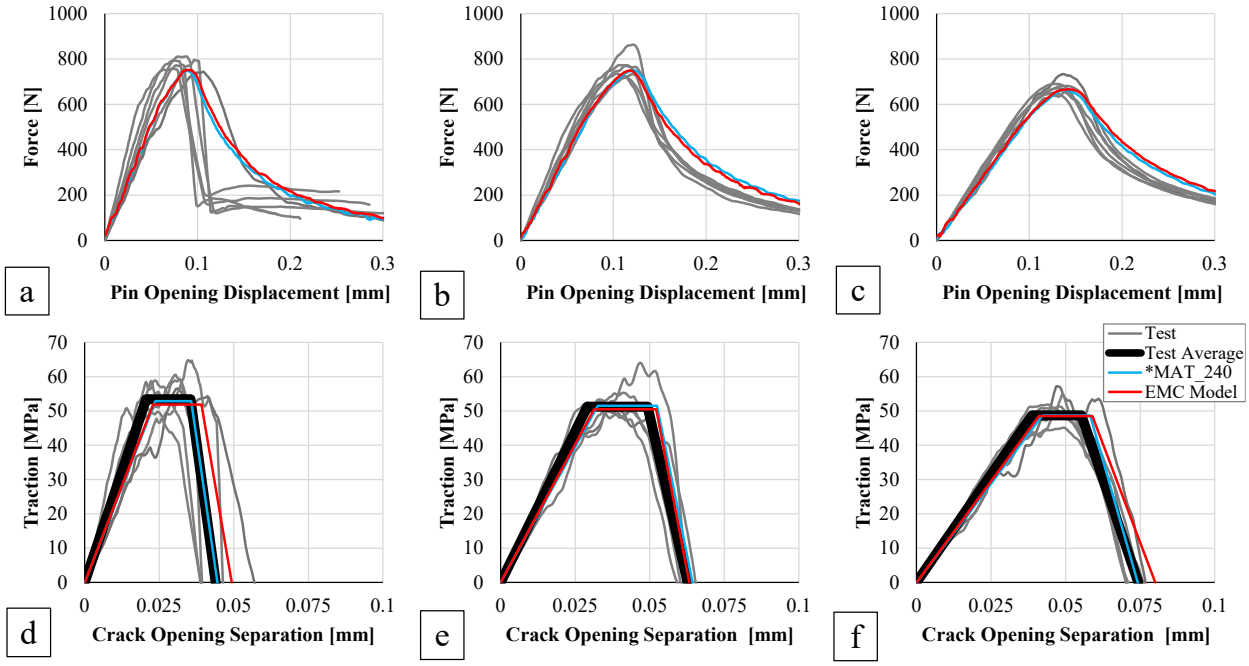

Figure 84: Comparison of RDCB CZM models to experimental force-displacement response and corresponding output of traction-separation for nominal bond line thicknesses of 0.18 mm (a,d), 0.3 mm (b,e), and 0.64 mm (c,f)

Next, the model force-displacement responses (Figure 84a, b and c) were converted to the respective traction-separation responses (Figure 84d, e and f) using the same approach as with the experimental results to assess the degree to which the traction-separation response changes during the analysis process. The *MAT_240 models provided an average % difference to the test average of 12% for δ^0, 4% for δ^s, 1% for δ^f and 1% for σ_0 compared to 8%, 8%, 7%, and 2%, respectively, for the EMC. The difference associated with the *MAT_240 model can be attributed entirely to the effect of using deformable adherends. The models used the exact average parameters for each bond line thickness, thus giving a quantifiable estimate of the error associated with the rigidity assumption of the test analysis. The response of the model of the RDCB tests shows not only that the analysis technique is able to accurately reproduce the force-displacement response for a given

input traction-separation (and *vice versa*), but also that the rigidity assumption used in the development of the analysis was realistic.

6.2.2 EMC Model Verification for BSS and MM configuration (Mode II, 45º and 75º Mixed Mode)

The force-displacement responses of the BSS and MM models were converted to traction-separation responses for each bond line thickness (Figure 85) for ease of comparison to the model input. The average difference between the test and model separation-to-plateau, separation-to-softening and separation-to-failure was within 8% for the EMC model. The *MAT_240 model differed by 11% on average, attributed to the assumption of a zero-slope plateau for shear loading. Both the EMC and *MAT_240 models were within 1% of the mean of σ_0 and σ_s measured in the tests. As with the single element models, other metrics would better highlight the fact that the *MAT_240 model was unable capture the hardening traction response, which, in part, necessitated the develop the EMC model.

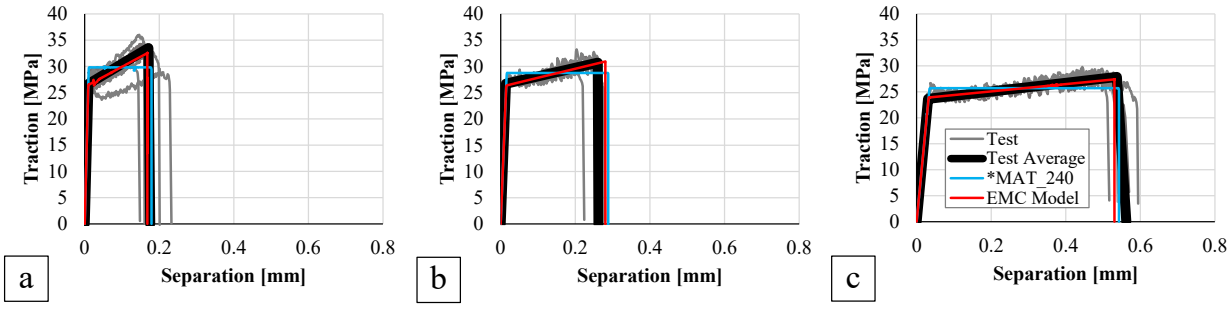

Figure 85: Comparison of BSS CZM models to experimental traction-separation response for nominal bond line thicknesses of 0.18 mm (a), 0.3 mm (b), and 0.64 mm (c)

For the 75º MM specimen geometry models (Figure 86), the EMC provided separation values within an average of 10% of the test response and 2% of the average plateau traction test response, compared to 24% and 9%, respectively, for the *MAT_240 model. This level of fit was similar for the 45º MM specimen geometry (Figure 87) using the EMC (7% difference in separation and 2% difference in traction), with higher error for the *MAT_240 model (24% and 14%, respectively). As with the single element cases, the *MAT_240 MM model plateau traction was generally larger than the experimental value, along with a shorter plateau region and a much lower unloading slope. One feature of note with the 45° MM models was the tendency for a small amount (less than 2% deviation from the expected plateau traction) of noise in the plateau region of the curve. This noise was primarily associated with the defined contact between the rigid pins and very stiff (relative to the adhesive) steel adherends, which were rotating on the pins in the MM case (unlike the BSS case). While additional damping could be defined to reduce or eliminate this oscillation in the model, given the nature of the test traction-separation response used to develop extract the CZM parameters to defined this model, this noise was not of practical concern.

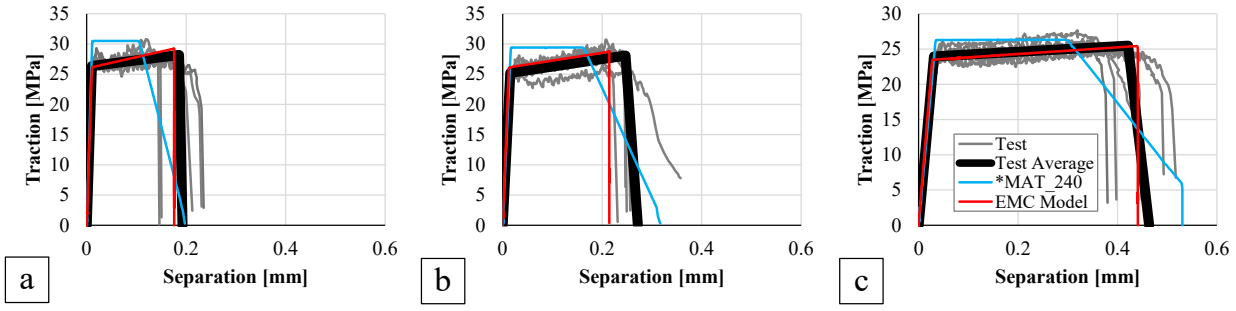

Figure 86: Comparison of 75º MM CZM models to experimental traction-separation response for nominal bond line thicknesses of 0.18 mm (a), 0.3 mm (b), and 0.64 mm (c)

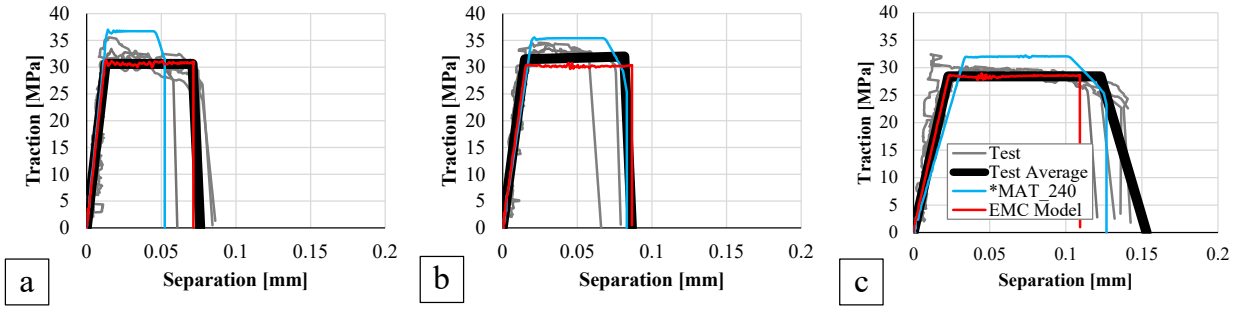

Figure 87: Comparison of 45º MM CZM models to experimental traction-separation response for nominal bond line thicknesses of 0.18 mm (a), 0.3 mm (b), and 0.64 mm (c)

The BSS and MM EMC models provided essentially the same traction-separation response as the single element case until the initiation of failure, which tended to occur very rapidly (as was also observed in the experiments). This deviation after failure initiation is most apparent in the 45º MM, 0.64 mm case in which the single element model unloading occurred over 0.03 mm while the model with deformable adherends failed with less than 0.001 mm unloading displacement. Due to deformation of the adherends, slight non-uniformity of the loading angle along the bond line (ranging from 43.5° to 47.6° throughout the simulation) led to the elements at the leading edge of the bond line eroding at slightly lower displacements than would be expected for 45º loading. Then, due to the relatively small displacement between the initiation of softening and failure, the remaining elements quickly eroded as the stress was rebalanced from the elements at the leading edge of the bond line. The fidelity of the model using deformable adherends compared to the expected fit indicates that the rigid-adherend assumption used during characterization of the adhesive was reasonable.

6.2.3 Summary of Model Verification Simulations

In summarizing the differences between the EMC and *MAT_240 models and the measured data (Figure 88), several trends are apparent. The *MAT_240 model exhibited more deviation from the test data for the MM cases (absolute average of 20%) than for the RDCB and BSS models (absolute average of 6%). Given that equal weighting was assigned to all modes of loading during parameter fitting for the EMC, the EMC models exhibited roughly equal performance for the MM (7% average difference) and pure modes of loading (5% average difference). Both the EMC and *MAT_240 models exhibited some deviation from the experimental separation-to-plateau and separation-to-softening averages (18% for the *MAT_240 models and 6% for the EMC cases). The early separation-to-failure caused by non-uniform stress distribution of the BSS and MM specimens somewhat confounds the average difference between the test and models, which was 9% for both the EMC and *MAT_240 models. When considering Mode I, Mode II and mixed mode loading, the EMC models tended to produce better results than the *MAT_240 models, with lower average differences for both the separation (7% *vs*. 15%) and traction (2% *vs*. 6%) measurements.

The RDCB model with rigid adherends tended to provide a better fit to the experimental slope and peak force than with deformable adherends (1.2% vs. 5.9% average difference), although as the bond line thickness increased, these differences reduced. As with the single element models, the EMC model of the deformable RDCB tests exhibited slightly less fidelity than the *MAT_240 model due to the fitting process necessary to define bond line thickness dependency in a single model. The benefit of this approach is that a single set of material parameters can be used to model a range of bond line thicknesses, rather than needing to test and model each bond line thickness required in a model, as with typical CZM models such as *MAT_240. Under MM and Mode II

loading, *MAT_240 was not able to capture the hardening response that was measured experimentally, as the ECM model did. Furthermore, the MM predictability of the *MAT_240 models was generally quite poor due to the underlying assumptions of the model not corresponding to the measured results. By utilizing the measured MM data in the model definition, the EMC model was shown to better correspond to the MM data. Considering all the deficiencies identified for typical CZM models, it is not unsurprising that the average difference between experimental results and the *MAT_240 models (absolute average 13%, blue lines in Figure 88) was more than twice as large as the EMC cases (absolute average 6%, red lines in Figure 88).

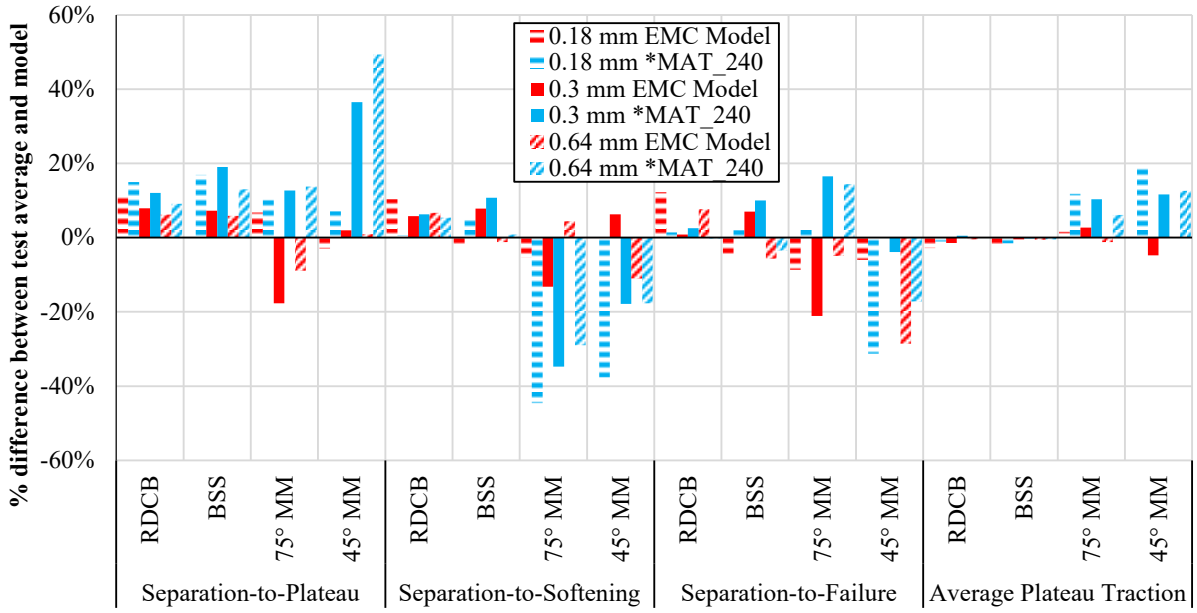

Figure 88: Summary of percent difference between average experimental test data and CZM models (EMC and *MAT_240)

6.3 Model Validation Simulations

This section discusses the results of the validation models carried out with the adhesive represented using the EMC and *MAT_240 models. Unlike the verification models, which were intended to

demonstrate the ability of the model to reproduce the characterization date used in the model definition, the validation models were wholly independent of the experimental data used to define the CZM. The results of the TDCB model are presented first, followed by the results of the SLS model.

6.3.1 Assessment of the EMC Model using the TDCB Test

Models of the TDCB tests were simulated to assess the Mode I response of both the *MAT_240 and ECM models independently of the characterization tests used to define the parameters of the models. The benefit of simulating the TDCB was to test the EMC against a commonly accepted test specimen and to introduce adherend deformation into the validation process.

The force-displacement responses of the *MAT_240 and EMC models (Figure 89) tended to show less bond line sensitivity than the test response. The difference of the average force predicted by the EMC models and the experimental measurements (between pin displacement of 1 mm and 3 mm) of the 0.3 mm and 0.64 mm specimens were -2.0% and 6.3%, respectively, while the 0.18 mm model overpredicted the force by 33.5% (Table 17). The overprediction of force for the 0.18 mm bond line thickness was not surprising given the challenges associated with using the RDCB test methodology. In order to extract the traction-separation response, a 21-point running average for the force-displacement response was needed in the RDCB analysis. This running average, when applied over the very short (1-2 samples) unloading time of the sample, extended the apparent displacement over which the unloading occurred, increasing the apparent energy absorbed by the specimen. This apparent increased energy was then manifest in an overestimation of the critical energy release rate measured by the RDCB sample for brittle materials. The difference between the model and test force response (33.5%) was comparable to the difference between the critical

energy release rate measured using the TDCB test specimen and the RDCB test specimen (38%). The differences between the measured and predicted force plateau and G_{IC} values for the 0.18 mm bond line thickness suggest that the TDCB test may be better at measuring the G_{IC} value for brittle adhesive than for ductile failure. In contrast, the ductile failure measured in specimens with thicker bond lines were captured well using the RDCB approach. Furthermore, the RDCB tests using the 0.18 mm bond line thickness exhibited unstable crack growth, while the TDCB specimens exhibited stable crack growth. The assumptions that underlie the TDCB analysis are based on linear elastic fracture mechanics, which generally assumes a brittle response of the adhesive rather than considering more advanced characterization techniques [Sorensen and Jacobsen, 2003]. The stable crack growth present in the 0.18 mm bond line thickness TDCB may be related to the elastic deformation of the TDCB adherends, unlike the RDCB adherends which exhibited essentially no deformation. The ability of the TDCB adherends to undergo large deformation may absorb some energy from the system that would otherwise be put into causing unstable fracture of the adhesive. Further investigation into this phenomenon and the transition from brittle to ductile fractures, and a method to model this transition, should be undertaken to further refine the EMC.

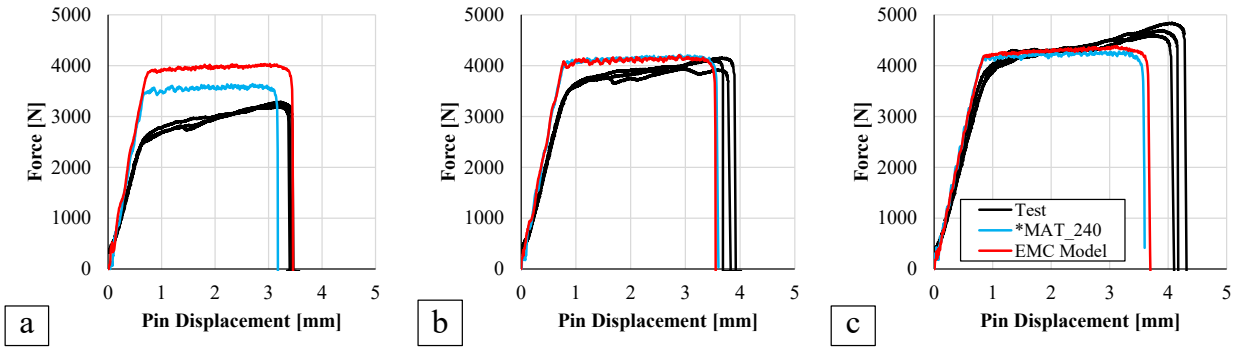

Figure 89: TDCB test modeled using EMC and *MAT_240 models for nominal bond line thicknesses of 0.18 mm (a), 0.3 mm (b), and 0.64 mm (c)

When using the *MAT_240 model with properties measured for each nominal bond line thickness, the results lacked differentiation between the 0.3 mm and 0.64 mm cases. The similar force-displacement responses for the two bond line thicknesses were attributed to the measured RDCB G_{IC} values, which are directly related to the plateau force being similar (2.125 N/mm *vs*. 2.216 N/mm). This small difference was somewhat amplified due to the TDCB bond line thicknesses not exactly matching the nominal bond line thickness, especially for the nominally 0.64 mm case, which had an average measured thickness of 0.72 mm and thus a larger G_{IC}. Using experimental RDCB test data with a larger bond line thickness in the model, rather than extrapolating based on data from thinner bond lines would likely improve this fit. The largest bond line thickness in the TDCB test was above that used for characterization testing and thus required some extrapolation for the model fitting by using the CZM element thickness (0.72 mm) in the equations used to define the response surface for each parameter (See Section 5.1.1). As the simple beam theory used to develop the TDCB specimen geometry would suggest, the models all predicted a flat plateau, unlike the increasing slope present experimentally. This effect was noted by Blackman *et al.* [2003a], who explained this behaviour may be due to compliance of the load frame that is not present in the model.

Table 17: Comparison of TDCB model to experimental force

		Test	EMC Model		*MAT_240 Model	
Nominal Bond Line Thickness [mm]	**Measured Bond Line Thickness [mm]**	**Average Plateau Force [N]**	**Average Plateau Force [N]**	**Difference [%]**	**Average Plateau Force [N]**	**Difference [%]**
0.18	0.158	2972	3968	33.5%	3565	20.0%
0.3	0.329	3867	4112	6.3%	4134	6.9%
0.64	0.723	4376	4289	-2.0%	4213	-3.7%

The models also predicted a well-defined demarcation between the initial slope of the force-displacement response and the plateau region, whereas the measured response exhibited a more gradual transition. The sharp transition in the model response may be related to the simplification of the traction-separation response from a smooth curve to a sharp-cornered trapezoid.

Using the EMC predicted force values (Table 17) to compute the critical energy release rate, as described in the ASTM D3433 standard, resulted in values of 1.73 N/mm, 1.86 N/mm, and 2.02 N/mm for the 0.18 mm, 0.3 mm and 0.64 mm nominal bond line thicknesses, respectively. These values were between 14.3% lower and 12.5% higher than the expected values, based on the input critical energy release rates. Such incongruence between values of G_{IC} measured using the ASTM D3433 specification and more advanced techniques has been noted by other authors [Lopes *et al.*, 2016].

6.3.2 Assessment of the EMC Model using Single Lap Shear Test Data

The full force-displacement responses (Figure 90a to Figure 93a) and rotation-displacement responses (Figure 90b to Figure 93b) highlight several differences between the two models. The initial portion of these responses were nearly identical between the two CZM models, meaning the initial portion of the response was dominated by the adherend material and boundary conditions of the model. The differences between the two CZM models is more apparent later in loading when the difference in damage and softening between the two CZM models begins to take effect.

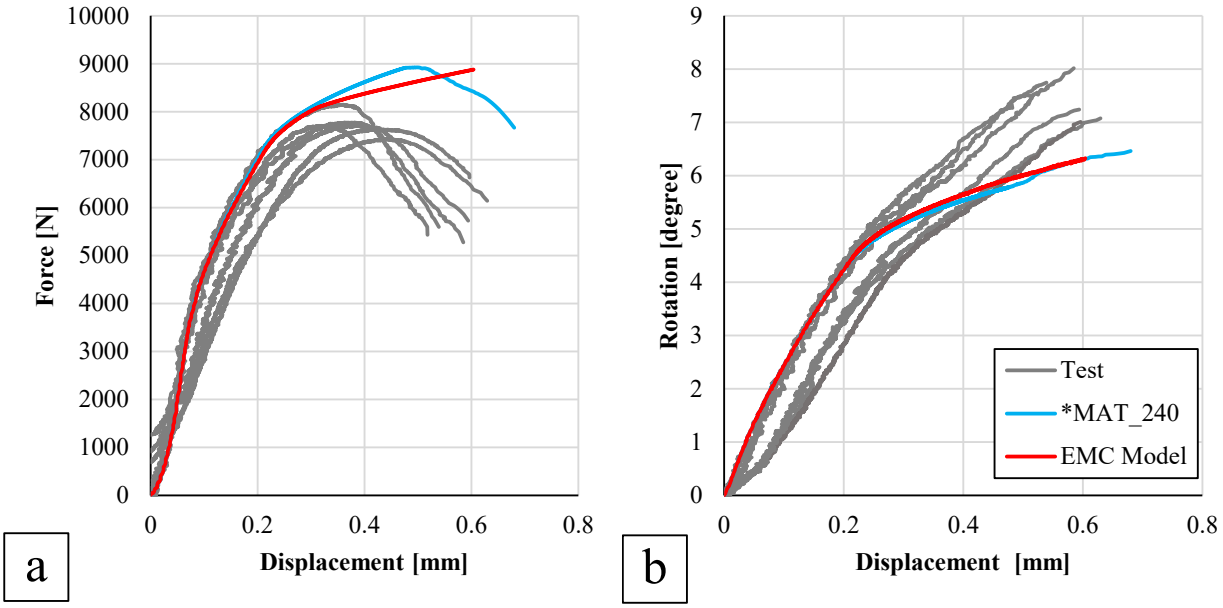

Figure 90: Single lap shear model force–displacement (a), and rotation–displacement (b) response for A366 steel adherends with a 0.3 mm bond line thickness

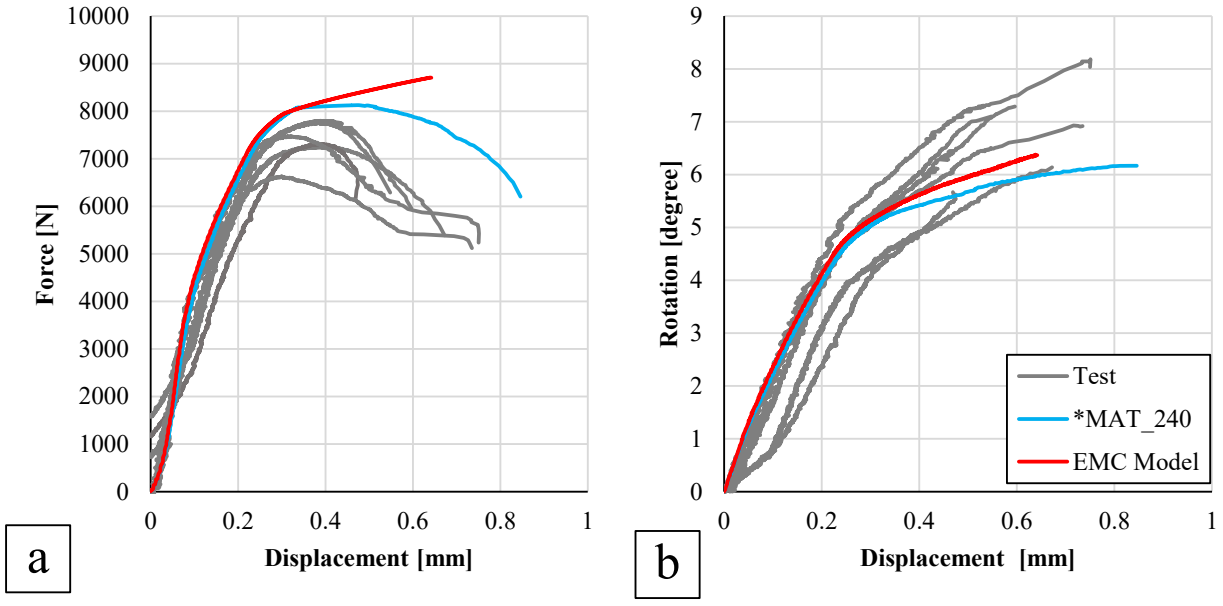

Figure 91: Single lap shear model force–displacement (a), and rotation–displacement (b) response for A366 steel adherends with a 0.64 mm bond line thickness

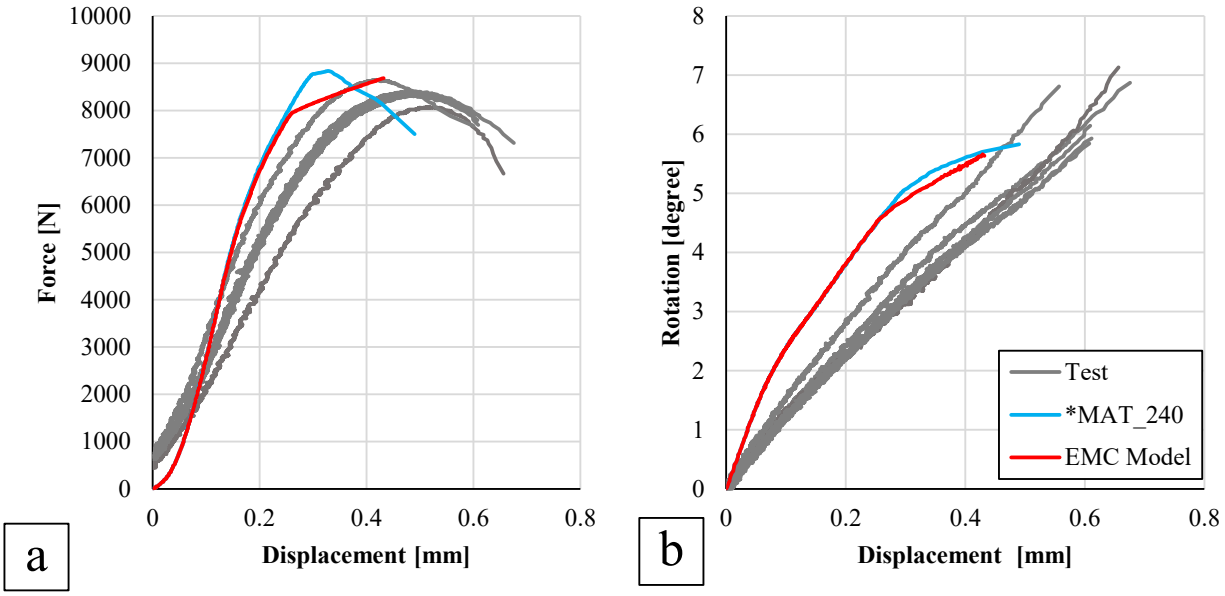

Figure 92: Single lap shear model force–displacement (a), and rotation–displacement (b) response for 6061-T6 adherends with a 0.3 mm bond line thickness

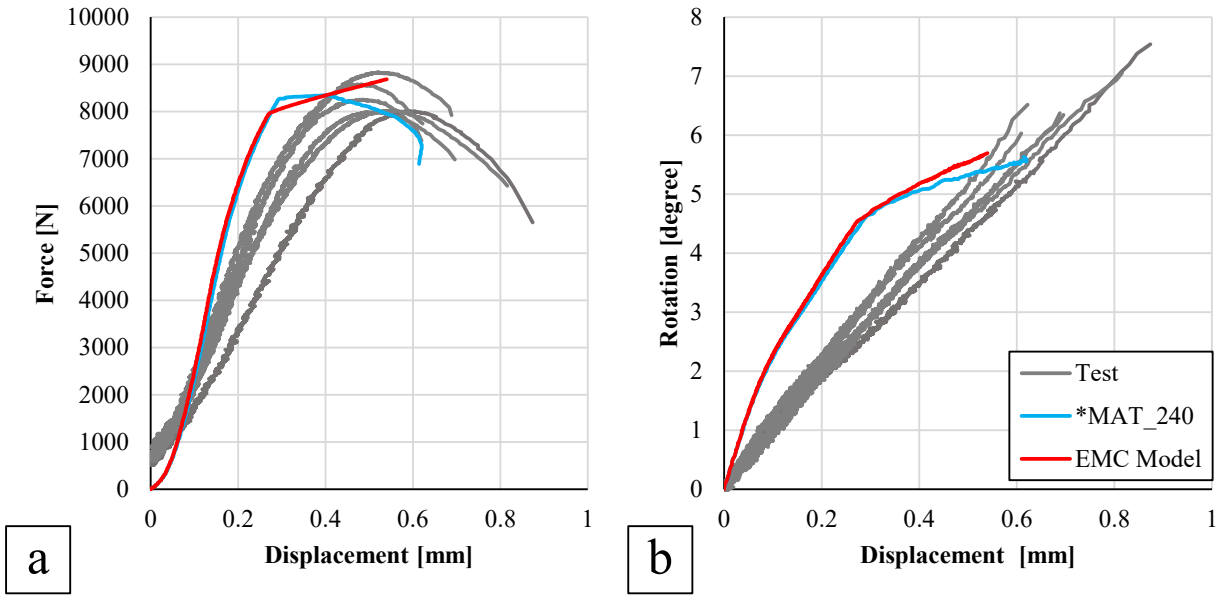

Figure 93: Single lap shear model force–displacement (a), and rotation–displacement (b) response for 6061-T6 adherends with a 0.64 mm bond line thickness

The failure displacement, maximum force, and maximum rotation of both the EMC and *MAT_240 validation models were compared to the average measurements obtained experimentally (Table 18). The average absolute difference between the experimental results and the EMC model predictions were 0.10 mm, 802 N and 0.84°. For the *MAT_240 model these differences were 0.14 mm, 621N and 0.83°.

Table 18: Comparison of single lap shear model force, displacement, and rotation to experimental test average results

		0.3 mm Nominal Bond Line Thickness			0.64 mm Nominal Bond Line Thickness		
Adherend	Response	Test Average	EMC	*MAT 240	Test Average	EMC	*MAT 240
A336 Steel	Failure Displacement [mm]	0.577	0.604	0.680	0.630	0.642	0.846
	Failure Displacement % Difference		4.7%	17.9%		2.0%	34.4%
	Maximum Force [N]	7736	8880	8925	7373	8708	8128
	Maximum Force % Difference		14.8%	15.4%		18.1%	10.2%
	Maximum Rotation [degree]	7.43	6.33	6.46	6.89	6.38	6.17
	Maximum Rotation % Difference		-14.9%	-13.1%		-7.4%	-10.4%
Al 6061-T6	Failure Displacement [mm]	0.627	0.432	0.490	0.719	0.540	0.620
	Failure Displacement % Difference		-31.1%	-21.8%		-24.9%	-13.8%
	Maximum Force [N]	8360	8685	8838	8281	8684	8345
	Maximum Force % Difference		3.9%	5.7%		4.9%	0.8%
	Maximum Rotation [degree]	6.45	5.66	5.83	6.64	5.70	5.63
	Maximum Rotation % Difference		-12.3%	-9.7%		-14.3%	-15.2%

The average % difference between the EMC model prediction and the test data for maximum displacement, maximum force and maximum rotation was 12.8% (red bars in Figure 94) compared to 14.0% for the *MAT_240 model (blue bars in Figure 94). Due to the small values of failure displacement and maximum rotation, the % difference between the models and experimental data tended to be larger for these measures than for the maximum force. The models collectively exhibited a larger average difference for displacement (18.8%) than for force (9.2%) or maximum

rotation (12.2%). Little difference was apparent in the predictability of the steel adherend models (13.6% average difference) compared to the aluminum adherend models (13.2%).

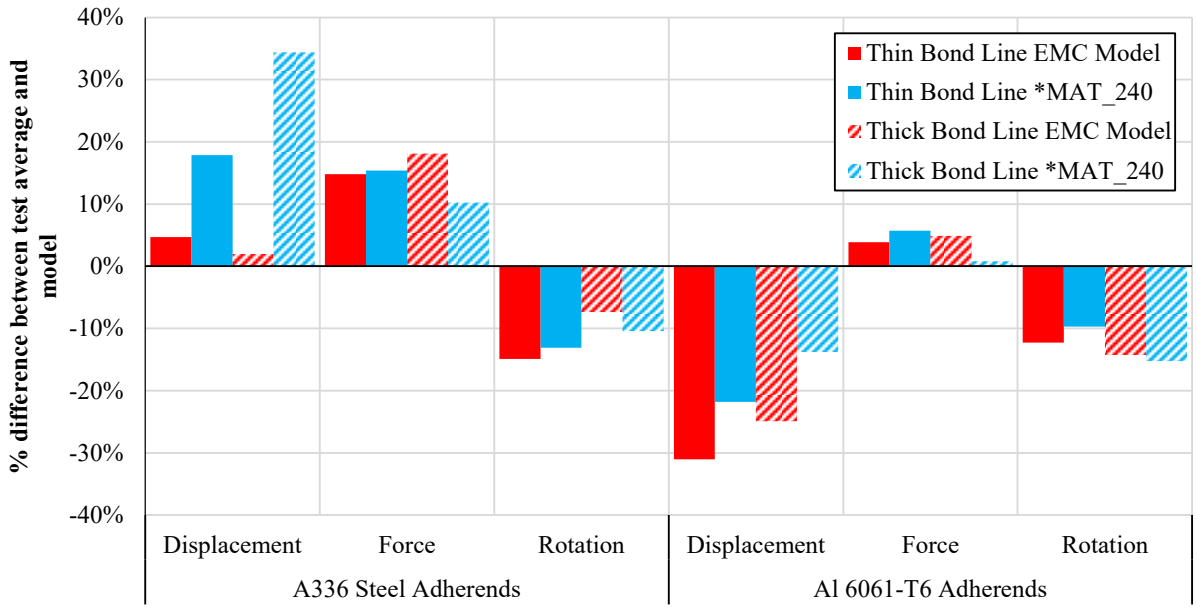

Figure 94: Summary of percent difference between average single lap shear test data and CZM model predictions

In all cases, the adherends reached their plastic limit very early during loading (roughly 0.1 to 0.2 mm). The small displacement associated with the SLS tests made capturing the initial slope somewhat difficult, especially for the aluminum adherend models. An overlay of the 0.3 mm bond line thickness, aluminum adherend EMC model on the test video (Figure 95A) demonstrates the minor differences between the model and test at the onset of yielding, with a deviation of roughly 1°. The steel adherend models, provided an even closer match.

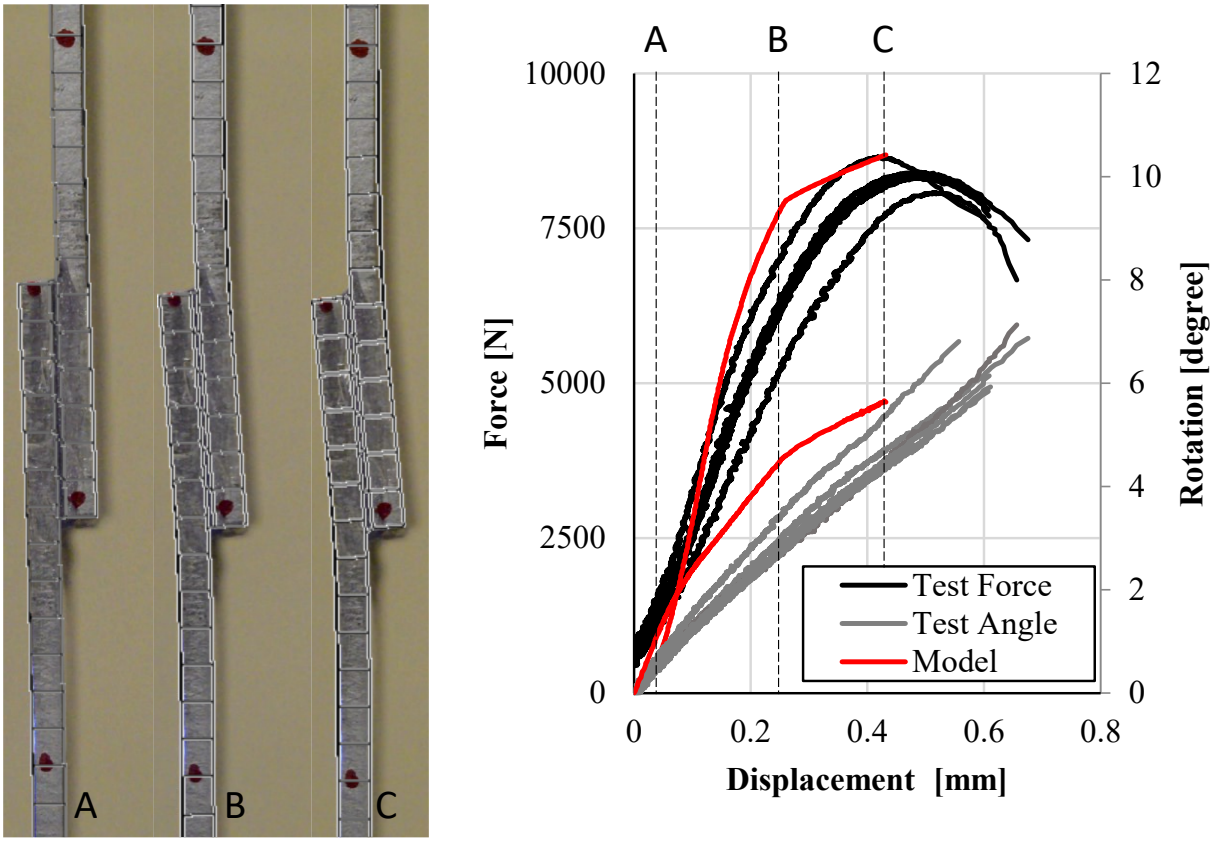

Figure 95: Overlay of 0.3mm bond line thickness aluminum adherend model on test image at displacement corresponding to: onset of adherend plastic deformation at 0.075 mm displacement (shown as A); change in rotation slope at 0.25 mm displacement (shown as B), and maximum force at 0.42 mm displacement (shown as C)

Despite the plasticity in the adherends, as loading continued, the force-displacement and rotation-displacement responses continued to exhibit essentially linear behavior until the CZM elements began to reach their plateau traction, after which the slope of both responses began to reduce (Figure 95B). In contrast, this slope in the *MAT_240 models tended to reduce more than that in the EMC models, even becoming negative (see Figure 90 through Figure 93), owing to the flat plateau of the CZM traction-separation response, and more pronounced softening behaviour. As loading continued, ultimate failure of the joint occurred rapidly after the first CZM element

reached zero traction (Figure 95C) due to the relatively small distance between the separation-to-softening and separation-to-failure values measured during the characterization experiments. The effect of adherend plasticity on the model response can be seen when comparing the response with plastic adherends to the same model using adherends defined using purely elastic material properties (Figure 96).

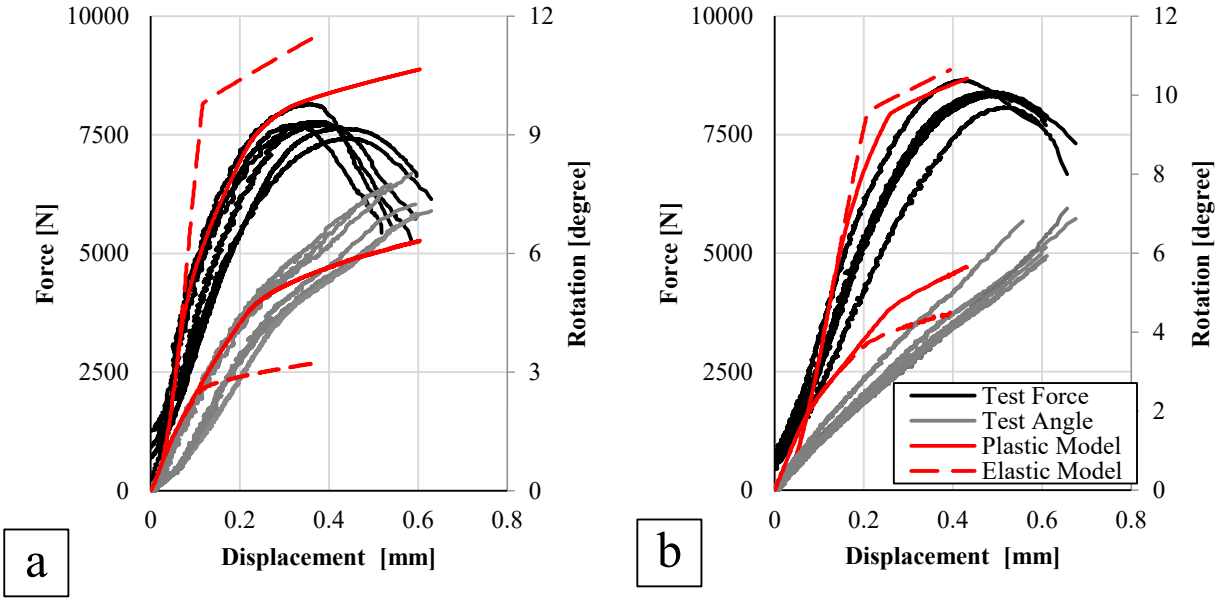

Figure 96: Comparison between plastic and elastic adherends for 0.3 mm bond line thickness EMC models with steel (a), and aluminum (b) adherends

The degree to which the plastic material behaviour dominated the overall force-displacement and rotation-displacement response can be seen by the deviation between the initial slope of the force-displacement response for the models of the steel adherends tests (Figure 96a). A slight change in the slope of the force-displacement response began at roughly 0.1 mm of displacement. The abrupt change in slope of the force-displacement response when the CZM elements began to reach the plateau tractions was considerably less pronounced, due to the plasticity of the adherends, than

was predicted when using elastic adherends. Furthermore, the slope of the force-displacement response above 7500 N was considerably lower for the model with plastic adherends, compared to the elastic case. The reduction in slope accounted for a difference of 8% between the maximum forces. The effect of plasticity on the rotation-displacement response was even more pronounced, with a maximum rotation of roughly half for the case with elastic adherends compared to that of the plastic steel adherends. The cumulative effect of these differences demonstrated the importance of the plastic response to the model predictions. The responses predicted using the current modelling approach suggest that the current plasticity model overpredicts the yield strength of the material; more so for the aluminum than the steel adherends. Further investigation and a more in-depth approach to modeling these adherend materials may improve the overall response of these models, but was outside the scope of the current work.

To explain the unloading response of the *MAT_240 models compared the EMC models, it was useful to consider the traction-separation response of the CZMs at 75º (Figure 86b and Figure 86c). When examining these MM traction-separation responses, it was clear that the *MAT_240 model exhibited an exaggerated softening response (*i.e.* a large difference between the δ^f and δ^s), which caused the more-pronounced reduction in force between the displacement at maximum force and the final failure of the SLS model. While this behavior somewhat improved the correspondence between the SLS test and model response, the large amount of softening displacement was not present in the characterization testing. Clearly, further investigation into the softening behavior would be beneficial to better understand this aspect of the EMC and SLS behavior.

Some aspects of the simplifications used in the model definition may also contribute to the differences between the model and experimental results. For example, the CZM definition does not define tensile stress along the bond line. This stress is assumed to be encapsulated in the Mode

II response, but is somewhat different (*i.e*. distortion vs. dilation stresses). The larger strain in the adherends of the SLS test may have more of an effect in this case than in the other load cases, where the adhered strain was more modest. Furthermore, the offset constraint between the CZM elements and shell mid plane may have some effect on the results, by not accounting for the shear deformation of the adherend during bending. Given the thinness of the adherend, this effect was likely small, although hard to quantify due to the simplification of through thickness shear effects in the shell formulation used. To investigate the effect of mixity on the model response, the average mixity angle of the CZM element node pairs along the edge of the bond area were averaged to provide a measure of mixty angle vs. displacement for each model (Figure 97). The mixity response was dependent on adherend material (and thickness), bond line thickness and CZM model, although all responses shared a similar pattern. Initially, the mixity rose until the adherend reached yield strength and began to plastically deform. The mixity angle then began to decline until the plateau traction of the CZM was reached, after which the mixity angle began to increase again until reaching a maximum value at failure. The average mixty angle at failure was 70^{o} for the EMC models and 73^{o} for the *MAT_240 model with thinner bond line thicknesses exhibiting less mixty prior to failure. Importantly, these values were between the mixity angles measured during characterization, although the varying nature of the mixity present in the SLS model was not necessary captured by the monotonic loading at fixed angles during characterization.

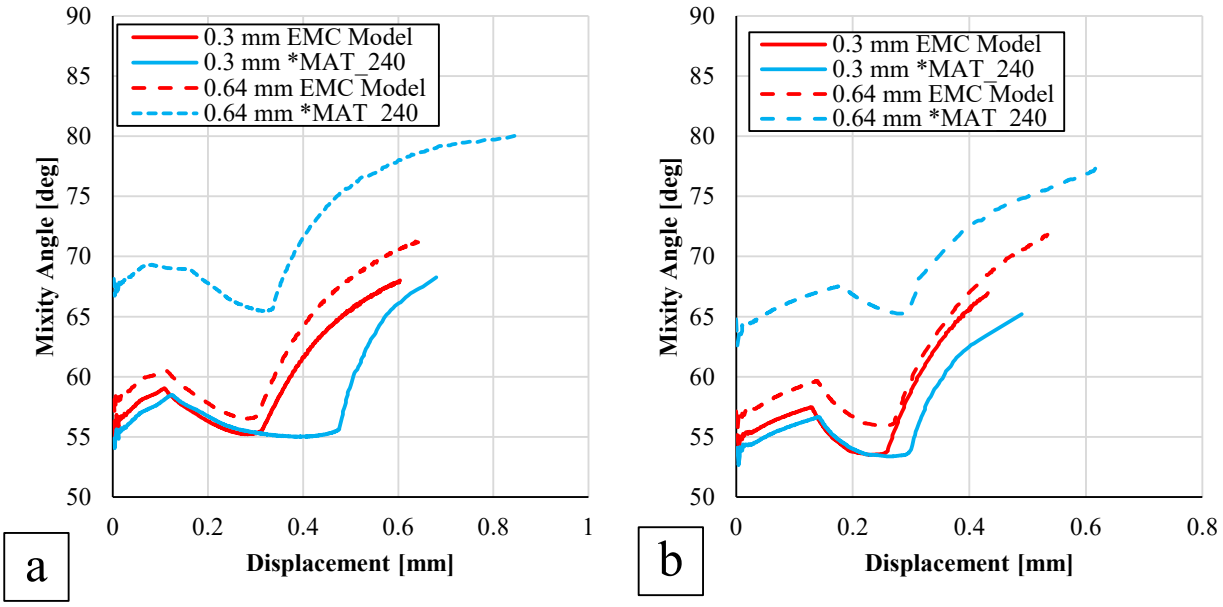

Figure 97: Displacement-mixity angle response for models with steel (a), and aluminum adherends (b)

The results of the *MAT_240 and EMC SLS models highlighted an important consideration in the use of CZM modelling of adhesive joints. Despite the EMC clearly predicting the traction-separation response of the characterization tests with better fidelity than the *MAT_240 CZM, the SLS models were roughly equivalent in the ability to predict the test response. The current results suggested that the MM traction-separation response may be less important for cases in which the adherends exhibit a large amount of deformation. However, in the case of the characterization test models, for which the adherends were very stiff, the shape of the traction-separation response clearly has an effect on the outcome of model. Watson *et al.* [2019b] noted that, in cases where SLS samples were constructed with ultra high-strength steel, higher detail was needed in the CZM traction-separation response. When large deformation was observed in the SLS tests of that study (for example when medium strength aluminum or magnesium adherends were used), the CZM response was of secondary importance to the adherend response. Thus, the importance of

accurately capturing the traction-separation response increases with high stiffness and strength materials; an important consideration when designing structures with the advanced high-strength steels that are becoming increasingly common in automobile BIW applications.

Chapter 7 Conclusions and Future Work

Key accomplishments of the current work include, first, the development of a systematic methodology to characterize the full traction-separation response of a toughened structural adhesive joint for a variety of bond line thicknesses and MM loading angles. A new user defined cohesive zone model, the Enhanced Mixed Mode Cohesive Zone Model (EMC), has been developed that addresses several shortcomings identified in typical CZM implementations, namely, improving the mixed mode (MM) response, correctly capturing the hardening behaviour of the traction-separation response, and modeling the effects of bond line thickness. The EMC has been implemented within a user defined CZM, suitable for large scale modeling efforts, such as vehicle crash simulations incorporating adhesive joints. Validation studies have demonstrated that this user-defined CZM is able to capture the MM loading, as demonstrated in a single lap shear test.

7.1 Conclusions

The main conclusions that can be drawn from this work are:

- The refinement of the Rigid Double Cantilever (RDCB) specimen and improved analysis technique enabled measurement of the full traction-separation response and was verified by reproducing the experimental force-displacement within a model of the characterization test.
- For the thinnest nominal bond line thickness tested (0.18 mm), the RDCB specimen exhibited unstable crack growth. Thicker nominal bond lines (0.3 mm and 0.64 mm) led to

ductile crack growth, demonstrating an ability for the RDCB specimen to capture a brittle-to-ductile transition, based on bond line thickness.

- The proposed Bonded Shear Specimen (BSS) and MM specimen geometry, in conjunction with optical measurement of separation, enabled measurement of full traction-separation responses under both Mode II and MM loading for the same bond line thickness as the RDCB tests.
- The experimentally measured Mode II traction-separation response exhibited a positive slope hardening response, as opposed to the flat plateau typically assumed in previous CZM implementations. This rising traction response was found to gradually diminish as the loading angle decreased towards Mode I loading.
- Bulk material testing under shear loading demonstrated failure at locations of high hydrostatic stress within the test specimen. This behaviour was associated with failure of the BSS test specimens, in which shear cusps were formed during crack initiation normal to the resolved tensile loading direction.
- For both Mode I and Mode II loading, the effect of bond line thickness was statistically significant for all CZM parameters, except for the ratio of area under the stress plateau to critical energy release rate in Mode II. Therefore, it is critical that bond line thickness effects be integrated in CZM approaches.
- The typical power law and Benzeggagh-Kenane criteria used in CZM models were able to fit the measured separation-to-plateau and separation-to-softening response to within within the variability of the measured data using the MM specimens and the RDCB and BSS test results for a given bond line thickness. The power law description of separation-

to-softening, however, significantly underpredicted the measured separation-to softening response, substantially altering the resulting predicted MM traction-separation response.

- In single element simulations of pure and MM loading, the Enhanced Mixed Mode Cohesive Zone Model (EMC), developed in this work, was able to significantly improve the mixed mode predictions when compared to a typical CZM implementation (7% *vs*. 15% average difference to experimental separation to plateau, softening, and failure; and 2% *vs*. 6% difference in mean plateau traction). Importantly, the EMC incorporated the post-yield positive traction-separation response under Mode II loading, as well as bond line thickness effects, with a single set of material parameters.
- Modeling of the characterization tests using the EMC demonstrated that the assumption of rigid adherends in the RDCB, BSS, and MM specimen analysis was acceptable.
- Due to the underlying assumption of ductile crack growth used in the definition of the CZM approach, the model of the 0.18 mm bond line thickness RDCB test was not able to capture the unstable crack growth observed experimentally.
- The TDCB model of the thinnest bond line thickness demonstrated the limitation of using the RDCB test to measure brittle adhesive response by significantly over predicting the test force-displacement response. The difference between the model prediction and experiment was due to the assumption of stable crack growth in the RDCB analysis and the filtering required to analyze the RDCB tests.
- Unlike the models of the characterization tests, in models of SLS testing the EMC model performed only slightly better than the *MAT_240 models (12.8% *vs*. 14.0% average difference to test data, respectively) due to large deformation of the adherends, which

exerted a strong influence on the overall force-displacement and rotation-displacement response.

- The characterization methodology developed in this work led to the development of an improved CZM formulation, which demonstrated significant improvements in the ability to model adhesive joints of various bond line thicknesses under Mode I, Mode II and mixed modes of loading.

7.2 Future Work

Aside from extending the approach outlined in this study to characterize and model more adhesive systems, one area that warrants further investigation is the effect of elevated loading rate on traction-separation response. While the specimen geometries developed in this work were designed to be amenable for high-rate testing through the use of specimens with low mass, such experiments were not carried out in the current work. Using the specimens developed in this work under high-rate loading could provide full traction-separation responses across a range of loading rates, quantifying the rate sensitivity of toughened structural adhesives. This high-rate characterization information could then be incorporated in the EMC model and, potentially, the interaction between bond line thickness and loading rate, which has not been thoroughly investigated in the literature.

A deeper investigation of the adhesive joint softening response between the onset of softening and failure with the BSS and MM specimens may result in an improved unloading response in the SLS tests. This work would involve additional high-speed imaging to better understand the rapid unloading behavior observed experimentally.

Further experimental investigation into the brittle response measured using thin bond line RDCB specimens would be beneficial to better understand this behaviour and to potentially identify the brittle-to-ductile transition bond line thickness. Updates to the CZM modelling approach to capture this effect would also be useful, in order to expand the range of materials that could take advantage of the CZM approach, from materials exhibiting only ductile failure, to those that exhibit rapid failure, such as neat epoxy resins.

Finally, the RDCB, BSS, and MM specimens developed in this work could be used to investigate the effect of environmental and manufacturing factors such as temperature, humidity, effects of over and under curing, *etc.*, on the traction-separation response of structural adhesives. This information is of great interest in automotive applications due to the uncertainty these factors impart to the overall response of components that experience a wide variety of in-service environments.

References

3M (2016). "3M™ Impact Resistant Structural Adhesive – Technical Data", Available on-line: https://multimedia.3m.com/mws/media/1467016O/07333-irsa-technical-data-sheet.pdf, Accessed Feb 13, 2019.

3M (2018). "3M™ Safety Data Sheet - 3M™ Impact Resistant Structural Adhesive", Available on-line: https://multimedia.3m.com/mws/mediawebserver?mwsId=SSSSSuUn_zu8l00xmxm9PYtxmv70k17zHvu9lxtD7SSSSSS--, Accessed Feb 13, 2019.

Adams, R. D., & Coppendale, J. (1976). Measurement of the elastic moduli of structural adhesives by a resonant bar technique. *Journal of Mechanical Engineering Science*, 18(3), 149-158.

Adams, R.D. & Coppendale, J. (1979). The Stress-Strain Behaviour of Axially- Loaded Butt Joints, *The Journal of Adhesion*, 10(*1*), 49-62.

Alfano, G., & Crisfield, M. (2001). Finite element interface models for the delamination analysis of laminated composites: mechanical and computational issues. *International journal for numerical methods in engineering*, 50(7), 1701-1736.

Álvarez, D., Blackman, B. R. K., Guild, F. J., & Kinloch, A. J. (2014). Mode I fracture in adhesively-bonded joints: A mesh-size independent modelling approach using cohesive elements. *Engineering Fracture Mechanics*, 115, 73-95.

Anderson, T. L. (2017). *Fracture mechanics: fundamentals and applications*. CRC press.

Arcan, M., Hashin, Z. A., & Voloshin, A. (1978). A method to produce uniform plane-stress states with applications to fiber-reinforced materials. *Experimental mechanics*, 18(4), 141-146.

Arenas, J. M., Narbón, J. J., & Alía, C. (2010). Optimum adhesive thickness in structural adhesives joints using statistical techniques based on Weibull distribution. *International Journal of Adhesion and Adhesives*, 30(3), 160-165.

ASME (2006). Guide for Verification and Validation in Computational Solid Mechanics. ASME PTC V&V 10 - 2006. ASME Committee PTC 60.

ASTM B831 (2014). B831-10. Standard Test Method for Shear Testing of Thin Aluminum Alloy Products. Annual Book of ASTM Standards. ASTM International.

ASTM D638 (2014). D695-10. Standard Test Method for Tensile Properties of Plastics. Annual Book of ASTM Standards. ASTM International.

ASTM D695 (2010). D695-10. Standard Test Method for Compressive Properties of Rigid Plastics. Annual Book of ASTM Standards. ASTM International.

ASTM D907 (2005). D907-12a. Standard Terminology of Adhesives. Annual Book of ASTM Standards. ASTM International.

ASTM D1002 (2005). D1002-05. Standard Test Method for Apparent Shear Strength of Single-Lap-Joint Adhesively Bonded Metal Specimens by Tension Loading (Metal-to- Metal). Annual Book of ASTM Standards. ASTM International.

ASTM D2095 (2015). D2095-96. Standard Test Method for Tensile Strength of Adhesives by Means of Bar and Rod Specimens. Annual Book of ASTM Standards. ASTM International

ASTM D3165 (2007). D3165–07. Standard Test Method for Strength Properties of Adhesives in Shear by Tension Loading of Single-Lap-Joint Laminated Assemblies. Annual Book of ASTM Standards. ASTM International.

ASTM D3433 (2012). D3433-99 - Standard Test Method for Fracture Strength in Cleavage of Adhesives in Bonded Metal Joints. Annual Book of ASTM Standards. ASTM International.

ASTM D5656 (2010). D5656−10. Standard Test Method for Thick-Adherend Metal Lap-Shear Joints for Determination ofthe Stress-Strain Behavior of Adhesives in Shear by Tension Loading. Annual Book of ASTM Standards. ASTM International.

ASTM E1820 (2015). E1820-15a. Standard Test Method for Measurement of Fracture Toughness. Annual Book of ASTM Standards. ASTM International.Bardelcik, A., Worswick, M. J., & Wells, M. A. (2014). *The influence of martensite, bainite and ferrite on the as-quenched constitutive response of simultaneously quenched and deformed boron steel–Experiments and model*. Materials & Design, 55, 509-525.

Avalle, M., Peroni, L., Peroni, M., & Scattina, A. (2010). Bi-material joining for car body structures: experimental and numerical analysis. *The Journal of Adhesion*, 86(5-6), 539-560.

Banea, M. D., Rosioara, M., Carbas, R. J. C., & Da Silva, L. F. M. (2018). Multi-material adhesive joints for automotive industry. *Composites Part B: Engineering*, 151, 71-77.

Barenblatt, G. I. (1962). The mathematical theory of equilibrium cracks in brittle fracture. In *Advances in applied mechanics* (Vol. 7, pp. 55-129). Elsevier.

Barrett, J. D., & Foschi, R. O. (1977). Mode II stress-intensity factors for cracked wood beams. *Engineering Fracture Mechanics*, 9(2), 371-378.

Bascom, W. D., & Cottington, R. L. (1976). Effect of temperature on the adhesive fracture behavior of an elastomer-epoxy resin. *The Journal of Adhesion*, 7(4), 333-346.

Becker, M. C., Salvatore, P., & Zirpoli, F. (2005). The impact of virtual simulation tools on problem-solving and new product development organization. *Research Policy, 34*(9), 1305-1321.

Benzeggagh, M. L., & Kenane, M. (1996). Measurement of mixed-mode delamination fracture toughness of unidirectional glass/epoxy composites with mixed-mode bending apparatus. *Composites science and technology*, 56(4), 439-449.

Biel, A., & Stigh, U. (2010). Damage and plasticity in adhesive layer: an experimental study. *International journal of fracture*, 165(1), 93-103.

Blackman, B. R. K., Hadavinia, H., Kinloch, A. J., Paraschi, M., & Williams, J. G. (2003a). The calculation of adhesive fracture energies in mode I: revisiting the tapered double cantilever beam (TDCB) test. *Engineering Fracture Mechanics*, 70(2), 233-248.

Blackman, B. R. K., Kinloch, A. J., Paraschi, M., & Teo, W. S. (2003b). Measuring the mode I adhesive fracture energy, GIC, of structural adhesive joints: the results of an international round-robin. *International journal of adhesion and adhesives*, 23(4), 293-305.

Brown, D., & Christian, W. (2011). Simulating what you see: combining computer modeling with video analysis. In *8th International Conference on Hands on Science*. Ljubljana, Slovenija.

Bryant, R. W., & Dukes, W. A. (1964). Bonding threaded joints(Shear strength of planar cemented joints, compared with failing torque of threaded joints, bonded with various thread cements). *Engineering Materials and Design*, 7, 170-172.

Bucknall, C. B., & Yoshii, T. (1978). Relationship between structure and mechanical properties in rubber-toughened epoxy resins. *British Polymer Journal*, 10(1), 53-59.

Camanho, P. P., Davila, C. G., & De Moura, M. F. (2003). Numerical simulation of mixed-mode progressive delamination in composite materials. *Journal of composite materials*, 37(16), 1415-1438.

Campilho, R. D., Banea, M. D., Pinto, A. M., da Silva, L. F., & De Jesus, A. M. P. (2011). Strength prediction of single-and double-lap joints by standard and extended finite element modelling. *International Journal of Adhesion and Adhesives*, 31(5), 363-372.

Chai, H. (1988). Shear fracture. *International Journal of Fracture*, 37(2), 137-159.

Chandra, N., Li, H., Shet, C., & Ghonem, H. (2002). Some issues in the application of cohesive zone models for metal–ceramic interfaces. *International Journal of Solids and Structures*, 39(10), 2827-2855.

Chaves, F. J., Da Silva, L. F. M., De Moura, M. F. S. F., Dillard, D. A., & Esteves, V. H. C. (2014). Fracture mechanics tests in adhesively bonded joints: a literature review. *The Journal of Adhesion*, 90(12), 955-992.

Choupani, N. (2008). Mixed-mode cohesive fracture of adhesive joints: Experimental and numerical studies. *Engineering fracture mechanics*, 75(15), 4363-4382.

Chow, C. L., Woo, C. W., & Sykes, J. L. (1979). On the determination and application of COD to epoxy-bonded aluminium joints. *The Journal of Strain Analysis for Engineering Design*, 14(2), 37-42.

Cognard, J. Y., Créac'hcadec, R., Sohier, L., & Davies, P. (2008). Analysis of the nonlinear behavior of adhesives in bonded assemblies—Comparison of TAST and Arcan tests. *International Journal of Adhesion and Adhesives*, 28(8), 393-404.

Cognard, J. Y., Davies, P., Gineste, B., & Sohier, L. (2005). Development of an improved adhesive test method for composite assembly design. *Composites Science and Technology*, 65(3-4), 359-368.

Conklin, J., Beals, R., and Brown, Z., (2015) "BIW Design and CAE," SAE Technical Paper 2015-01-0408, doi:10.4271/2015-01-0408

da Silva, L. F., & Campilho, R. D. (2012). *Advances in numerical modelling of adhesive joints* (pp. 1-93). Springer Berlin Heidelberg.

da Silva, L. F., da Silva, R. A. M., Chousal, J. A. G., & Pinto, A. M. G. (2008). Alternative methods to measure the adhesive shear displacement in the thick adherend shear test. *Journal of Adhesion Science and Technology*, 22(1), 15-29.

da Silva, L. F., Dillard, D. A., Blackman, B., & Adams, R. D. (Eds.). (2012). *Testing adhesive joints: best practices*. Weinheim, Germany: John Wiley & Sons.

Dastjerdi, A. K., Pagano, M., Kaartinen, M. T., McKee, M. D., & Barthelat, F. (2012). Cohesive behavior of soft biological adhesives: experiments and modeling. *Acta Biomaterialia*, 8(9), 3349-3359.

Dastjerdi, A. K., Tan, E., & Barthelat, F. (2013). Direct measurement of the Cohesive Law of adhesives using a rigid double cantilever beam technique. *Experimental Mechanics*, 53(9), 1763-1772.

Dassault Systèmes. (2008). Abaqus Analysis User's Manual Volume IV: Elements - Version 6.8. Simulia Corp. Providence, RI, USA.

DeLollis, N. J. (1970). *Adhesives for metals: theory and technology*. New York, NY: Industrial Press.

De Moura, M. F. S. F., Gonçalves, J. P. M., Chousal, J. A. G., & Campilho, R. D. S. G. (2008). Cohesive and continuum mixed-mode damage models applied to the simulation of the mechanical behaviour of bonded joints. *International Journal of adhesion and Adhesives*, *28*(8), 419-426.

Dolev, G., & Ishai, O. (1981). Mechanical characterization of adhesive layer in-situ and as bulk material. *The Journal of Adhesion*, 12(4), 283-294.

Dugdale, D. S. (1960). Yielding of steel sheets containing slits. *Journal of the Mechanics and Physics of Solids*, 8(2), 100-104.

ESI Group. (2016). Virtual Performance Solution 2016 Solver Reference Manual. ESI Group, Paris, France.

EU Parliament, (2014) 'amending Regulation (EC) No 443/2009 to define the modalities for reaching the 2020 target to reduce CO2 emissions from new passenger cars', http://eur-lex.europa.eu/legal-content/EN/TXT/PDF/?uri=CELEX:32014R0333&from=EN, accessed Aug. 7, 2015

García, J. A., Chiminelli, A., García, B., Lizaranzu, M., & Jiménez, M. A. (2011). Characterization and material model definition of toughened adhesives for finite element analysis. *International Journal of Adhesion and Adhesives*, 31(4), 182-192.

Gardner, K. A. (2013). Experimental Techniques for Shear Testing of Thin Sheet Metals and Compression Testing at Intermediate Strain Rates (Doctoral dissertation, The Ohio State University).

Goded, M. (2009). Sustainable Production Technologies of Emission reduced Lightweight car concepts (SuperLIGHT-CAR) Integrated Project - Publishable Final Activity Report. Available on-line: http://cordis.europa.eu/publication/rcn/12428_en.html. Accessed May 16, 2016.

Goglio, L., Peroni, L., Peroni, M., & Rossetto, M. (2008). High strain-rate compression and tension behaviour of an epoxy bi-component adhesive. *International journal of adhesion and adhesives*, 28(7), 329-339.

Goncalves, J. P. M., De Moura, M. F. S. F., & De Castro, P. M. S. T. (2002). A three-dimensional finite element model for stress analysis of adhesive joints. *International Journal of Adhesion and Adhesives*, 22(5), 357-365.

Gong, X. J., & Benzeggagh, M. (1995). Mixed mode interlaminar fracture toughness of unidirectional glass/epoxy composite. In Composite Materials: Fatigue and Fracture: Fifth Volume. ASTM International.

Greenhalgh, E. S., Rogers, C., & Robinson, P. (2009). Fractographic observations on delamination growth and the subsequent migration through the laminate. *Composites Science and Technology, 69*(14), 2345-2351.

Griffith, A. A. (1921). The phenomena of rupture and flow in solids. *Philosophical Transactions of the Royal Society of London*. A221, 163-198.

Guess, T. R., Allred, R. E., & Gerstle, F. P. (1977). Comparison of lap shear test specimens. *Journal of Testing and Evaluation*, 5(2), 84-93.

Hallquist, J. O. (2017a). LS-DYNA Theory Manual. Livermore Software Technology Corporation.

Hallquist, J. O. (2017b). LS-DYNA Keyword User's Manual Volume II – Material Models. Livermore Software Technology Corporation.

Hillerborg, A., Modéer, M., & Petersson, P. E. (1976). Analysis of crack formation and crack growth in concrete by means of fracture mechanics and finite elements. *Cement and concrete research*, 6(6), 773-781.

Högberg, J. L., & Stigh, U. (2006). Specimen proposals for mixed mode testing of adhesive layer. *Engineering fracture mechanics*, 73(16), 2541-2556.

Ikegami, K., Fujii, T., Kawagoe, H., Kyogoku, H., Motoie, K., Nohno, K., & Yoshida, F. (1996). Benchmark tests on adhesive strengths in butt, single and double lap joints and double-cantilever beams. *International journal of adhesion and adhesives*, 16(4), 219-226.

IIHS (Insurance Institute for Highway Safety), (2009) "New crash tests demonstrate the influence of vehicle size and weight on safety in crashes; results are relevant to fuel economy policies", Available on-line: http://www.iihs.org/iihs/news/desktopnews/new-crash-tests-demonstrate-the-influence-of-vehicle-size-and-weight-on-safety-in-crashes-results-are-relevant-to-fuel-economy-policies, accessed June 28, 2016.

IIHS (Insurance Institute for Highway Safety), (2014) "Moderate Overlap Frontal Crashworthiness Evaluation Crash Test Protocol (Version XV)", http://www.iihs.org/iihs/ratings/technical-information/technical-protocols, accessed Aug. 7, 2015.

Irwin, G. R. (1956). Onset of fast crack propagation in high strength steel and aluminum alloys. *Sagamore Research Conference Proceedings*, 2, 289-305.

Johnson, G.R. and W.H. Cook, "A Constitutive Model and Data for Metals Subjected to Large Strains, High Strain Rates and High Temperatures." *Proceedings of the Seventh International Symposium on Ballistics*, 541-547, The Hague, The Netherlands, April 1983.

Karac, A., Blackman, B. R. K., Cooper, V., Kinloch, A. J., Sanchez, S. R., Teo, W. S., & Ivankovic, A. (2011). Modelling the fracture behaviour of adhesively-bonded joints as a function of test rate. *Engineering Fracture Mechanics*, 78(6), 973-989.

Kinloch, A. J. (2003). Toughening epoxy adhesives to meet today's challenges. *MRS bulletin*, 28(06), 445-448.

Kinloch, A. J., & Shaw, S. J. (1981) The Fracture Resistance of a Toughened Epoxy Adhesive, *The Journal of Adhesion*, 12(1), 59-77.

Kinloch, A. J., Shaw, S. J., Tod, D. A., & Hunston, D. L. (1983). Deformation and fracture behaviour of a rubber-toughened epoxy: 1. Microstructure and fracture studies. *Polymer*, 24(*10*), 1341-1354.

Kinloch, A.J. & Young, R.J. (1983). *Fracture Behaviour of Polymers*. London, UK: Elsevier Science Publishers Ltd.

Lasdon, L. S., Waren, A. D., Jain, A., & Ratner, M. (1978). Design and testing of a generalized reduced gradient code for nonlinear programming. *ACM Transactions on Mathematical Software* (TOMS), 4(1), 34-50.

Liao, C.H., Watson, B., Worswick, M.J, & Cronin, D.S. (2017) "Mode I RDCB Test and Analysis Incorporating Adhesive Compliance Applied to Structural Adhesives", 2017 Conference and Exposition on Experimental and Applied Mechanics, Indianapolis, USA

Lißner, M., Alabort, E., Cui, H., Rito, R., Blackman, B. R. K., & Petrinic, N. (2019). Experimental characterisation and numerical modelling of the influence of bondline thickness, loading rate, and

deformation mode on the response of ductile adhesive interfaces. *Journal of the Mechanics and Physics of Solids*, 130, 349-369.

Littell, J. D., Ruggeri, C. R., Goldberg, R. K., Roberts, G. D., Arnold, W. A., & Binienda, W. K. (2008). Measurement of epoxy resin tension, compression, and shear stress–strain curves over a wide range of strain rates using small test specimens. *Journal of Aerospace Engineering*, 21(3), 162-173.

Liu, K., & Piggott, M. R. (1998). Fracture failure processes in polymers. I: Mechanical tests and results. *Polymer Engineering & Science*, 38(*1*), 60-68.

Liu, Z., Gibson, R. F., & Newaz, G. M. (2002). The use of a modified mixed mode bending test for characterization of mixed-mode fracture behavior of adhesively bonded metal joints. *The Journal of Adhesion*, 78(3), 223-244.

Lopes, R. M., Campilho, R. D. S. G., da Silva, F. J. G., & Faneco, T. M. S. (2016). Comparative evaluation of the Double-Cantilever Beam and Tapered Double-Cantilever Beam tests for estimation of the tensile fracture toughness of adhesive joints. *International Journal of Adhesion and Adhesives*, 67, 103-111.

LS-DYNA Aerospace Working Group. (2012). 'Modeling Guidelines Document'. Available on-line: awg.lstc.com/tiki/tiki-download_file.php?fileId=167, accessed Aug. 12, 2016.

Marzi, S. (2012). Measuring the critical energy release rate in mode II of tough, structural adhesive joints using the tapered end-notched flexure (TENF) test. *The European Physical Journal Special Topics*, 206(1), 35-40.

Marzi, S., Hesebeck, O., Brede, M., & Kleiner, F. (2009). An end-loaded shear joint (ELSJ) specimen to measure the critical energy release rate in mode II of tough, structural adhesive joints. *Journal of Adhesion Science and Technology*, 23(15), 1883-1891.

Marzi, S., Hesebeck, O., Brede, M., & Kleiner, F. (2009b). A rate-dependent, elasto-plastic cohesive zone mixed-mode model for crash analysis of adhesively bonded joints. In *7th European LS-DYNA conference*.

May, M., Hesebeck, O., Marzi, S., Böhme, W., Lienhard, J., Kilchert, S., ... & Hiermaier, S. (2015). Rate dependent behavior of crash-optimized adhesives–Experimental characterization, model development, and simulation. *Engineering Fracture Mechanics*, 133, 112-137.

Meyers, M.A. (1994). *Dynamic Behaviour of Materials*. John Wiley & Sons, Inc.

Meschke, J., Tölle, J., & Berger, L. (2017). Multi-material concept for a battery electric vehicle. *ATZ Worldwide*, 119(11), 48-53.

Meschut, G., Janzen, V., & Olfermann, T. (2014). Innovative and highly productive joining technologies for multi-material lightweight car body structures. *Journal of materials engineering and performance*, 23(5), 1515-1523.

Morin, D., Haugou, G., Bennani, B., & Lauro, F. (2010). Identification of a new failure criterion for toughened epoxy adhesive. *Engineering fracture mechanics*, 77(17), 3481-3500.

Neumayer, J., Kuhn, P., Koerber, H., & Hinterhölzl, R. (2016). Experimental determination of the tensile and shear behaviour of adhesives under impact loading. *The Journal of Adhesion*, 92(7-9), 503-516.

NHTSA (National Highway Traffic Safety Administration), (2015) "New Car Assessment Program (NCAP) – Request for comments." Docket NHTSA-2015-0119, Available on-line: https://www.regulations.gov/document?D=NHTSA-2015-0119-000, accessed June 29, 2016.

Natural Resources Canada (2015) 'Fuel Consumption Testing', https://www.nrcan.gc.ca/energy/efficiency/transportation/cars-light-trucks/buying/7491, accessed Aug. 7, 2015.

Packham, D. E. (2018). Theories of fundamental adhesion. Handbook of adhesion technology, 11-41.

Palmonella, M., Friswell, M. I., Mottershead, J. E., & Lees, A. W. (2005). Finite element models of spot welds in structural dynamics: review and updating. *Computers & structures*, 83(8-9), 648-661.

Peirs, J., Verleysen, P., & Degrieck, J. (2012). Novel technique for static and dynamic shear testing of Ti6Al4V sheet. *Experimental mechanics*, 52(7), 729-741.

Plueddemann, E. P. (1991). Nature of adhesion through silane coupling agents. In *Silane coupling agents* (pp. 115-152). Springer, Boston, MA.

Pujol, S. (2010). Multi-material adhesive joining in the automotive sector. In *Structural Connections for Lightweight Metallic Structures*. (pp. 195-217). Eds. Moreira, P., da Silva, L., de Castro, P. Springer, Berlin, Heidelberg.

Purslow, D. (1986). Matrix fractography of fibre-reinforced epoxy composites. *Composites, 17*(4), 289-303.

Rahmaan, T., Butcher, C., Abedini, A., & Worswick, M. (2015). Effect of strain rate on shear properties and fracture characteristics of DP600 and AA5182-O sheet metal alloys. In *EPJ web of conferences* (Vol. 94, p. 01033). EDP Sciences.

Ren, D., Liu, L., & Li, Y. (2012). Investigation on overlap joining of AZ61 magnesium alloy: laser welding, adhesive bonding, and laser weld bonding. *The International Journal of Advanced Manufacturing Technology*, *61*(1-4), 195-204

Ripling, E. J., Mostovoy, S., & Patrick, R. L. (1964). Application of fracture mechanics to adhesive joints. In *Adhesion*. ASTM International.

Roache, P. J. (1994). Perspective: a method for uniform reporting of grid refinement studies. *Journal of fluids engineering*, 116(3), 405-413.

Roache, P. J. (1997). Quantification of uncertainty in computational fluid dynamics. *Annual review of fluid Mechanics*, 29(1), 123-160.

Roache, P. J. (1998). Verification of codes and calculations. *AIAA journal*, 36(5), 696-702.

Rocha, R. J. B., & Campilho, R. D. S. G. (2018). Evaluation of different modelling conditions in the cohesive zone analysis of single-lap bonded joints. *The Journal of Adhesion*, 94(7), 562-582.

Siemens AG. (2016). NX Nastran 11 Release Guide. Siemens PLM, Plano, TX, USA.

Sørensen, B. F., & Jacobsen, T. K. (2003). Determination of cohesive laws by the J integral approach. Engineering fracture mechanics, 70(14), 1841-1858.

Spaggiari, A., & E. Dragoni. (2013). Effect of Mechanical Surface Treatment on the Static Strength of Adhesive Lap Joints. *Journal of Adhesion* 89(9): 677–96.

Thrall, E. W., & Shannon, R. W. (1985). *Adhesive bonding of aluminum alloys*. New York, NY: Marcel Dekker, Inc.

Trimino, L. F. (2012). Analysis and performance of adhesively bonded crush tube structures (Master's thesis, University of Waterloo).

Trimino, L. F., & Cronin, D. S. (2016). Evaluation of numerical methods to model structural adhesive response and failure in tension and shear loading. *Journal of Dynamic Behavior of Materials*, 2(1), 122-137.

Tvergaard, V., & Hutchinson, J. W. (1992). The relation between crack growth resistance and fracture process parameters in elastic-plastic solids. *Journal of the Mechanics and Physics of Solids*, 40(6), 1377-1397.

US Federal Register (Environmental Protection Agencey and Department of Transportation), (2012) '2017 and Later Model Year Light-Duty Vehicle Greenhouse Gas Emissions and Corporate Average Fuel Economy Standards; Final Rule' http://www.gpo.gov/fdsys/pkg/FR-2012-10-15/pdf/2012-21972.pdf, accessed Aug. 7, 2014.

Watson, B., Liao, C. H., Worswick, M. J., & Cronin, D. S. (2020a). Mode I traction-separation measured using rigid double cantilever beam applied to structural adhesive. *The Journal of Adhesion*, 96(8), 717-737. doi.org/10.1080/00218464.2018.1502666

Watson, B., Nandwani, Y., Worswick, M. J., & Cronin, D. S. (2019b). Metallic multi-material adhesive joint testing and modeling for vehicle lightweighting. *International Journal of Adhesion and Adhesives*, 95, 102421. https://doi.org/10.1016/j.ijadhadh.2019.102421

Watson, B., Worswick, M. J., & Cronin, D. S. (2019a). Identification of Shear Sample Test Geometry for Bulk Adhesive Characterization. In *Mechanics of Biological Systems & Micro-and Nanomechanics, Volume 4* (pp. 47-50). Springer, Cham. doi.org/10.1007/978-3-319-95062-4_11

Watson, B., Worswick, M. J., & Cronin, D. S. (2020b). Quantification of Mixed Mode Loading and Bond Line Thickness on Adhesive Joint Strength Using Novel Test Specimen Geometry. *The International Journal of Adhesion and Adhesives*, 102**,** 102682. https://doi.org/10.1016/j.ijadhadh.2020.102682

Weissberg, V., & Arcan, M. (1988). A uniform pure shear testing specimen for adhesive characterization. In *Adhesively Bonded Joints: Testing, Analysis*, and Design. ASTM International.

Yee, A. F. & Pearson, R. A. (1986). Toughening mechanisms in elastomer-modified epoxies. *Journal of materials science*, 21(*7*), 2462-2474.

Yokoyama, T. (2003). Experimental determination of impact tensile properties of adhesive butt joints with the split Hopkinson bar. *The Journal of Strain Analysis for Engineering Design*, 38(3), 233-245.

Yokoyama, T., & Shimizu, H. (1998). Determination of impact shear strength of adhesive joints with the split Hopkinson bar. *Key Engineering Materials*, 317-322.

Young, R.J. & Lovell, P.A. (1991) *Introduction to Polymers, 2nd Ed*. London, UK: Chapman & Hall.

Appendix A – Summary of Characterization Testing for CZM Parameter Extraction

A.1 Mode I Response

The parameters extracted from each RDCB test used to define the CZM response throughout this thesis are presented in Table A1, along with the displacement measures for a given set of CZM parameters. The CZM fit and the respective test traction-separation responses are also presented for 0.18 mm (Figure A1), 0.3 mm (Figure A2), and 0.64 mm (Figure A3) nominal bond line thicknesses.

Table A1: CZM parameters extracted from RDCB testing

Test	Bond Line Thickness [mm]	Initial Stiffness [MPa/mm]	Plateau Stress [MPa]	Critical Energy Release Rate [N/mm]	Area Ratio	Plateau Displacement [mm]	Softening Displacement [mm]	Failure Displacement [mm]
7R1	0.200	1941.56	55.49	1.709	0.4950	0.0286	0.0438	0.0464
7R2	0.173	1947.22	52.50	1.935	0.4535	0.0270	0.0437	0.0570
7R3	0.211	3755.09	47.50	1.330	0.6040	0.0126	0.0296	0.0391
7R4	0.171	2365.15	53.50	1.419	0.5050	0.0226	0.0360	0.0396
7R5	0.153	2570.21	55.77	1.597	0.5001	0.0217	0.0360	0.0429
7R6	0.231	2952.02	55.50	1.424	0.4750	0.0188	0.0310	0.0391
12R1	0.312	1622.62	48.50	2.181	0.5146	0.0299	0.0530	0.0668
12R2	0.309	2009.27	45.50	2.097	0.6350	0.0226	0.0519	0.0629
12R3	0.323	1928.56	51.50	1.974	0.4441	0.0267	0.0437	0.0596
12R4	0.309	1918.63	48.50	2.028	0.5450	0.0253	0.0481	0.0608
12R5	0.311	1648.42	53.59	2.172	0.4250	0.0325	0.0497	0.0638
12R6	0.309	1442.33	59.82	2.298	0.3647	0.0415	0.0555	0.0628
25R1	0.619	1338.30	42.50	2.030	0.5050	0.0318	0.0559	0.0714
25R2	0.623	1112.27	52.01	2.416	0.3345	0.0468	0.0623	0.0774
25R3	0.628	1089.01	51.32	2.118	0.1350	0.0471	0.0527	0.0770
25R4	0.629	1274.66	47.50	2.129	0.4050	0.0373	0.0554	0.0715
25R5	0.627	1392.56	49.50	2.425	0.4350	0.0355	0.0569	0.0767
25R6	0.630	1348.96	49.50	2.176	0.3750	0.0367	0.0532	0.0714

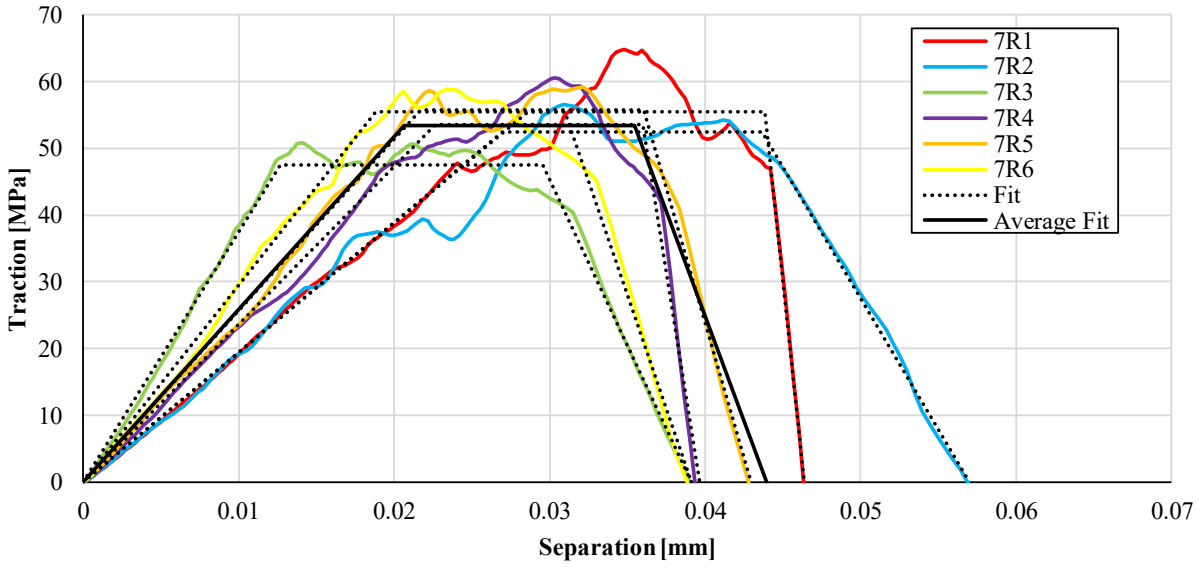

Figure A1: RDCB test results and flat CZM fit (including average) for 0.18 mm nominal bond line thickness specimens

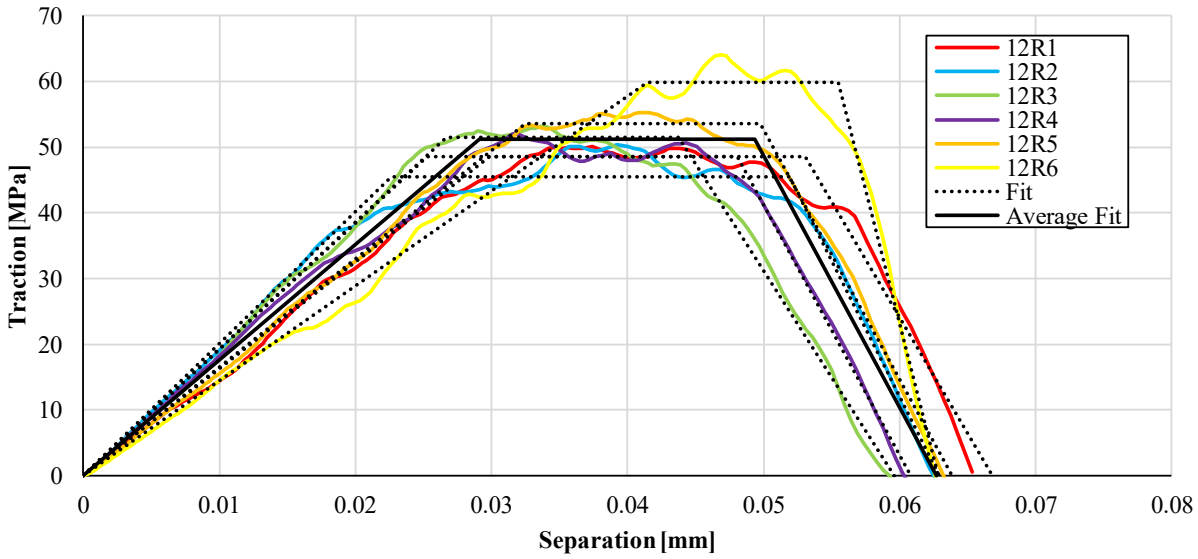

Figure A2: RDCB test results and flat CZM fit (including average) for 0.3 mm nominal bond line thickness specimens

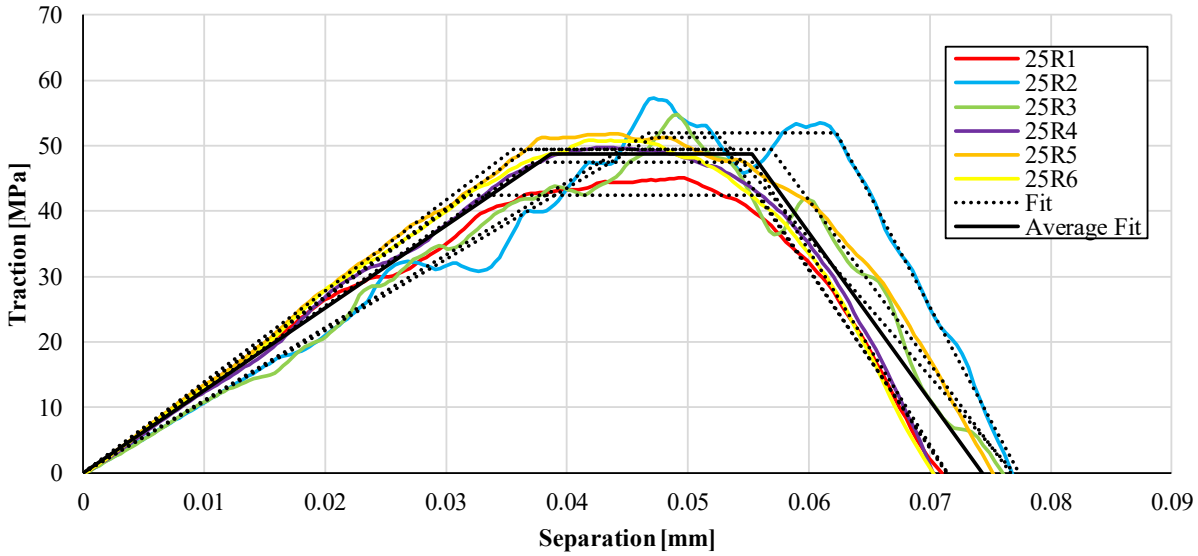

Figure A3: RDCB test results and flat CZM fit (including average) for 0.64 mm nominal bond line thickness specimens

A.2 Mode II Response

The parameters extracted from each BSS test used to define the *MAT_240 model described in Chapter 5 are presented in Table A2, along with the displacement measures for a given set of CZM parameters. The CZM fit and the respective test traction-separation response are also presented for 0.18 mm (Figure A4), 0.3 mm (Figure A5), and 0.64 mm (Figure A6) nominal bond line thicknesses.

Table A2: CZM parameters extracted from bonded shear testing

Test	Bond Line Thickness [mm]	Initial Stiffness [MPa/mm]	Plateau Stress [MPa]	Critical Energy Release Rate [N/mm]	Area Ratio	Plateau Displacement [mm]	Softening Displacement [mm]	Failure Displacement [mm]
7B1	0.169	1900.06	27.94	3.893	0.9157	0.0147	0.1423	0.1511
7B2	0.219	3000.55	32.57	5.603	0.9685	0.0109	0.1775	0.1775
7B3	0.245	2340.86	29.59	5.839	0.9400	0.0126	0.1982	0.2092
7B4	0.196	2911.11	29.64	5.325	0.9634	0.0102	0.1833	0.1863
7B5	0.194	3287.92	31.22	4.869	0.9696	0.0095	0.1607	0.1607
7B6								
12B7	0.340	1908.46	28.36	6.097	0.9577	0.0149	0.2208	0.2241
12B8	0.421	1542.37	28.58	7.241	0.9498	0.0185	0.2591	0.2661
12B9								
12B10	0.371	1813.54	28.97	7.427	0.9644	0.0160	0.2632	0.2654
12B11	0.415	2628.56	29.12	8.113	0.9522	0.0111	0.2764	0.2919
12B12	0.363	1507.66	27.82	7.525	0.9659	0.0185	0.2797	0.2797
25B1	0.554	801.10	25.70	12.916	0.9681	0.0321	0.5186	0.5186
25B2	0.597	618.28	25.01	13.706	0.9175	0.0404	0.5433	0.5933
25B3	0.605	723.49	25.64	13.311	0.9596	0.0354	0.5336	0.5402
25B4	0.580	738.97	26.25	13.947	0.9645	0.0355	0.5480	0.5503
25B5	0.550	709.87	25.78	13.474	0.9653	0.0363	0.5408	0.5408
25B6	0.622	968.23	25.47	14.783	0.9563	0.0263	0.5814	0.6058

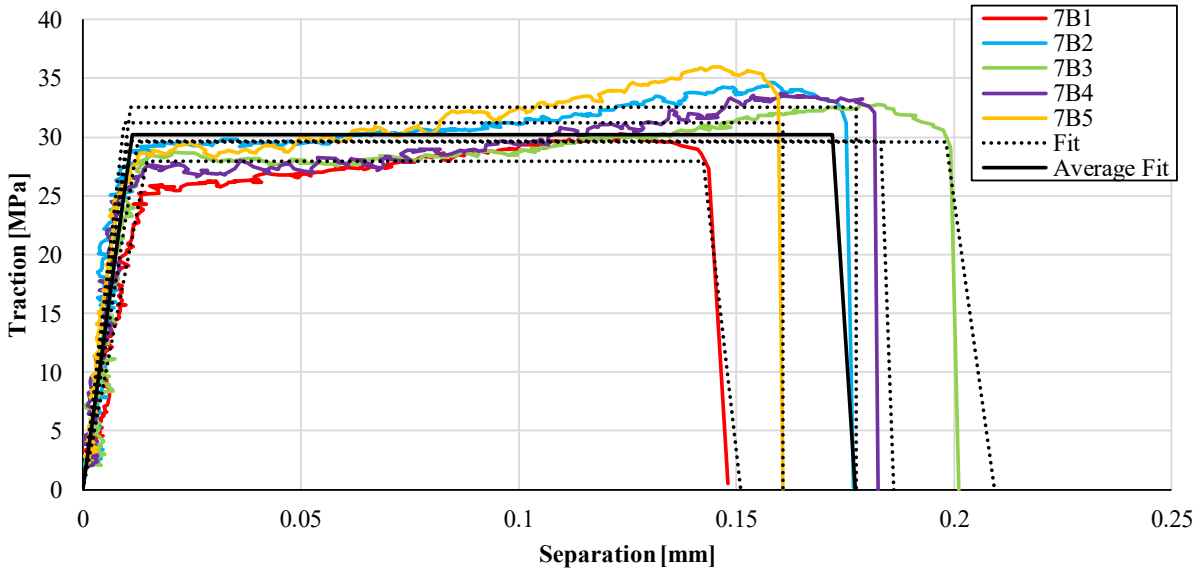

Figure A4: Bonded shear test results and flat CZM fit (including average) for 0.18 mm nominal bond line thickness specimens

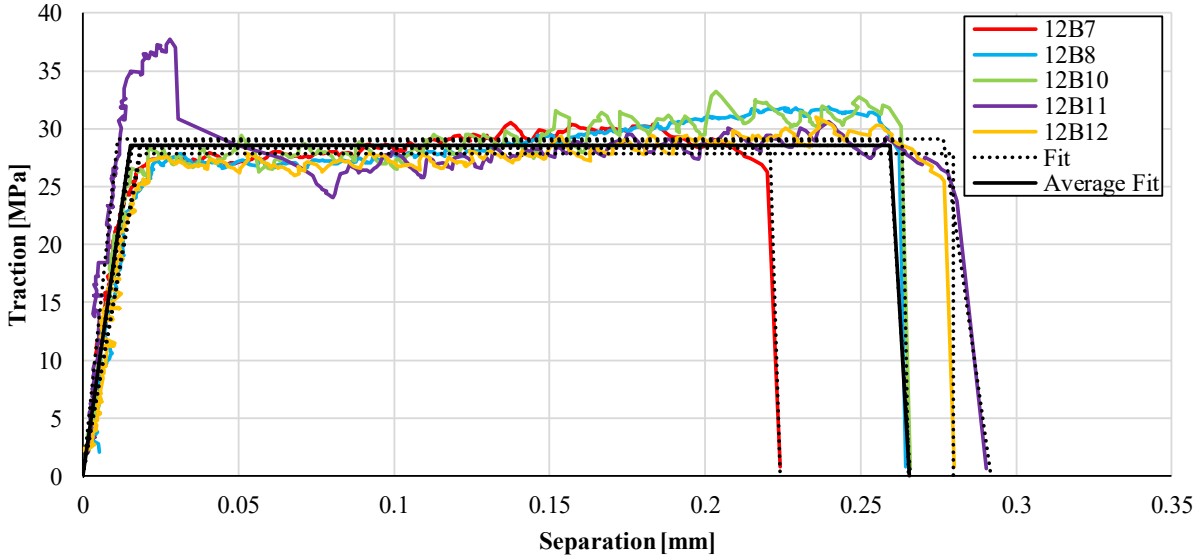

Figure A5: Bonded shear test results and flat CZM fit (including average) for 0.3 mm nominal bond line thickness specimens

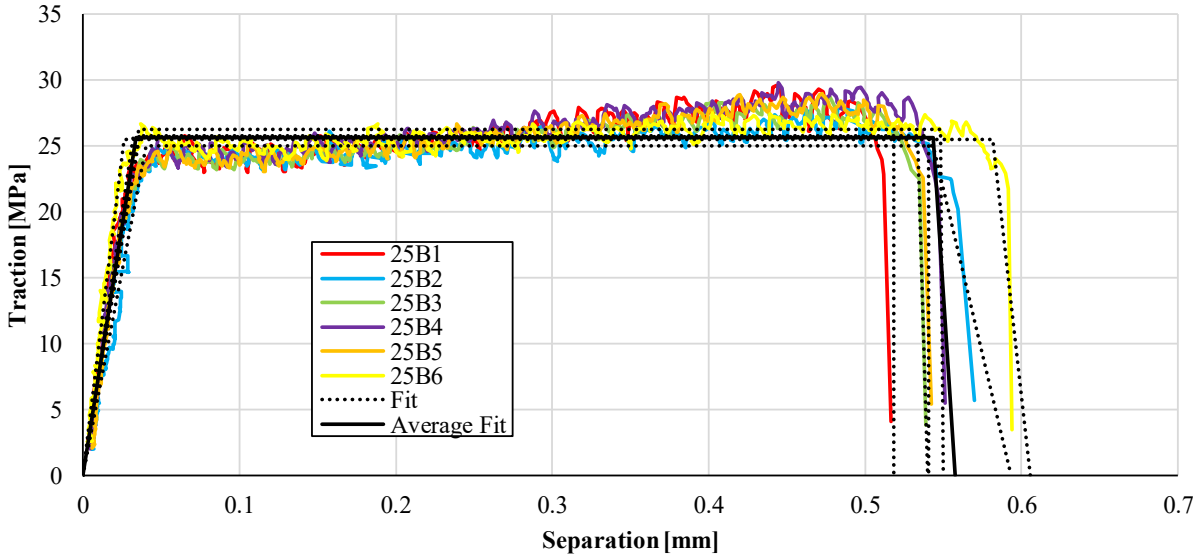

Figure A6: Bonded shear test results and flat CZM fit (including average) for 0.64 mm nominal bond line thickness specimens

A.3 45º Mixed Mode Response

The parameters extracted from each 45° MM test used to assess the MM response of the adhesive presented in Chapter 4 and Chapter 5 are presented in Table A3, along with the displacement measures for a given set of CZM parameters. The CZM fit and the respective test traction-separation response are also presented for 0.18 mm (Figure A7), 0.3 mm (Figure A8), and 0.64 mm (Figure A9) nominal bond line thicknesses.

Table A3: CZM parameters extracted from 45° mixed mode testing

Test	Bond Line Thickness [mm]	Initial Stiffness [MPa/mm]	Plateau Stress [MPa]	Critical Energy Release Rate [N/mm]	Area Ratio	Plateau Displacement [mm]	Softening Displacement [mm]	Failure Displacement [mm]
7M45-1	0.162	2484.13	29.98	2.284	0.8929	0.0121	0.0801	0.0843
7M45-2	0.222	2550.15	31.64	1.692	0.8744	0.0124	0.0592	0.0602
7M45-3								
7M45-4	0.234	1888.64	31.79	2.147	0.8544	0.0168	0.0745	0.0774
7M45-5	0.217	2740.25	28.59	1.889	0.8836	0.0104	0.0688	0.0738
7M45-6	0.291	2348.51	31.15	2.301	0.8230	0.0133	0.0741	0.0869
12M45-1	0.281	1265.39	32.25	2.474	0.8339	0.0255	0.0895	0.0895
12M45-2	0.316	2246.77	31.76	2.253	0.8932	0.0141	0.0775	0.0785
12M45-3								
12M45-4	0.359	2443.52	31.13	2.351	0.8786	0.0127	0.0791	0.0847
12M45-5	0.308	1926.14	33.79	1.789	0.7631	0.0175	0.0579	0.0655
12M45-6	0.379	2991.71	28.97	3.280	0.9573	0.0097	0.1181	0.1181
25M45-1	0.583	1106.70	28.91	4.024	0.7427	0.0261	0.1295	0.1750
25M45-2	0.601	1504.06	28.87	3.120	0.8697	0.0192	0.1132	0.1221
25M45-3	0.601	1118.37	28.69	3.305	0.8422	0.0257	0.1227	0.1334
25M45-4								
25M45-5	0.579	1472.23	28.07	3.729	0.8383	0.0191	0.1304	0.1543
25M45-6	0.651	1009.77	26.74	2.816	0.8178	0.0265	0.1126	0.1245

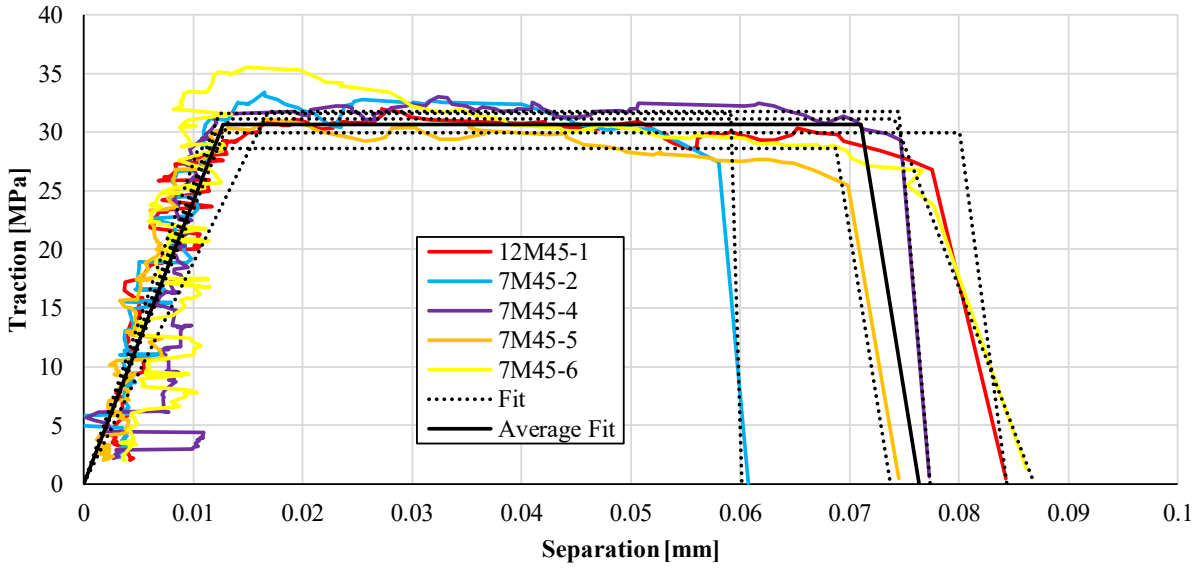

Figure A7: 45º mixed mode test results and flat CZM fit (including average) for 0.18 mm nominal bond line thickness specimens

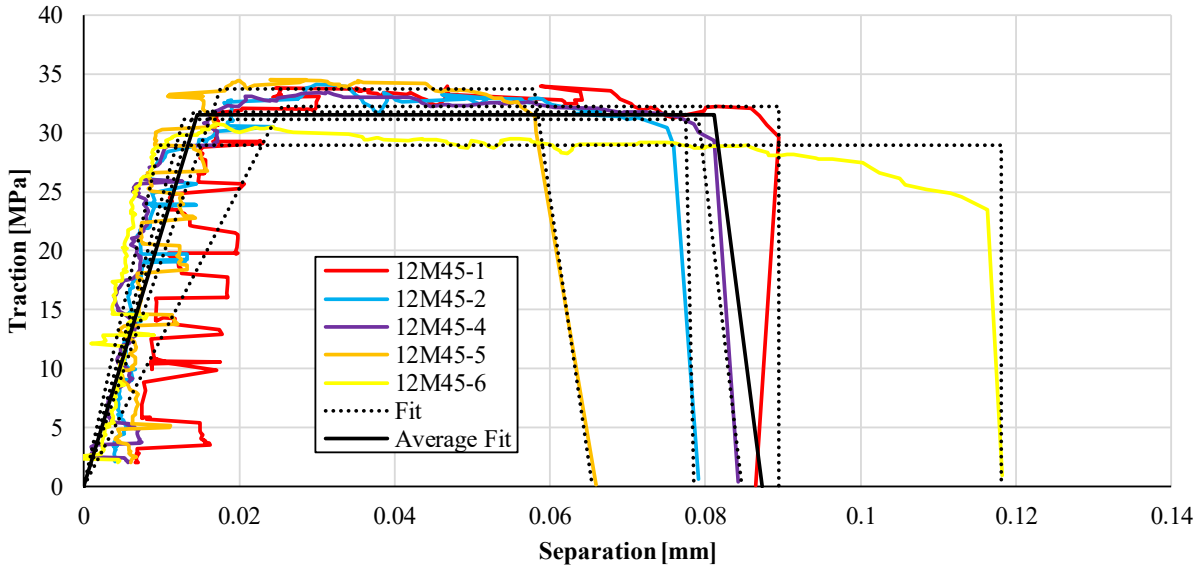

Figure A8: 45º mixed mode test results and flat CZM fit (including average) for 0.3 mm nominal bond line thickness specimens

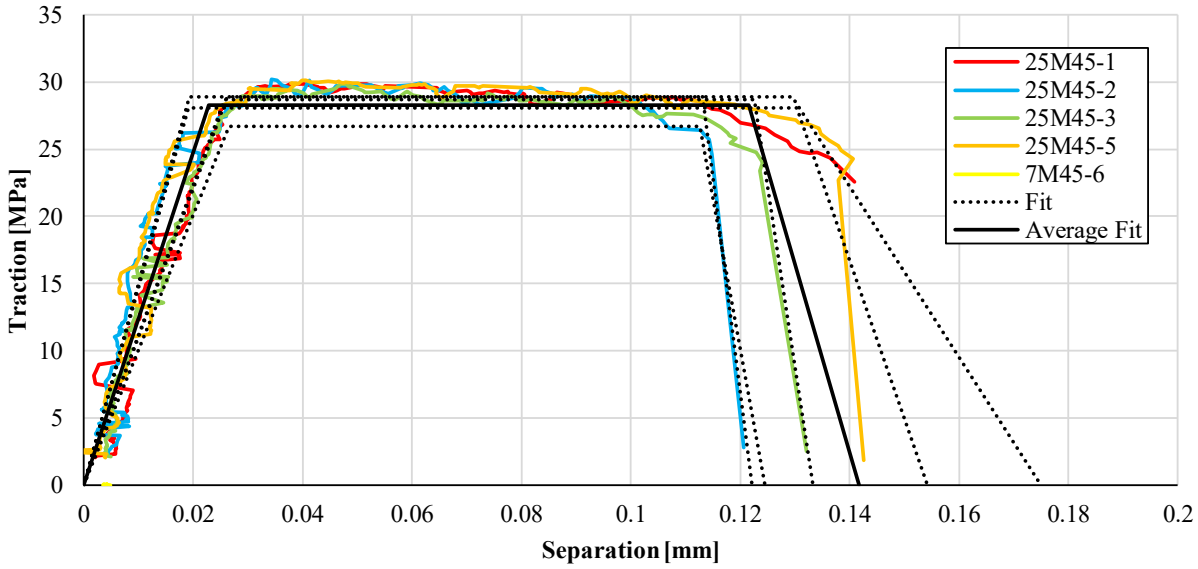

Figure A9: 45º mixed mode test results and flat CZM fit (including average) for 0.64 mm nominal bond line thickness specimens

A.4 75º Mixed Mode Response

The parameters extracted from each 75º MM test used to assess the MM response of the adhesive presented in Chapter 4 and Chapter 5 are presented in Table A4, along with the displacement measures for a given set of CZM parameters. The CZM fit and the respective test traction-separation response are also presented for 0.18 mm (Figure A10), 0.3 mm (Figure A11), and 0.64 mm (Figure A12) nominal bond line thicknesses.

Table A4: CZM parameters extracted from 75º mixed mode testing

Test	Bond Line Thickness [mm]	Initial Stiffness [MPa/mm]	Plateau Stress [MPa]	Critical Energy Release Rate [N/mm]	Area Ratio	Plateau Displacement [mm]	Softening Displacement [mm]	Failure Displacement [mm]
7M75-1	0.214	2483.20	26.45	5.336	0.9517	0.0107	0.2026	0.2115
7M75-2	0.277	2556.99	26.93	6.072	0.9264	0.0105	0.2194	0.2421
7M75-3	0.213	2749.78	27.58	3.893	0.9645	0.0100	0.1462	0.1462
7M75-4	0.270	2722.11	27.62	3.966	0.9640	0.0101	0.1486	0.1487
7M75-5								
7M75-6	0.246	2176.36	26.14	5.795	0.9511	0.0120	0.2229	0.2326
12M75-1								
12M75-2	0.329	2068.69	27.14	6.530	0.9727	0.0131	0.2471	0.2471
12M75-3	0.314	1694.53	27.70	6.668	0.9660	0.0163	0.2489	0.2489
12M75-4	0.348	1422.36	27.76	6.803	0.9446	0.0195	0.2511	0.2587
12M75-5	0.283	1339.57	26.08	5.701	0.9476	0.0195	0.2266	0.2301
12M75-6	0.323	1556.58	24.37	7.906	0.7661	0.0157	0.2642	0.4003
25M75-1	0.620	677.83	24.00	11.342	0.9594	0.0354	0.4887	0.4917
25M75-2	0.577	933.62	25.09	8.993	0.9502	0.0269	0.3674	0.3762
25M75-3	0.620	683.79	24.71	9.320	0.9429	0.0361	0.3918	0.3987
25M75-4	0.621	802.63	26.07	11.318	0.7641	0.0325	0.3642	0.5365
25M75-5	0.634	718.09	25.20	10.627	0.9496	0.0351	0.4355	0.4430
25M75-6	0.599	820.25	23.57	11.775	0.9320	0.0287	0.4943	0.5335

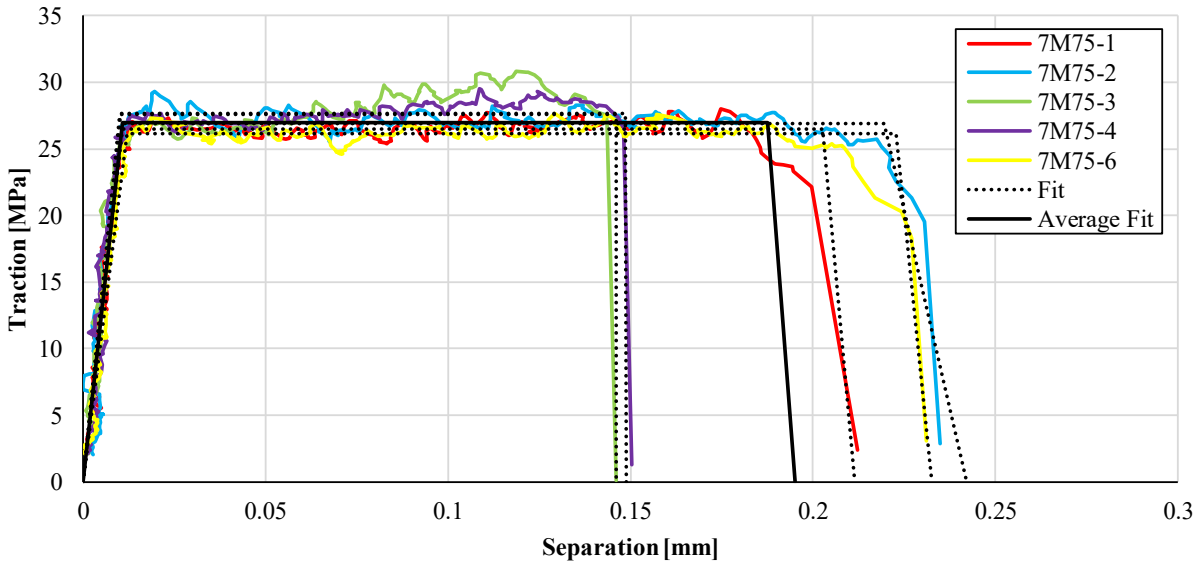

Figure A10: 75º mixed mode test results and flat CZM fit (including average) for 0.18 mm nominal bond line thickness specimens

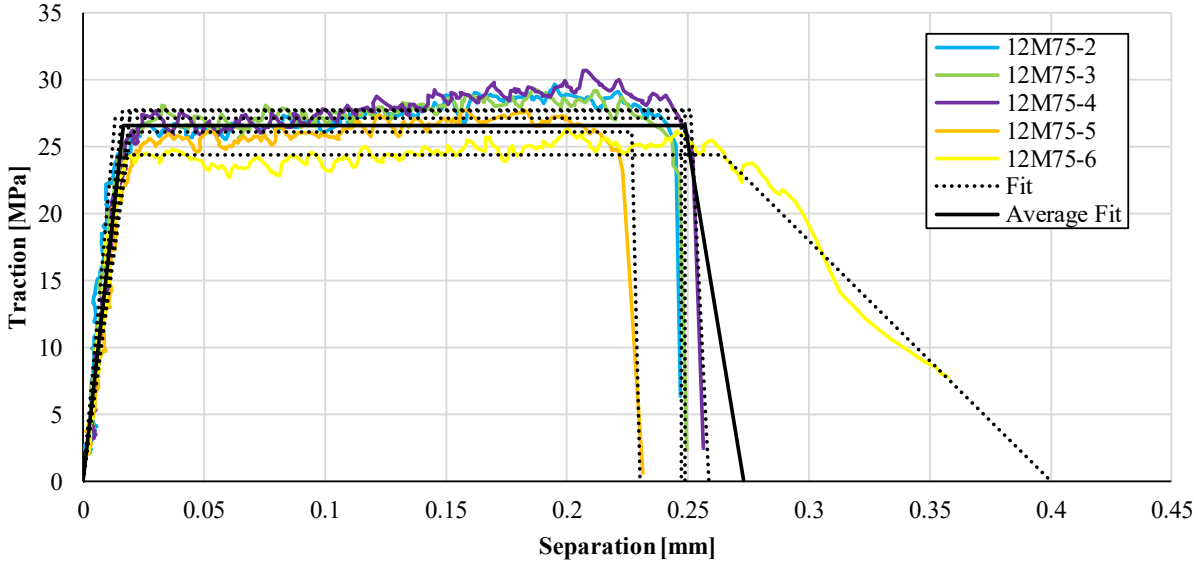

Figure A11: 75º mixed mode test results and flat CZM fit (including average) for 0.3 mm nominal bond line thickness specimens

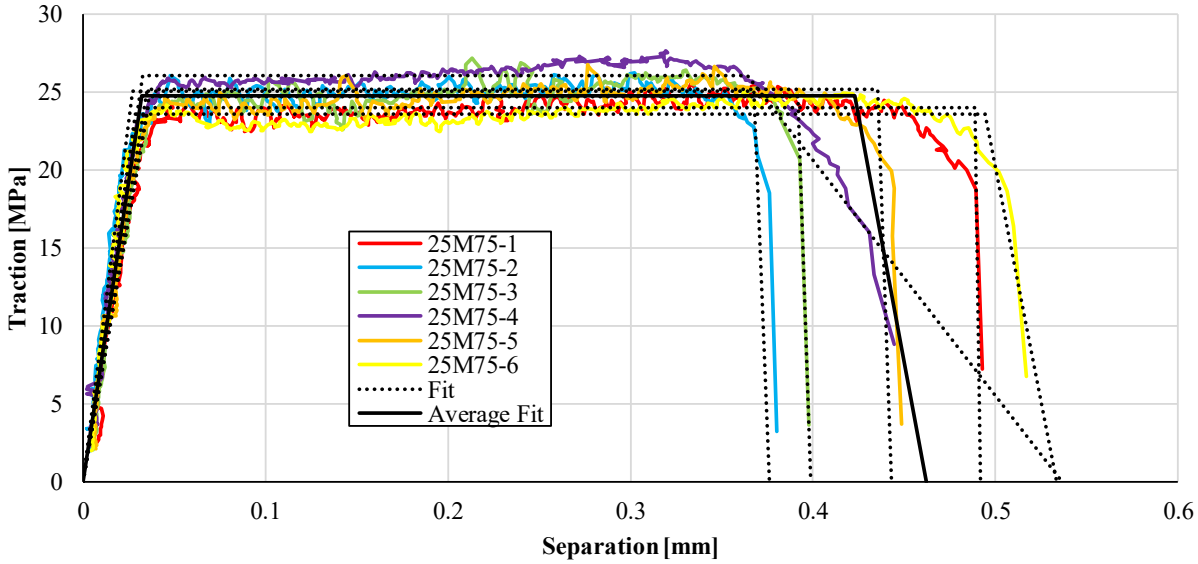

Figure A12: 75º mixed mode test results and flat CZM fit (including average) for 0.64 mm nominal bond line thickness specimens

A.5 Mode II Response – Rising Stress Plateau

The parameters extracted from each BSS test used to define the EMC model (*i.e*. assuming a hardening stress response) are presented in Table A5, along with the displacement measures for a given set of CZM parameters. The CZM fit and the respective test traction-separation response are also presented for 0.18 mm (Figure A13), 0.3 mm (Figure A14), and 0.64 mm (Figure A15) nominal bond line thicknesses.

Table A5: Displacement-hardening CZM parameters extracted from bonded shear tests

Test	Bond Line Thickness [mm]	Initial Stiffness [MPa/mm]	Plateau Stress [MPa]	Critical Energy Release Rate [N/mm]	Area Ratio	Tangent Modulus [MPa/mm]	Plateau Displacement [mm]	Softening Displacement [mm]	Failure Displacement [mm]	Max Stress [Mpa]
7B1	0.169	1926.62	25.34	3.895	0.9322	40.33	0.0132	0.1430	0.1494	30.58
7B2	0.219	2905.37	28.06	5.336	0.9698	39.14	0.0097	0.1750	0.1765	34.53
7B3	0.245	2388.29	26.88	5.836	0.9497	29.54	0.0113	0.1982	0.2070	32.40
7B4	0.196	2919.41	25.84	5.325	0.9634	45.07	0.0089	0.1814	0.1862	33.62
7B5	0.194	3322.98	27.13	4.869	0.9741	58.99	0.0082	0.1585	0.1593	35.99
7B6										
12B7	0.340	1921.47	26.81	6.111	0.9577	16.51	0.0140	0.2193	0.2240	30.20
12B8	0.421	1573.81	25.83	7.336	0.9694	25.14	0.0164	0.2623	0.2631	32.01
12B9										
12B10	0.371	1819.25	26.47	7.443	0.9741	20.95	0.0146	0.2638	0.2638	31.70
12B11	0.415	2732.24	28.44	8.120	0.9818	3.78	0.0104	0.2857	0.2857	29.48
12B12	0.363	1466.07	26.00	7.423	0.9689	15.02	0.0177	0.2752	0.2752	29.87
25B1	0.554	813.55	23.32	12.916	0.9710	10.35	0.0287	0.5142	0.5170	28.34
25B2	0.597	618.90	23.61	13.823	0.9082	6.00	0.0381	0.5381	0.5996	26.61
25B3	0.605	745.08	23.31	13.321	0.9520	9.31	0.0313	0.5264	0.5461	27.92
25B4	0.580	762.19	23.63	13.992	0.9542	10.49	0.0310	0.5387	0.5577	28.96
25B5	0.550	718.47	23.32	13.491	0.9567	10.15	0.0325	0.5317	0.5462	28.39
25B6	0.622	971.20	24.72	15.002	0.9460	3.66	0.0254	0.5772	0.6142	26.73

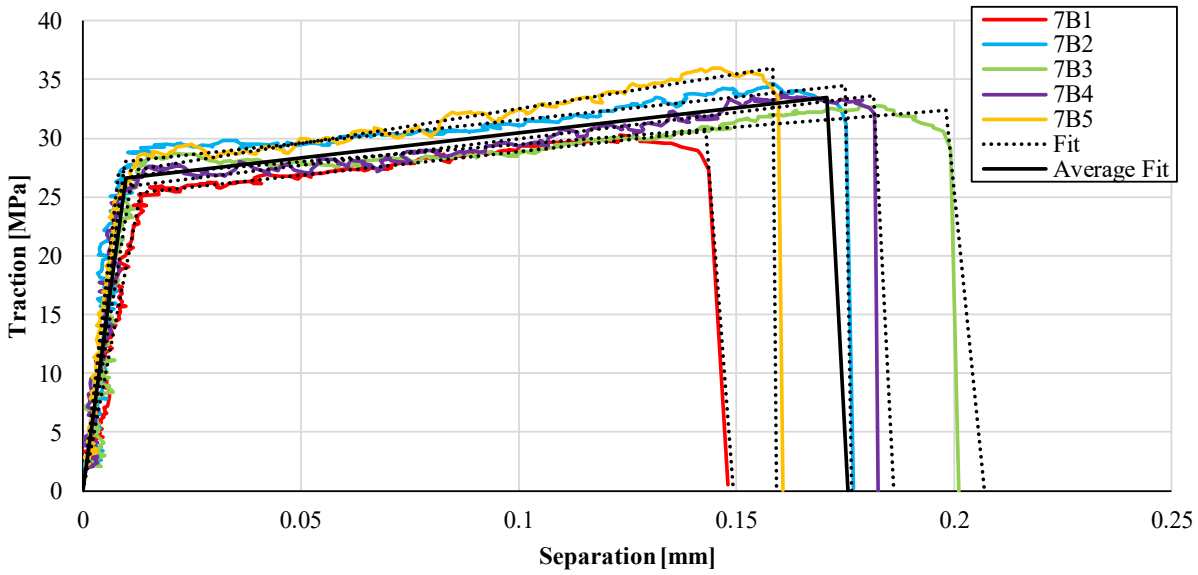

Figure A13: Bonded shear test results and displacement-hardening CZM fit (including average) for 0.18 mm nominal bond line thickness specimens

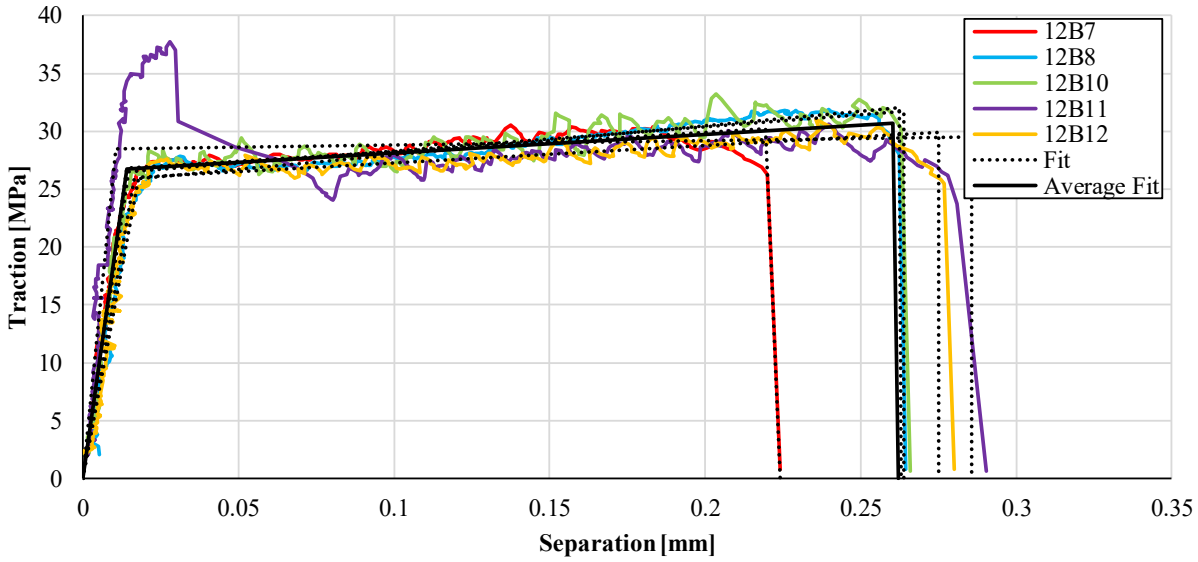

Figure A14: Bonded shear test results and displacement-hardening CZM fit (including average) for 0.3 mm nominal bond line thickness specimens

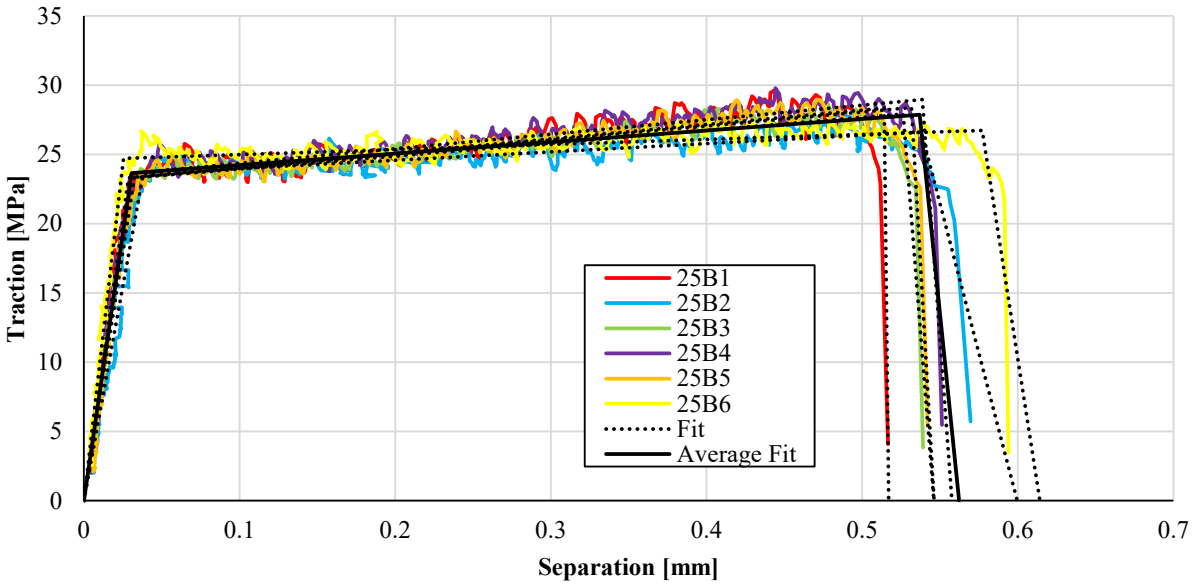

Figure A15: Bonded shear test results and displacement-hardening CZM fit (including average) for 0.64 mm nominal bond line thickness specimens

Appendix B – Single Element Simulation Output of User Defined Cohesive Model

In order to fully assess the robustness of the EMC model developed in this work, a total of 36 load cases were investigated. Broadly speaking, these were based on monotonic loading to failure, load-reload cycles to different portions of the traction-separation response, or load-unload-full reversal loading. These load cases were investigated for various mixity loading modes. Additionally, load cases where additional loading modes were introduced after an initial load, and load cases extracted from various finite element models of ultra-high strength and multi-material tests (see Lui [2019]) were modeled. Cohesive elements with thicknesses of 0.18 mm (Figure B1 to Figure B36), 0.3 mm (Figure B37 to Figure B72) and 0.64 mm (Figure B73 to Figure B108) were used and compared to the response of the *MAT_240 material model discussed in Chapter 5. The loading input for each model was input via prescribed displacement *vs.* time boundary conditions on the top surface of the CZM element while the bottom surface was fixed in all directions. These curves were defined such that failure was generally expected at 1 s of simulation time, although due to changes in mode mixty during the simulation, this may not apply in all cases.

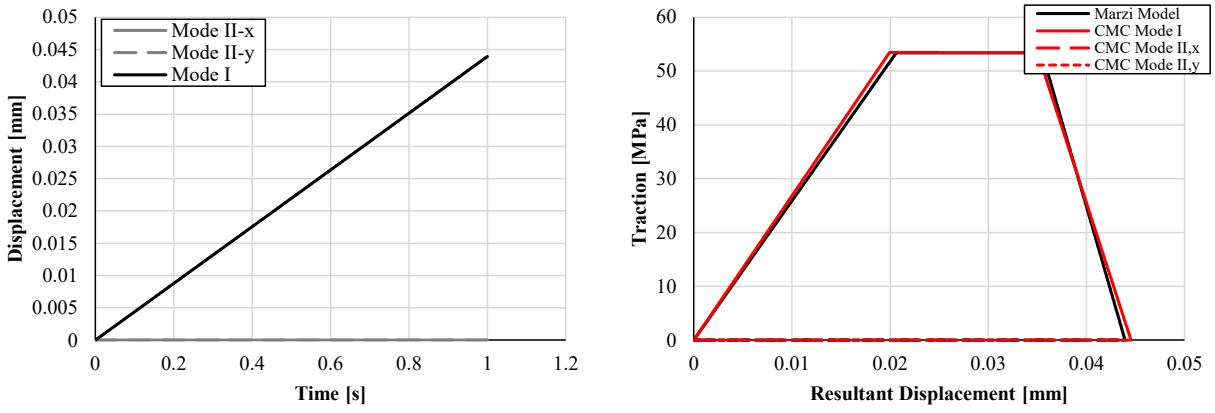

Figure B1: Input (left) and output (right) for Mode I loading for 0.18 mm CZM element

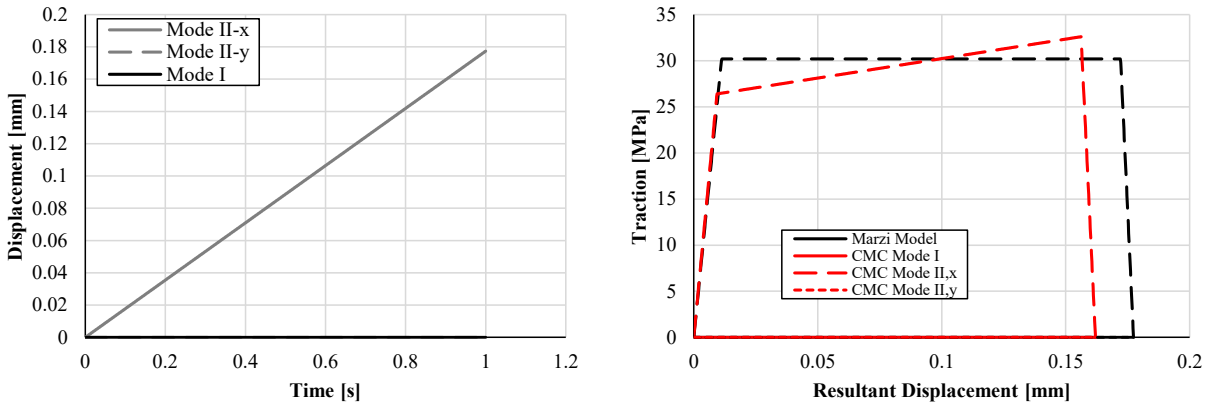

Figure B2: Input (left) and output (right) for Mode II loading for 0.18 mm CZM element

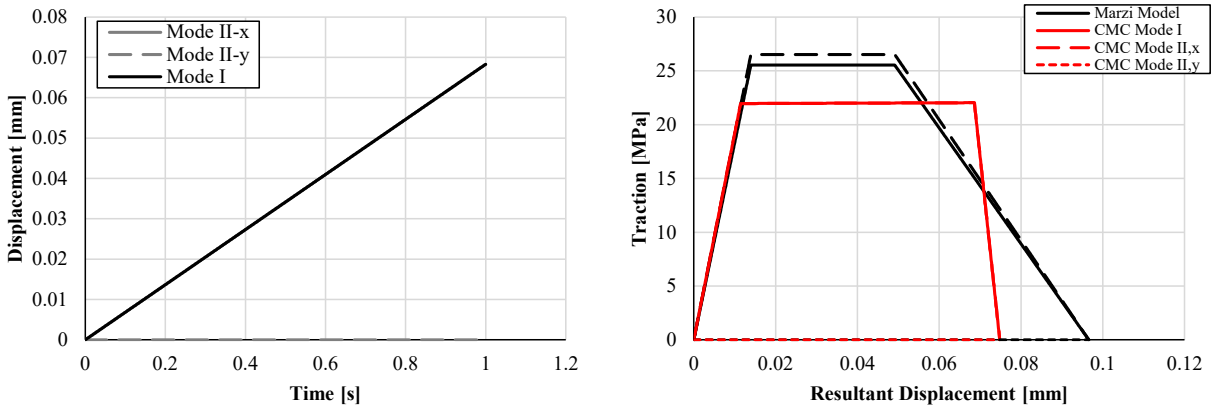

Figure B3: Input (left) and output (right) for 45º mixed mode loading for 0.18 mm CZM element

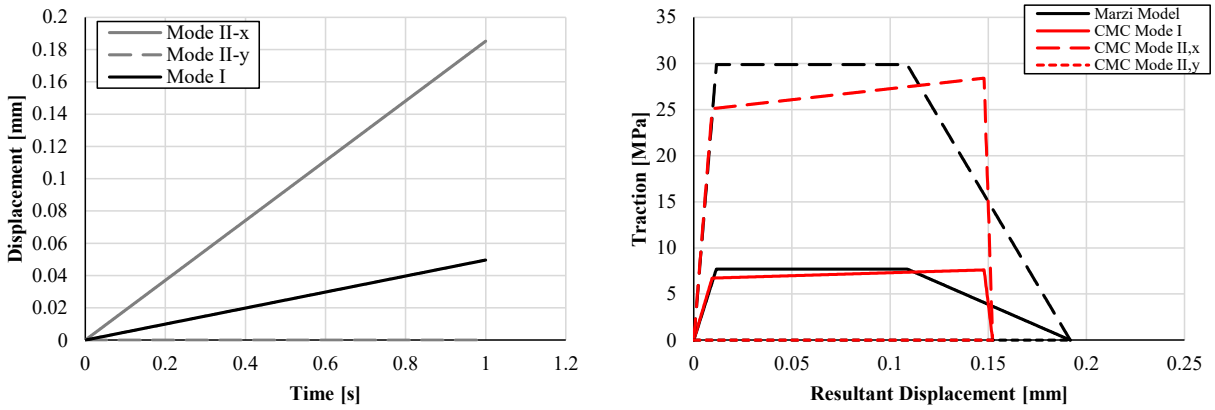

Figure B4: Input (left) and output (right) for 75 º mixed mode loading for 0.18 mm CZM element

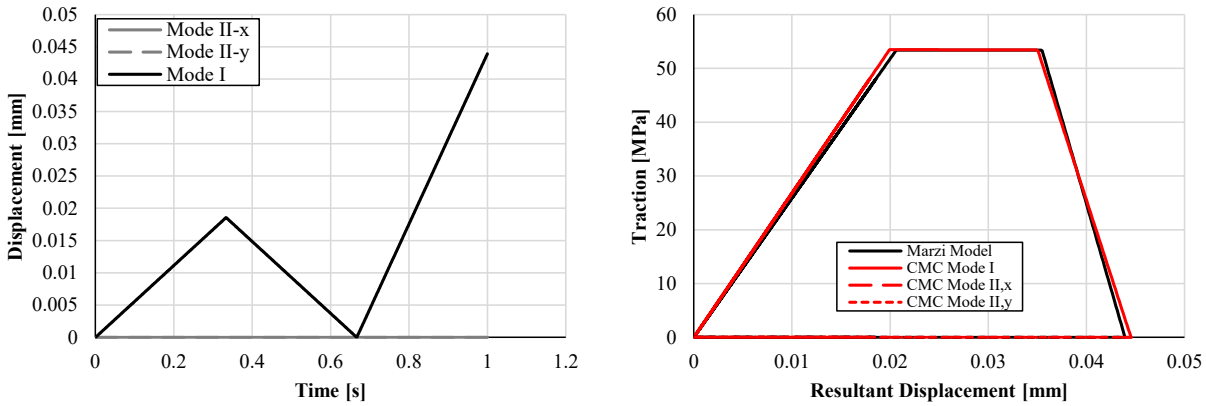

Figure B5: Input (left) and output (right) for Mode I load to segment I-unload-reload to failure cycle for 0.18 mm CZM element

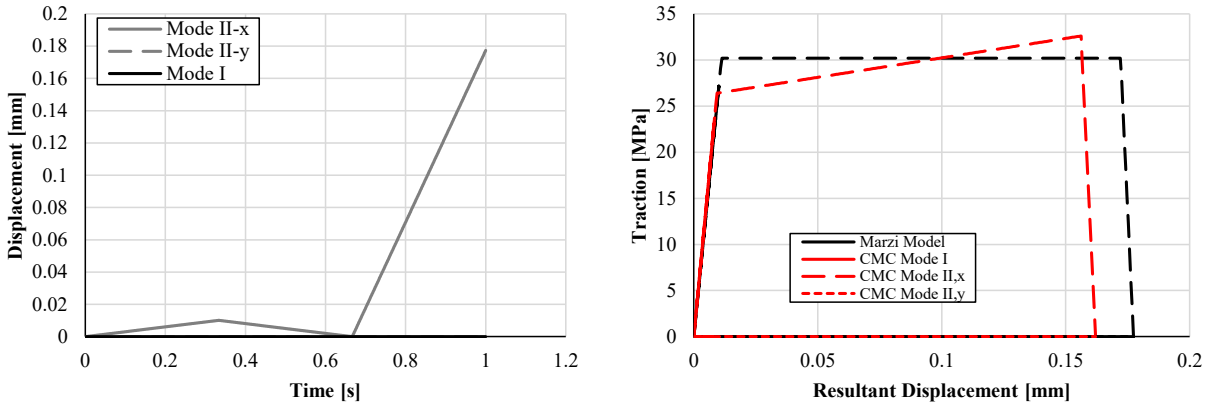

Figure B6: Input (left) and output (right) for Mode II load to segment I-unload-reload to failure cycle for 0.18 mm CZM element

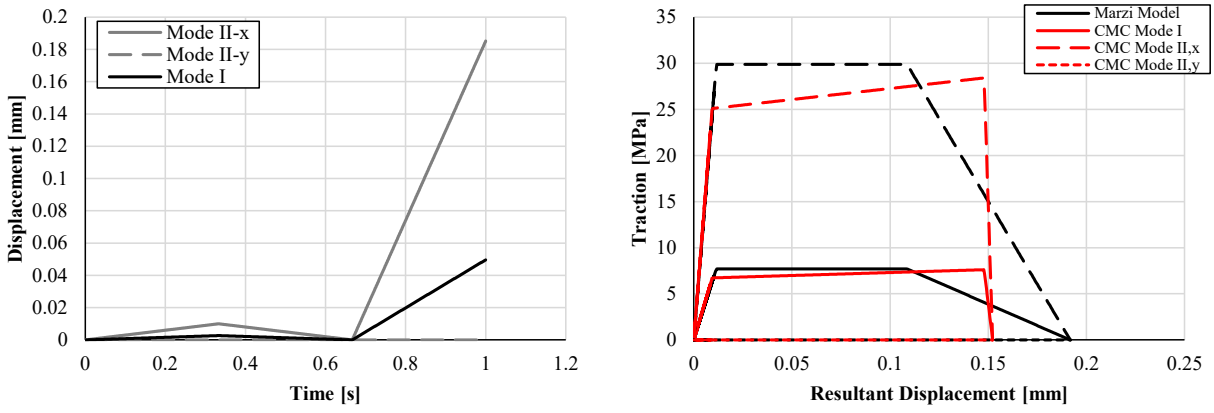

Figure B7: Input (left) and output (right) for 75 º mixed mode load to segment I-unload-reload to failure cycle for 0.18 mm CZM element

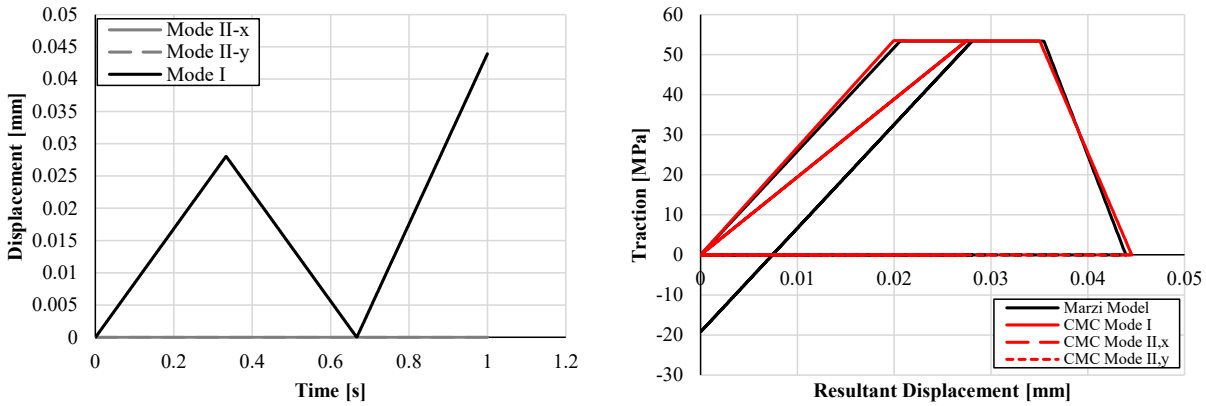

Figure B8: Input (left) and output (right) for Mode I load to segment II-unload-reload to failure cycle for 0.18 mm CZM element

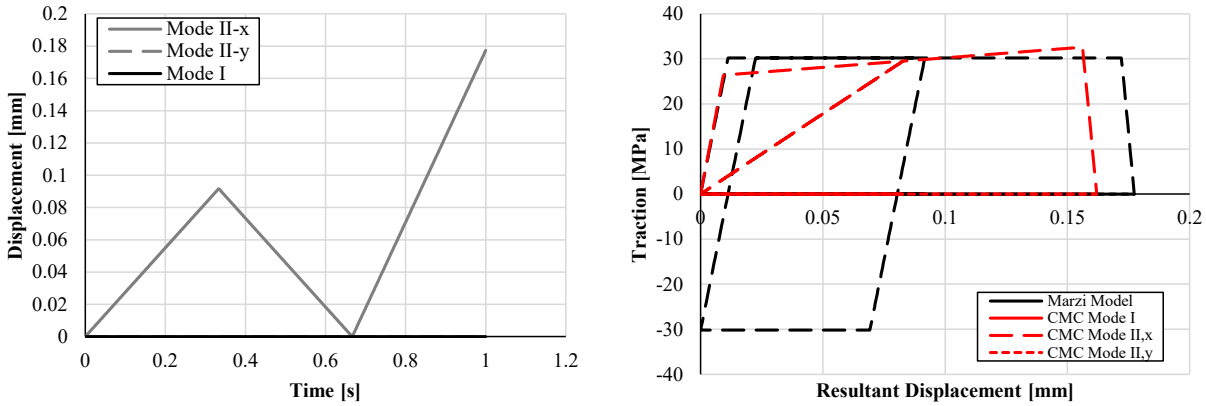

Figure B9: Input (left) and output (right) for Mode II load to segment II-unload-reload to failure cycle for 0.18 mm CZM element

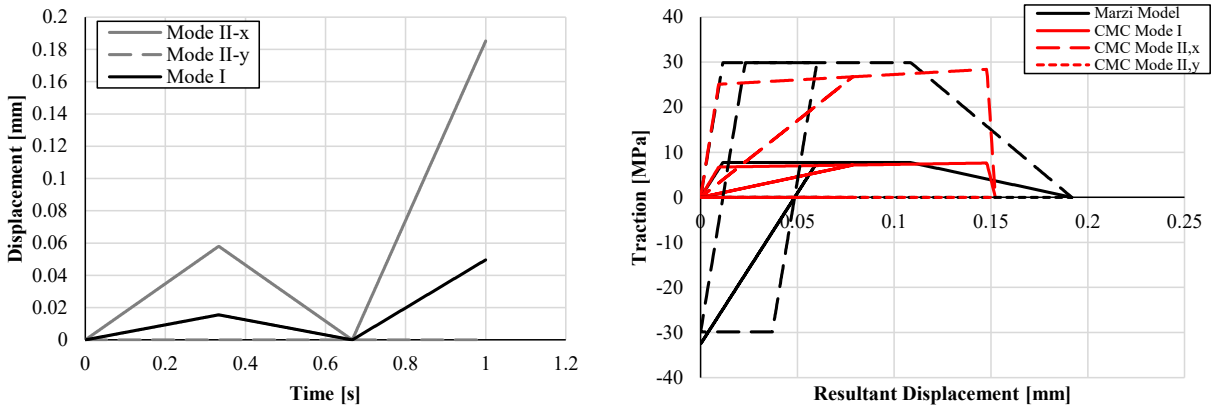

Figure B10: Input (left) and output (right) for 75 º mixed mode load to segment II-unload-reload to failure cycle for 0.18 mm CZM element

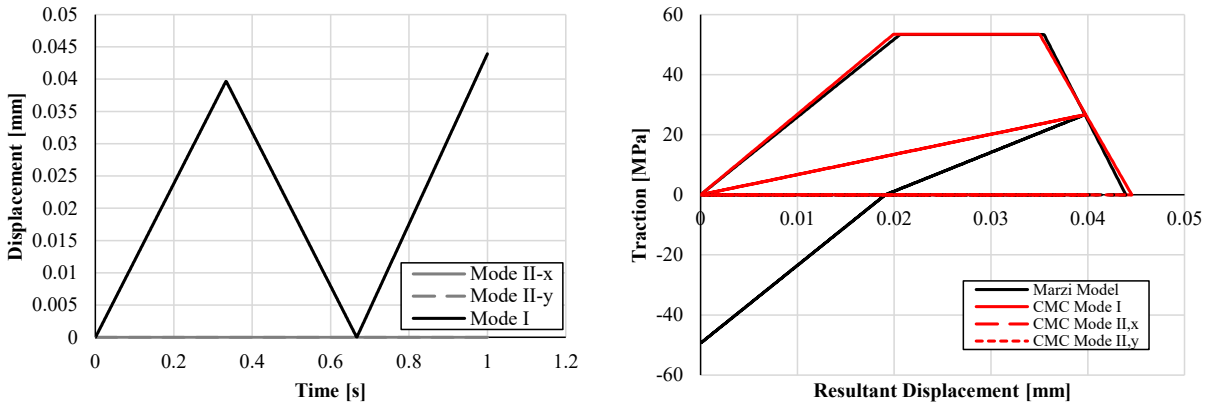

Figure B11: Input (left) and output (right) for Mode I load to segment III-unload-reload to failure cycle for 0.18 mm CZM element

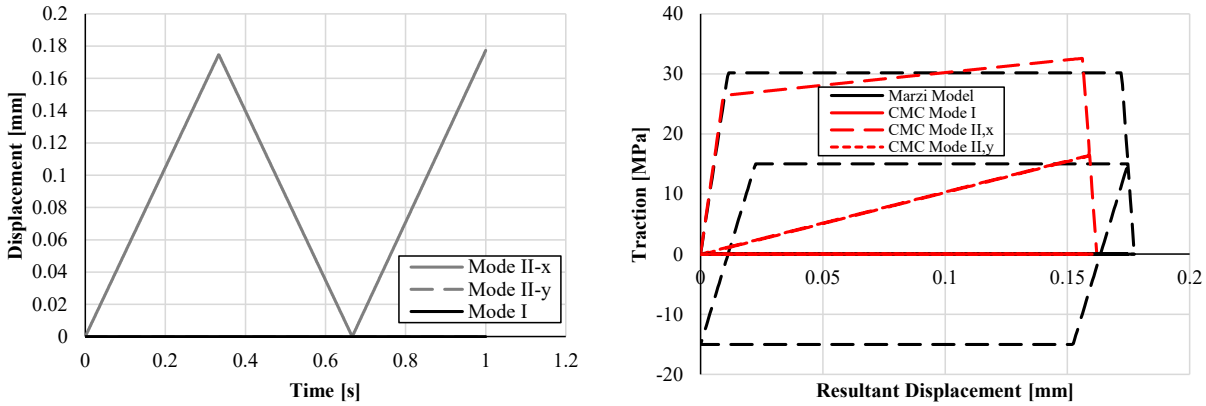

Figure B12: Input (left) and output (right) for Mode II load to segment III-unload-reload to failure cycle for 0.18 mm CZM element

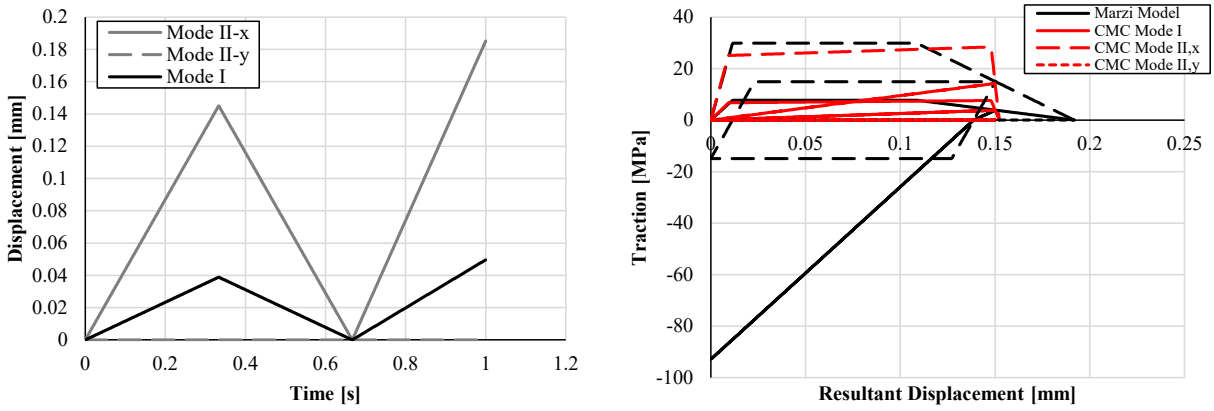

Figure B13: Input (left) and output (right) for 75 º mixed mode load to segment III-unload-reload to failure cycle for 0.18 mm CZM element

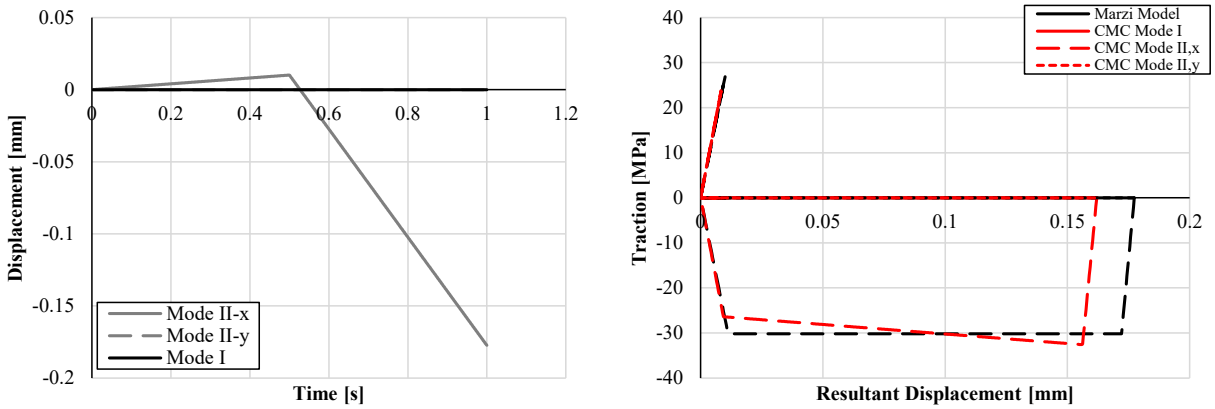

Figure B14: Input (left) and output (right) for Mode II load to segment I-unload-full reversal to failure cycle for 0.18 mm CZM element

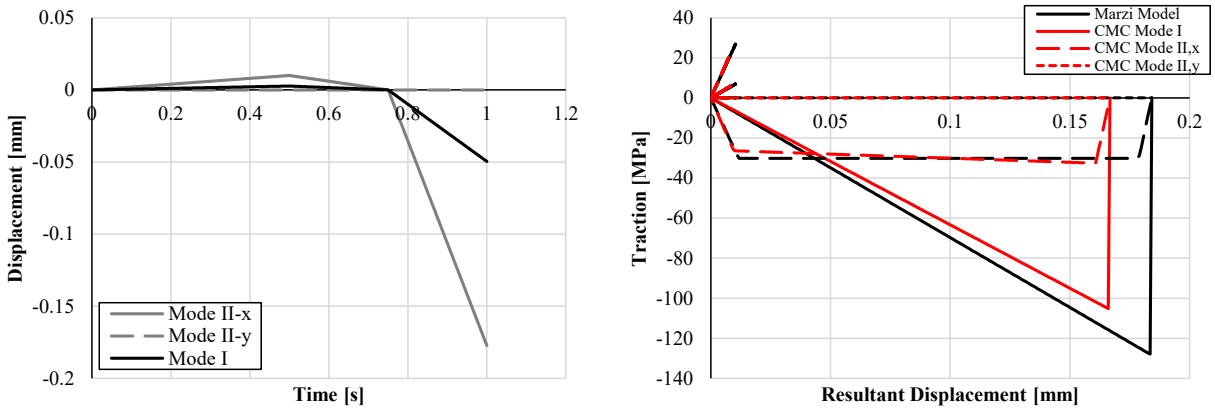

Figure B15: Input (left) and output (right) for 75 º mixed mode load to segment I-unload-full reversal to failure cycle for 0.18 mm CZM element

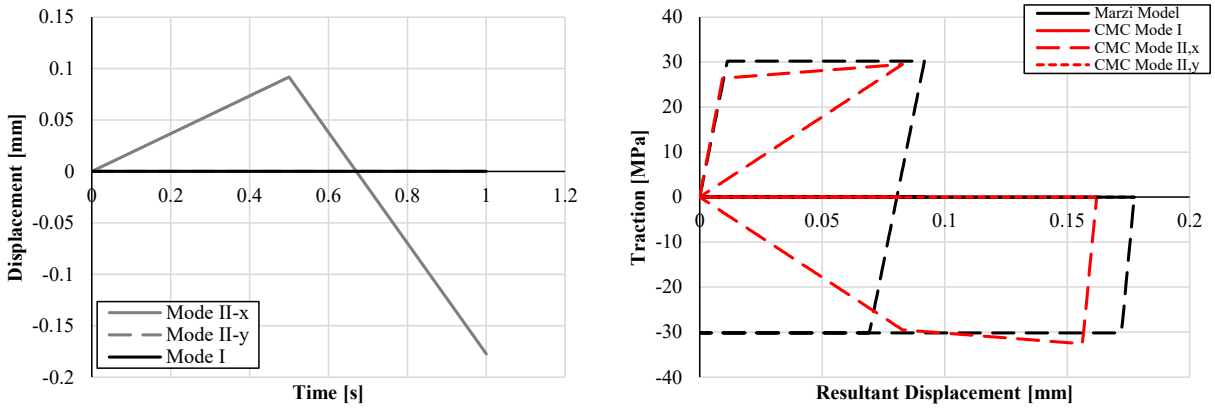

Figure B16: Input (left) and output (right) for Mode II load to segment II-unload-full reversal to failure cycle for 0.18 mm CZM element

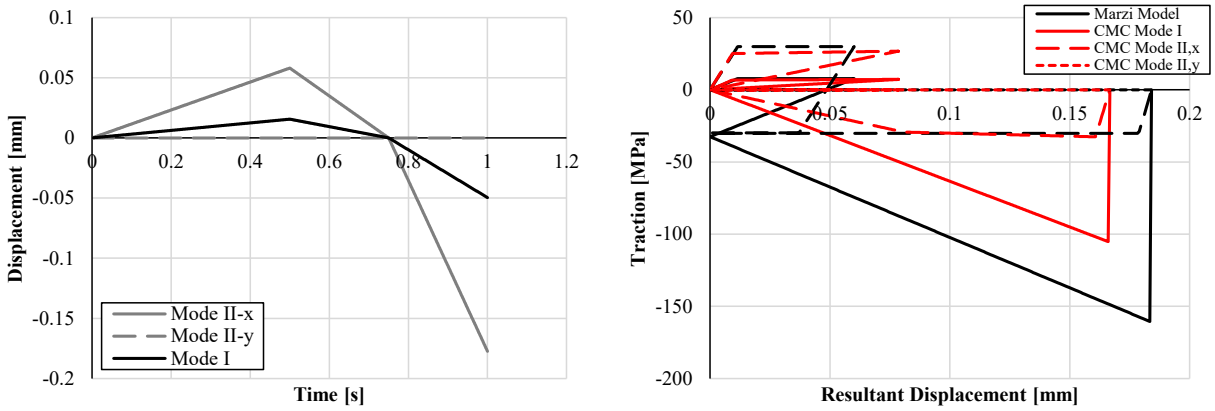

Figure B17: Input (left) and output (right) for 75 º mixed mode load to segment II-unload-full reversal to failure cycle for 0.18 mm CZM element

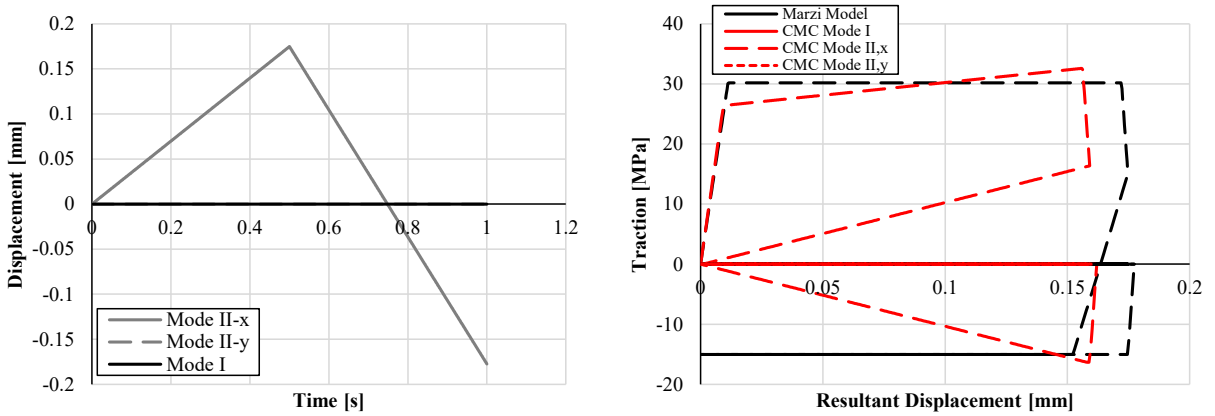

Figure B18: Input (left) and output (right) for Mode II load to segment III-unload-full reversal to failure cycle for 0.18 mm CZM element

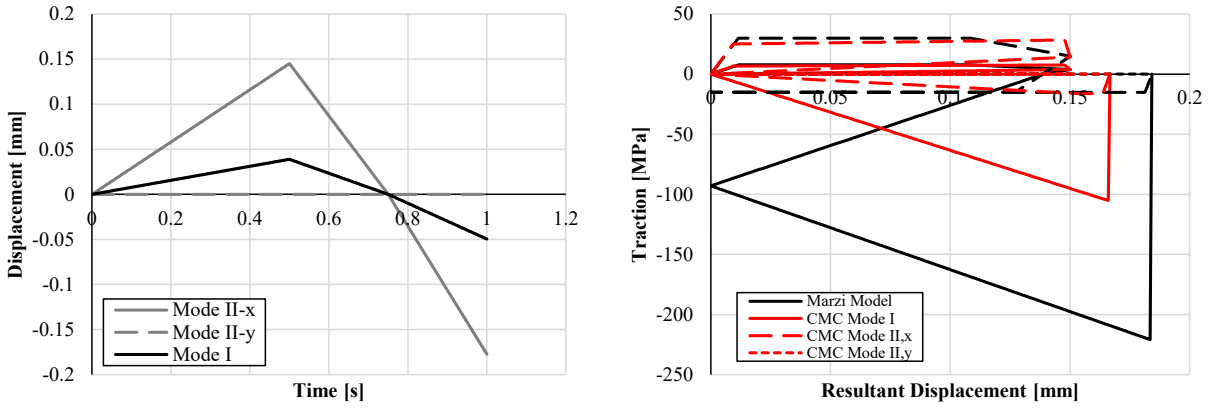

Figure B19: Input (left) and output (right) for 75 º mixed mode load to segment III-unload-full reversal to failure cycle for 0.18 mm CZM element

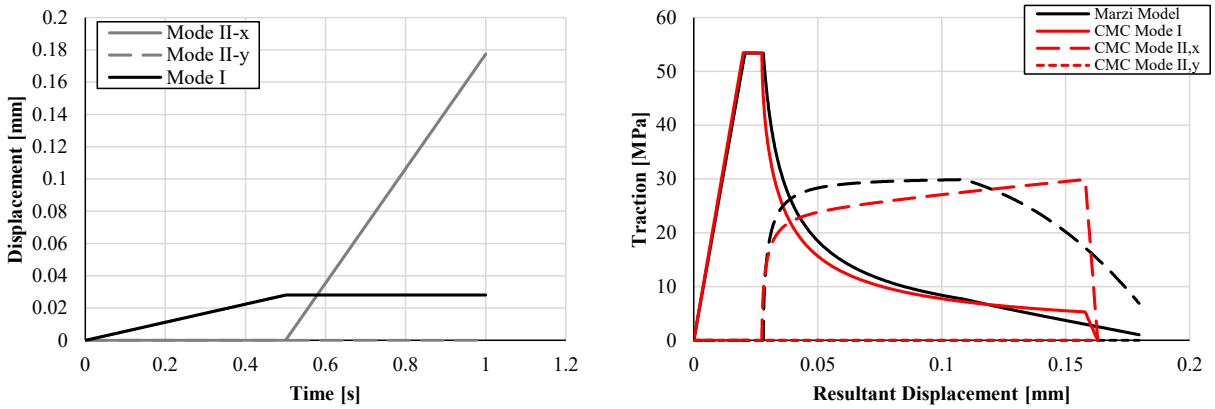

Figure B20: Input (left) and output (right) for arrested Mode I (Segment 2) loading followed by Mode II loading in positive 1 direction for 0.18 mm CZM element

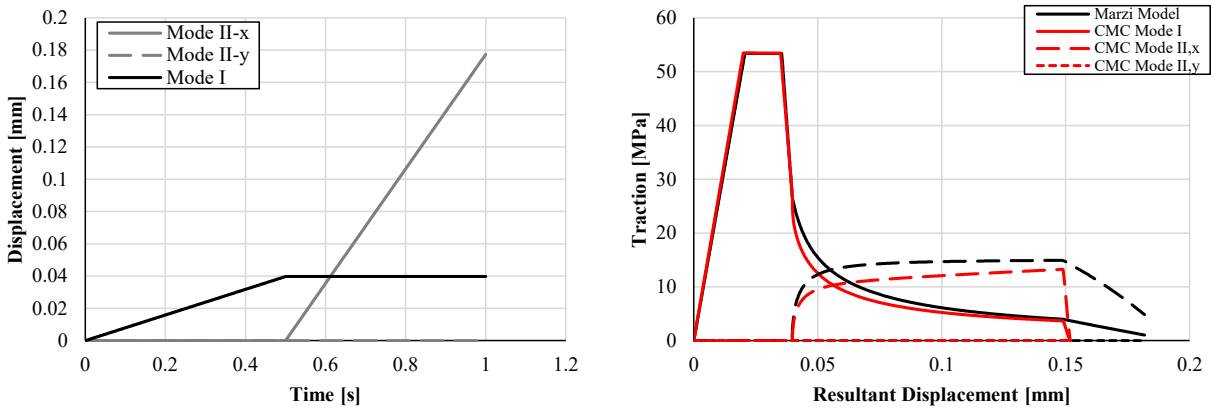

Figure B21: Input (left) and output (right) for arrested Mode I (Segment 3) loading followed by Mode II loading in positive 1 direction for 0.18 mm CZM element

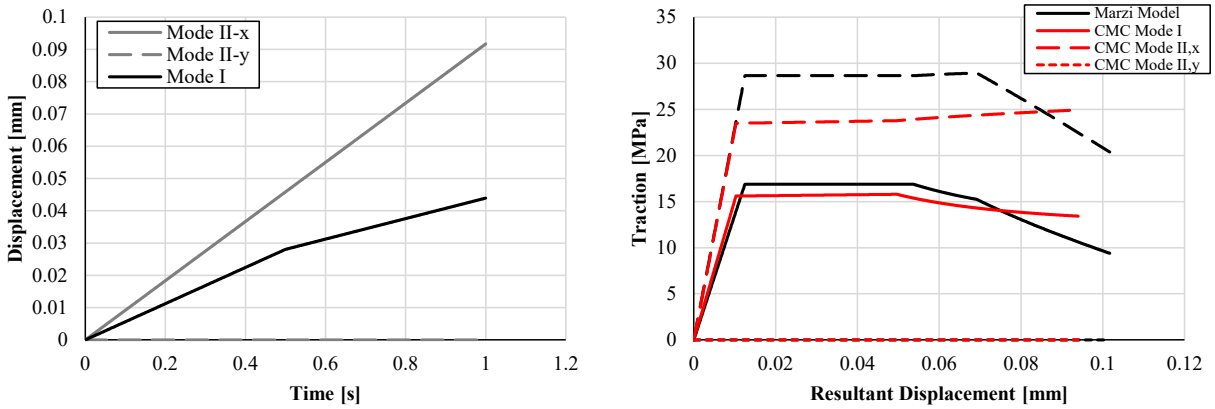

Figure B22: Input (left) and output (right) for constant Mode II velocity and variable Mode I velocity loading for 0.18 mm CZM element

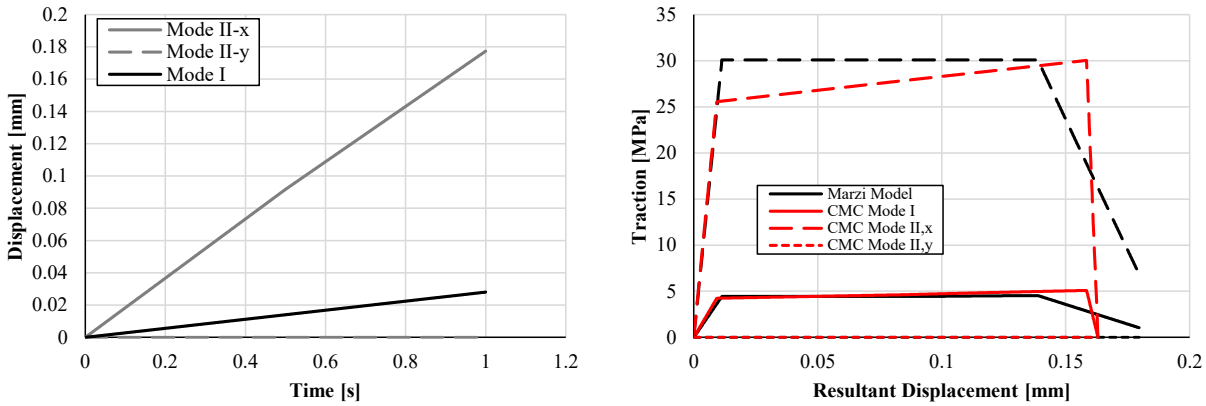

Figure B23: Input (left) and output (right) for variable Mode II velocity and variable Mode I velocity loading for 0.18 mm CZM element

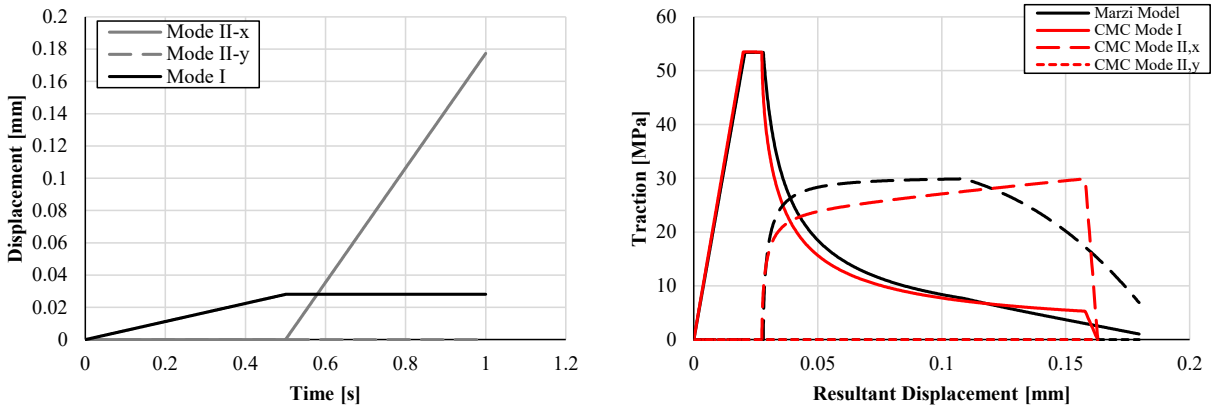

Figure B24: Input (left) and output (right) for tensile Mode I loading (Segment 2) with additional Mode II loading in the positive 1 direction for 0.18 mm CZM element

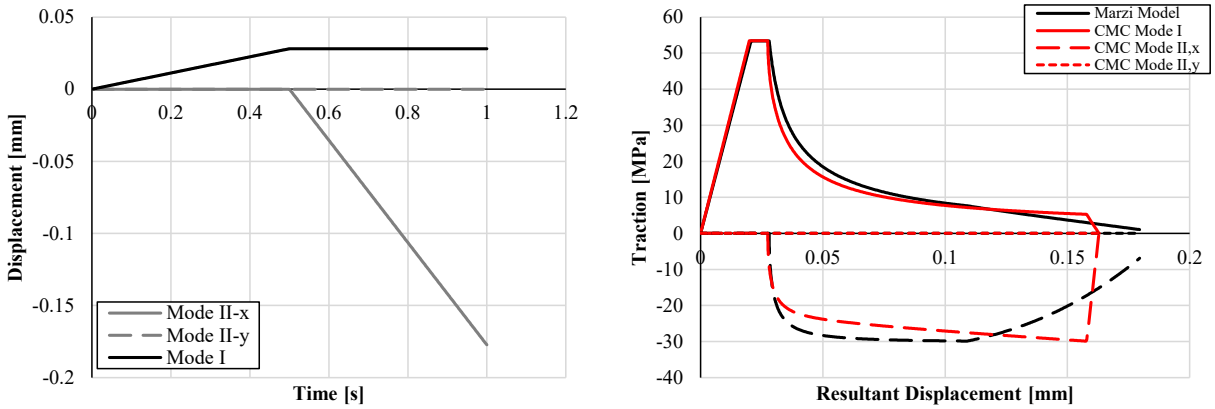

Figure B25: Input (left) and output (right) for tensile Mode I loading (Segment 2) with additional Mode II loading in the negative 1 direction for 0.18 mm CZM element

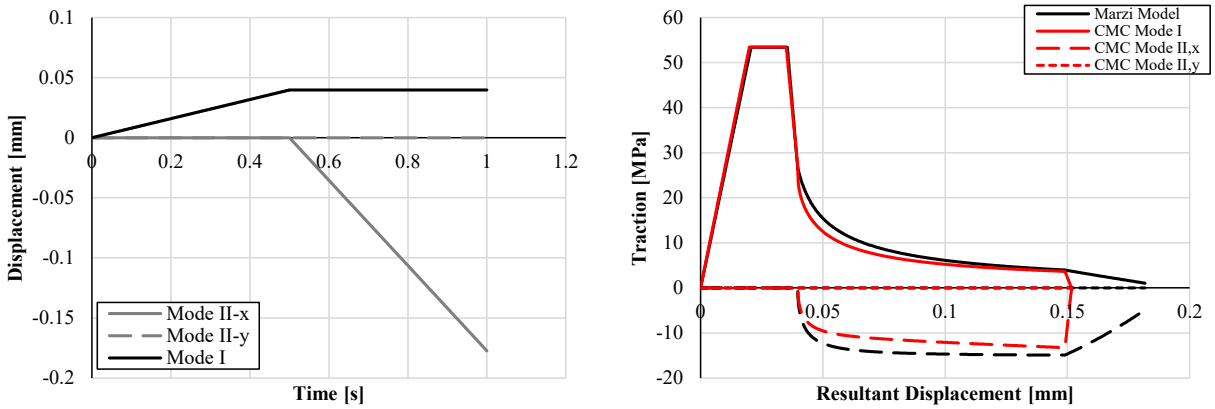

Figure B26: Input (left) and output (right) for tensile Mode I loading (Segment 3) with additional Mode II loading in the negative 1 direction for 0.18 mm CZM element

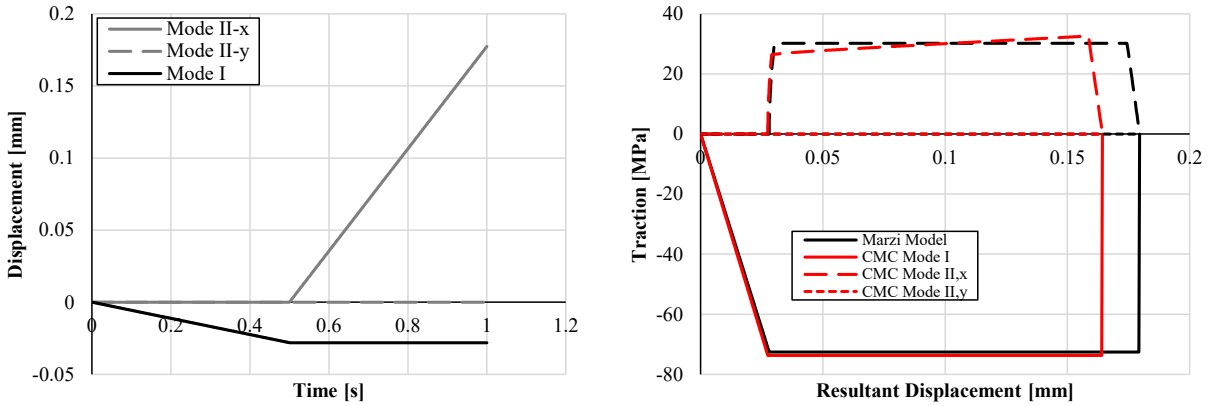

Figure B27: Input (left) and output (right) for compressive Mode I loading (Segment 2) with additional Mode II loading in the positive 1 direction for 0.18 mm CZM element

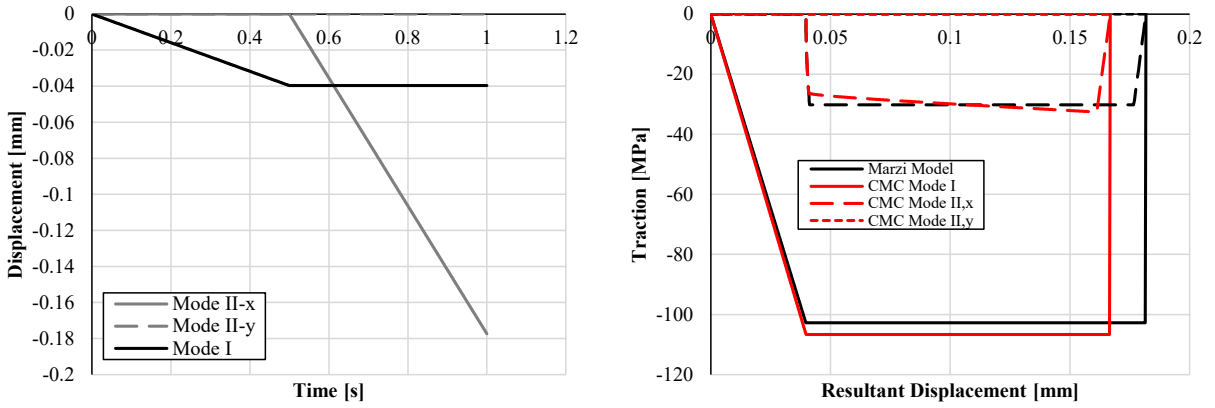

Figure B28: Input (left) and output (right) for compressive Mode I loading (Segment 3) with additional Mode II loading in the negative 1 direction for 0.18 mm CZM element

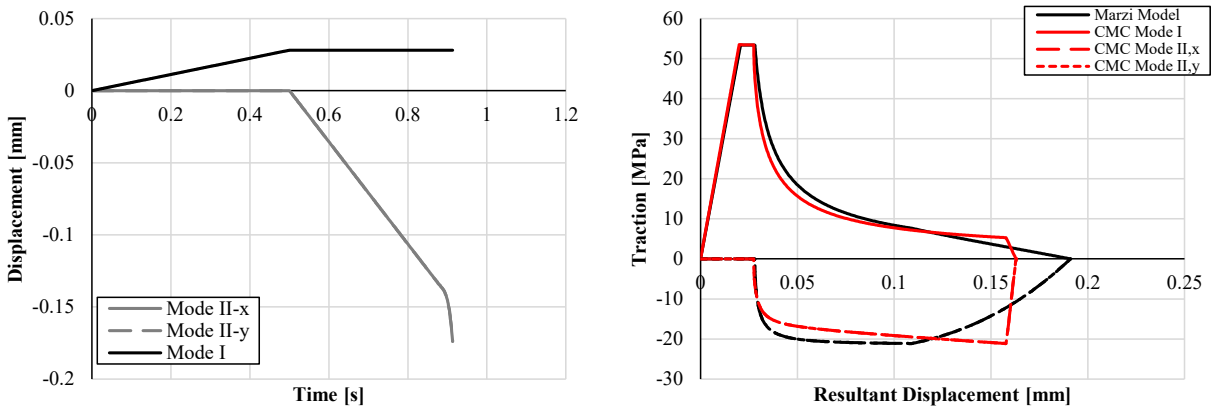

Figure B29: Input (left) and output (right) for tensile Mode I loading (Segment 2) with added equal Mode II loading in the negative 1 and 2 directions for 0.18 mm CZM element

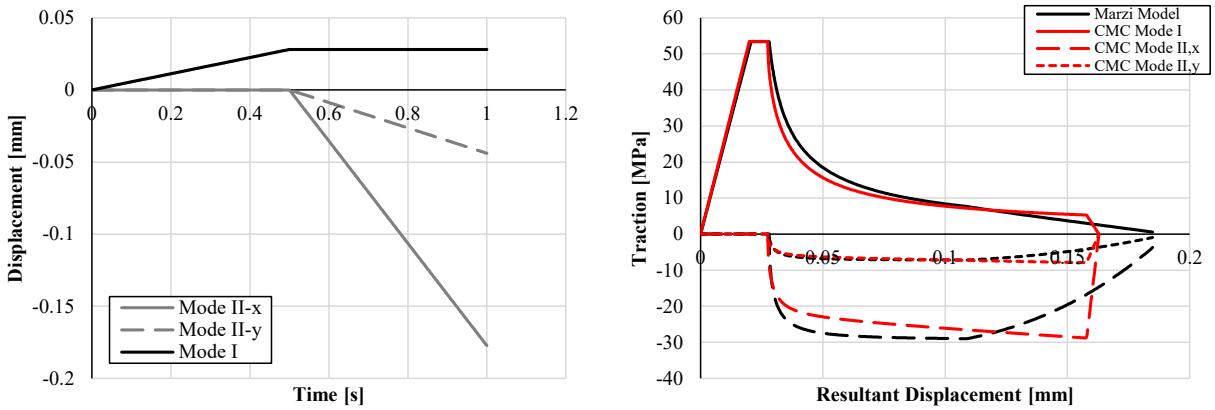

Figure B30: Input (left) and output (right) for tensile Mode I loading (Segment 2) with added unequal Mode II loading in negative 1 and 2 directions for 0.18 mm CZM element

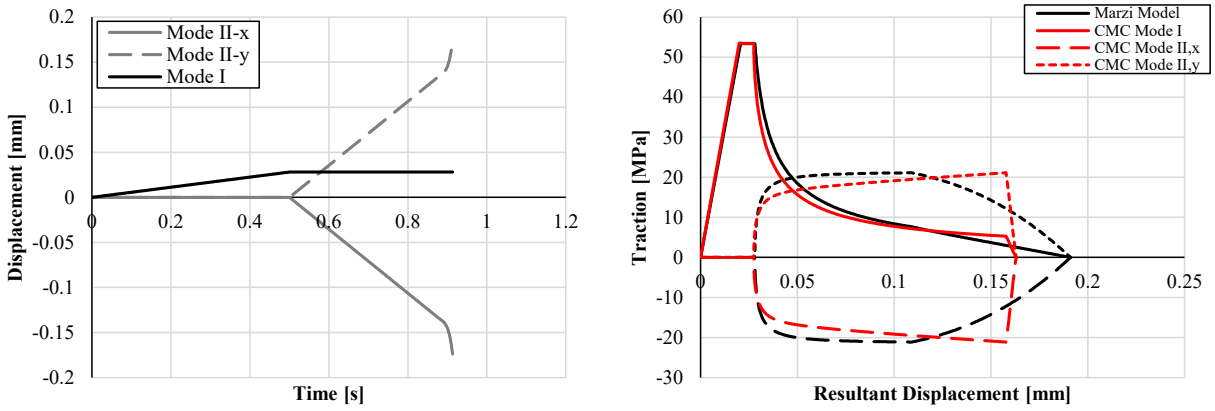

Figure B31: Input (left) and output (right) for tensile Mode I loading (Segment 2) with added unequal Mode II loading in positive 1 and negative 2 directions for 0.18 mm CZM element

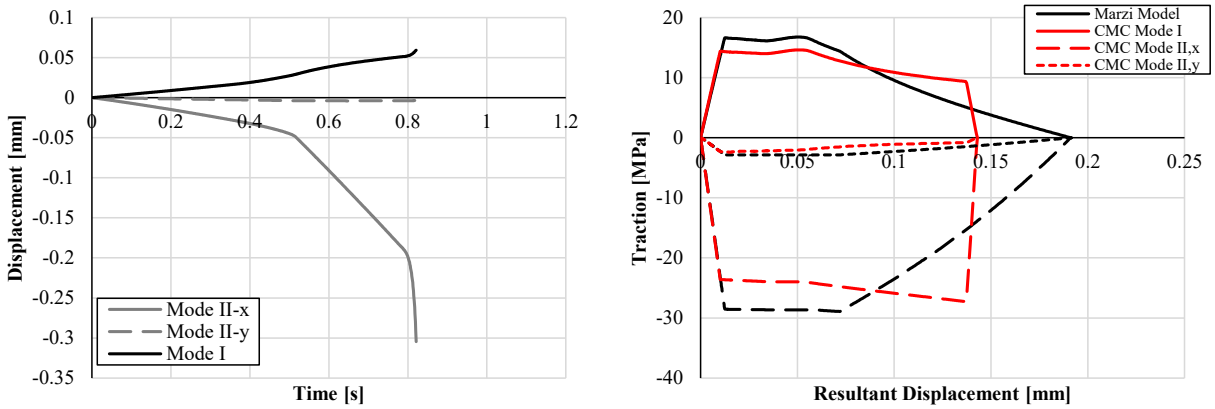

Figure B32: Input (left) and output (right) for loading extracted from a model of a UHSS – UHSS single lap shear test for 0.18 mm CZM element

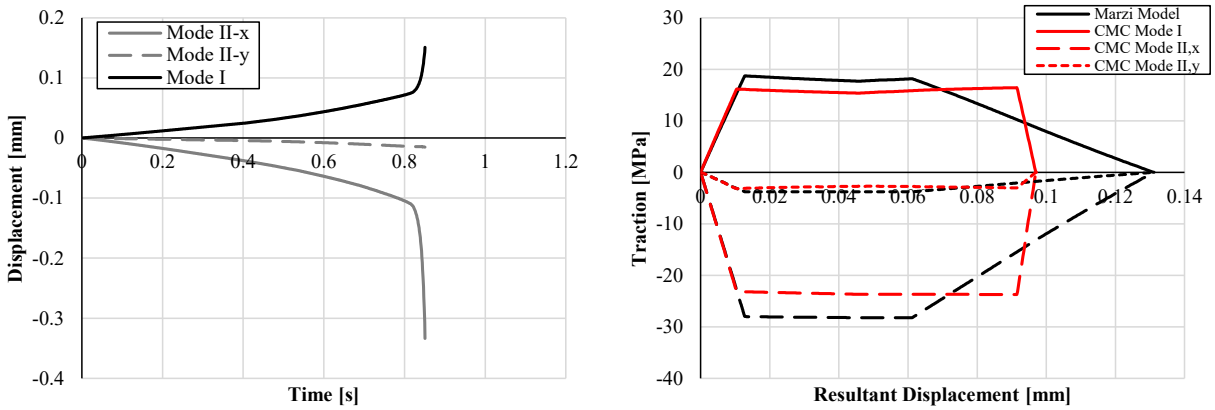

Figure B33: Input (left) and output (right) for loading extracted from a model of an aluminum – aluminum single lap shear test for 0.18 mm CZM element

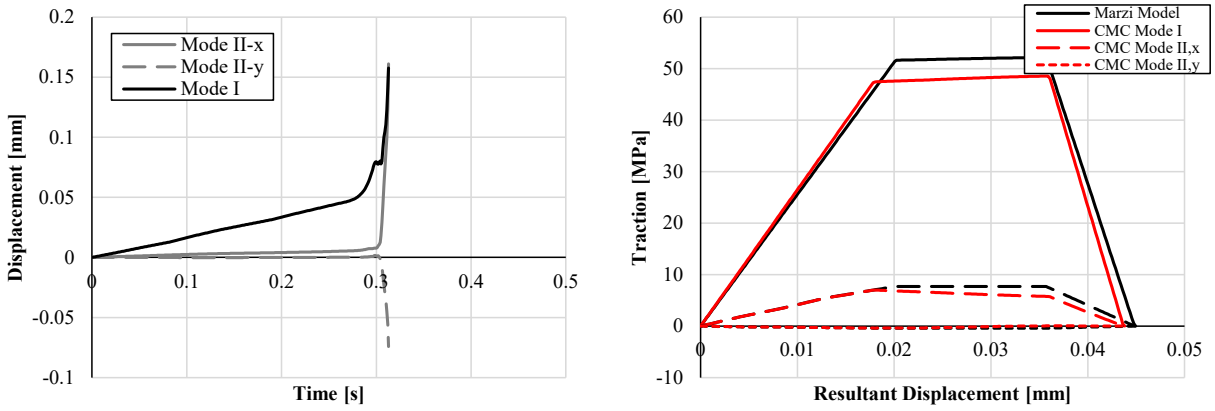

Figure B34: Input (left) and output (right) for loading extracted from a model of a UHSS – aluminum single lap shear test for 0.18 mm CZM element

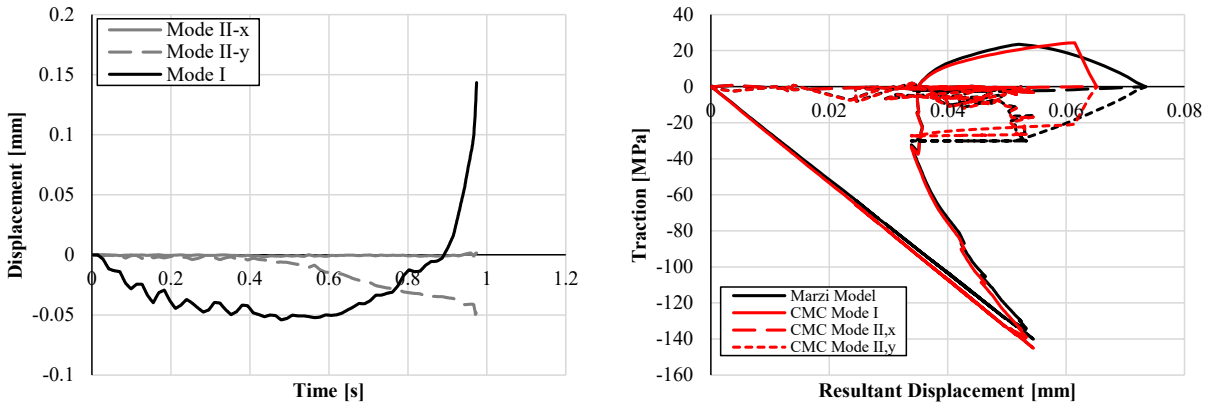

Figure B35: Input (left) and output (right) for loading extracted from a model of an adhesively bonded UHSS axial crush tube for 0.18 mm CZM element

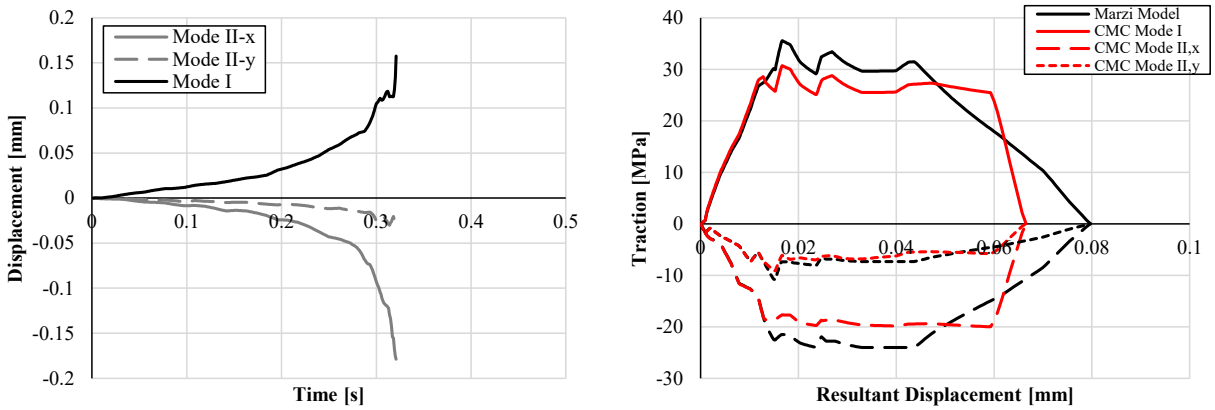

Figure B36: Input (left) and output (right) for loading extracted from a model of an adhesively bonded UHSS 3-point bend test for 0.18 mm CZM element

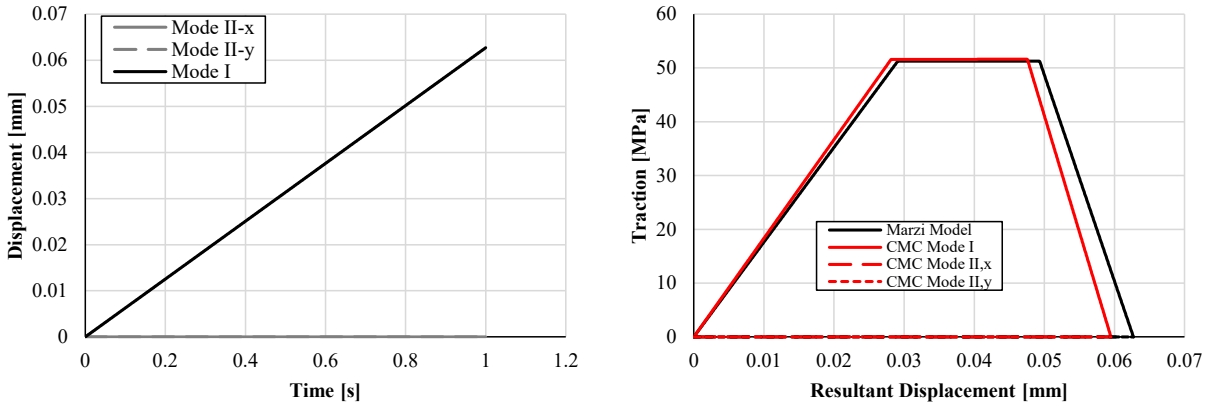

Figure B37: Input (left) and output (right) for Mode I loading for 0.3 mm CZM element

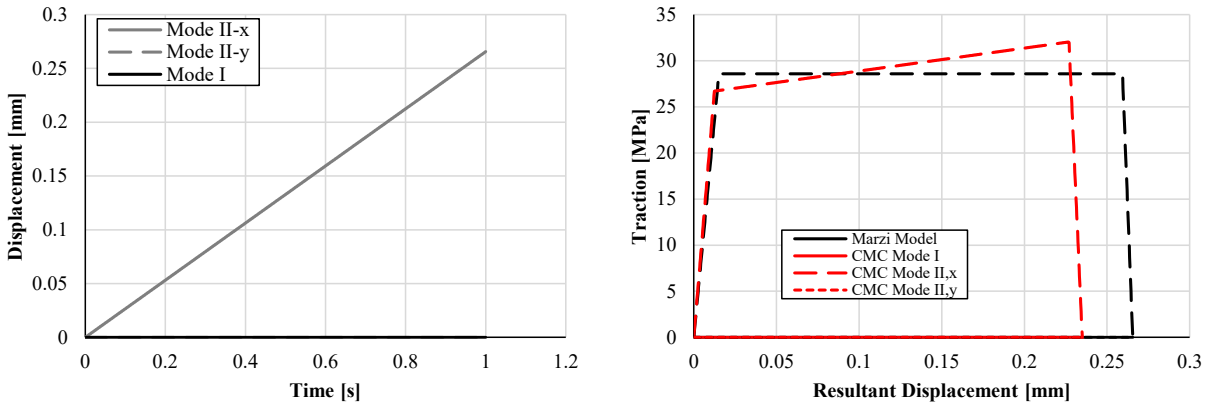

Figure B38: Input (left) and output (right) for Mode II loading for 0.3 mm CZM element

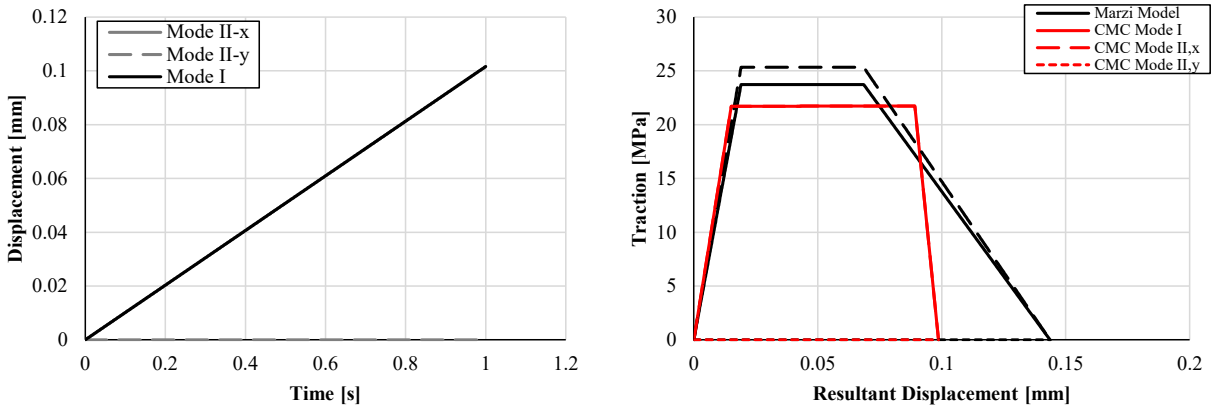

Figure B39: Input (left) and output (right) for 45 º mixed mode loading for 0.3 mm CZM element

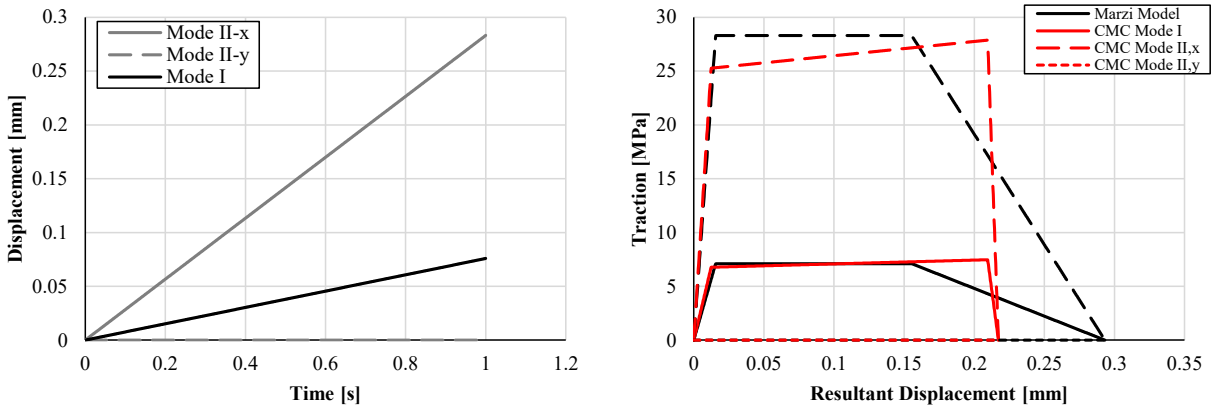

Figure B40: Input (left) and output (right) for 75 º mixed mode loading for 0.3 mm CZM element

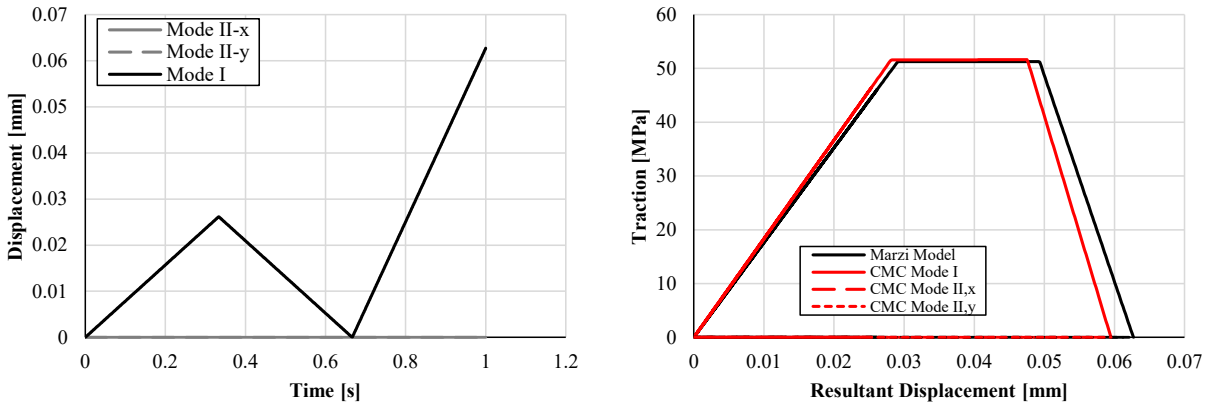

Figure B41: Input (left) and output (right) for Mode I load to segment I-unload-reload to failure cycle for 0.3 mm CZM element

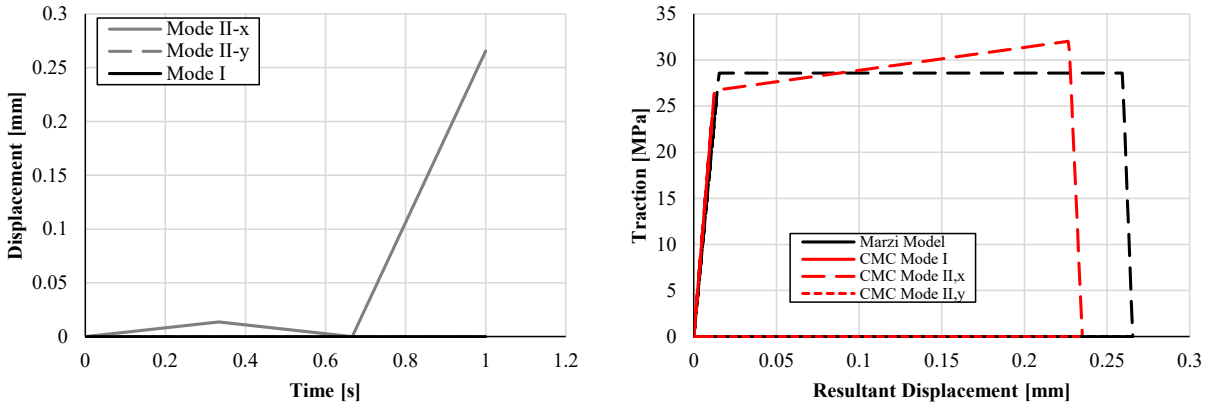

Figure B42: Input (left) and output (right) for Mode II load to segment I-unload-reload to failure cycle for 0.3 mm CZM element

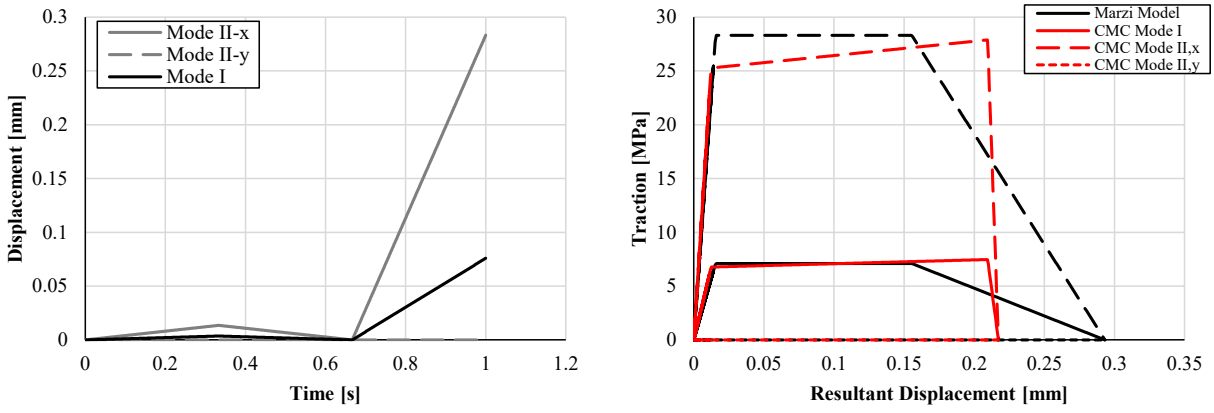

Figure B43: Input (left) and output (right) for 75 º mixed mode load to segment I-unload-reload to failure cycle for 0.3 mm CZM element

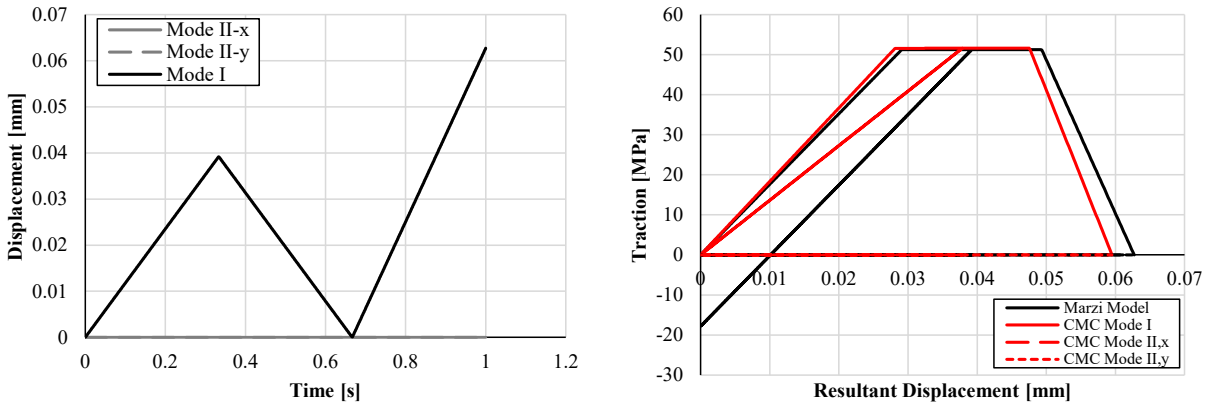

Figure B44: Input (left) and output (right) for Mode I load to segment II-unload-reload to failure cycle for 0.3 mm CZM element

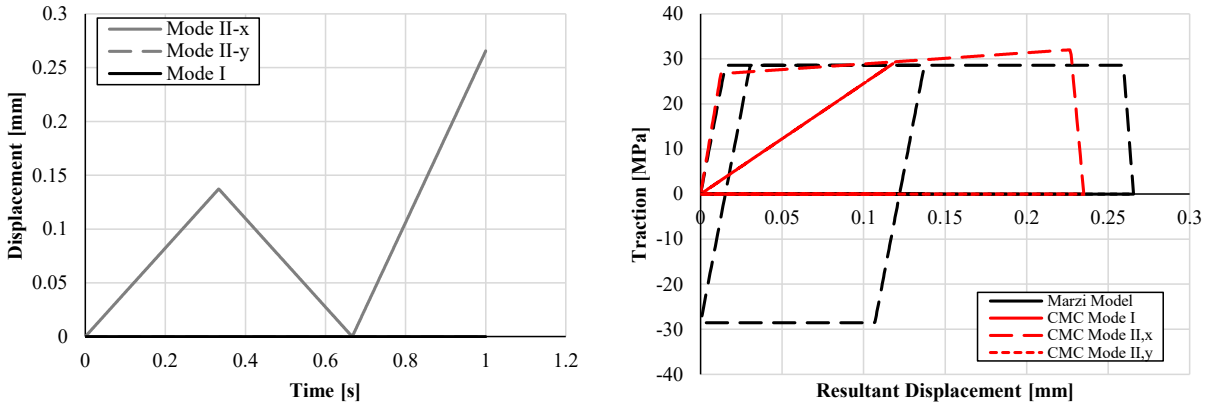

Figure B45: Input (left) and output (right) for Mode II load to segment II-unload-reload to failure cycle for 0.3 mm CZM element

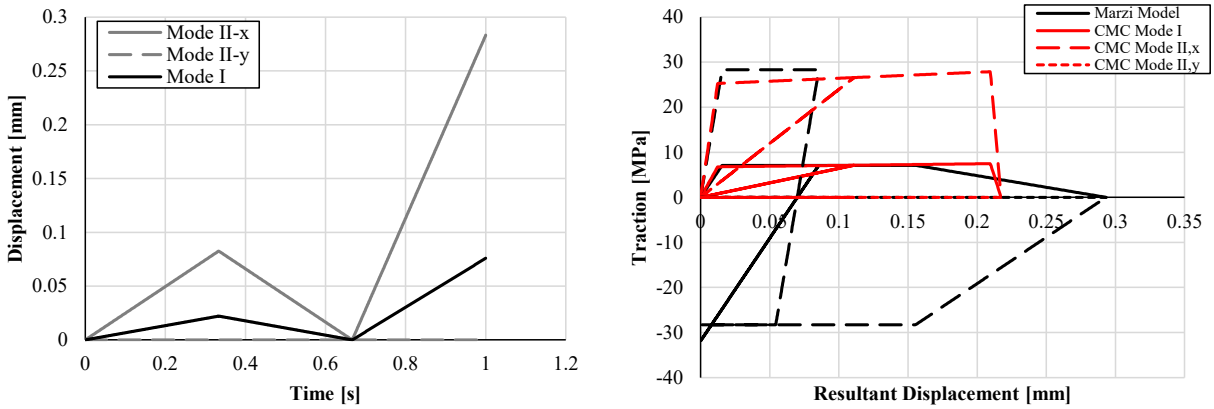

Figure B46: Input (left) and output (right) for 75 º mixed mode load to segment II-unload-reload to failure cycle for 0.3 mm CZM element

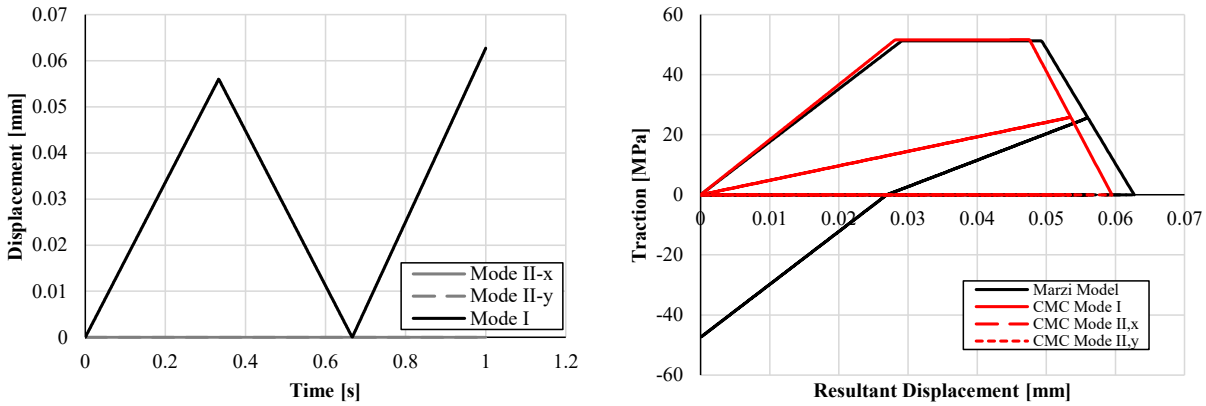

Figure B47: Input (left) and output (right) for Mode I load to segment III-unload-reload to failure cycle for 0.3 mm CZM element

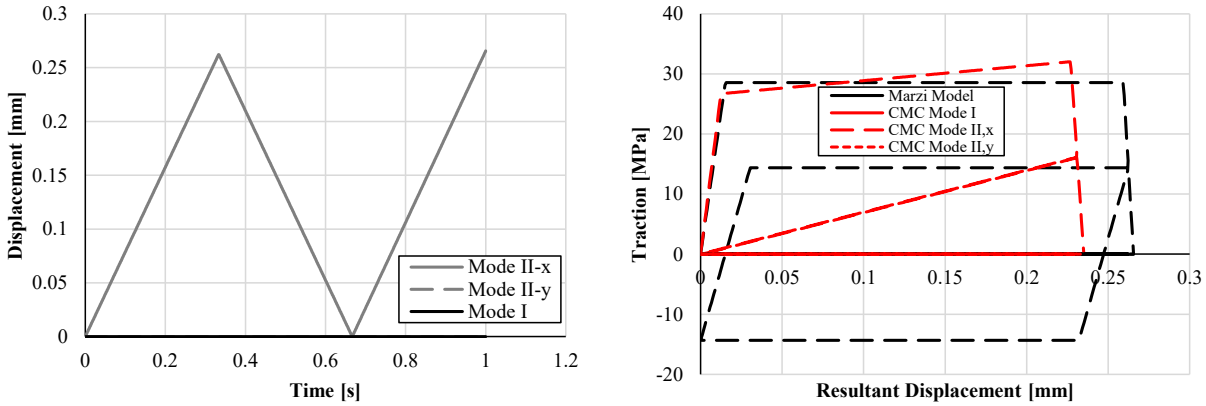

Figure B48: Input (left) and output (right) for Mode II load to segment III-unload-reload to failure cycle for 0.3 mm CZM element

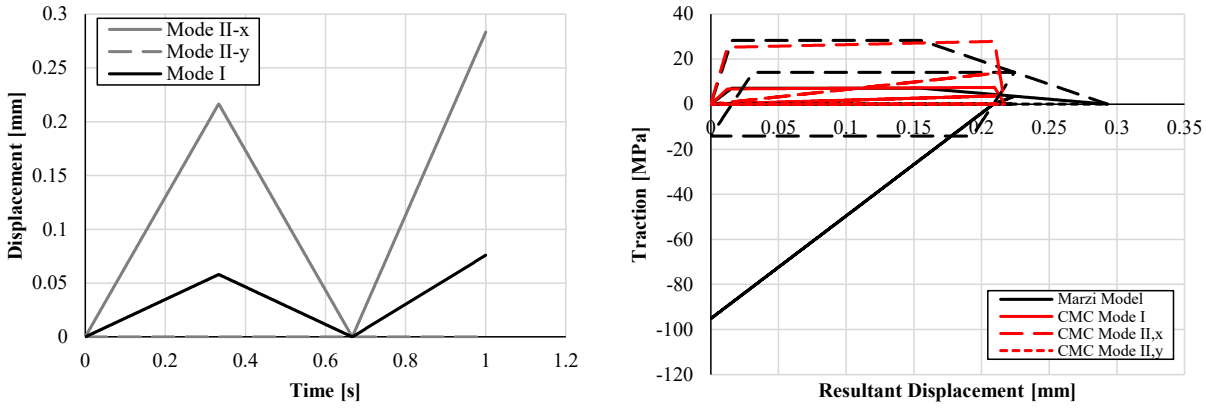

Figure B49: Input (left) and output (right) for 75 º mixed mode load to segment III-unload-reload to failure cycle for 0.3 mm CZM element

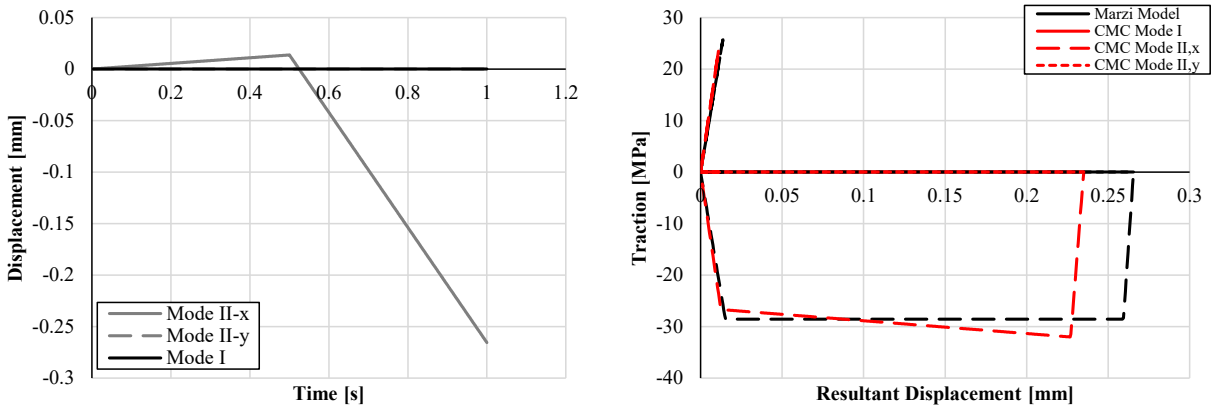

Figure B50: Input (left) and output (right) for Mode II load to segment I-unload-full reversal to failure cycle for 0.3 mm CZM element

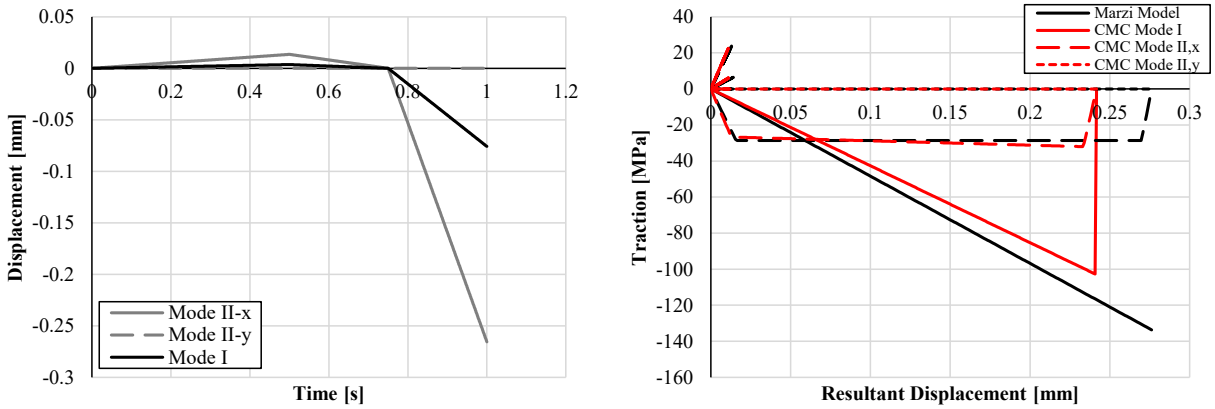

Figure B51: Input (left) and output (right) for 75 º mixed mode load to segment I-unload-full reversal to failure cycle for 0.3 mm CZM element

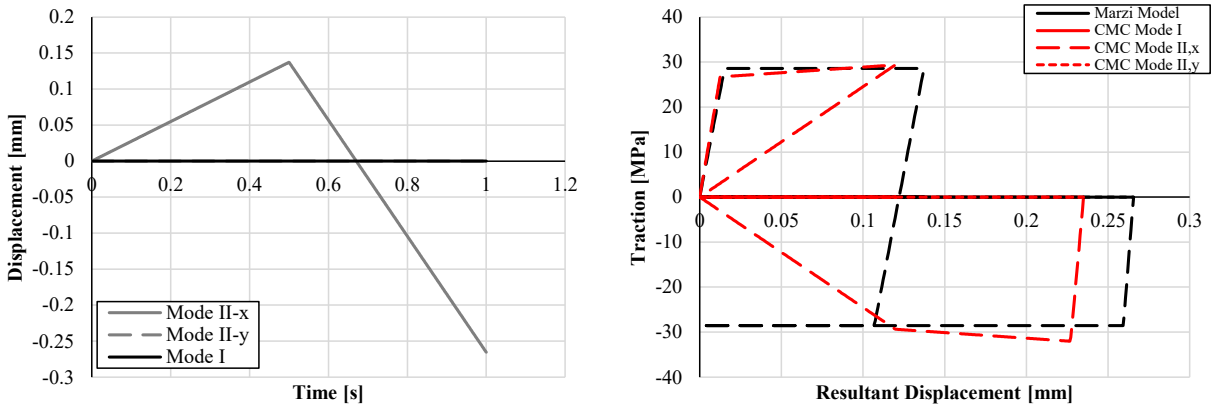

Figure B52: Input (left) and output (right) for Mode II load to segment II-unload-full reversal to failure cycle for 0.3 mm CZM element

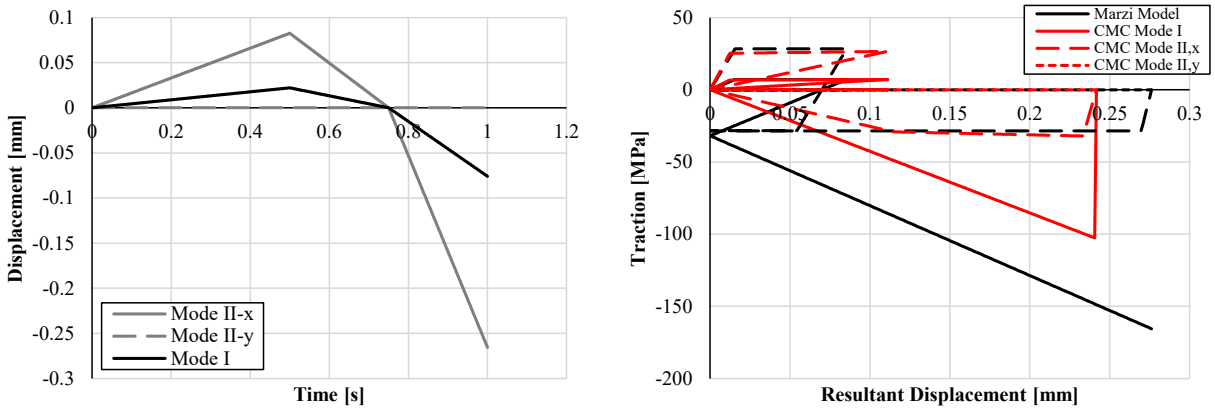

Figure B53: Input (left) and output (right) for 75 º mixed mode load to segment II-unload-full reversal to failure cycle for 0.3 mm CZM element

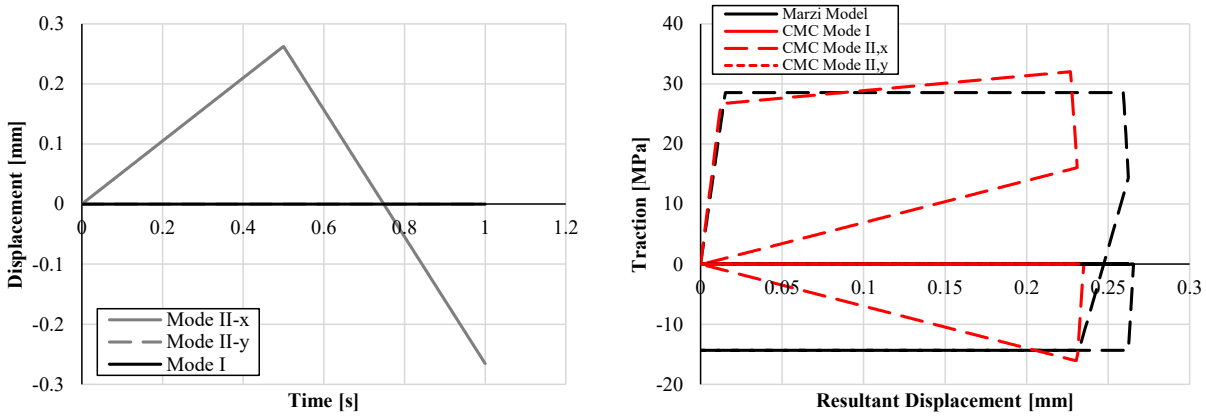

Figure B54: Input (left) and output (right) for Mode II load to segment III-unload-full reversal to failure cycle for 0.3 mm CZM element

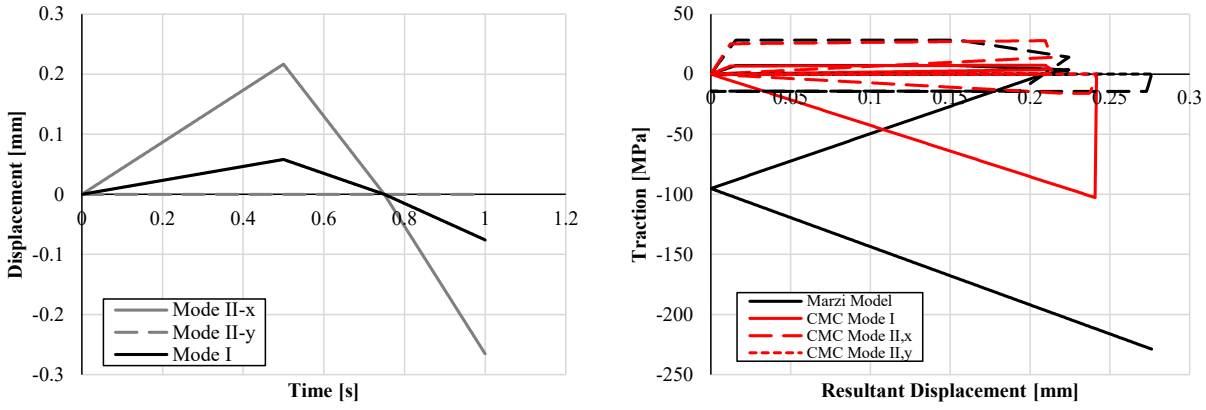

Figure B55: Input (left) and output (right) for 75 º mixed mode load to segment III-unload-full reversal to failure cycle for 0.3 mm CZM element

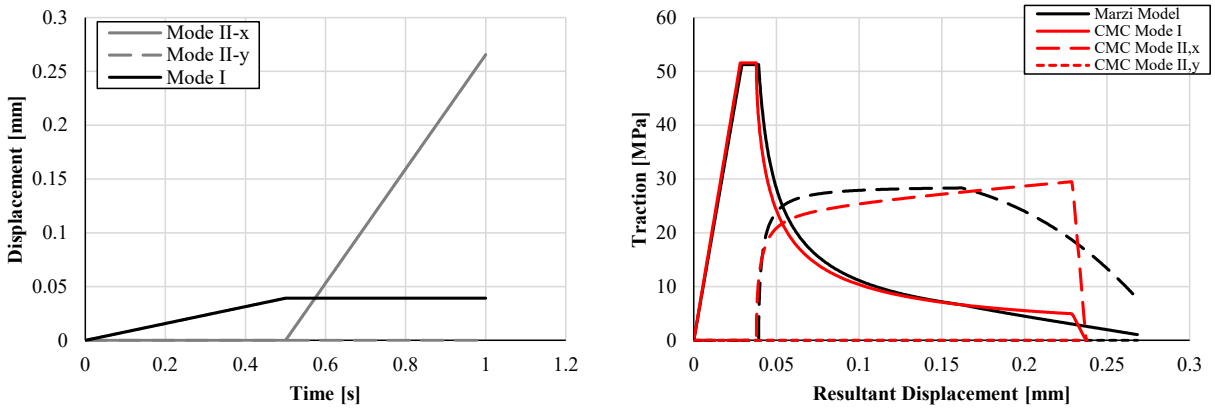

Figure B56: Input (left) and output (right) for arrested Mode I (Segment 2) loading followed by Mode II loading in positive 1 direction for 0.3 mm CZM element

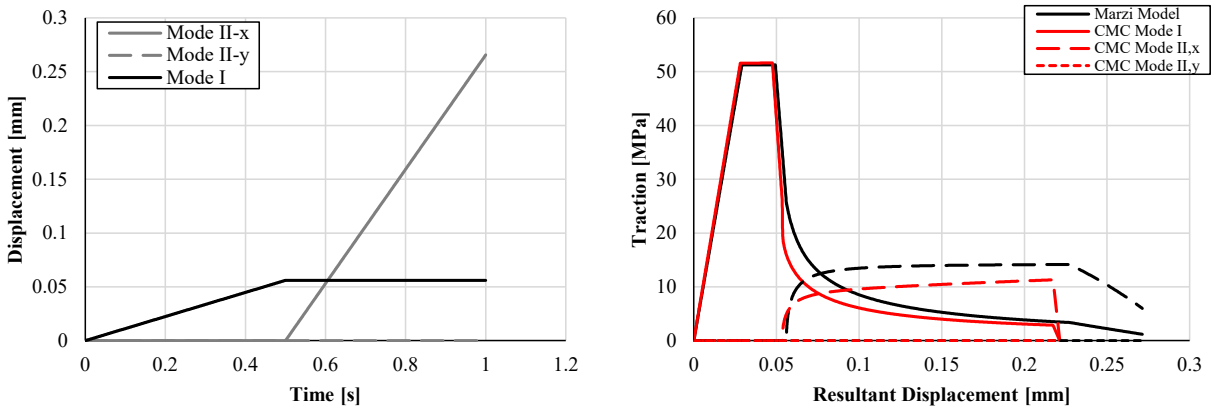

Figure B57: Input (left) and output (right) for arrested Mode I (Segment 3) loading followed by Mode II loading in positive 1 direction for 0.3 mm CZM element

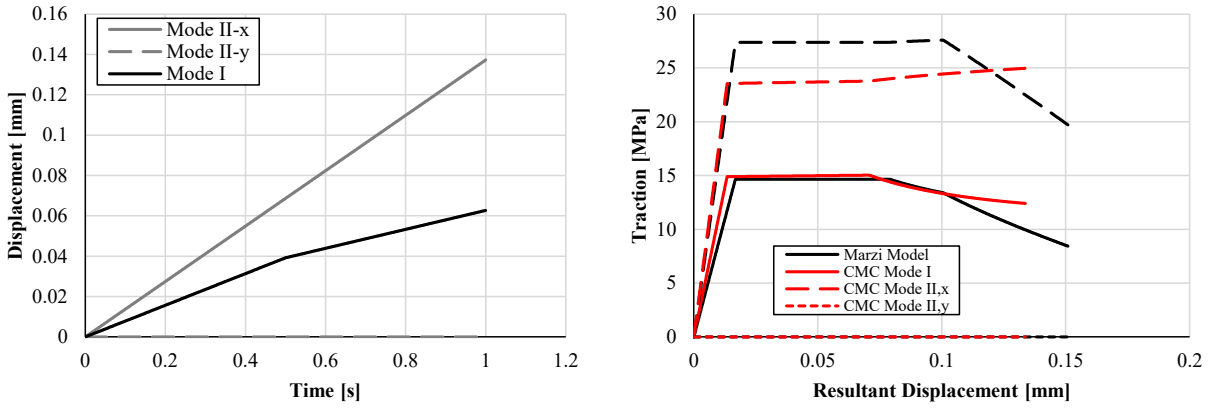

Figure B58: Input (left) and output (right) for constant Mode II velocity and variable Mode I velocity loading for 0.3 mm CZM element

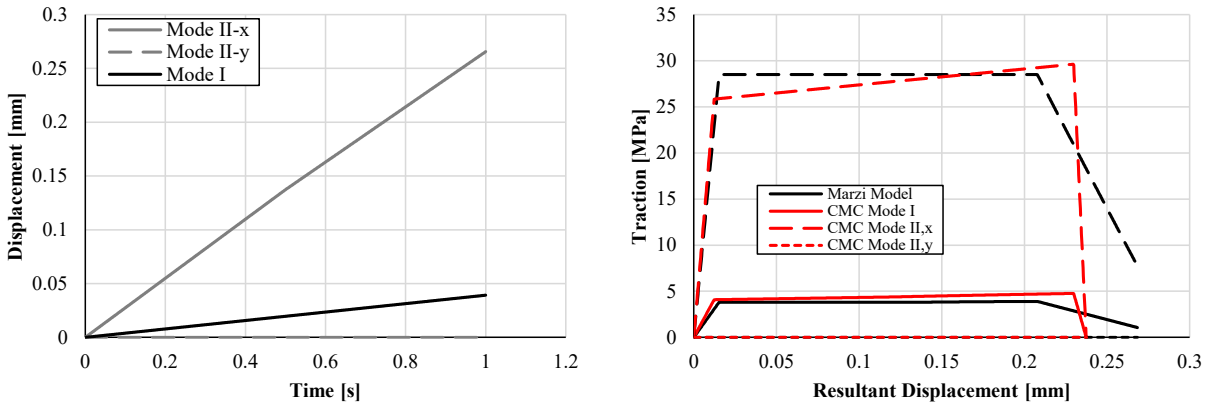

Figure B59: Input (left) and output (right) for variable Mode II velocity and variable Mode I velocity loading for 0.3 mm CZM element

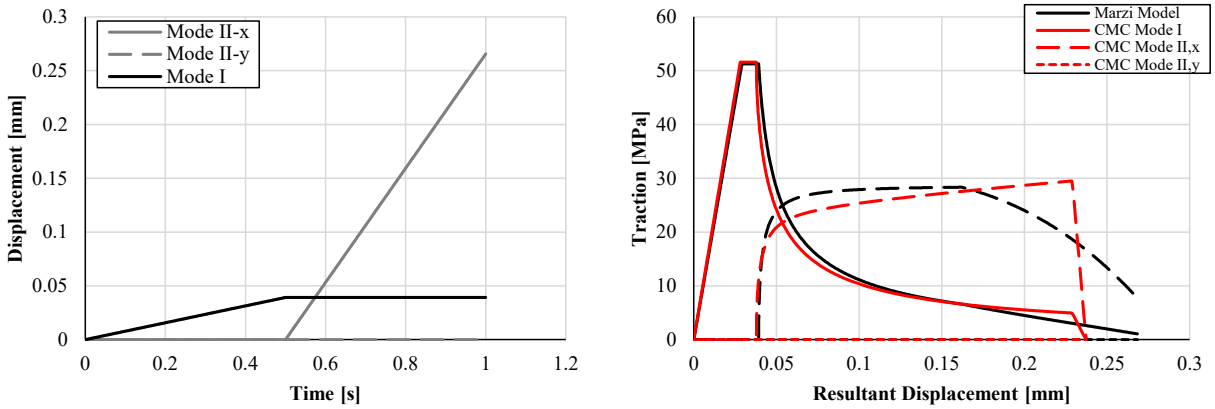

Figure B60: Input (left) and output (right) for tensile Mode I loading (Segment 2) with additional Mode II loading in the positive 1 direction for 0.3 mm CZM element

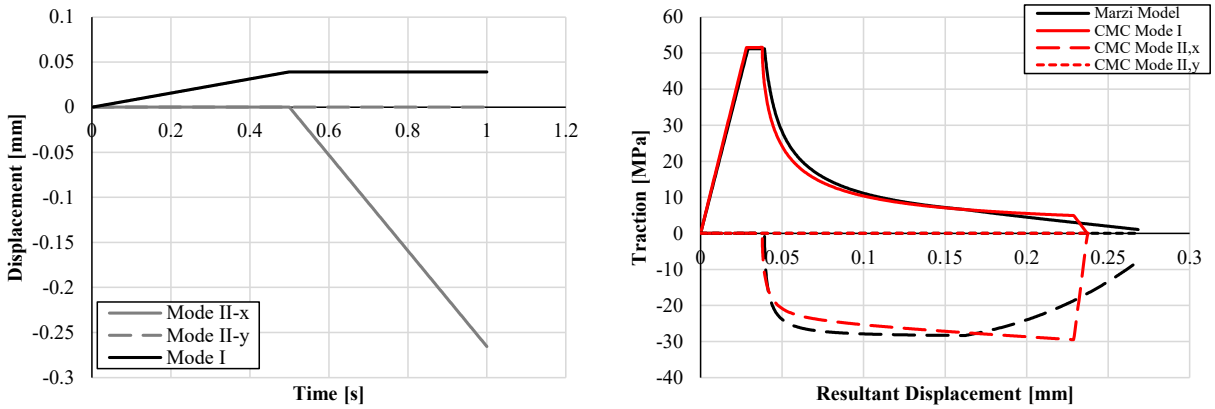

Figure B61: Input (left) and output (right) for tensile Mode I loading (Segment 2) with additional Mode II loading in the negative 1 direction for 0.3 mm CZM element

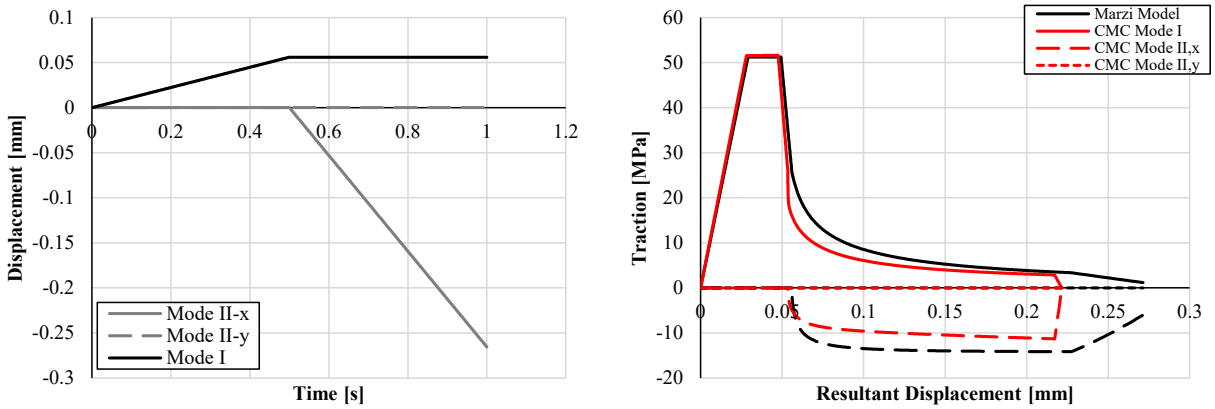

Figure B62: Input (left) and output (right) for tensile Mode I loading (Segment 3) with additional Mode II loading in the negative 1 direction for 0.3 mm CZM element

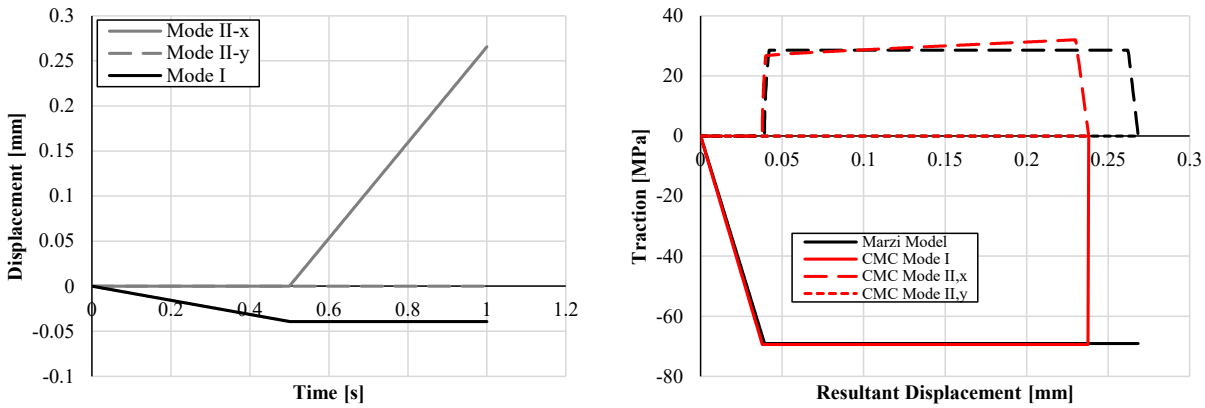

Figure B63: Input (left) and output (right) for compressive Mode I loading (Segment 2) with additional Mode II loading in the positive 1 direction for 0.3 mm CZM element

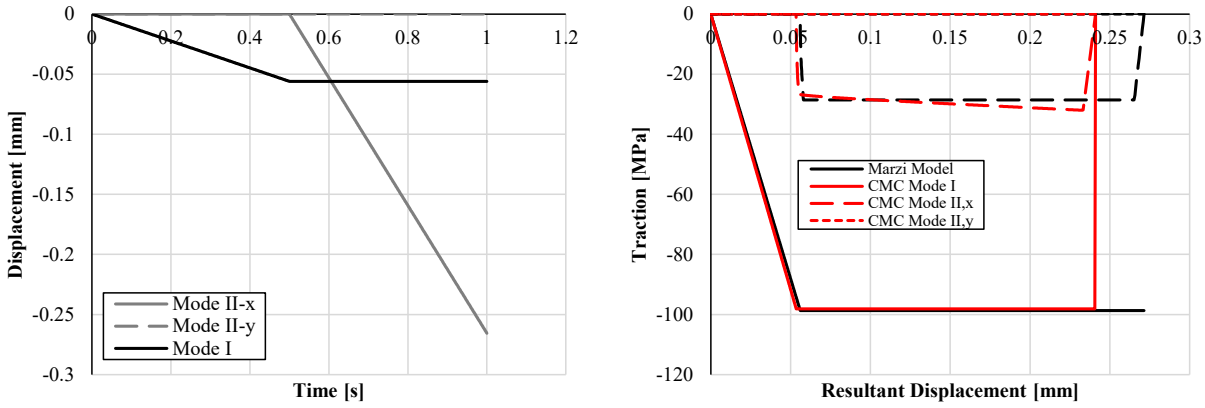

Figure B64: Input (left) and output (right) for compressive Mode I loading (Segment 3) with additional Mode II loading in the negative 1 direction for 0.3 mm CZM element

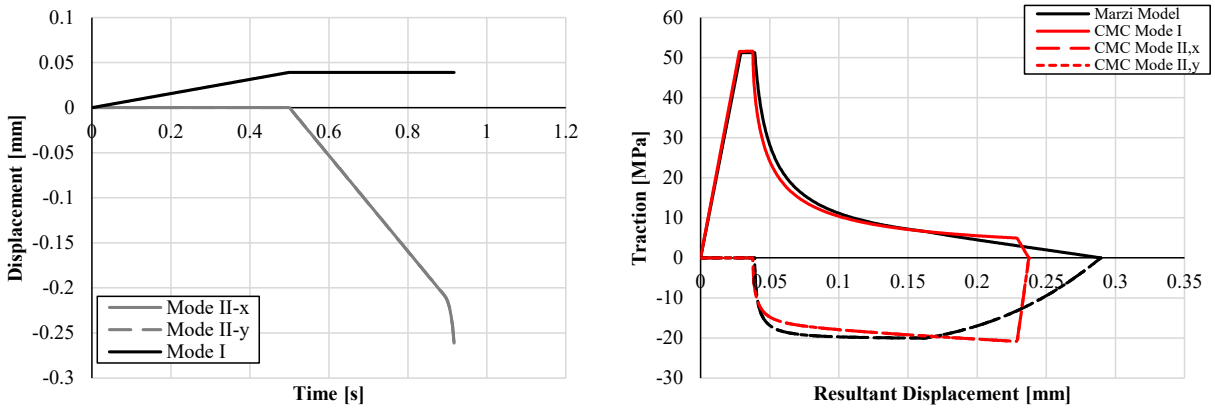

Figure B65: Input (left) and output (right) for tensile Mode I loading (Segment 2) with added equal Mode II loading in the negative 1 and 2 directions for 0.3 mm CZM element

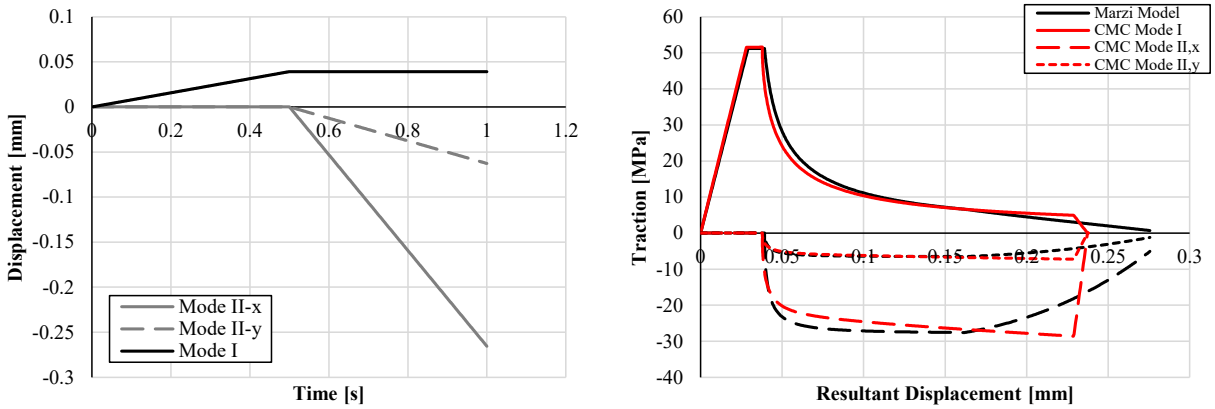

Figure B66: Input (left) and output (right) for tensile Mode I loading (Segment 2) with added unequal Mode II loading in the negative 1 and 2 directions for 0.3 mm CZM element

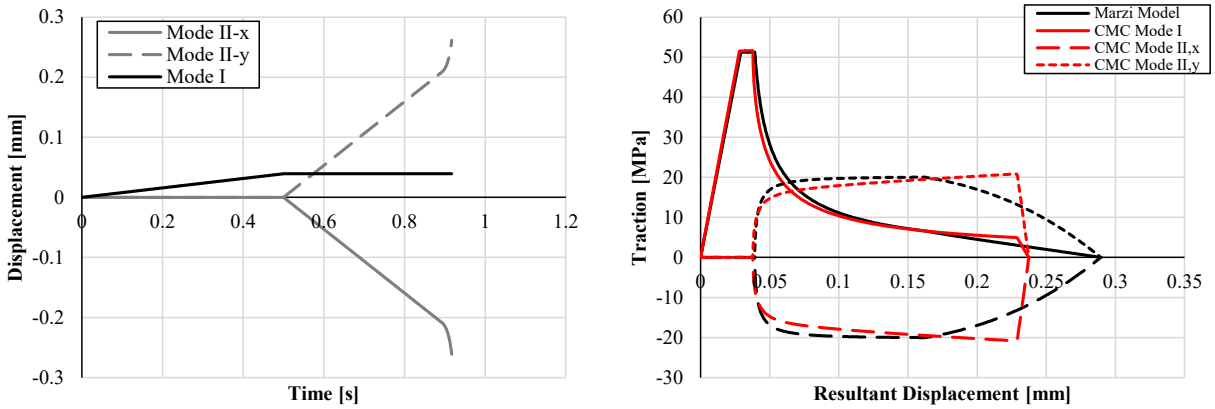

Figure B67: Input (left) and output (right) for tensile Mode I loading (Segment 2) with added unequal Mode II loading in the positive 1 and negative 2 directions for 0.3 mm CZM element

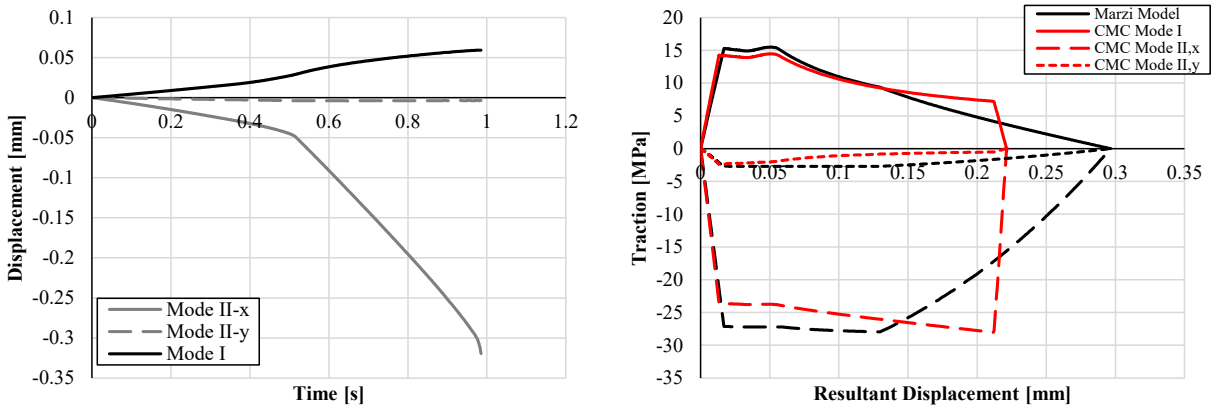

Figure B68: Input (left) and output (right) for loading extracted from a model of a UHSS – UHSS single lap shear test for 0.3 mm CZM element

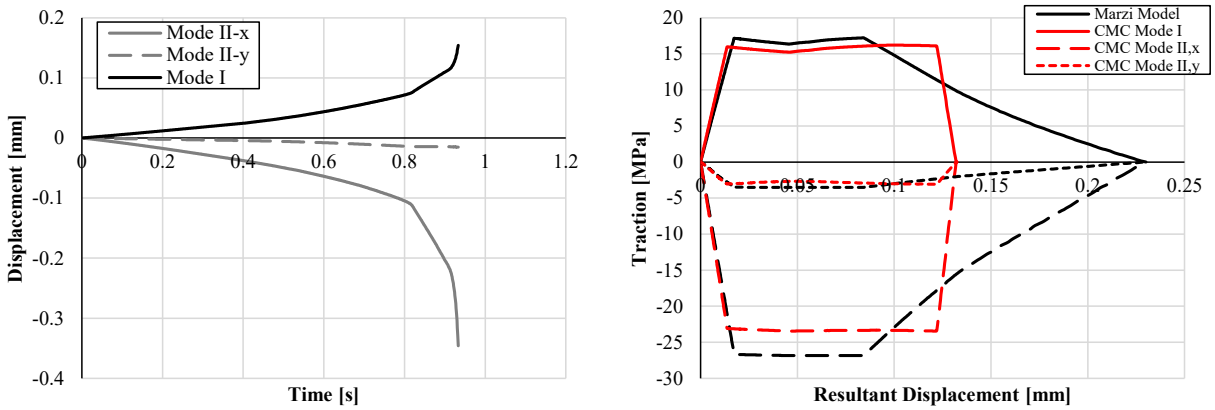

Figure B69: Input (left) and output (right) for loading extracted from a model of an aluminum – aluminum single lap shear test for 0.3 mm CZM element

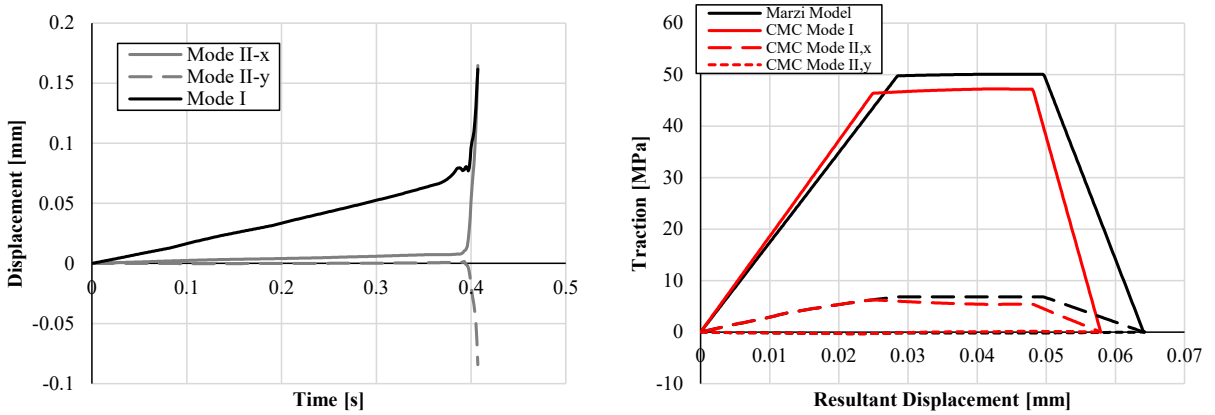

Figure B70: Input (left) and output (right) for loading extracted from a model of a UHSS – aluminum single lap shear test for 0.3 mm CZM element

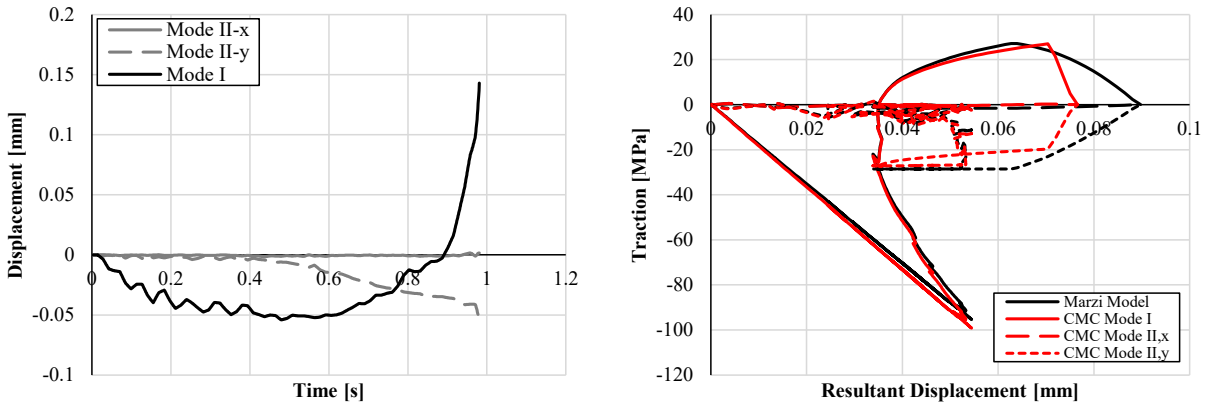

Figure B71: Input (left) and output (right) for loading extracted from a model of an adhesively bonded UHSS axial crush tube for 0.3 mm CZM element

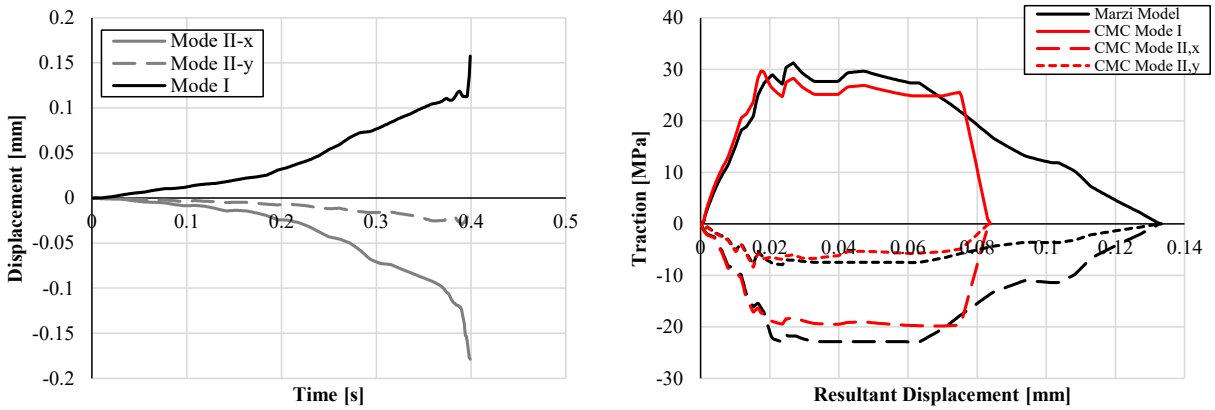

Figure B72: Input (left) and output (right) for loading extracted from a model of an adhesively bonded UHSS 3-point bend test for 0.3 mm CZM element

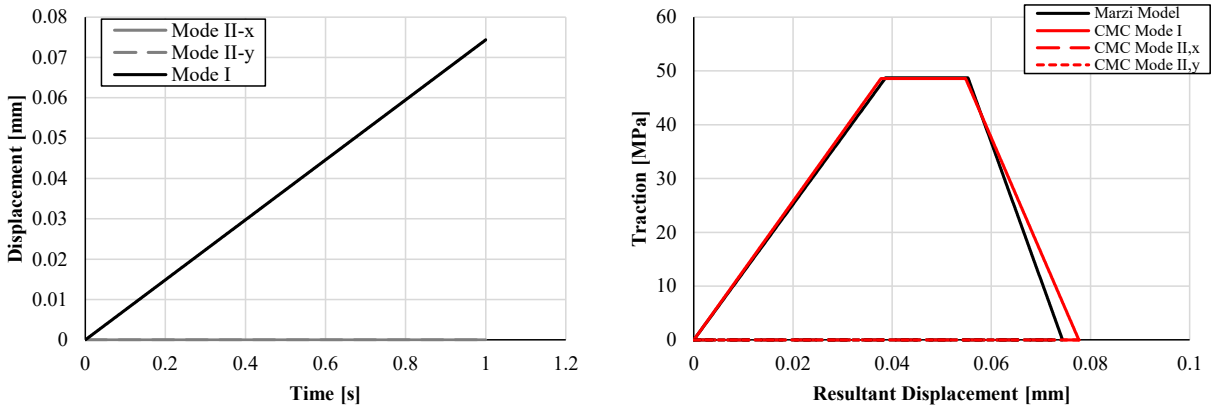

Figure B73: Input (left) and output (right) for Mode I loading for 0.64 mm CZM element

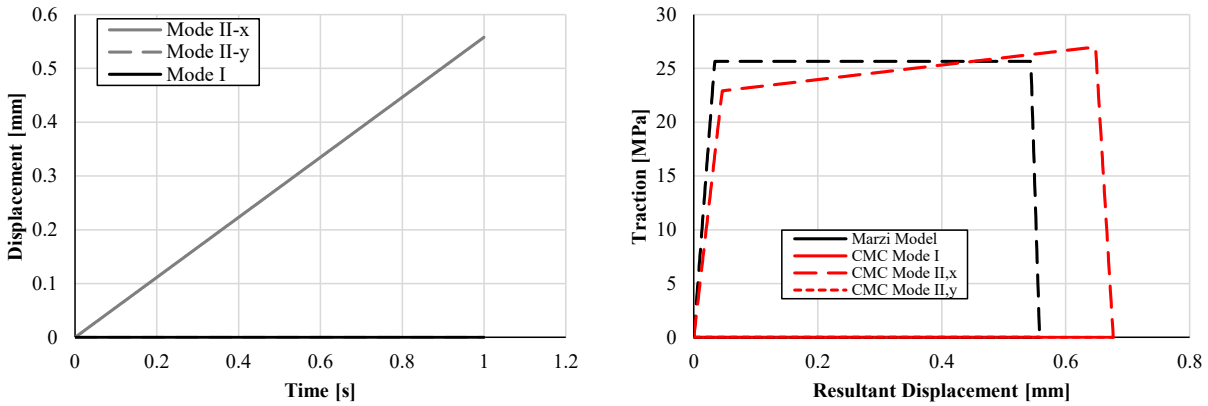

Figure B74: Input (left) and output (right) for Mode II loading for 0.64 mm CZM element

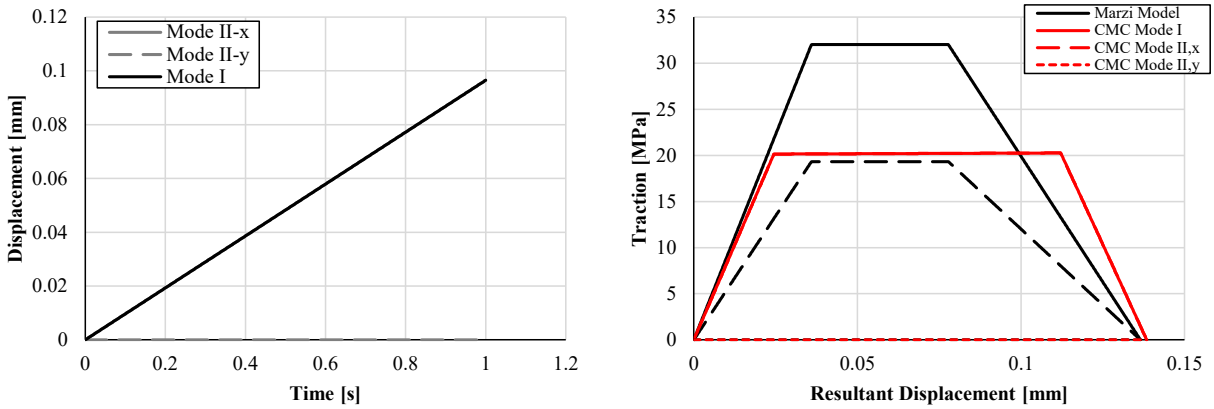

Figure B75: Input (left) and output (right) for 45 º mixed mode loading for 0.64 mm CZM element

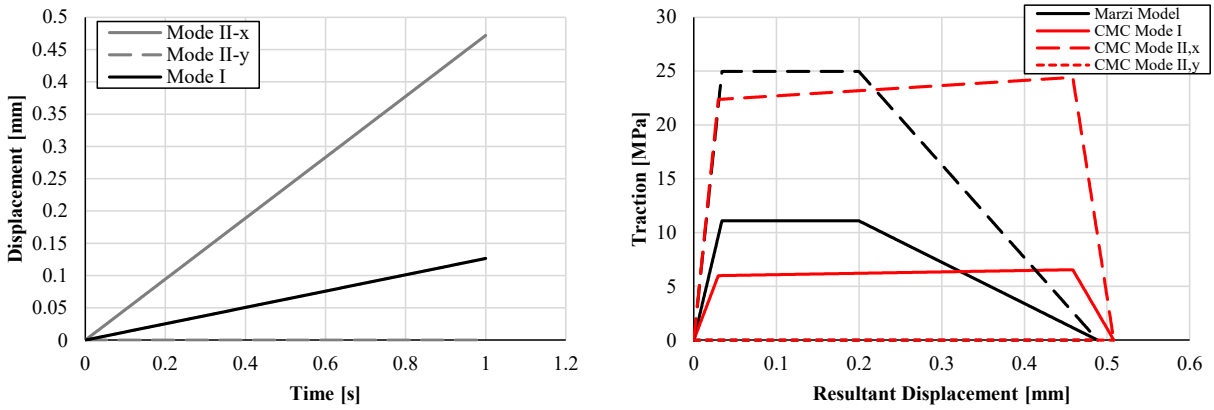

Figure B76: Input (left) and output (right) for 75 º mixed mode loading for 0.64 mm CZM element

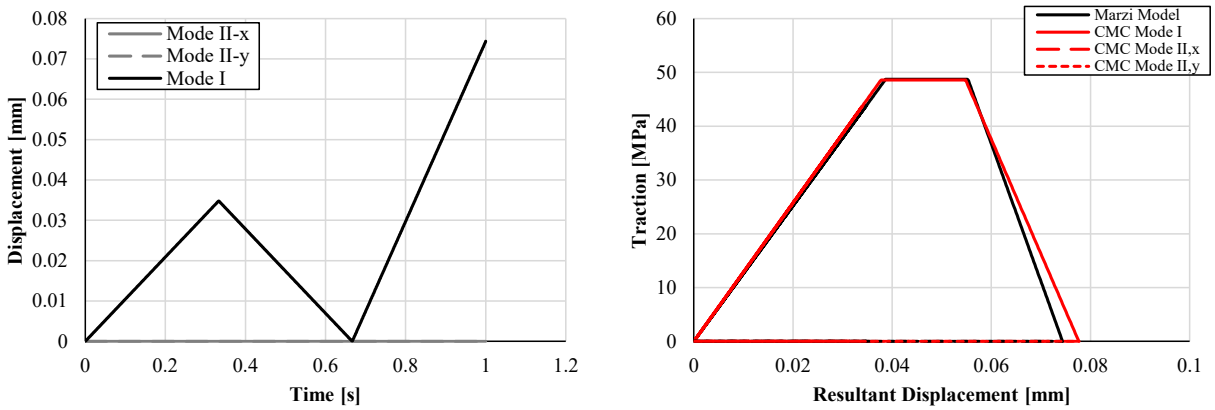

Figure B77: Input (left) and output (right) for Mode I load to segment I-unload-reload to failure cycle for 0.64 mm CZM element

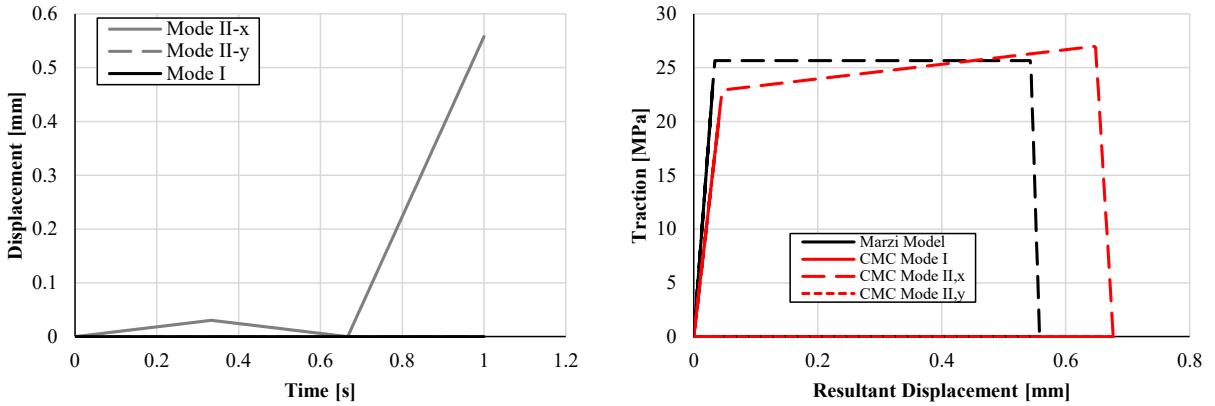

Figure B78: Input (left) and output (right) for Mode II load to segment I-unload-reload to failure cycle for 0.64 mm CZM element

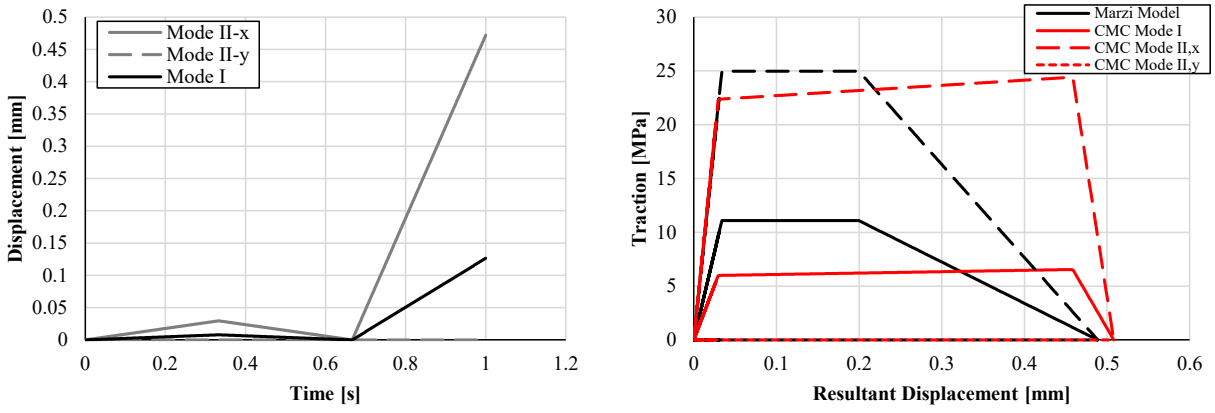

Figure B79: Input (left) and output (right) for 75 º mixed mode load to segment I-unload-reload to failure cycle for 0.64 mm CZM element

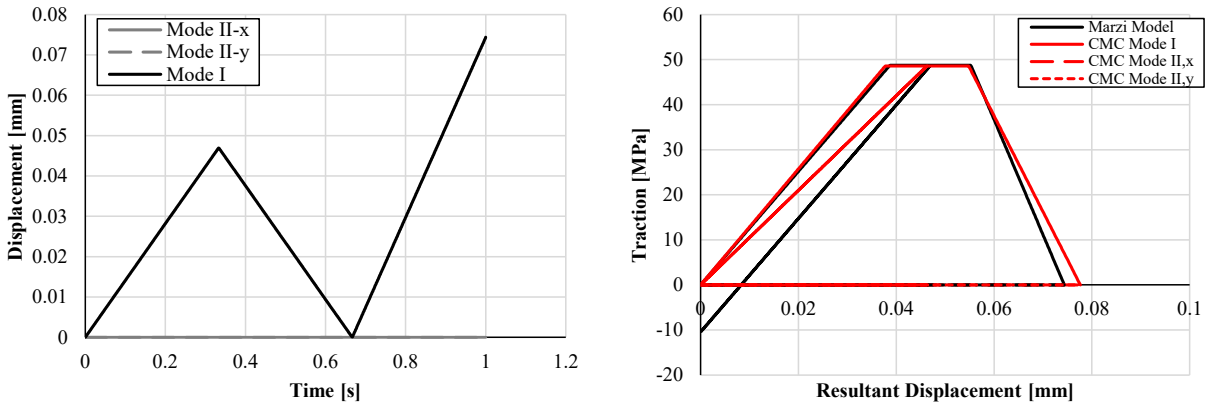

Figure B80: Input (left) and output (right) for Mode I load to segment II-unload-reload to failure cycle for 0.64 mm CZM element

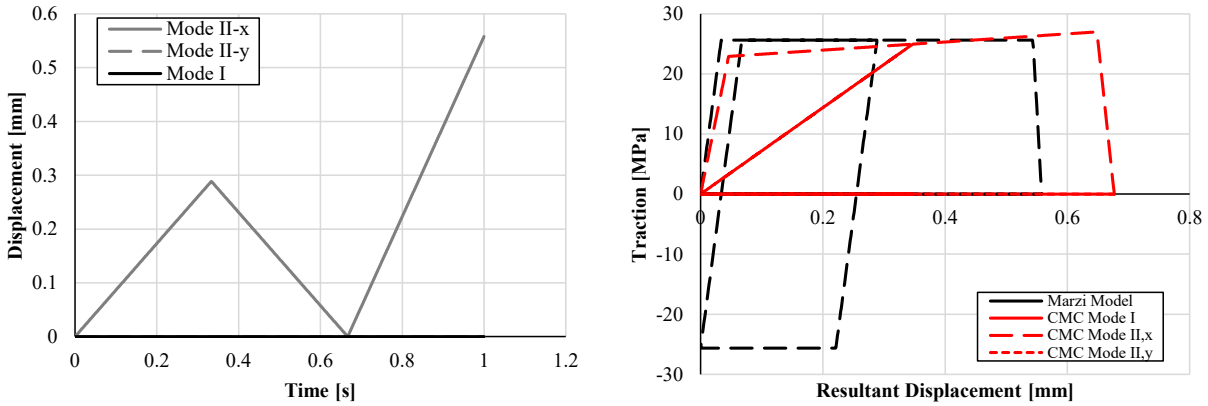

Figure B81: Input (left) and output (right) for Mode II load to segment II-unload-reload to failure cycle for 0.64 mm CZM element

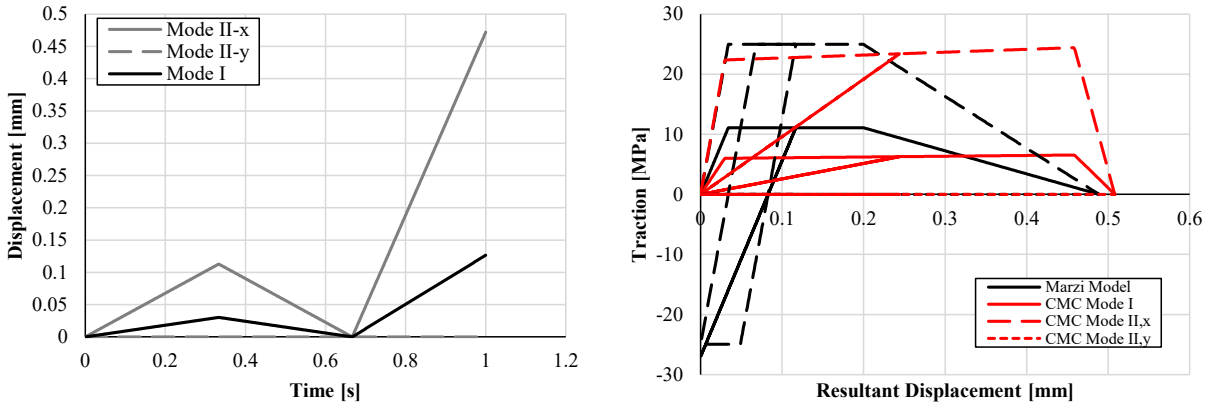

Figure B82: Input (left) and output (right) for 75 º mixed mode load to segment II-unload-reload to failure cycle for 0.64 mm CZM element

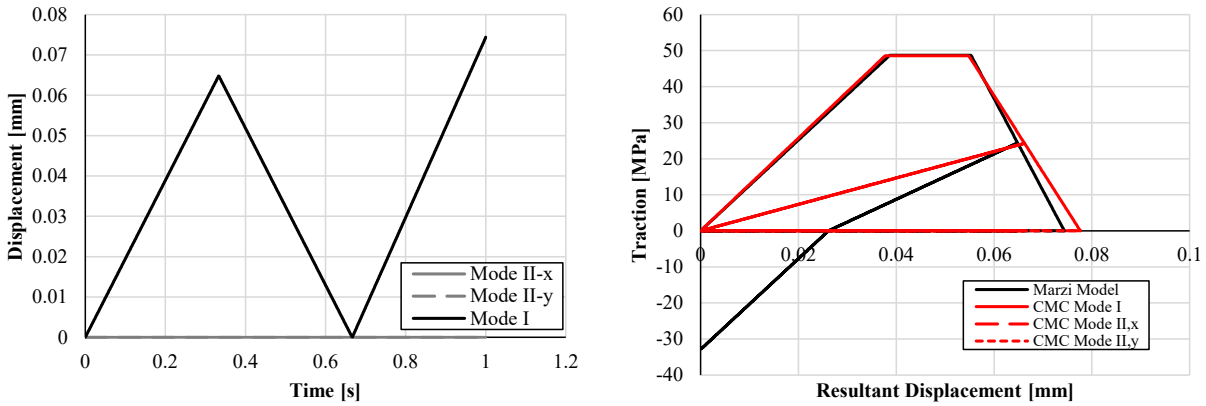

Figure B83: Input (left) and output (right) for Mode I load to segment III-unload-reload to failure cycle for 0.64 mm CZM element

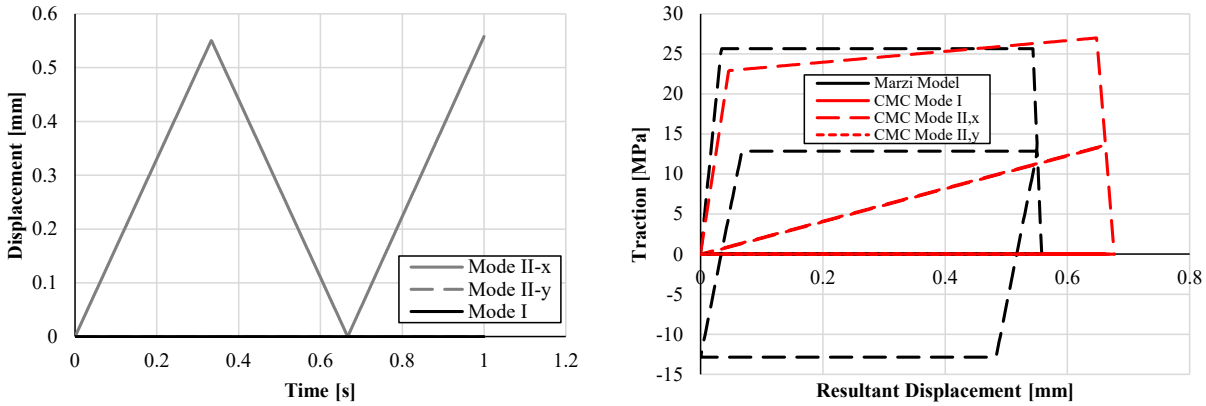

Figure B84: Input (left) and output (right) for Mode II load to segment III-unload-reload to failure cycle for 0.64 mm CZM element

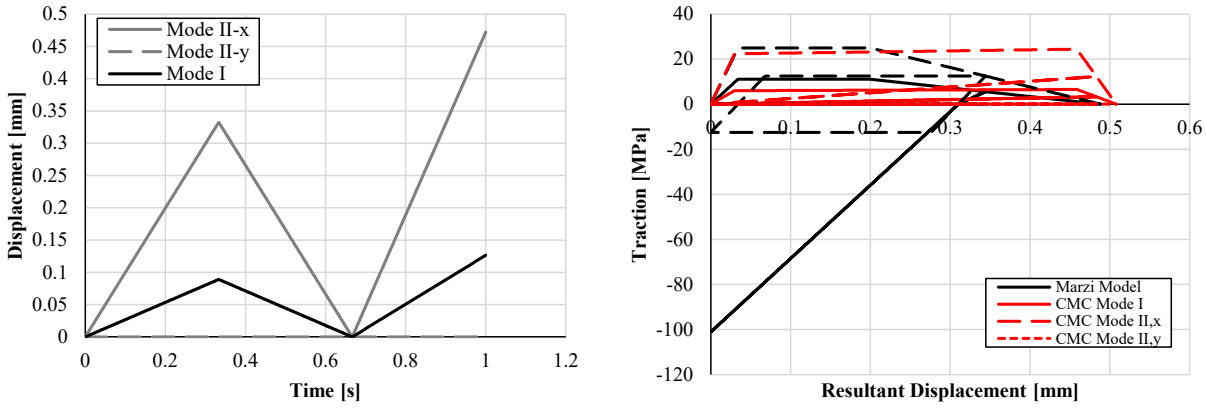

Figure B85: Input (left) and output (right) for 75 º mixed mode load to segment III-unload-reload to failure cycle for 0.64 mm CZM element

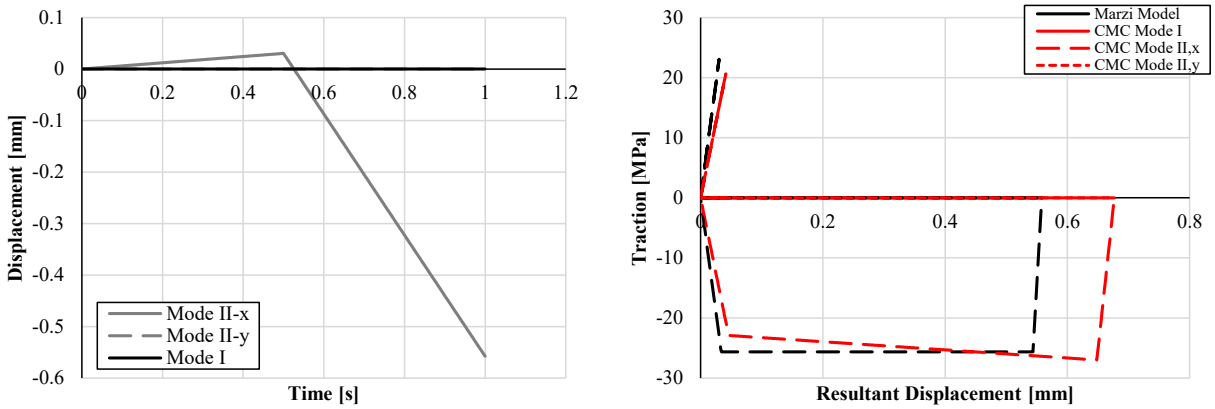

Figure B86: Input (left) and output (right) for Mode II load to segment I-unload-full reversal to failure cycle for 0.64 mm CZM element

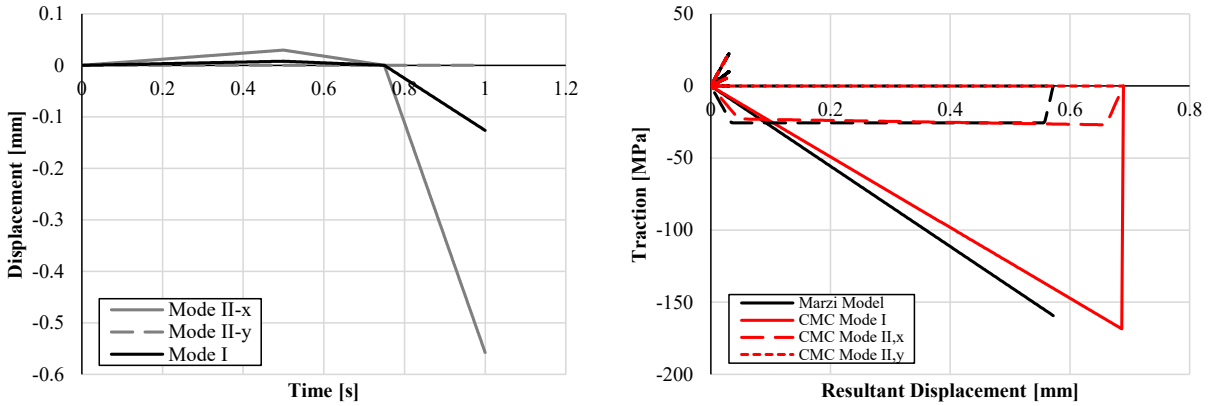

Figure B87: Input (left) and output (right) for 75 º mixed mode load to segment I-unload-full reversal to failure cycle for 0.64 mm CZM element

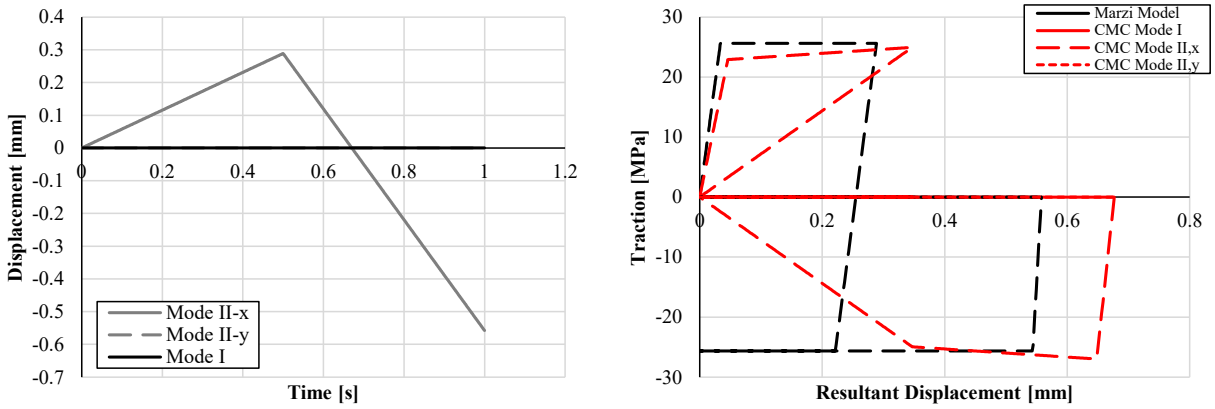

Figure B88: Input (left) and output (right) for Mode II load to segment II-unload-full reversal to failure cycle for 0.64 mm CZM element

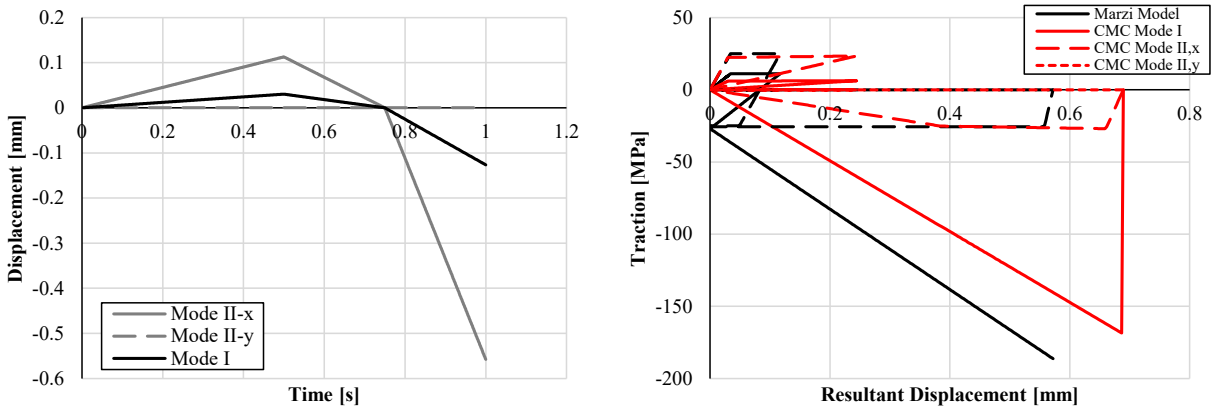

Figure B89: Input (left) and output (right) for 75 º mixed mode load to segment II-unload-full reversal to failure cycle for 0.64 mm CZM element

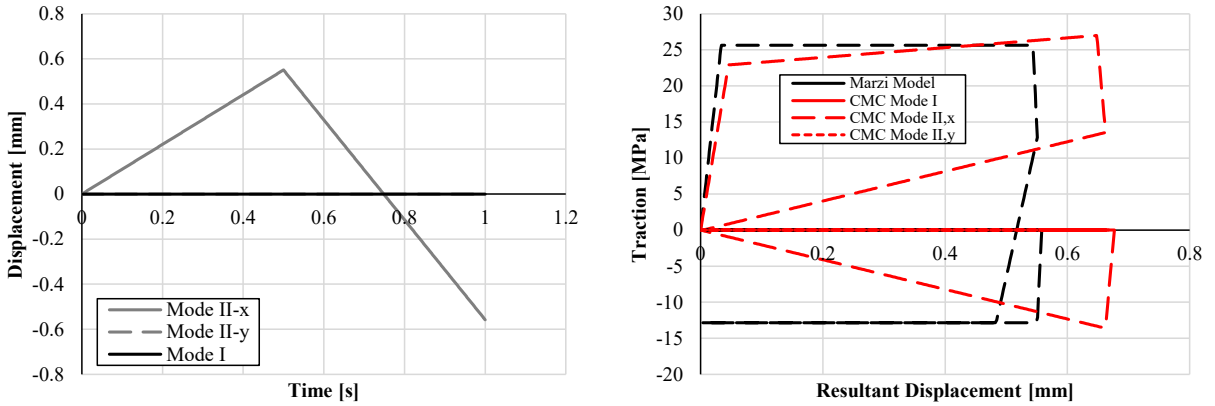

Figure B90: Input (left) and output (right) for Mode II load to segment III-unload-full reversal to failure cycle for 0.64 mm CZM element

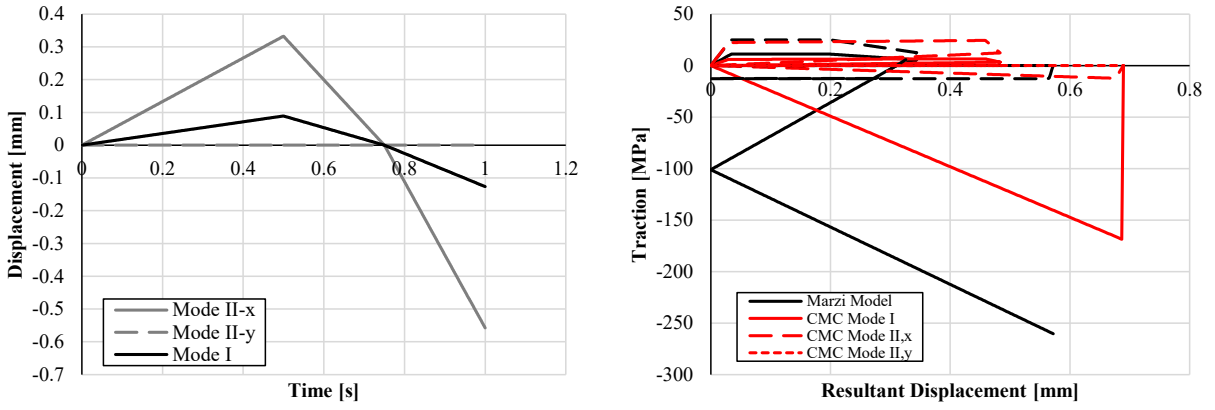

Figure B91: Input (left) and output (right) for 75 º mixed mode load to segment III-unload-full reversal to failure cycle for 0.64 mm CZM element

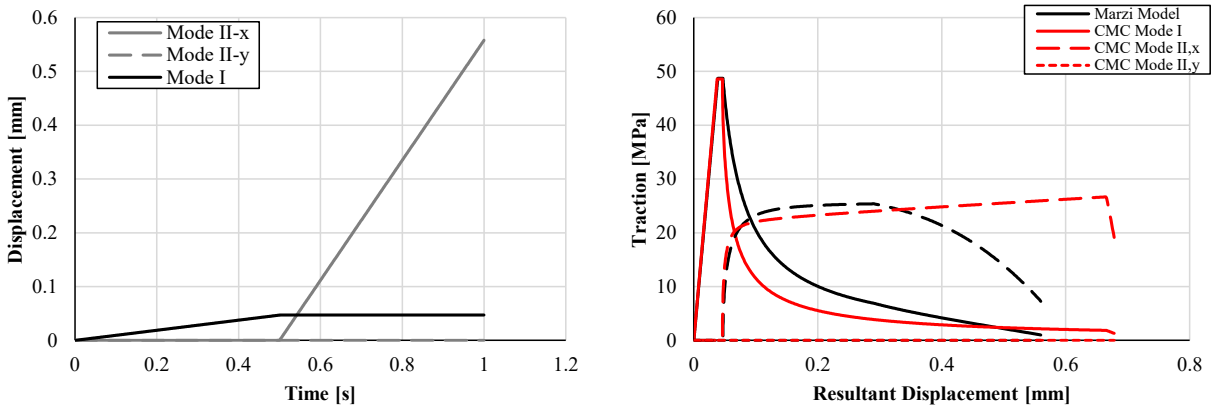

Figure B92: Input (left) and output (right) for arrested Mode I (Segment 2) loading followed by Mode II loading in positive 1 direction for 0.64 mm CZM element

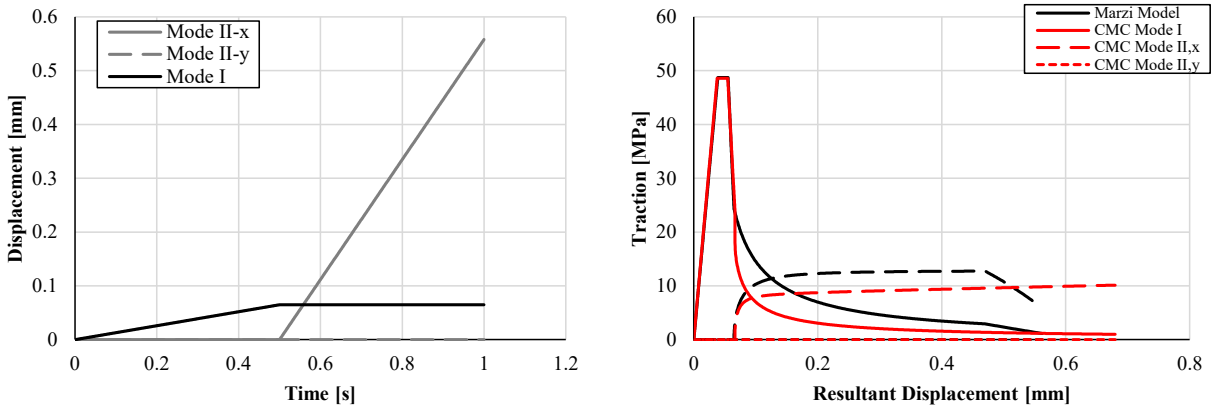

Figure B93: Input (left) and output (right) for arrested Mode I (Segment 3) loading followed by Mode II loading in positive 1 direction for 0.64 mm CZM element

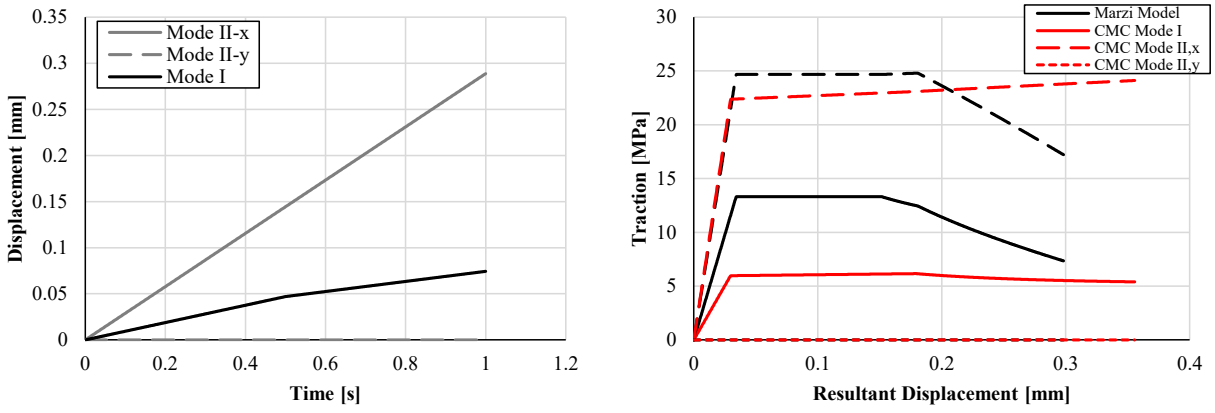

Figure B94: Input (left) and output (right) for constant Mode II velocity and variable Mode I velocity loading for 0.64 mm CZM element

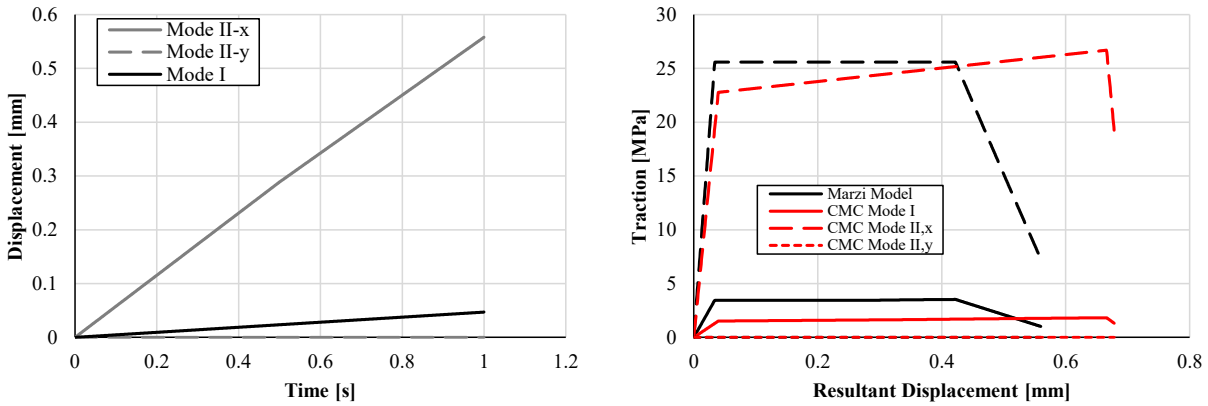

Figure B95: Input (left) and output (right) for variable Mode II velocity and variable Mode I velocity loading for 0.64 mm CZM element

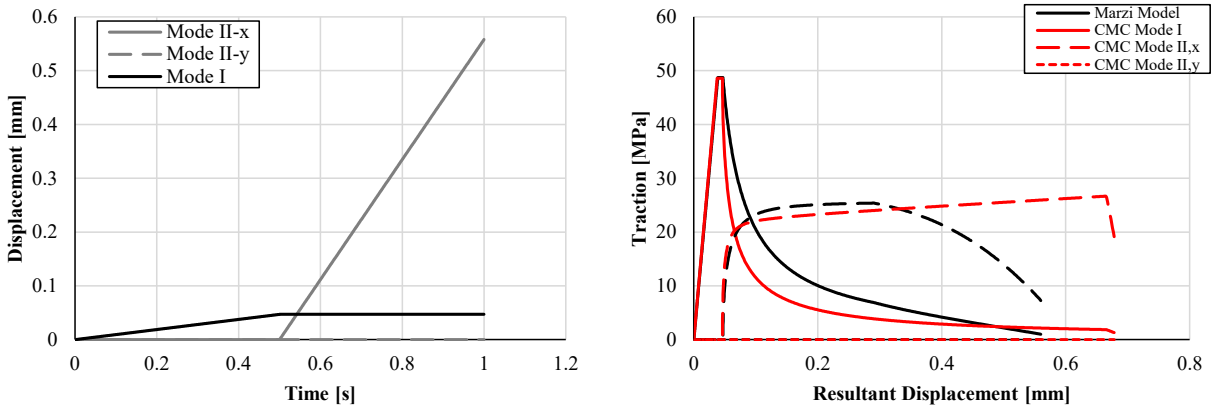

Figure B96: Input (left) and output (right) for tensile Mode I loading (Segment 2) with additional Mode II loading in the positive 1 direction for 0.64 mm CZM element

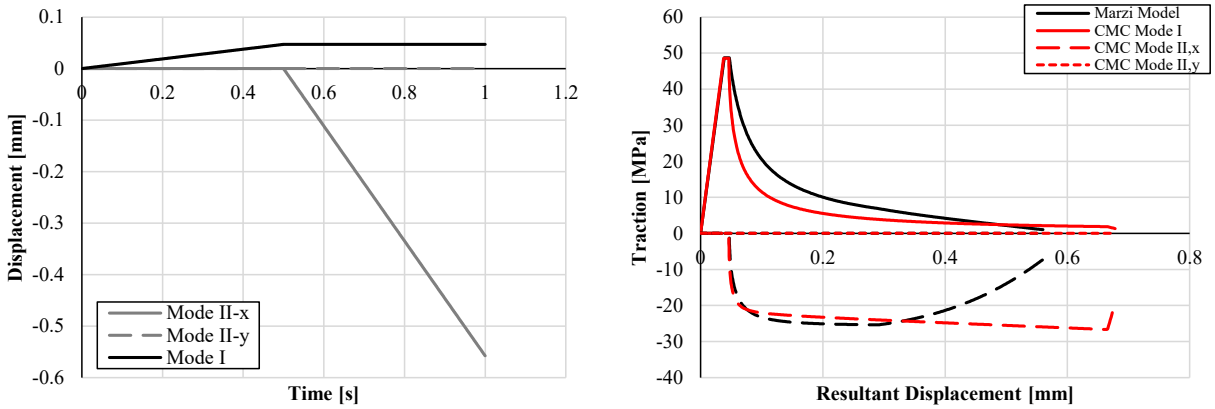

Figure B97: Input (left) and output (right) for tensile Mode I loading (Segment 2) with additional Mode II loading in the negative 1 direction for 0.64 mm CZM element

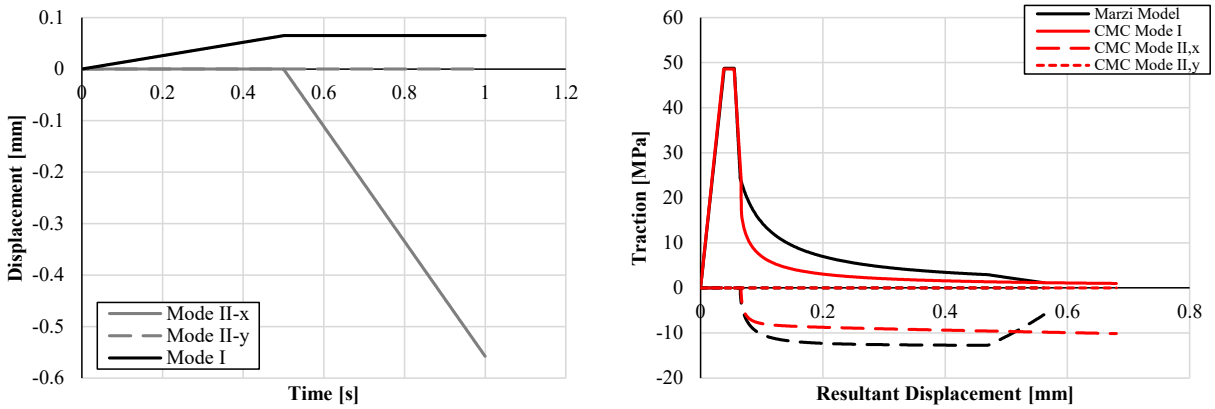

Figure B98: Input (left) and output (right) for tensile Mode I loading (Segment 3) with additional Mode II loading in the negative 1 direction for 0.64 mm CZM element

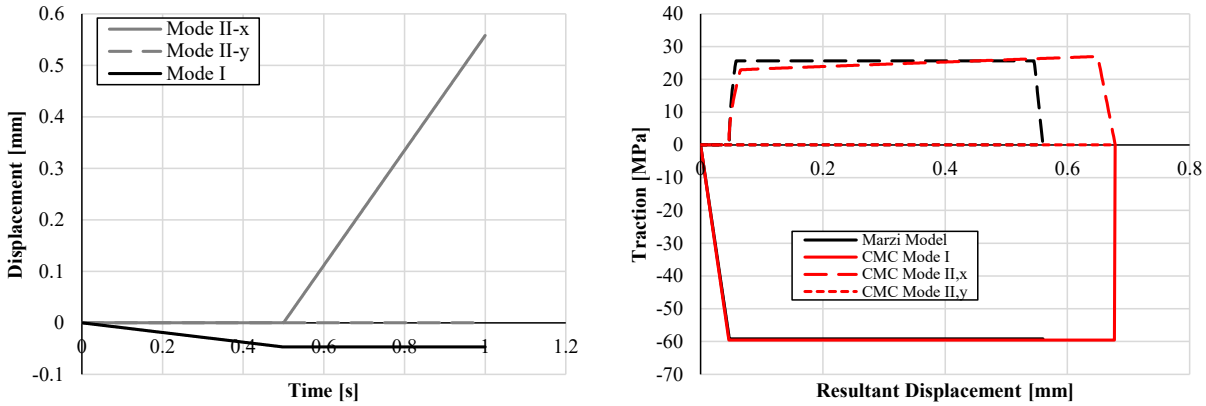

Figure B99: Input (left) and output (right) for compressive Mode I loading (Segment 2) with additional Mode II loading in the positive 1 direction for 0.64 mm CZM element

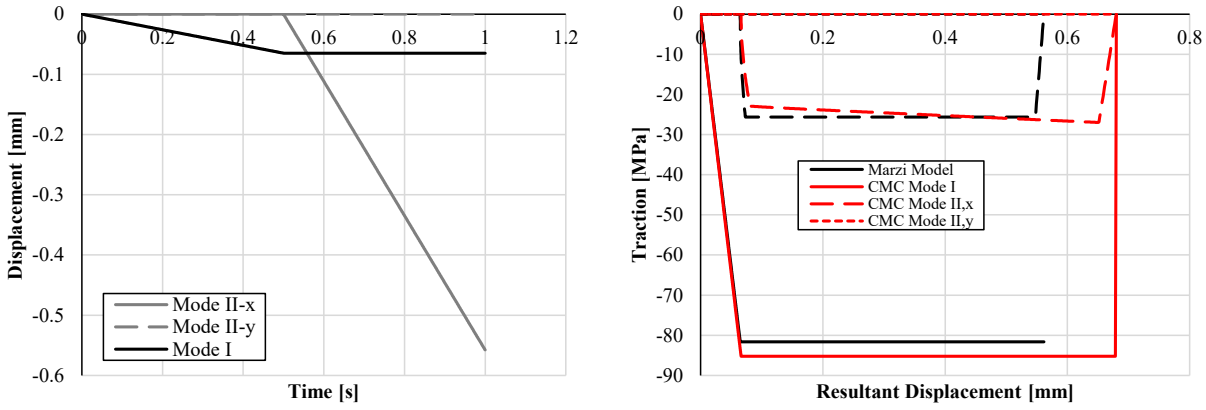

Figure B100: Input (left) and output (right) for compressive Mode I loading (Segment 3) with additional Mode II loading in the negative 1 direction for 0.64 mm CZM element

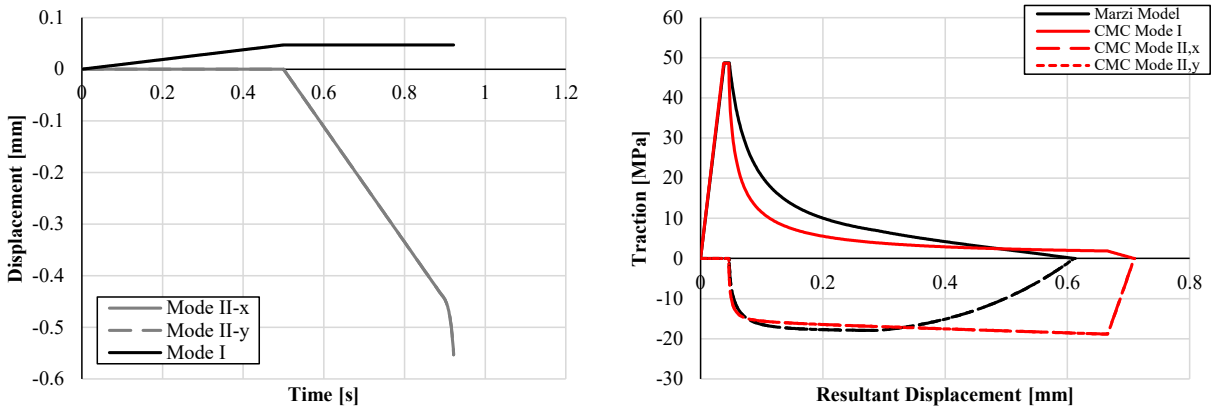

Figure B101: Input (left) and output (right) for tensile Mode I loading (Segment 2) with added equal Mode II loading in the negative 1 and 2 directions for 0.64 mm CZM element

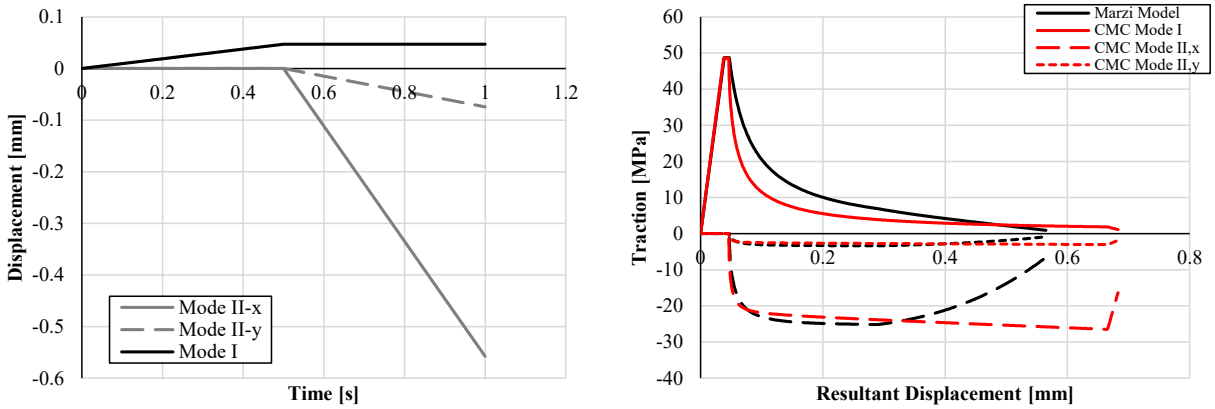

Figure B102: Input (left) and output (right) for tensile Mode I loading (Segment 2) with added unequal Mode II loading in negative 1 and 2 directions for 0.64 mm CZM element

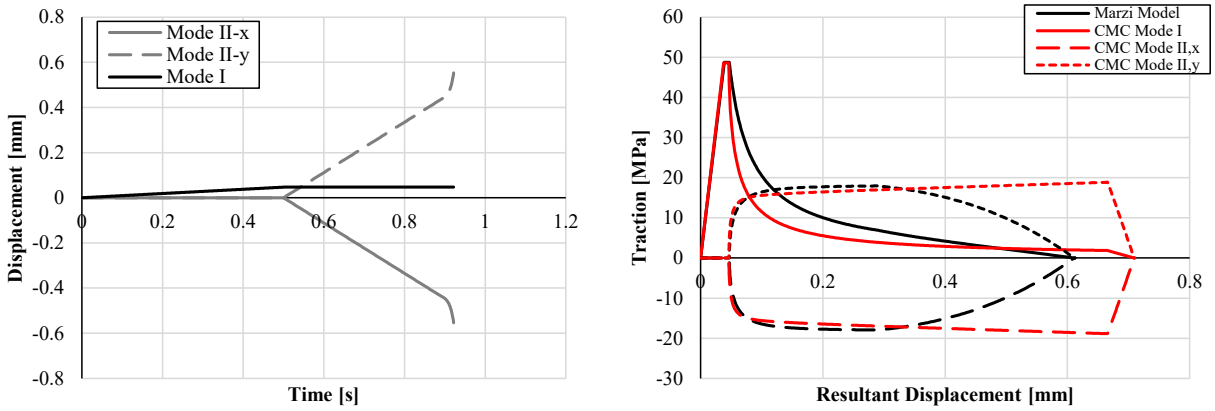

Figure B103: Input (left) and output (right) for tensile Mode I loading (Segment 2) with added unequal Mode II loading in positive 1 and negative 2 directions for 0.64 mm CZM element

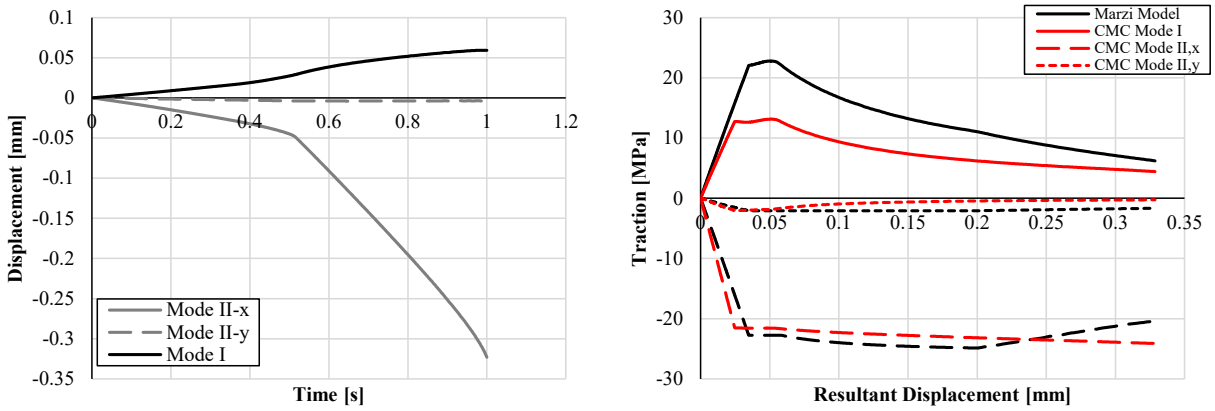

Figure B104: Input (left) and output (right) for loading extracted from a model of a UHSS – UHSS single lap shear test for 0.64 mm CZM element

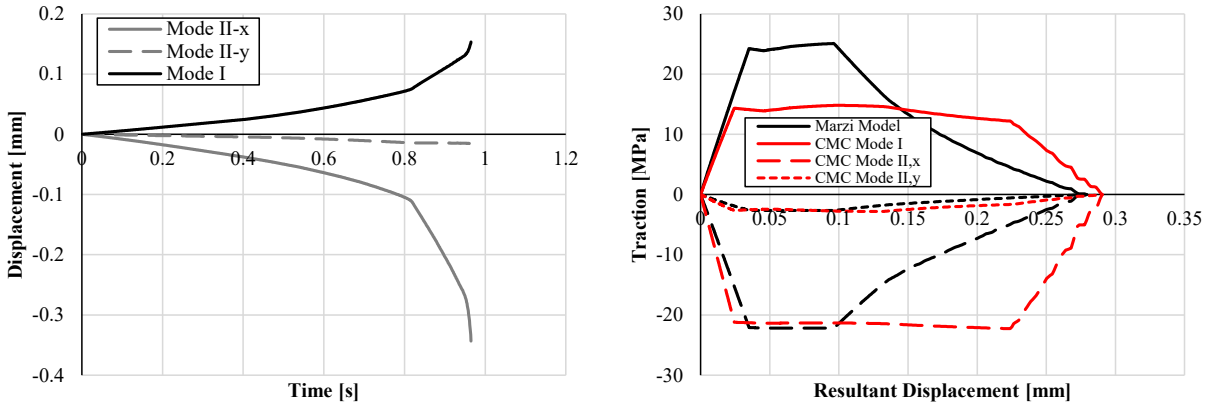

Figure B105: Input (left) and output (right) for loading extracted from a model of an aluminum – aluminum single lap shear test for 0.64 mm CZM element

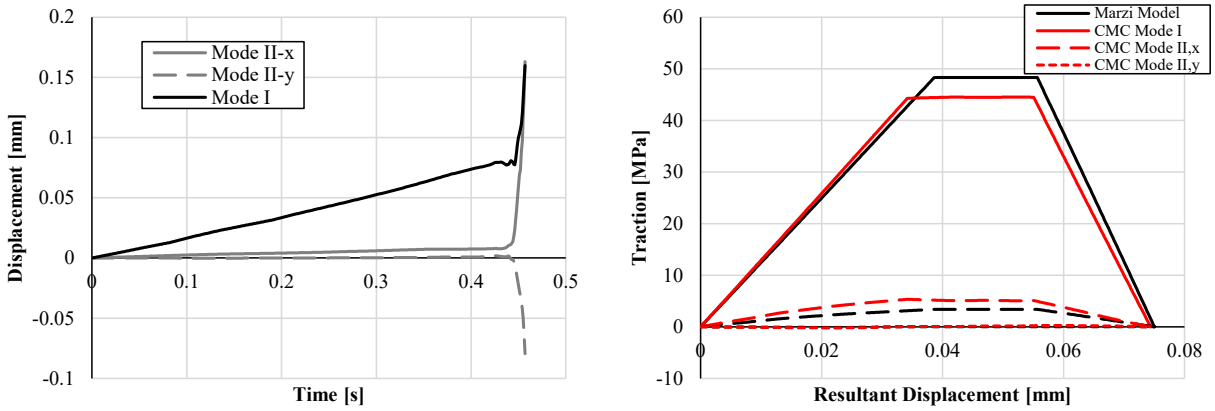

Figure B106: Input (left) and output (right) for loading extracted from a model of a UHSS – aluminum single lap shear test for 0.64 mm CZM element

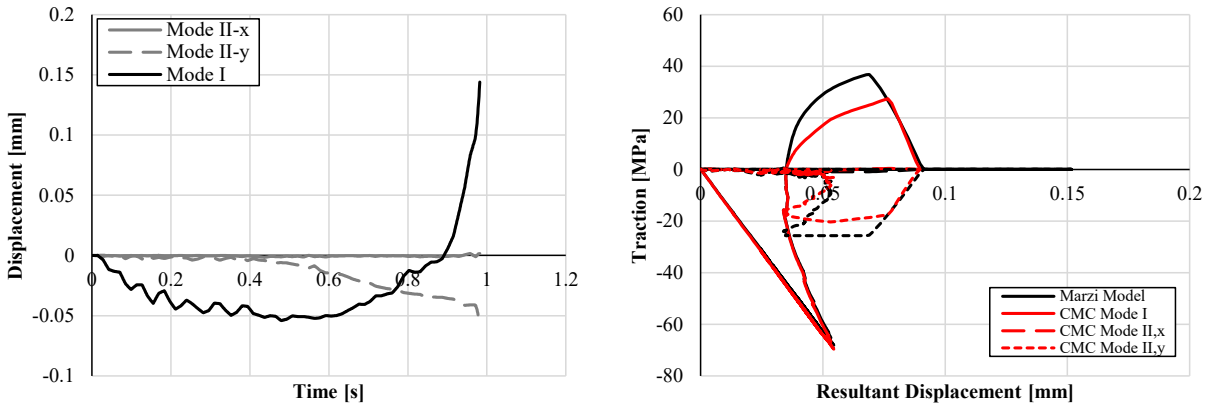

Figure B107: Input (left) and output (right) for loading extracted from a model of an adhesively bonded UHSS axial crush tube for 0.64 mm CZM element

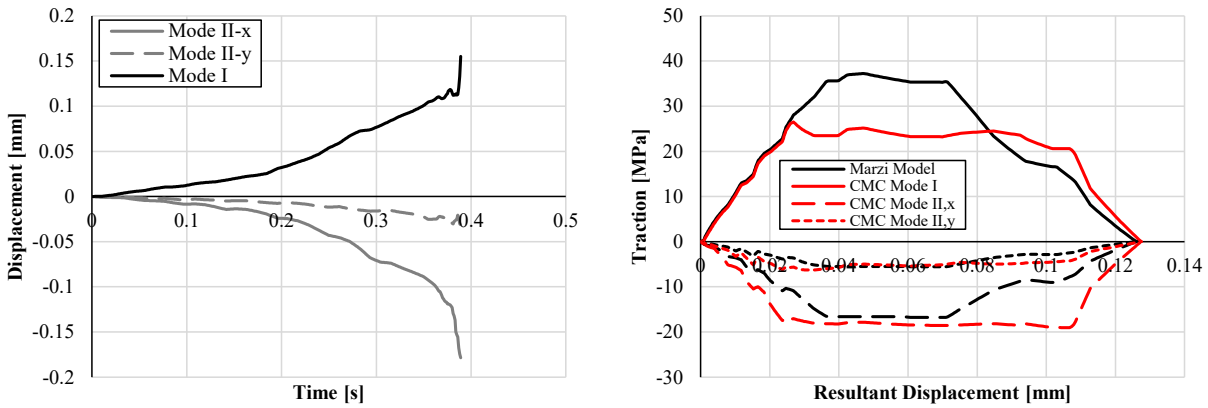

Figure B108: Input (left) and output (right) for loading extracted from a model of an adhesively bonded UHSS 3-point bend test for 0.64 mm CZM element

Appendix C – Letters of Copywrite Permission

C1: License for Figure 2a

ELSEVIER LICENSE
TERMS AND CONDITIONS
Jul 29, 2020

This Agreement between University of Waterloo -- Brock Watson ("You") and Elsevier ("Elsevier") consists of your license details and the terms and conditions provided by Elsevier and Copyright Clearance Center.

License Number	4878360519116
License date	Jul 29, 2020
Licensed Content Publisher	Elsevier
Licensed Content Publication	Engineering Fracture Mechanics
Licensed Content Title	Identification of a new failure criterion for toughened epoxy adhesive
Licensed Content Author	D. Morin,G. Haugou,B. Bennani,F. Lauro
Licensed Content Date	Nov 1, 2010
Licensed Content Volume	77
Licensed Content Issue	17
Licensed Content Pages	20
Start Page	3481
End Page	3500
Type of Use	reuse in a thesis/dissertation
Portion	figures/tables/illustrations
Number of figures/tables/illustrations	1
Format	both print and electronic
Are you the author of this Elsevier article?	No
Will you be translating?	No
Title	PhD Thesis
Institution name	University of Waterloo
Expected presentation date	Dec 2020
Portions	Figure 30
Requestor Location	University of Waterloo 200 University Ave W Waterloo, ON N2L 3G1 Canada
Publisher Tax ID	GB 494 6272 12

C2: License for Figure 2b

ELSEVIER LICENSE
TERMS AND CONDITIONS
Jul 29, 2020

This Agreement between University of Waterloo -- Brock Watson ("You") and Elsevier ("Elsevier") consists of your license details and the terms and conditions provided by Elsevier and Copyright Clearance Center.

License Number	4878360394380
License date	Jul 29, 2020
Licensed Content Publisher	Elsevier
Licensed Content Publication	International Journal of Adhesion and Adhesives
Licensed Content Title	Characterization and material model definition of toughened adhesives for finite element analysis
Licensed Content Author	J.A. García,A. Chiminelli,B. García,M. Lizaranzu,M.A. Jiménez
Licensed Content Date	Jun 1, 2011
Licensed Content Volume	31
Licensed Content Issue	4
Licensed Content Pages	11
Start Page	182
End Page	192
Type of Use	reuse in a thesis/dissertation
Portion	figures/tables/illustrations
Number of figures/tables/illustrations	1
Format	both print and electronic
Are you the author of this Elsevier article?	No
Will you be translating?	No
Title	PhD Thesis
Institution name	University of Waterloo
Expected presentation date	Dec 2020
Portions	Figure 3.4
Requestor Location	University of Waterloo 200 University Ave W Waterloo, ON N2L 3G1 Canada
Publisher Tax ID	GB 494 6272 12

C3: License for Figure 55

ELSEVIER LICENSE
TERMS AND CONDITIONS
Jul 31, 2020

This Agreement between University of Waterloo -- Brock Watson ("You") and Elsevier ("Elsevier") consists of your license details and the terms and conditions provided by Elsevier and Copyright Clearance Center.

License Number	4879410891064
License date	Jul 31, 2020
Licensed Content Publisher	Elsevier
Licensed Content Publication	Composites
Licensed Content Title	Matrix fractography of fibre-reinforced epoxy composites
Licensed Content Author	D. Purslow
Licensed Content Date	Oct 1, 1986
Licensed Content Volume	17
Licensed Content Issue	4
Licensed Content Pages	15
Start Page	289
End Page	303
Type of Use	reuse in a thesis/dissertation
Portion	figures/tables/illustrations
Number of figures/tables/illustrations	1
Format	both print and electronic
Are you the author of this Elsevier article?	No
Will you be translating?	No
Title	PhD Thesis
Institution name	University of Waterloo
Expected presentation date	Dec 2020
Portions	Figure 13
Requestor Location	University of Waterloo 200 University Ave W Waterloo, ON N2L 3G1 Canada
Publisher Tax ID	GB 494 6272 12